TECHNISCHE UNIVERSITÄT WIEN

DISSERTATION

Metal chalcogen based molecular clusters for light-driven hydrogen evolution reaction

ausgeführt zum Zwecke der Erlangung des akademischen Grades einer Doktorin der Naturwissenschaften unter der Leitung von

Uni. Prof. Dominik Eder
und
Asst. Prof. Alexey Cherevan

E165
Institut für Materialchemie

eingereicht an der Technischen Universität Wien
Fakultät für Technische Chemie

von

Samar Batool

12045098

Wien, am 14 Februar 2024

Acknowledgement

I would like to express my heartfelt gratitude to the following individuals and organizations, without whom the completion of this thesis would not have been possible:

First and foremost, I am deeply thankful to my supervisor, Prof. Dominik Eder for enabling my Ph.D. journey by offering me the position of "Project Assistant". Our discussions, filled with agreements and disagreements, have consistently provided me with insightful ideas on how to advance my work. I would like to especially thank my co-supervisor and mentor Asst. Prof. Alexey Cherevan, for his unwavering support, invaluable mentorship, and guidance throughout my research journey. His wisdom and expertise have been instrumental in shaping my academic and research pursuits.

I extend my appreciation to my lab colleagues (Stephen Myakala, Pablo Ayala, Jasmin Schubert) and fellow researchers for their significant contributions to my research. Their dedication and collaboration have enriched the depth and scope of my work. My sincere thanks go to my collaborators, who have expanded the horizons of my research beyond the boundaries of my main project. Their insights and shared expertise have been truly enlightening. I am also grateful to the funding bodies that provided financial support for my research endeavors. Their investment has played a vital role in the realization of this work. I wish to acknowledge the support of TU Wien, which provided me with research infrastructure enabling me to accomplish my research projects and facilitated my participation in conferences in order to disseminate my research findings and establish valuable connections for future collaborations.

To my dear friends, whose presence in my life has been a source of immense comfort and joy. Thanks to them for making life outside of work enjoyable, for traveling with me, cooking delicious meals, sharing laughter, and offering encouragement during challenging times. I owe an immeasurable debt of gratitude to my parents. Their unwavering support, encouragement to explore new horizons, and being my backbone in every sense have been the pillars of my journey. Last, but certainly not least, I want to express my deepest thanks to my husband. His unwavering support, readiness to be there whenever I needed him, and the small gestures like serving me food in bed during the intense phases of thesis writing have made all the difference. His celebrations of every milestone I achieved during my PhD have been a constant source of motivation.

To all the individuals, I extend my heartfelt thanks for being an integral part of my academic and personal journey, and for contributing to the successful completion of this thesis.

Lastly, I would like to express gratitude to the generative AI tools (Chatgpt, elicit, etc.) that I used to improve the writing of this thesis as well as to skim through and find the relevant literature.

"Everything you've ever wanted is on the other side of fear." George Addair

Contents

Abstract

The rising global energy demand and the depletion of fossil fuels with associated sustainability challenges and global warming require the exploration of efficient and renewable energy sources. Photocatalytic water splitting is a viable strategy to produce green hydrogen using renewable resources. However, most of these renewable materials come from noble metals that are scarce and costly. Therefore, in this thesis earth abundant chalcogenide-based molecular clusters (polyoxometalates and thiomolybdates) are investigated as catalysts/co-catalysts for photocatalytic hydrogen evolution reaction (HER).

In the first part of this thesis, I present an extensive review of the relevant field featuring examples from literature employing thiomolybdates for electrocatalytic and photocatalytic hydrogen evolution reaction. This review discusses the active sites of the thiomolybdate cluster responsible for hydrogen evolution reaction in homogeneous and heterogeneous phases. It further highlights the possible reaction mechanisms, heterogenization on different substrates, and the structure-activity relationship.

The first experimental project of this thesis was to examine the photocatalytic hydrogen evolution performance of a homogeneous photosystem by employing molecular clusters as catalysts i.e. novel Ni-based POMs ($Ni_{12}W_{27}$ and $Ni_{12}W_{30}$) in our case. I show that the HER performance of these novel Ni-POMs surpasses the benchmark Ni_4W_{18} POM and is dependent on the number of cubane cores in the POM structure. The $Ni_{12}W_{30}$ POM exhibits an exceptional quantum yield of 10.42% which is so far the highest reported for Ni-based POMs. Furthermore, I investigate the HER mechanism through photoluminescence spectroscopy (PL) and demonstrate the factors that restrict the performance of Ni-POMs under turnover conditions. Since the stability of such a photosystem is compromised due to the use of organic photosensitizer, the next aim was to design a heterogeneous photocatalyst in which the molecular cluster is stabilized by attaching it to a light-absorbing solid-state oxide support. In the second experimental project of this thesis, I employed Mo_3S_{13} (Mo_3) cluster as a co-catalyst and titania (TiO_2) as a support and photosensitizer. The clusters are attached to titania by forming a strong Mo-O-Ti bond. I show that the attachment is strictly dependent on the surface area of support. The Mo_3/TiO_2 photocatalyst is shown to be highly active and stable suggesting that Mo_3 can effectively co-catalyze the hydrogen evolution reaction. Thermal treatment of Mo_3/TiO_2 photocatalyst under nitrogen and oxygen atmosphere lowered its activity. Therefore, it is concluded that the structural coherence and the original configuration of disulfide ligands are critical in determining the performance of co/catalyst.

The final project of this thesis was to develop a heterogeneous photosystem utilizing visible light absorbing support to allow for the direct comparison to the homogeneous photosystem featuring typical ruthenium photosensitizer (Mo_3/Ru). Therefore, I employ a metal-free carbon nitride support for the attachment of Mo_3 clusters to establish Mo_3/GCN heterogeneous photosystem. I optimize the hydrogen evolution reaction conditions of both the photosystems by changing the concentration/loading of the catalyst/co-catalyst and the kind of sacrificial donor used. Both the photosystems show similar turnover numbers (TOFs) per Mo_3 cluster. However, in terms of stability, the Mo_3/GCN photosystem outperforms the Mo_3/Ru photosystem. Therefore, I conclude that the homogeneous photosystem despite showing promising HER

activity is not stable compared to the heterogeneous photosystem.

Overall in this thesis, I combine and compare the homogeneous and heterogeneous photocatalytic approaches featuring molecular clusters and functional inorganic substrates to tackle the limitations of both photosystems. I further underline the significance of heterogenization to improve HER activity/stability and unravel reaction mechanisms/active sites. My research outcomes not only provide fundamental insights into the structure-activity relationship, performance, and stability but also lay the foundation to develop photosystems employing other complex molecular clusters to generate hydrogen fuel.

Aim and structure of this thesis

Hydrogen fuel holds enormous potential to meet the demand for renewable and environment-friendly energy sources. In this context, this thesis is primarily dedicated to explore the photocatalysts with the capacity to produce green hydrogen from water in the presence of sunlight. The main objective of this thesis is to investigate the hydrogen evolution reaction (HER) performance of earth-abundant transition metal chalcogenide-based catalysts i.e. polyoxometalates and thiometalates under homogeneous and heterogeneous conditions. This thesis further provides an experimental demonstration of bridging the homogeneous and heterogeneous photocatalytic approaches. To accomplish this task, TiO_2 is used as a model photocatalyst to immobilize the molecular thiomolybdate cluster as a co-catalyst. Furthermore, a comparative analysis is conducted to assess the photocatalytic HER performance of the thiomolybdate catalyst in solution, employing a ruthenium photosensitizer, in contrast to its performance when immobilized onto a carbon nitride support.

The first chapter of this thesis covers the fundamental concepts of photocatalysis specifically photocatalytic water splitting, homogeneous photocatalysis, and heterogeneous photocatalysis. The second chapter presents the motivation behind the research, providing a rationale and context for the study. The third chapter of this thesis covers the instruments and methods employed to characterize the materials and carry out photocatalytic experiments. In chapter four, as this thesis comprises a cumulative collection of published articles, the summary of all the published articles is elaborated with an emphasis on their notable contribution to the state-of-the-art. Finally, the last chapter outlines the conclusions of the research findings and highlights the potential future experimental work and open questions that can lead to the exploration of complex systems.

Introduction

1.1 Energy consumption and global warming

In the modern world, the global energy demand is escalating with the consumption of approximately 19 TW in the year 2023. The global energy market is dominated by 40% of biomass, followed by 21% of electricity, and 20% of natural gas.[1] The growing population of the world and rapid industrialization are driving factors to further increase energy usage with the prediction to reach 14000 million tonnes of crude oil by the year 2040.[2] Currently, 80% of the world's energy is produced by burning fossil fuels. Fossil fuels constitute of coal, oil, and natural gas with carbon as the main element, and the combustion of these fuels to generate energy produces greenhouse gases (GHGs). These gases (mainly CO_2) are capable of absorbing infrared radiations reflected by the earth's surface and persist in the environment for thousands of years, posing a potential threat of a 1.5°C increment in earth's current temperature by 2050.[3] This increase in temperature can have catastrophic impacts on the climate and the natural ecosystem. Furthermore, fossil fuels are consumed at a much faster rate than their natural replenishment leading to their gradual exhaustion and depletion. On the other hand, our planet receives a vast amount of solar energy - which is nontoxic and inexhaustible - making it the best candidate for producing renewable energy. Therefore, utilizing sunlight to generate clean and green hydrogen fuel by splitting water is a suitable alternative to reduce GHG emissions.

1.2 Green hydrogen

Hydrogen is the simplest and most abundant element on earth with H_2 having the highest specific energy density (120 MJ/kg) among all substances known. However, it rarely exists as a gas naturally but rather as a component of coal, natural gas, oil, water, and living things. Molecular hydrogen stores immense energy in its chemical bond which can used by internal combustion engines or fuel cells. At the industrial scale, most of the hydrogen is still produced by the gas reforming method. Green hydrogen is a clean renewable source that only produces water as a byproduct, versatile, storable, and 100% sustainable. Green hydrogen can be generated by the electrolysis of water that uses electrical energy to convert water into hydrogen fuel. However, the electrical energy used is not generated by renewable resources. The most effective method includes a photovoltaic solar cell coupled with a water electrolysis cell, that is able to generate green electricity to produce hydrogen. Nevertheless, the extensive use of solar cells is restricted due to their high cost and low efficiencies.[4] In contrast to these methods, photocatalysis is an attractive approach as it only uses solar power to split water into hydrogen fuel and oxygen, without requiring any external source of energy. At present, the poor efficiency of photocatalytic systems leads to their limited applications on an industrial scale. On account of this, scientists have dedicated efforts to explore materials capable of harnessing sunlight for

this reaction and gaining insights into the underlying mechanisms. The subject of this thesis focuses on the topic of photocatalysis to carry out hydrogen evolution reaction through the process of water splitting, making an effort to contribute to the evolution of green hydrogen technologies.

1.3 Fundamentals of photocatalysis

The word photocatalysis is derived from two terms: "**photo**" associated with photon and "**catalysis**" related to catalyst. A catalyst, according to the IUPAC, is defined as **"a substance that increases the rate of a reaction without modifying the overall standard Gibbs energy change in the reaction"**.[5] Therefore, photocatalysts are materials that can accelerate a chemical reaction by the absorption of light. The IUPAC defines the process of photocatalysis as **"change in the rate of a chemical reaction or its initiation under the action of ultraviolet, visible or infrared radiation in the presence of a substance - the photocatalyst - that absorbs light and is involved in the chemical transformation of the reaction partners"**.[5] This process was first observed and reported by Fujishima and Honda in 1972 by which they were able to split water into H_2 and O_2 by using TiO_2 and platinum photocatalysts.[6]

1.3.1 Artificial Photosynthesis

For billions of years, nature has utilized complex biochemical machinery to convert sunlight into usable energy, primarily through the reduction of carbon dioxide to carbohydrates and the oxidation of water to produce oxygen.[7,8] This process is crucial for sustaining life on earth, providing oxygen and food.[9] It also plays a key role in the global food chain and meets a significant portion of the world's energy needs. Efforts are being made to mimic natural photosynthesis through artificial systems, with the goal of improving efficiency and sustainability.[10] Numerous materials suggested for use in artificial photosynthetic systems suffer from inefficiency, lack of durability, high cost, and toxicity. Overcoming these challenges in artificial photosynthesis involves employing cost-effective and environmentally friendly compounds, similar to those used by nature in photosynthesis.[11] Therefore, the process of converting solar energy to chemical energy by mimicking the natural phenomena of photosynthesis is termed as artificial photosynthesis as shown in the figure 1.1.[12]

The typical chemical reactions involved in artificial photosynthesis are: (i) visible-light-driven water splitting process to generate hydrogen fuel, and (ii) the carbon dioxide reduction reaction to form C_1, C_2 based products like methane and methanol (figure 1.2). The solar-to-fuel conversion can be carried out using photocatalysis, photoelectrocatalysis, electrocatalysis, electrolysis, photovoltaic cells etc. The ultimate goal of the diverse artificial photosynthetic approaches is to produce sustainable and clean energy, tackling the challenge of global warming by utilizing renewable resources.

1.3.2 Photocatalytic water splitting

Photocatalytic splitting water is a commonly used method to generate hydrogen fuel. Water splitting has two half-reactions: hydrogen evolution reaction (HER) and oxygen evolution reaction (OER) as described in the equations below:

$$2\,H^+ + 2\,e^- \longrightarrow H_2 \tag{1.1}$$

$$2\,H_2O + 4\,h^+ \longrightarrow 4\,H^+ + O_2 \tag{1.2}$$

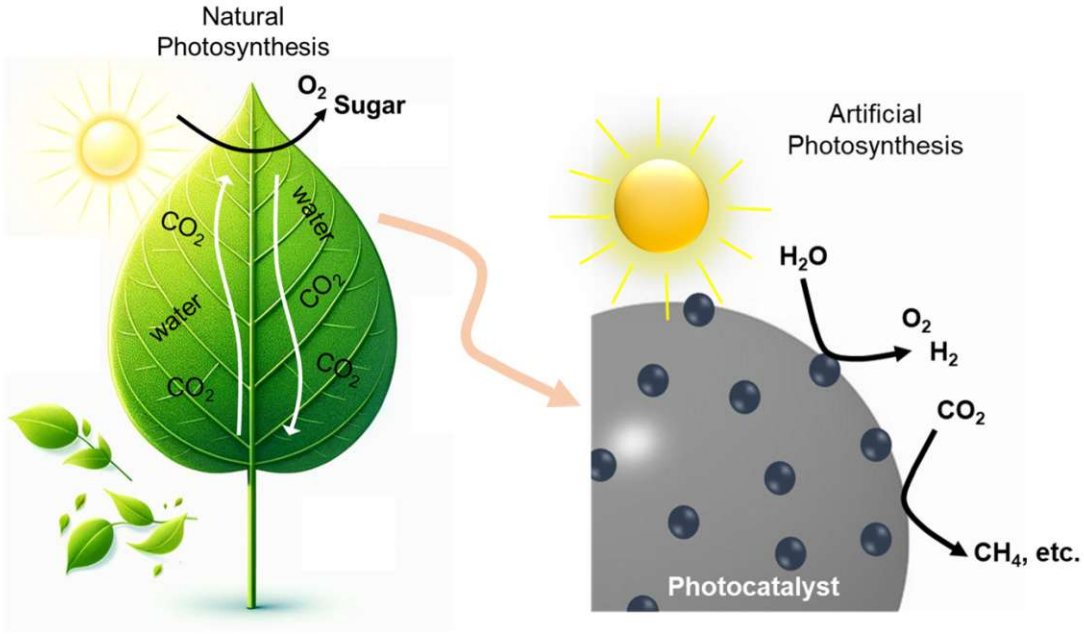

Figure 1.1: Natural photosynthesis vs. Artificial photosynthesis.

The overall water splitting reaction occurs at the surface of the photocatalyst by the photoabsorption and subsequent generation of electrons in the conduction band and holes in the valence band of a semiconductor (figure 1.2a). The electron-hole pair has strong reduction and oxidation potential that can be utilized for the water-splitting reaction. The overall water splitting consumes two electrons or four holes to generate one molecule of hydrogen or oxygen. This is plausible if the conduction band of the photocatalyst is more negative compared to the H^+/H_2 (0 V vs standard hydrogen electrode (SHE) at pH = 0), and the valence band of photocatalyst is more positive than the oxidation potential of O_2/H_2O (+1.23 V vs SHE at pH = 0) (figure 1.2b). Therefore, the theoretical minimum photon energy required is 1.23 eV, which is equivalent to a wavelength of approximately 1000 nm and lies in the near-infrared range. However, the overpotential is required to cross this energy barrier of redox reactions between charge carriers and water molecules. Thus, a photocatalyst with a band gap larger than the minimum requirement of 1.23 eV should be utilized. The solar spectrum constitute of 52-55 % infrared light (above 700 nm), 42-43 % visible light (400–700 nm), and 3-5 % ultraviolet light (below 400 nm). Therefore, the band gap of photocatalysts should be narrower than 3.1 eV to harvest more visible light from the solar spectrum but also exhibit a sufficiently low overpotential, to ensure a reasonably efficient overall water splitting reaction.[13] However, it is a challenging task due to the intrinsic constraints of the photocatalyst used such as charge recombination, catalytic active sites, light absorption capabilities, and photocorrosion etc.[14,15]

The efficiency of photocatalytic water splitting can be determined by evaluating the performance of overall water splitting without using sacrificial agents. However, there are certain obstacles to accomplish this reaction i.e. (i) the activation barrier generated due to the back reaction of hydrogen and oxygen to reproduce water, (ii) the Gibbs free energy required for overall water splitting is +237.13 kJ/mol which is not favored thermodynamically, and (iii) both the reduction and oxidation half-reactions are rate-limiting steps as they are multistep processes and involve different number of electrons and holes. Therefore, these limitations can be circumvented by introducing sacrificial reagents to the oxidation or reduction half-reactions that can efficiently capture photogenerated holes or electrons in order to prevent these half-reactions from being the rate-limiting steps. For example, methanol is the sacrificial donor for hydrogen evolution reaction and it reacts with water to generate CO_2 and H_2.[17–19] The use of

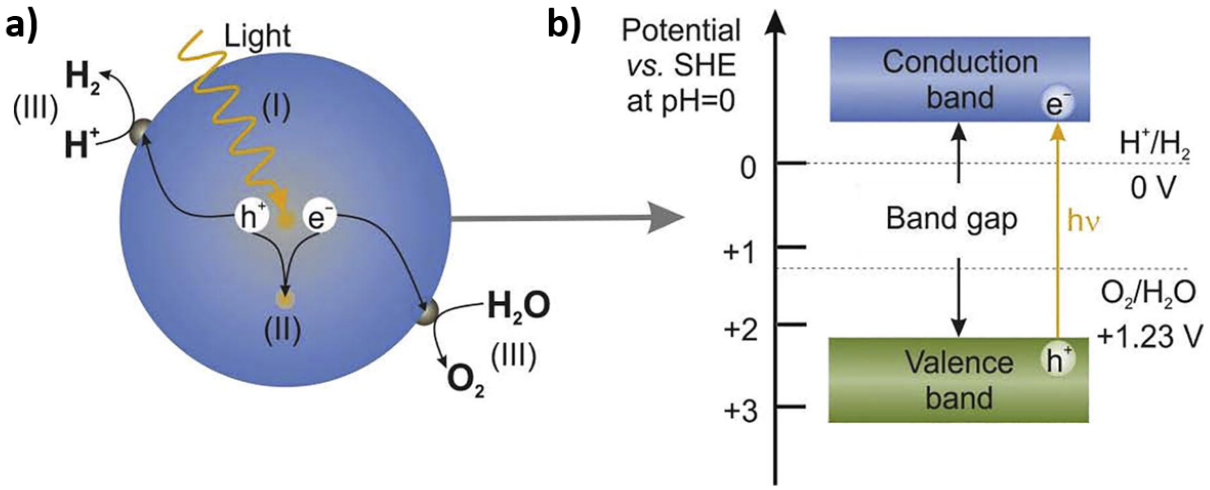

Figure 1.2: a) Steps of the photocatalytic process: (1) absorption of light, (2) generation of charge carriers and their migration to the surface, and (3) the corresponding chemical reaction. b) Depiction of photocatalyst band positions with respect to oxidation and reduction potential of water.[16]

methanol significantly reduces Gibb's free energy of the reaction, inhibits the back reaction as it produces CO_2 instead of O_2, and reduces the charge recombination by efficient scavenging of holes.[20] Therefore, sacrificial water splitting is a promising approach to investigating the HER performance of a photocatalyst.

1.3.3 Mechanism of HER

The process of hydrogen evolution reaction is a two-electron transfer process that occurs in two steps. The first of HER is the Volmer step or discharge step. It involves the transfer of electrons to the adsorbed hydrogen ions (H^+), resulting in the formation of hydrogen intermediates (H^*) bound to the catalyst surface. Considering the acidic pH of the solution, this process can be expressed as follows:

$$H^+ + e^- + {}^* \longrightarrow H^* \tag{1.3}$$

After this step, the molecular hydrogen H_2 is generated via two distinct reaction pathways, depending on the coverage of (H^*) on the surface. In the case of low surface coverage, H_2 will form following electrochemical desorption which is termed as Heyrovsky reaction. In this reaction, another electron is transferred to the adsorbed hydrogen coupled with the transfer of another proton from the solution to release molecular H_2 as shown in the chemical equation below:

$$H^+ + e^- + H^* \longrightarrow H_2 + {}^* \tag{1.4}$$

However, when the surface coverage is high, hydrogen is formed by coupling two adjacent hydrogen atoms adsorbed on the surface. This step is termed as Tafel reaction and is unaffected by of solution pH. This reaction is expressed as follows:

$$2\,H^* \longrightarrow H_2 + 2\,{}^* \tag{1.5}$$

Regardless of the reaction mechanism, it is clear that hydrogen intermediates H^* play a key role in every step of the process. Consequently, the Gibbs free energy of hydrogen adsorption (ΔGH^*) is an important indicator for assessing the efficiency of a HER catalyst. According to

the Sabatier principle,[21] and as empirically shown by Nørskov et al.,[22] the strength of the bond between the catalyst surface and hydrogen atoms should neither be too weak nor too strong. This suggests that achieving an ideal bond strength is essential for optimizing HER rates.

This thesis is devoted to investigate the photocatalytic hydrogen evolution reaction which can be done via two different approaches: homogeneous photocatalysis and heterogeneous photocatalysis. The choice of a particular approach depends on the type of catalyst used.

1.4 Homogeneous photocatalysis

In homogeneous photocatalysis, both the catalyst and reaction medium are in the same phase. In this case, a transition metal complex often plays the role of catalytically active specie or a photocatalyst that utilizes its photo- or redox chemistry to drive a chemical reaction. However, in this approach, the photocatalyst alone is not capable of catalyzing a light-activated process. Therefore, it requires an additional molecular component that is responsible for the light absorption step and is known as the photosensitizer (PS).

1.4.1 Molecular photosensitizers

It is important to consider various aspects while choosing a suitable photosensitizer:

- The absorption of light must initiate the excitation of electrons from the highest occupied molecular orbital (HOMO) of the PS to the lowest unoccupied molecular orbital (LUMO), generating the excited photosensitizer state (PS*).
- The PS* should be able to promote charge separation, meaning that the electrons must be segregated at different regions of the molecule, in order to reduce the charge recombination.
- The redox potentials of the photosensitizer and catalyst molecules must be aligned thermodynamically so that the PS* molecule can efficiently transport the excited electrons to the catalyst molecules to carry out the reduction reaction.

Considering these factors, molecules based on ruthenium and iridium polypyridyl complexes emerge as the most suitable choice to function as a photosensitizer. These complexes exhibit remarkable photophysical and redox properties, prolonged lifetime in the excited state, and photochemical stability, coupled with their ability to absorb light in the visible spectrum. A notable example in homogeneous photocatalysis for hydrogen evolution reaction include $[Ru(bpy)_3]^{2+}$ cation.[23,24] The $[Ru(bpy)_3]^{2+}$ complex features a slightly distorted octahedral structure, with a Ru^{2+} ion at its core, attached to three bipyridyl ligands. Its absorption spectrum is characterized by three distinct peaks: firstly, at 250 nm, corresponding to a metal-to-ligand charge transfer (MLCT), followed by a strong ligand-centered (LC) peak at $\lambda = 300$ nm; secondly, at 350 nm, a weaker absorption peak indicative of the metal-centered transition; and thirdly, at around 450 nm, lies the prominent MLCT band in the visible range, signifying the spin-allowed transition from the $d\pi$ orbital of the metal to the π^* orbital of the ligand.[25] Furthermore, it is highly luminescent with an emission at a wavelength of around 610 nm. This $[Ru(bpy)_3]^{2+}$ complex was utilized as a photosensitizer in the article # 4. For further details, refer to this particular article.

Additionally, Ir(III) complexes are capable of photoredox catalysis similar to $[Ru(bpy)_3]^{2+}$ and emerged as an attractive candidate to be used as photosensitizer due to several reasons: (1) tunability of photophysical and electrochemical properties by varying the cyclometalated

and/or ancillary ligands,[26,27] (2) they exhibit phosphorescence at room temperature with long-lived excited state (microsecond timescale), and (3) demonstrate greater ligand-field stabilization energy and a more stable/less dissociative triplet metal-centered (^{3}MC) state in comparison with Ru(II) complexes.[28] Ir(III) can be classified into four different categories based on their structures: (i) cationic Ir(III) complexes with general formula $[Ir(ppy)_2bpy]^+$ (ppy: phenylpyridine, bpy: bipyridine), (ii) neutral Ir(III) complexes with general formula $[Ir(ppy)_3]$, (iii) Ir(III) complexes having coumarin ancillary ligands, and (iv) Ir(III) complex conjugates based on bimetallic frameworks.[27] In this thesis, we employed $[Ir(ppy)_2(dtbbpy)]^+$ complex (fall in category ii) as a photosensitizer for photocatalytic hydrogen evolution reaction. For more details see the corresponding article.

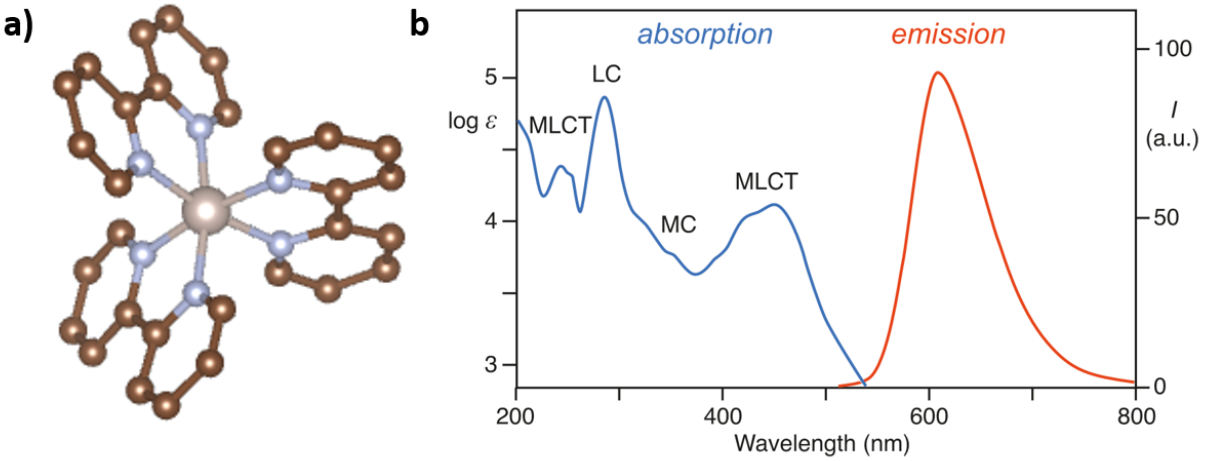

Figure 1.3: a) Structure of $[Ru(bpy)_3]^{2+}$ complex (grey: ruthenium, wine: carbon, blue: nitrogen, hydrogen atoms are removed for simplicity). b) Absorption and emission spectra of $[Ru(bpy)_3]^{2+}$ complex.[29]

The long-lived triplet excited state of the photosensitizer upon excitation allows for the efficient electron transfer to the catalyst, thereby, forming an excited photosensitizer molecule. The excited PS* molecule undergoes a regeneration process by oxidative or reductive quenching pathways, consequently, relaxing to the stable ground state. The charge transfer pathways can be estimated using Stern-Volmer quenching analysis of the quenched photosensitizers.[30] Thus, these photosensitizers are of great interest due to their unique photophysical and photochemical properties.

1.4.2 Molecular catalysts

In this thesis, our research is focused on inorganic molecular clusters: polyoxometalates (POMs) and thiometalates (PTMs), which formed the core catalytic elements of our homogeneous photosystems.

1.4.2.1 Polyoxometalates (POMs)

Polyoxometalates (POMs) are considered the molecular analogs of typical solid-state metal oxide materials. These are anionic clusters with their structure typically consists of transition metals (M), mostly tungsten (W), molybdenum (Mo), and vanadium (V), coordinated to oxo-ligands giving rise to oxo-anions of the general formula, $[MOy]^{n-}$ with y = 4-7. Here, y represents the coordination number of the addenda metal ion M which is usually 6, thus generating an octahedra MO_6. These octahedra are capable of aggregating during the synthesis by means

of oligo-condensation reaction to form multinuclear structures with general formula $[MxOy]^{m-}$. These multinuclear structural units often contain additional heteroatoms such as Si, P, As, and Ge, forming a polyoxometalate framework with general formula $[XzMnOy]^{q-}$ given the $z \leq n$. In the POM structure, the octahedra are interconnected via oxygen atoms at its corners, edges, or facets, offering a diverse range of structures. Therefore, various archetypes of POMs can be built and the most common ones are Anderson $[XM_6O_{24}]^{n-}$, Dawson $[X_2M_{18}O_{62}]^{n-}$, and Keggin $[XM_{12}O_{40}]^{n-}$ heteropolyanions. It is further possible to form a transition metal substituted polyoxometalate (TMSP) structure by sandwiching various metal ions between the principal structural units, giving rise to a versatile sandwich-type TMSP. An example of such TMSP POM is the first ever $[(Ru_4O_4(OH)_2(H_2O)_4)(SiW_{10}O_{36})_2]^{10-}$ POM reported for water oxidation catalysis, in which the RuO_4 unit is sandwiched between two lacunary SiW_4 units (figure).[31,32] Therefore, the structural modification and tunability of the POMs make them the most versatile class of inorganic materials.

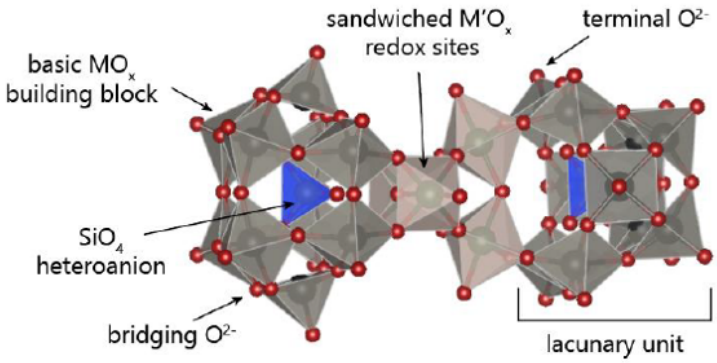

Figure 1.4: Structural representation of a sandwiched polyoxometalate cluster $[(Ru_4O_4(OH)_2(H_2O)_4)(SiW_{10}O_{36})_2]^{10-}$, consisting of the basic $[MO_6]$ building blocks (grey), $[SiO_4]$ heteroanion (blue), bridging and terminal $O_2{}^-$ ligands (red), sandwiched M'Ox redox sites, where M' is the transition metal ion. The dilacunary unit shown is $[SiW_{10}]$.

POMs showcase several distinctive features which include; (i) well-defined structure, (ii) structural compositions can be modified through the integration of heteroatoms with a variety of functionalities, (iii) significant acid-base strength, (iv) high redox activity, (v) high absorption in the near visible and UV region of solar spectrum, and (vi) highly soluble in aqueous and organic mediums. These qualities have triggered extensive research into the synthesis and design of POMs, progressively expanding their applications in thermal catalysis,[33] photo- and electrochemistry,[34–36] and fuel cell technology.

Over the past few decades, extensive research has been devoted to investigate POMs for homogeneous catalysis owing to their structural tunability and robustness against oxidative decomposition along with their diverse acid-base properties. Therefore, various transition metal-based POMs that mimic the cubane-like Fe_4S_4 cluster of natural photosystem I, have been designed by various scientists for photocatalytic hydrogen evolution reaction.[37–39] It is well known that among transition metals, Ni is known to be the ninth most abundant element on earth and is a highly efficient catalyst for hydrogen evolution reaction, serving as a cheaper alternative to noble metal platinum.[40,41] In nature, hydrogenase enzymes composed of earth-abundant metals (including Ni) act as efficient catalysts for producing hydrogen.[42,43] Therefore, it was established theoretically and experimentally that Ni-based POMs containing Ni_4O_4 cubane cores - bearing resemblance to the $[Fe_4S_4]$ cubane core of [FeFe]-hydrogenases - serve as the efficient reacting units for visible light driven hydrogen evolution reaction.[44,45] In this thesis, we investigated the hydrogen evolution performance of novel Ni-POMs under strict homogeneous conditions. For detailed information on the structural aspects and the

structure-performance trends, please consult article # 2.

1.5 Heterogeneous photocatalysis

In heterogeneous photocatalysis, the catalyst and the reaction medium are in different phases. Heterogeneous photosystems typically constitute of solid-state photocatalysts that are capable of light absorption and driving subsequent redox reactions. These photocatalysts are generally semiconductors. Semiconductors have a band gap (Eg) $<$ 1.5 to 3.0 eV and have the capability to conduct electricity even at room temperature when exposed to sunlight. As discussed in section 1.3.2, the energy of photons absorbed by the semiconductor excites the electron from the valence band (VB) to the conduction band (CB) of the semiconductor, generating an electron-hole pair (figure 1.2a). This indicates that both oxidation and reduction reaction environment is provided by the semiconductor. These semiconductors additionally act as photosensitizers when come in contact with other materials like co-catalysts (will be discussed in detail later in this section).

1.5.1 Inorganic photocatalysts

Most of the semiconductors utilized for photocatalytic hydrogen evolution reaction are based on metal oxides due to their desired electronic structure, light absorption properties, and ability to transport the charge carriers. Metal oxides like TiO_2, Fe_2O_3, ZnO, and In_2O_3 etc. have been investigated for the application of photocatalytic hydrogen evolution reaction.[46–49] The choice of these semiconductor materials depends on the position of the CB and VB of the semiconductor compared to the redox potentials of oxidation and reduction half-reactions of the water-splitting reaction. The reduction half-reaction would be feasible when the CB edge of the semiconductor has a more negative potential than the reduction reaction. Figure 1.5 demonstrates the energy band gaps of the most commonly used semiconductors as well as their CB and VB positions in comparison to the potentials of oxidation and reduction half-reaction.

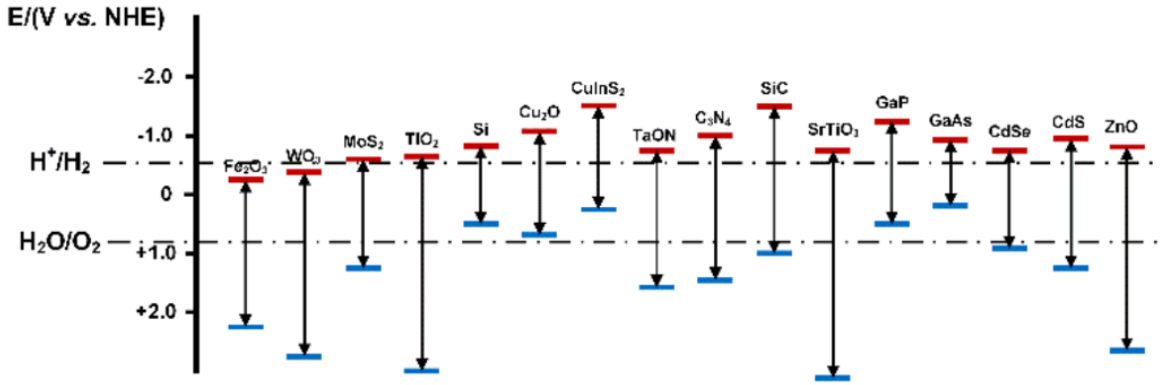

Figure 1.5: Conduction band (CB) and valence band (VB) potentials of some of the common semiconductor materials with respect to the redox potentials of the half-reactions of water splitting. Reprinted with permission from RSC Advances.[50]

Among these metal oxides, TiO_2 marks the top position for its use as a photocatalyst for several obvious reasons: (i) it has good chemical and thermal stability, (ii) it exists in abundance, (iii) it possesses excellent physiochemical properties, and (iv) it is non-toxic.[51] Therefore, the scientific community showed a remarkable interest in this material for its potential to generate solar fuels.[52]

1.5.1.1 TiO_2

TiO_2 exists in three different crystalline structures i.e. anatase, rutile, and brookite.[53] These lattice arrangements of TiO_2 greatly impact the energy of the atomic orbitals, leading to the transformation of its charge transport and photophysical properties.[54–56] The anatase and brookite phases are metastable and can be irreversibly transformed into a stable rutile phase upon heating. Among these crystalline phases, only anatase and rutile demonstrate light-induced catalysis. The crystalline structure of rutile is the distorted octahedra TiO_6 that are shared via corner oxygen atoms in a tetragonal structure.[57] The presence of in-plane and out-of-plane Ti-O bond lengths as well as the deviation of in-plane Ti-Ti bond angles distort the perfect octahedral O_h symmetry to D_{2h} symmetry. However, in the crystalline structure of anatase, the TiO_6 octahedra are shared via edge O-atoms in a tetragonal geometry[58] (figure 1.6). Both rutile and anatase are wide band gap semiconductors and have a band gap of 3.0 and 3.2 eV with absorption edges (385 nm and 415 nm) in the UV region of the solar spectrum. Therefore, both the polymorphs can be utilized as photocatalysts for hydrogen evolution reaction. However, anatase has superior HER efficiency than rutile due to the higher reduction potential and longer lifetime of the electrons in its CB generated after photoexcitation,[59] smaller particle size, higher mobility of electrons.[60,61] The VB of TiO_2 is filled with electron density mainly from oxygen atoms and the empty Ti3d states make up the unoccupied CB, both of these bands separated by an energy gap (E_g). In this thesis, we used anatase TiO_2 as a photocatalyst to drive HER. For more details, please refer to the article # 3.

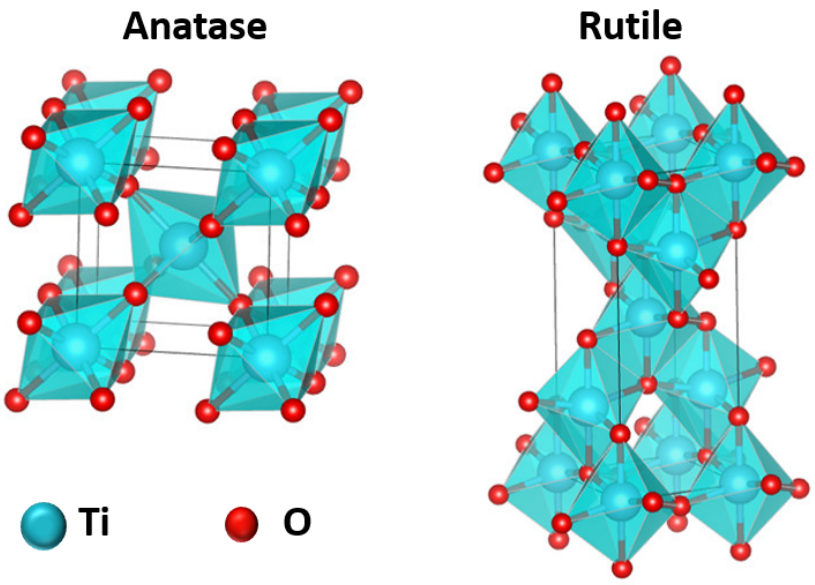

Figure 1.6: Crystal structures of anatase and rutile phases of TiO_2.[62]

Semiconductor-based materials offer various challenges: (i) charge recombination, (ii) large band gap, (iii) charges absorbed on the surface of the semiconductor, (iv) minimal absorption in the visible region, and (v) lower redox potentials.[63] Therefore, these issues can be tackled by various approaches which are listed as follows:

- To increase the absorption by reducing the band gap e.g. by introducing the dopants. However, it is crucial to control these defect sites as they can act as recombination sites for charge carriers.
- To build the heterostructures that reduce the charge recombination by separating the photoexcited charge carriers.

- To employ a dedicated co-catalyst that adsorbs on the surface of the semiconductor and facilitates the charge separation.

- To increase the surface area by synthesizing material with a specific morphology (e.g. micro- and mesoporous nanoparticles), leading to the adsorption of more co-catalyst molecules on the surface.

Our sun emits 43% of the visible radiation that reaches the earth. As discussed earlier in this section, TiO_2 absorbs in the UV region up to 400 nm thereby exhibiting poor solar to hydrogen (STH) efficiency i.e. <2% in the case of water splitting reaction. Consequently, its utilization for photocatalytic hydrogen evolution reaction is limited by its inactivity in the visible range. Hence, employing photocatalysts that are capable of absorbing visible light up to 700-1000 nm could enhance the STH by ∼10-20 times.[64] In this context, employing photoactive materials with the ability to absorb visible light represents a promising strategy to improve the efficiency of STH conversion.

1.5.2 Organic photocatalysts

The conductive polymer molecules are organic semiconductors as the presence of conjugation allows for the formation of band structures similar to the inorganic semiconductors. Hence, the mechanism of photocatalysis and the photogeneration of electron-hole pairs in organic semiconductors closely resemble to that of inorganic semiconductors. The charge transport properties of organic semiconductors differ drastically from those of inorganic semiconductors due to their different properties and degrees of crystallographic arrangement.

1.5.2.1 gC_3N_4

Graphitic carbon nitride (gC_3N_4) is the most popular metal-free organic semiconductor material that has been investigated as a photocatalyst for visible-light-driven hydrogen evolution reaction in a pioneered study published in 2009.[65] It exists in two different chemical structures i.e. triazine and tri-s-triazine, depending on the precursors and synthesis method used (figure 1.7). gC_3N_4 ideally consists of only carbon and nitrogen, therefore, it can be synthesized cost-effectively with low toxicity. The structure of gC_3N_4 is composed of two-dimensional sheets of hexagonal rings constructed with sp^2 hybridized carbon and nitrogen atoms. These hexagonal rings are connected via nitrogen atoms of tertiary amines. The strong Van der Waals and π-stacking interactions between the sheets make this material highly crystalline.[66] This material is insoluble in most of the solvents. Furthermore, it exhibits distinct optical, electrical, structural, and physiochemical properties that particularly make it suitable for photocatalytic applications. It features a characteristic yellow color due to the band gap of 2.7 eV which corresponds to the absorption edge at a wavelength of 460 nm. The electronic band structure of gC_3N_4 is suitable for its application in photocatalytic hydrogen generation. In other words, the photogenerated electrons in gC_3N_4 possess enough energy to cross the thermodynamic barrier and reduce water into hydrogen.[67] However, the bulk gC_3N_4 demonstrate low efficiency for photocatalytic HER due to various reasons: (i) recombination of charge carriers by their hopping between the sheets, (ii) very low surface area (∼10 m^2/g), (iii) limited absorption in the visible region i.e. below 460 nm, (iv) limited availability of active sites for reaction at the interface, and (v) sluggish kinetics of reaction at the surface.[68,69] The solutions to mitigate these challenges include doping of metal/non-metals, band gap and surface engineering, and structural and morphological modifications, etc.

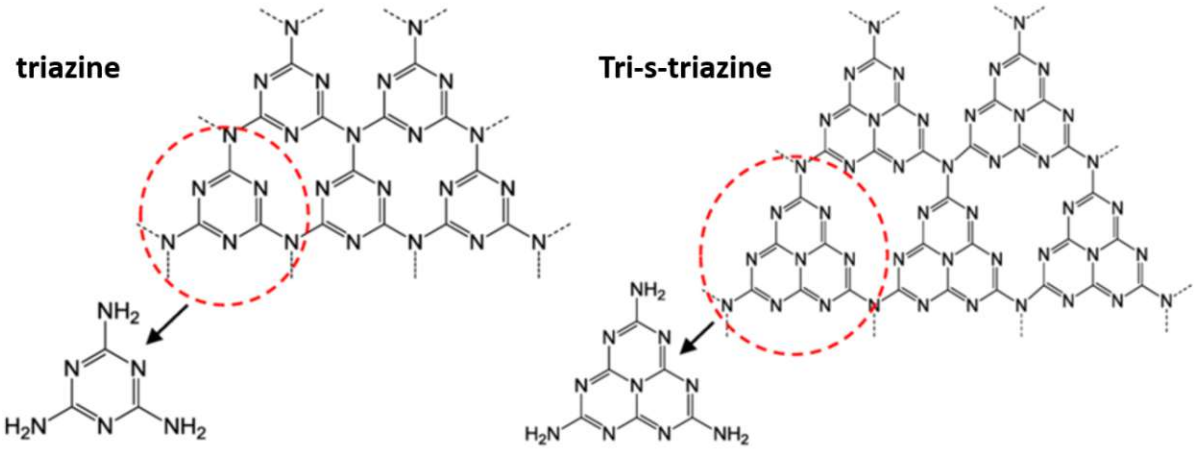

Figure 1.7: Chemical structures of triazine and tri-s-triazine based-gC_3N_4. Reprinted with permission from Springer Nature.[70]

In this thesis, we use the strategy of co-catalyst adsorption on the photoactive organic/inorganic semiconductor supports to tackle the prominent challenges that limit their performance for photocatalytic hydrogen evolution reaction.

1.5.3 Molecular co-catalysts

Noble metal Pt is the most active catalyst for producing hydrogen through water splitting. The scarcity, high cost, and toxicity of noble metal catalysts demand the exploration of abundant and cost-effective alternatives. Therefore, transition metal chalcogen-based HER catalysts such as MoS_2 demonstrated exceptional performance as electrocatalysts for hydrogen evolution reaction. Additionally, theoretical and experimental studies demonstrated that the edge sites of MoS_2 are the active sites for HER, however, its basal planes are mostly inactive.[71,72] Therefore, the HER activity of MoS_2 can be improved by exposing all the sulfur sites in its structure. A promising strategy is to utilize well-defined molecular MoSx-based catalysts that mimic the edge sites of MoS_2. In literature, several inorganic molecular analogs of MoS_2 have been reported for catalyzing the hydrogen evolution reaction. These analogs include triangular $Mo-S_2$ unit attached to pyridine ligands,[73] cationic $[Mo_3S_4]^{4+}$ cluster,[74] and anionic $[Mo_3S_{13}]^{2-}/[Mo_2S_{12}]^{2-}$ clusters.[75,76]

1.5.3.1 Thiomolybdates

The thiomolybdate $[Mo_3S_{13}]^{2-}$ clusters were first synthesized and characterized by Müller et al. in 1978.[77] These clusters are known to be the best-performing non-noble metal catalysts for hydrogen evolution reaction because all the sulfur ligands in its structure are fully exposed for hydrogen adsorption. These clusters have triangular geometry with three different kinds of disulfide ligands that resemble the edge sites of MoS_2. These are terminal disulfide ligands (S_2^{2-}) connected to a single molybdenum atom, bridging disulfide ligands (S_2^{2-}) linked to two molybdenum atoms, and apical disulfide (S^{2-}) shared by three molybdenum atoms (figure 1.8).

This thesis aims to investigate the HER performance of these cluster co-catalysts immobilized onto solid-state oxide supports. The $[Mo_3S_{13}]^{2-}$ clusters are employed to bridge the molecular and solid-state catalysts. Furthermore, over the course of this thesis, the HER performance of these clusters is compared in both homogeneous and heterogeneous phases using similar reaction conditions and parameters.

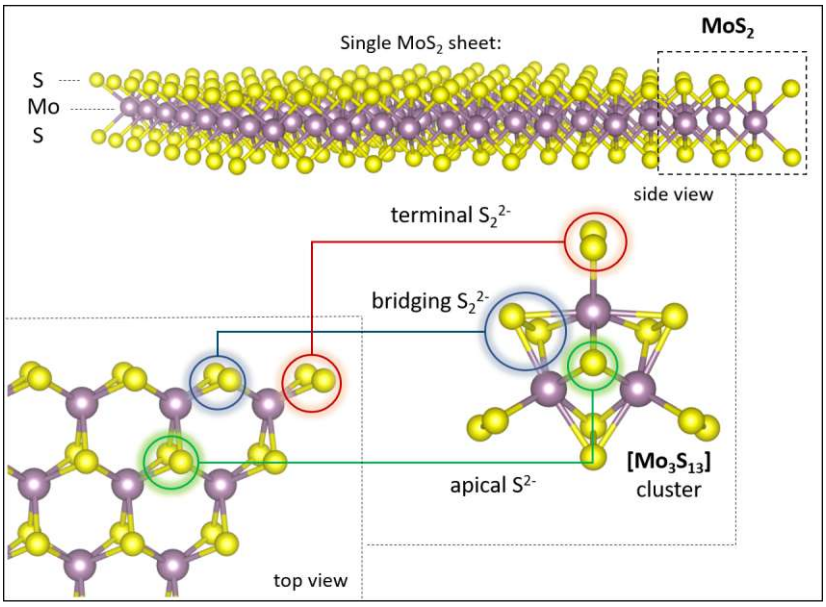

Figure 1.8: Structure of $[Mo_3S_{13}]^{2-}$ cluster, a molecular analog of MoS_2.

1.5.4 Heterogeneous photocatalytic system

The heterogeneous photocatalytic system employed for HER in this thesis consists of photoactive support (TiO_2 and gC_3N_4), co-catalyst ($[Mo_3S_{13}]^{2-}$), and sacrificial donor (methanol, ascorbic acid, or triethanolamine). The photocatalyst when irradiated with light of energy equivalent or higher than the band gap generates an electron-hole pair. The electrons in the CB migrate towards the surface of the photocatalyst where they are accepted by the co-catalyst and utilized for the reduction of protons to hydrogen. On the other hand, the holes in VB of the photocatalyst are taken by the sacrificial donor which itself converted to oxidized products. This process is repeated two times until the hydrogen evolution process is accomplished (figure 1.9).

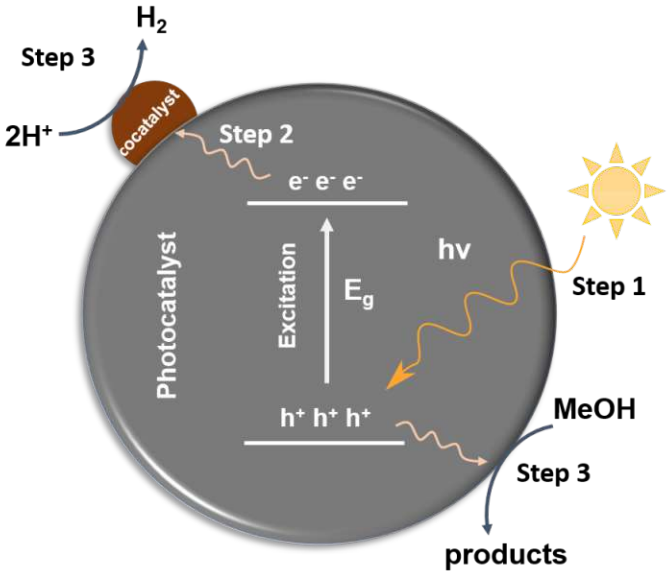

Figure 1.9: Photocatalytic HER mechanism using thiomolybdate clusters as co-catalyst.

Motivation

2.1 Challenges and aims

Photocatalytic water splitting to generate hydrogen stands as a prominent topic among energy conversion methods aimed at storing renewable energy through chemical bonds. As outlined in the previous chapter (specifically sections 1.3 and 1.4), this can be accomplished via homogeneous and heterogeneous photocatalytic approaches. Each of these approaches presents its advantages and challenges, that restrict their further development in the field.

The field of **homogeneous photocatalysis** presents two primary challenges: (i) molecular (photo)catalysts under turnover conditions lose their redox stability which is attributed to the formation of inactive species through oligomerization or aggregation, (ii) the need for molecular photosensitizers induces instability to the photosystem arising from the poor photostability of the sensitizing molecules. However, in the case of **heterogeneous photocatalysis**, the major challenge encountered by the community is the lack of understanding of the reaction mechanisms due to the poorly defined catalytic sites of the photocatalyst. Therefore, the model photocatalysts having well-defined components need to be designed, that feature well-defined catalytic sites (figure 2.1).

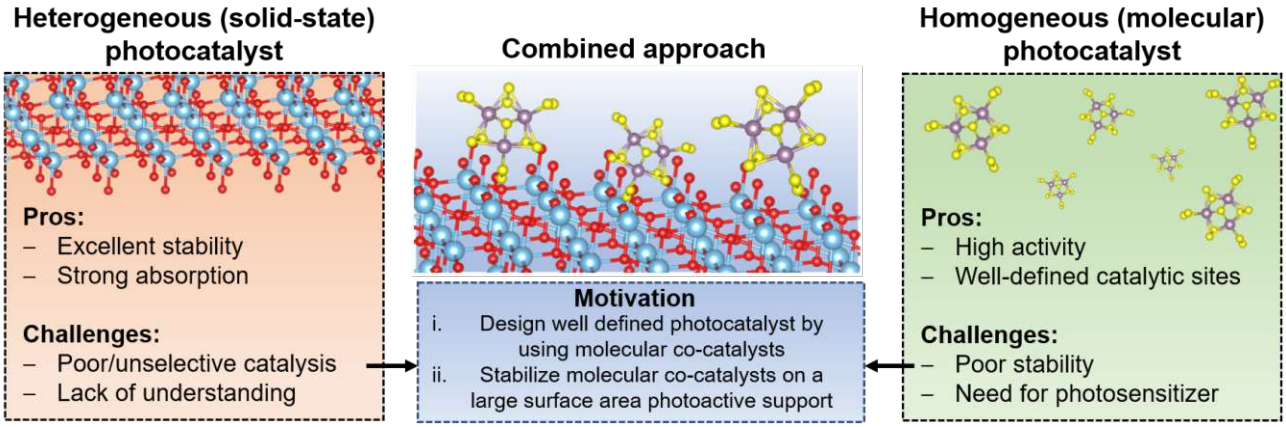

Figure 2.1: Combination of the homogeneous and heterogeneous photocatalytic approaches to bridge the gap between the two by exploiting their advantages.

Considering the fact that the advantages and challenges of both approaches are complementary to each other, in this thesis, I aim to overcome their challenges by designing a novel photocatalyst that combines the advantages of both. In the context of **heterogeneous photocatalysis**, the use of co-catalysts with structurally well-defined and compositionally tunable catalytic sites would enable the understanding of the reaction mechanisms as well as allow for performance optimization by tuning the interface. In the context of **homogeneous photocatalysis**, employing substrates with high surface area would stabilize the co-catalyst by

immobilizing them and thus inhibiting their aggregation or undesired degradation. Furthermore, the substrate would also play the role of a photosensitizer preventing the use of additional components for light absorption (figure 2.1).

In this thesis, I investigate the homogeneous and heterogeneous photosystem for photocatalytic hydrogen evolution reaction by utilizing polyoxometalates and thiomolybdates as molecular catalysts/co-catalysts and solid-state oxides (TiO_2) and graphitic carbon nitride (gC_3N_4) as support materials (see details in section 1.4 of introduction). However, the principal motive is to combine both photosystems and evaluate the performance of thiomolybdate co-catalysts by comparing them to their homogeneous counterparts.

Instrumentation and methods

This section provides the details of the methods used to characterize the molecular clusters and photocatalysts mentioned throughout this thesis. It additionally highlights the development and optimization of photocatalytic hydrogen evolution reaction setups as well as the methods employed to detect and quantify hydrogen. The synthesis of the clusters and the photocatalysts are discussed in the corresponding sections of the relevant articles.

3.1 Characterization techniques

3.1.1 Attenuated total reflection Fourier transform infrared spectroscopy (ATR-FTIR)

Infrared spectroscopy investigates the absorption, emission, and reflection of a sample by its interaction with the incoming infrared radiation. In ATR-FTIR, ATR sampling mode allows the direct examination of a solid or liquid sample without additional preparation. It works on the principle of total internal reflection that generates the evanescent field. The infrared light can interact with the sample through the evanescent wave that later gets detected by the detector to provide structural and chemical information about the sample. In contrast to the transmission mode, ATR measurement path length is independent of the thickness of the sample.

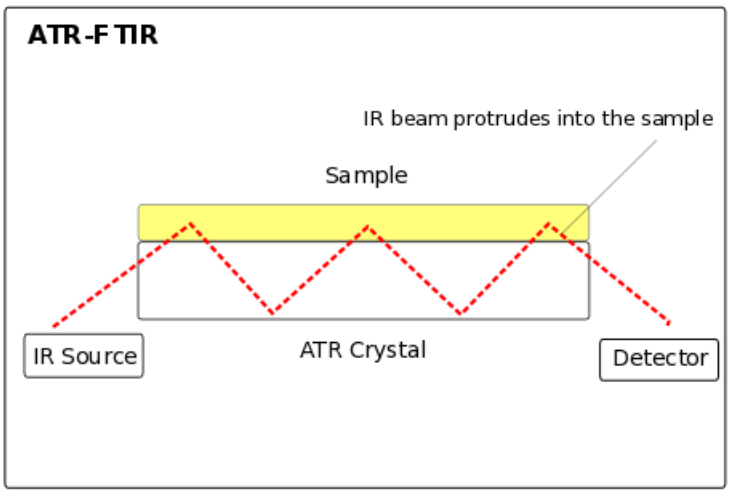

Figure 3.1: Schematic representation of the ATR-FTIR method. Reprinted with permission, license: CC BY-SA 4.0.[78]

The used machine in all articles was a PerkinElmer FTIR Spectral UATR-TWO with a spectrum two Universal ATR (Single Reflection Diamond) accessory.

3.1.2 Ultraviolet-Visible spectroscopy (UV-Vis)

Ultraviolet-visible spectroscopy (UV-Vis) is an analytical technique that measures the absorption or reflection of the molecules in a given sample with respect to the blank or reference sample (see figure 3.2a). The amount of light absorbed as a function of the wavelength of incident light provides information about electronic transitions occurring within the examined materials. In the case of transition metals and their complexes, these electronic transitions can be: ligand-to-metal charge transfer (LMCT), d-d transitions within the metals, metal-to-ligand charge transfer (MLCT), or interfacial charge transfer transitions (IFCT). The amount of light absorbed by the materials is directly related to the concentration and follows Beer-Lambert law.

$$A = Log_{10}\frac{I_0}{I} = \varepsilon cL, \tag{3.1}$$

Where A is the absorbance, I_0 is the intensity of the incident light, I is the intensity of transmitted light, ε is the molar attenuation coefficient or molar extinction coefficient that measures the extent of absorption of a material at a particular wavelength, c is the concentration of attenuating species, and L is the optical path length.

In UV-Vis spectroscopy, data can be collected in transmission mode or reflectance mode depending on the state of the sample (see figure 3.2b). In the case of the liquid sample, the standard transmission method is used to record the spectra. However, diffused reflectance spectroscopy (DRS) is employed to analyze the solid samples. In this thesis, to analyze the molecular clusters I used a standard method where the clusters were dissolved in a suitable solvent and later transferred to the cuvette for analysis. However, the composites were always analyzed in solid form using DRS spectroscopic method. For all the sample analysis, I used a Jasco V-670 UV-Vis photo spectrometer. A diffuse reflectance unit containing an Ulbricht sphere was used. A standard 3 cm cuvette was used as a sample holder for the liquid samples analysis. The powdered samples were fixed in the micro-sample holder with a diameter of 3 mm and $MgSO_4$ was used as a reference standard.

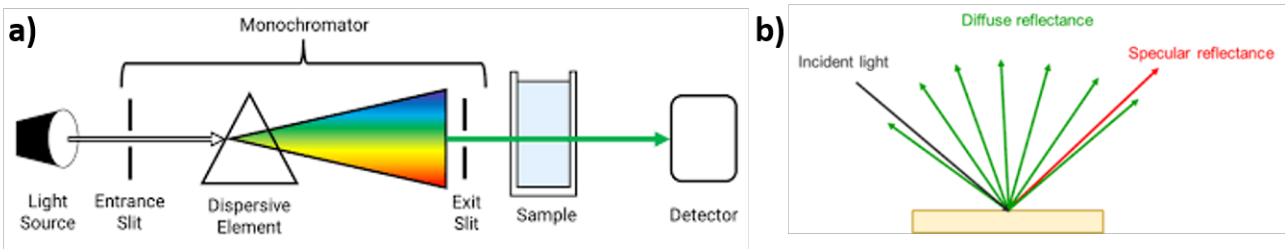

Figure 3.2: a) Schematic representation of UV-Vis spectrophotometer. Image taken from JASCO.[79] b) Interaction of incident light with the sample in transmission and reflectance modes of measurement. Image taken from JASCO.[80]

3.1.3 Raman spectroscopy

Raman spectroscopy is a scattering technique that is used for the qualitative and quantitative analysis of solid and liquid samples. The basic working principle of this technique relies on the Raman effect which states that the frequency of the scattered radiation differs from that of the monochromatic incident radiation. A Raman spectrum serves as the chemical fingerprint (500-2000 cm^{-1}) that contains a unique set of peaks characteristic of a specific molecule. It provides information about the chemical composition and properties, crystallinity, polymorphism, defects, and contamination.

A Raman spectrum provides useful information about the vibrational modes of a molecule based on the peak position. The peak intensity defines the strength of polarizability in a vibrating molecule. The width of the peak reveals crucial details about the local environment of vibrating bonds. However, instrument artifacts and sampling can also impact the intensity of a Raman peak. Therefore, to mitigate these influences, it becomes essential to normalize the data to a standard.

In this thesis, the data were recorded using Raman measurements performed with a WITec alpha 300 RSA+ Raman microscope equipped with a 632 nm excitation laser maintaining the laser intensity at 1 mW.

3.1.4 X-ray diffraction (XRD)

X-ray diffraction is a non-destructive method that allows to identify the structure and quantify the crystalline phases of solid materials. A diffractogram is generated when the constructive interference of monochromatic X-rays occurs with lattice planes of the sample at specific angles. The arrangement of atoms in the lattice determines the intensity of peaks in the XRD pattern. However, the shape of the XRD peak is affected by the scanning rate and the ratio of step size to full width at half maximum (FWMH). Bragg's law expresses the relationship between the angle of incidence at which the constructive interference occurs and the wavelength of the light being interfered with. This is shown by the Bragg's equation:

$$n\lambda = 2dsin\theta, \tag{3.2}$$

Where θ is the Bragg angle i.e. the angle between the incident X-rays and the lattice plane, λ is the wavelength of the incident X-rays, d is the spacing between the lattice planes, and n is the integer that defines the order of diffraction (see figure 3.3). By calculating the interlayer distance between facets, one can generate a 3D map of electron density in a crystal which provides information about the position of atoms.

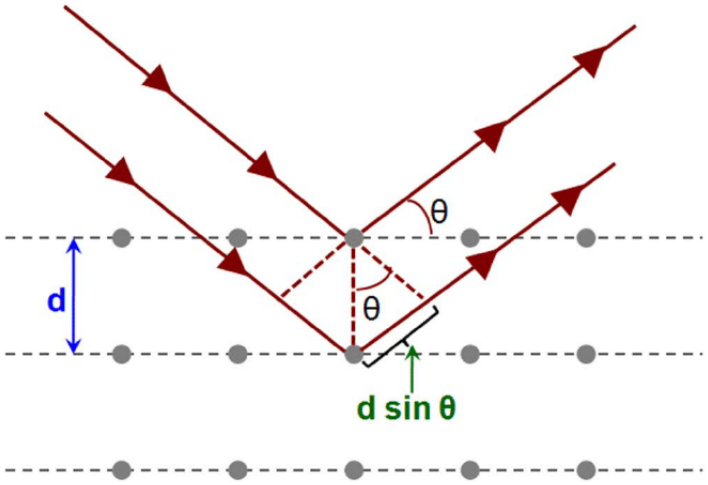

Figure 3.3: Schematic representing a two-dimensional crystal lattice with a set of imaginary planes and highlighted parameters of Bragg's equation.[81]

In this thesis, powder XRD measurements were conducted to investigate the crystallinity of the thiomolybdate clusters. For this purpose, I used an XPERT II: PANalytical XPert Pro MPD (θ–θ Diffractometer). The sample was placed on a Si sample holder and irradiated with a Cu X-ray source (8.04 keV, 1.5406 Å). The signals were then acquired with Bragg–Brentano θ/θ-diffractometer geometry ranging from 5° to 80° degrees using a semiconductor X'Celerator (2.1°) detector. I additionally performed in-situ XRD measurements to investigate the changes

in the crystal structure of thiomolybdate clusters (for more details see article 3) with respect to the change in temperature. For in-situ XRD measurements, I used an XPERT III: PANalytical XPert Pro MPD (θ–θ Diffractometer). For further details, see the corresponding article.

3.1.5 X-ray photoelectron spectroscopy (XPS)

X-ray photoelectron spectroscopy (XPS) is a surface-sensitive technique used for the non-destructive analysis of solids. The analysis is based on the kinetic energy of electrons photoexcited by X-rays (1-1.5 KV) from the core levels of the atoms in a solid sample. The resulting XPS spectrum generates peaks with specific binding energies which correspond to the kind of atoms (qualitative analysis) and their chemical environment on the solid surface (chemical shifts). The binding energy (BE) of the analyzed electrons in XPS is dependent on the light source used. Equation 3.3 shows the relationship between the binding energy (BE) and kinetic energy (KE) of the electrons, the excitation light source, and the work function (ϕ) of the detector

$$\mathrm{E_{Binding}} = \mathrm{E_{Kinetic}} - \mathrm{h}\nu + \phi, \tag{3.3}$$

The binding energy merely depends on the kinetic energy and the light source used, given that the ϕ is a constant for the detector used.

In this thesis, I used a custom-built SPECS XPS-spectrometer equipped with a monochromatized Al-K_α X-ray source (ν 350) and a hemispherical WAL-150 analyzer (acceptance angle: 60°). For the data analysis, I used the CASA XPS software employing a charge correction to the adventitious carbon peak (the C-C peak was shifted to 284.8 eV BE). For further details of the machines, measurement details, and data analysis, see the corresponding article.

3.1.6 Total reflection X-ray fluorescence spectroscopy (TXRF)

Total reflection X-ray fluorescence Spectroscopy (TXRF) is a highly sensitive analytical technique used for the elemental analysis of solid or liquid samples. The chemical composition is determined when the X-rays incident on the sample are totally reflected at an angle greater than the critical angle. The X-rays cause the atoms in the sample to excite and emit the characteristic X-rays that are later detected and analyzed by the detector (see figure 3.4). The intensities of the emitted X-rays correspond to the concentration of a particular element in a sample.

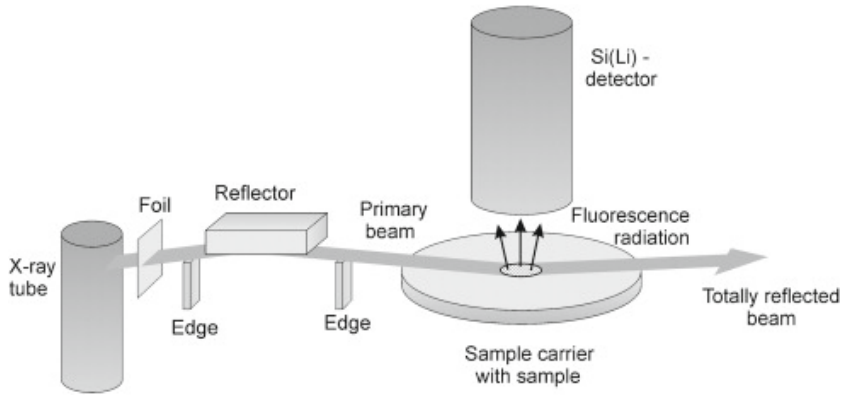

Figure 3.4: Schematic representation of TXRF spectrometer. Reprinted with permission of Elsevier.[82]

The measurements were performed with an ATOMIKA 8030C X-ray fluorescence analyzer (Atomika Instruments GmbH, Oberschleissheim, Munich, Germany). The excitation source

employed was a Wolfram X-ray tube (continuous spectrum) The excitation source employed was a Wolfram X-ray tube (continuous spectrum) at 50 kV and 47 mA. The samples were excited for 100 s and a Si(Li)-detector was used for X-rays acquisition. For further details, see the corresponding article.

3.1.7 Thermogravimetric analysis (TGA)

Thermogravimetric analysis (TGA) is a technique in which mass of the specimen changes as a function of temperature or time, under controlled temperature and atmospheric conditions. Upon completion of the measurement, the resulting TGA plot provides information about the changes in chemical composition, phase changes, and absorption or desorption of gases etc. In this thesis, I analyzed the decomposition of thiomolybdate clusters by applying a temperature gradient under air and nitrogen atmosphere to investigate the structural transformations of the clusters at different temperatures. For this purpose, I used a PerkinElmer Thermogravimetric Analyser TGA 8000 (see figure 3.5). For further details, see the corresponding section in the articles.

Figure 3.5: Image of PerkinElmer thermogravimetric analyzer TGA 8000 (Image taken from perkinElmer).[83]

3.1.8 Photoluminescence spectroscopy (PL)

Photoluminescence spectroscopy (PL) is a contactless and non-destructive method to probe the electronic and optical properties of materials. The phenomena of photoluminescence occurs when the light irradiated onto a sample creates an electron-hole pair and the relaxation of excited electrons generates photons. The energy of the emitted photons is higher than the energy of the bandgap between the conduction band (CB) and valence band (VB) in a semiconductor material and the energy difference between the highest occupied molecular orbital (HOMO) and lowest occupied molecular orbital (LUMO) in molecules. However, the point defects in semiconductors add states within the bandgap that cause the PL to occur at photon energies lower than the band gap. The emission of photons is partially radiative and partially non-radiative in nature. Radiative emission is the result of the relaxation of electrons within the vibrational levels in the excited state and non-radiative emission occurs through the electron's de-excitation from the excited state to the ground state. The process of photoluminescence is depicted in the figure 3.6a.

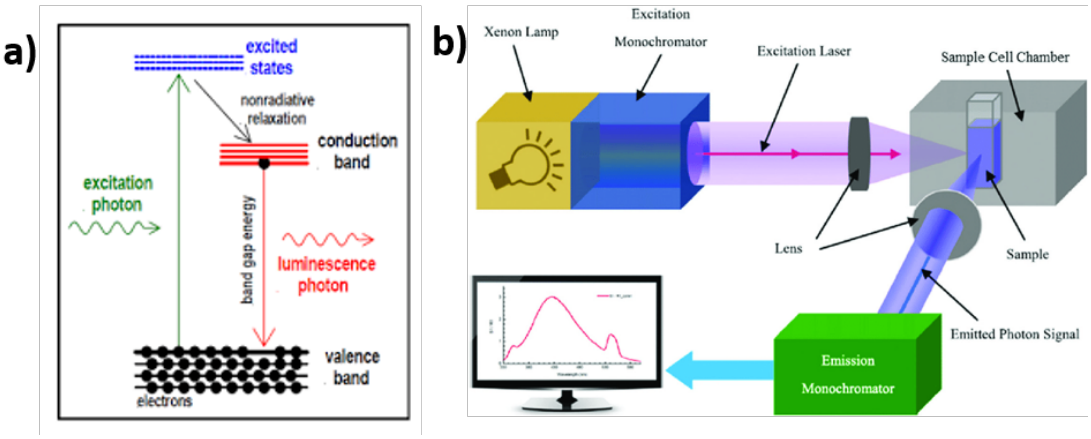

Figure 3.6: Image illustrating a) the principle of photoluminescence spectroscopy. b) the PL spectrophotometer.[84,85]

The PL spectrophotometer consists of a light source (Xenon lamp/monochromatic laser), monochromators, a sample holder, and a detector. The monochromators select and adjust the excitation and emission wavelengths as well as correct any fluctuations in the intensity of light from the source (see figure 3.6b). The detector receives the optical signal and converts it into the electronic signal, which is displayed as PL spectra in the computer. This instrument is employed to record three different types of spectra: emission spectra, excitation spectra, and time-resolved spectra.

In this thesis, I used a Picoquant FluoTime 300 photoluminescence spectrometer with two excitation sources: (i) a continuous-wave, ozone-free (300 W power) Xe arc lamp utilized for steady-state measurements with an excitation range of 250 to 800 nm (coupled with an excitation double monochromator), and (ii) a pulsed laser at 377 nm excitation. The detection system includes a PMA Hybrid 07 detector, that is coupled to an emission double monochromator. For lifetime measurements, the state-of-the-art time-correlated single photon counting (TCSPC) system is utilized. The PL data was collected and fitted using EasyTau2 software.

3.2 Photocatalytic HER experiments setup

In this thesis, I used two different types of hydrogen detection methods: a standard gas chromatography method employing a closed reactor setup, and a gas flow in-situ detection method utilizing a flow reactor setup. The type of method to be used was selected based on the nature of the photocatalyst.

3.2.1 Batch reactor setup

The photocatalytic hydrogen evolution reactions were carried out using a custom-built closed reactor with one neck utilized for two purposes: (i) degassing of the reaction mixture by purging Ar gas through inlet and outlet injection needles; and (ii) injection of produced hydrogen from the reactor's headspace to the GC-column using a specialized gas-tight syringe. The photocatalytic solution is side-illuminated using a SOLIS-365C LED lamp or the SOLIS-445C LED lamp (from ThorLabs) depending upon the type of photosensitizer used for the photocatalytic hydrogen evolution reaction. The upper part of the reactor does not need light illumination and therefore is covered with blue tape to avoid any interaction with the light. The reactor is also equipped with a water inlet and outlet to prevent heating of the reaction solution due to light illumination. This methodology can effectively quantify the amount of hydrogen but does

not encompass the rate of reaction in the associated process. The photocatalytic setup used is shown in figure 3.7. This method was employed in the article no. 2 and 4.

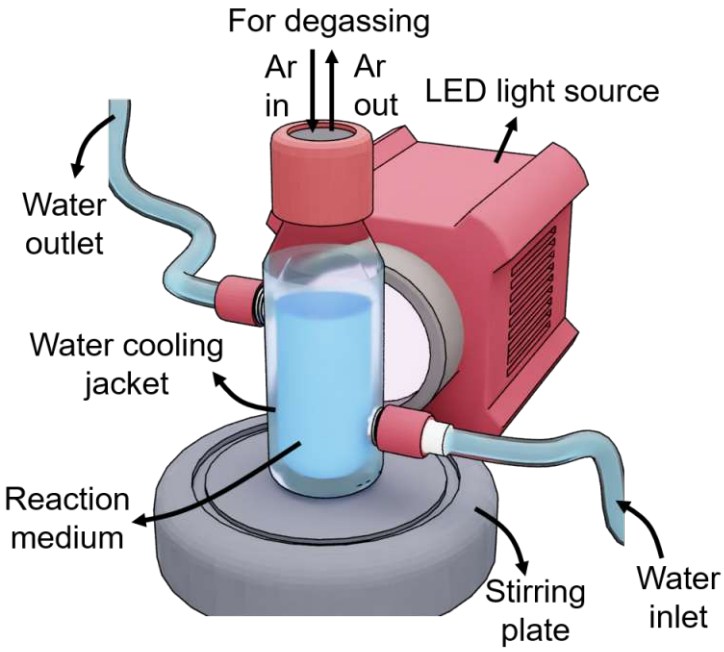

Figure 3.7: Photocatalytic HER set up employing a closed reactor for the hydrogen detection using GC.

The detection of hydrogen produced by using this experimental setup was carried out using the gas chromatography method.

3.2.1.1 Gas chromatography (GC) method

Gas chromatography (GC) is a commonly used analytical method to quantify various components of a sample. In GC system, the mobile phase is a carrier gas that transports the sample from the injection port to the column which is a stationary phase. The components of the sample exiting the column are quantified by the detector (figure 3.8). The retention time for each component in a sample depends on its interaction with a stationary phase. A chromatogram is recorded as a result of electrical signal output from the detector. A typical chromatogram displays the elution or retention time on the x-axis and the signal intensity on the y-axis. The area under the curve is used to interpret the amount of each component separated and detected.

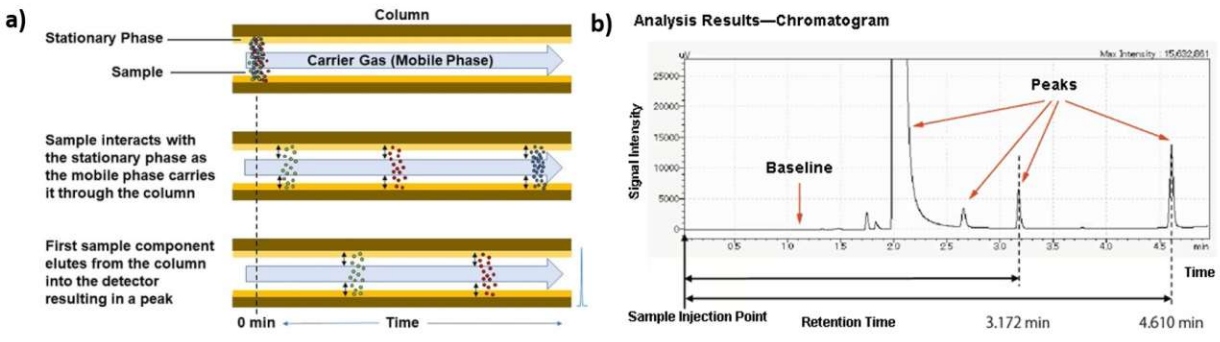

Figure 3.8: a) Working principle of the GC detection method. b) A typical chromatogram recorded in response to the GC measurement. Images taken from Agilent[86] and Shimadzu.[87]

In this thesis, I used a GC Nexis-2030 instrument equipped with a barrier ionization discharge detector and a Micropacked-ST column using helium as a carrier gas, to measure the amount of hydrogen produced by our photocatalytic system.

3.2.2 Flow reactor setup

In this thesis, I also used a gas flow in-situ detection system (figure 3.9), allowing for continuous detection of hydrogen and other gases over a long period. This approach facilitates the investigation of reaction activation/deactivation kinetics. For photocatalytic hydrogen evolution reactions, I used a custom-built reactor made of glass with a capacity of 100 mL by volume. The reactor consists of a gas inlet and outlet for purging the reaction mixture with Argon and the flow of Argon carrier gas. The reaction mixture is added from the top window of the reactor. The quartz lid is used to close the reactor and to make it transparent to UV light. The light source (LED 365 nm) is positioned at the top of the reactor. The reaction mixture is surrounded by a water-cooling jacket to keep a cool atmosphere during illumination. The Ar carrier gas carrying hydrogen gas is continuously flushed through the reactor. The flow of Ar is regulated by a mass flow controller (Q-flow 140 series, MCC Instruments). The carrier gas reaches the detector via a $CaCl_2$ trap to prohibit any moisture from reaching the detector. I used an Emerson X-stream gas analyzer, equipped with three different kinds of detectors able to measure up to four different gas components (H_2, CO/CO_2, and O_2) simultaneously. A thermal conductivity detector (TDC) is used for the H_2 detection, a photometric non-dispersive IR sensor is used for the CO and CO_2 detection, and a paramagnetic O_2 detector is used for the O_2 detection.

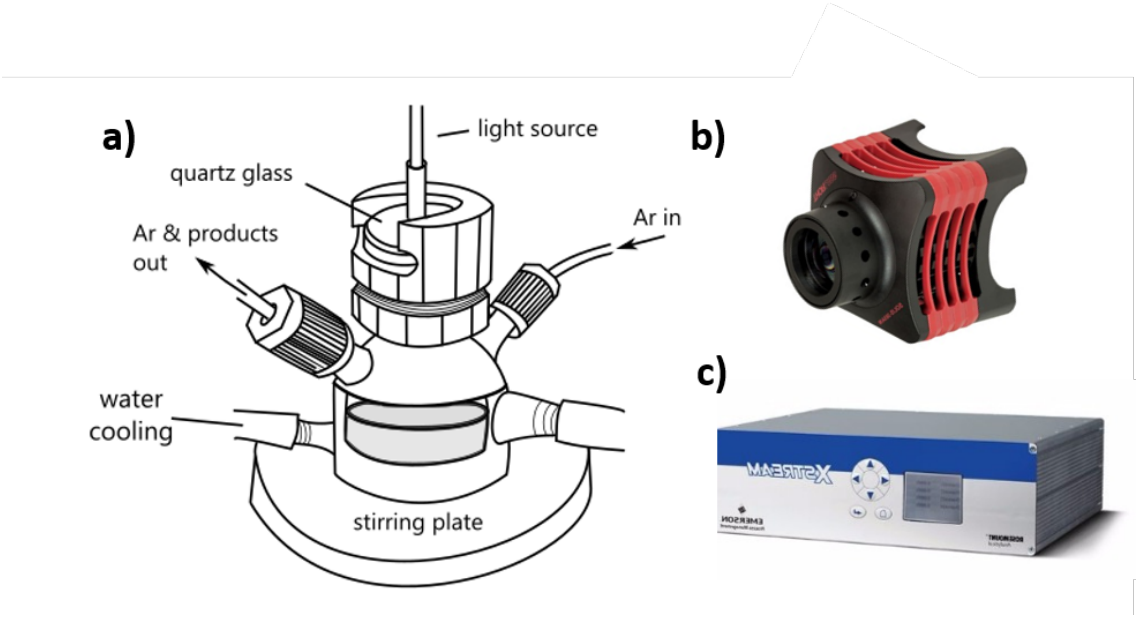

Figure 3.9: a) Photocatalytic HER set up employing a flow reactor for the hydrogen detection using (b) SOLIS-365C LED light source, and (c) Emerson detector.

3.2.3 Ensuring reproducible HER experiments

The efficiency of the reaction was significantly influenced by the following factors:

- Higher purging rates resulted in the adhesion of photocatalyst suspension particles to the reactor walls, preventing their exposure to the light source and consequently diminishing their contribution to the overall hydrogen production. Consequently, I deliberately

maintained a lower purging rate, allowing for an extended purging duration to effectively eliminate air dissolved in suspension and in the headspace.

- The syringe used for the manual injection of hydrogen from the reactor to the sample compartment of GC was meticulously cleaned by repetitive flushing of Argon to prevent any moisture from entering the column thereby mitigating any potential interference with the quantification of hydrogen.
- The light-sensitive components of the photocatalytic reaction were promptly prepared and handled in the dark to prevent potential degradation.
- The power efficiency of the light sources used fluctuates over time. Therefore, the power of the lamps was monitored every two months to maintain identical reaction conditions.

Results and discussion

This thesis is presented in a cumulative form and includes four peer-reviewed articles reprinted with the permission of respective journals.[88–90] The contributed articles are listed as follows:

Article #1:

"Thiomolybdate Clusters: from Homogeneous Catalysis to Heterogenization and Active Sites"

Samar Batool, Marcel Langer, Stephen Nagaraju Myakala, Magdalena Heiland, Dominik Eder, Carsten Streb, Alexey Cherevan

Advanced Materials, 2023, 2305730
DOI: https://doi.org/10.1002/adma.202305730

Article #2:

"Ni_{12} tetracubane cores with slow relaxation of magnetization and efficient charge utilization for photocatalytic hydrogen evolution"

Elias Tanuhadi, Joan Cano, Samar Batool, Alexey Cherevan, Dominik Eder, Annette Rompel

J. Mater. Chem. C, 2022, 10, 17048-17052
DOI: https://doi.org/10.1039/D2TC03508A

Article #3:

"Surface Anchoring and Active Sites of $[Mo_3S_{13}]^{2-}$ Clusters as Co-Catalysts for Photocatalytic Hydrogen Evolution"

Samar Batool, Sreejith P. Nandan, Stephen Nagaraju Myakala, Ashwene Rajagopal, Jasmin S. Schubert, Pablo Ayala, Shaghayegh Naghdi, Hikaru Saito, Johannes Bernardi, Carsten Streb, Alexey Cherevan, Dominik Eder

ACS Catalysis, 2022, 12, 11, 6641–6650
DOI: https://doi.org/10.1021/acscatal.2c00972

Article #4:

"Thiomolybdate Cluster for Visible-Light Driven Hydrogen Evolution: Comparison of Homogeneous and Heterogeneous Approaches"

Samar Batool, Jasmin S. Schubert, Pablo Ayala, Hikaru Saito, Maria J. Sampaio, Eliana S. Da Silva, Cláudia G. Silva, Joaquim L. Faria, Dominik Eder, Alexey Cherevan

Sustainable Energy & Fuels, Accepted
DOI: https://doi.org/10.1039/D3SE01658G

4.1 Summary of contributed articles

This thesis covers four distinct articles showcasing the research work of my PhD. The fundamental concept of these articles is based on the synthesis of structurally well-defined molecular clusters and the investigation of their performance as catalysts/co-catalysts toward the hydrogen evolution reaction (HER) in homogeneous and heterogenized states, to bridge the gap between homogeneous and heterogeneous photocatalysis. Article #1 serves as a broad literature review and highlights the well-known examples from the literature employing thiomolybdates for electro- and photocatalytic hydrogen evolution reaction. These studies investigate the active sites involved in the hydrogen evolution reaction to elucidate the correlation between the structure of the catalyst and the activity. The individual sections of the review explain the performance parameters of thiomolybdates in the solution phase and surface-supported. It is demonstrated that the thiomolybdate active sites taking part in the hydrogen evolution reaction depend on the state of the catalyst and the reaction conditions. Therefore, theoretical and experimental studies reported that these active sites govern the catalyst stability, reaction kinetics, and energetics. Furthermore, this review outlines the studies that explore the heterogenization of thiomolybdates on different substrates to unravel the role of catalyst-support interactions, their stability after anchoring and during catalysis and to examine their performance for electrocatalytic and photocatalytic HER. This review provides a deeper understanding of thiomolybdates in terms of their structural aspects, stability, reactivity, active sites, and their heterogenization strategies.

This thesis aims to combine the homogeneous and heterogeneous approaches to develop advanced photosystems. It was, therefore, crucial to study both systems experimentally to identify their advantages and limitations. Hence, in article #2, I use two novel Ni-based (TBA salts of $Ni_{12}W_{30}$ and $Ni_{12}W_{27}$) polyoxometalates (POMs) as molecular catalysts for visible-light-driven hydrogen evolution reaction under absolute homogeneous conditions. The photocatalytic system consisted of Ni-POMs as catalysts, $[Ir(dtbbpy)(ppy)_2]^+$ as the photosensitizer (PS), triethanolamine (TEOA) as an electron donor and 11:33:4 vol% $CH_3CN/DMF/H_2O$ as a solvent mixture (figure 4.1a). I investigate the concentration-dependent hydrogen evolution performance of the two Ni-POMs and show that hydrogen production increases with the increase in catalyst concentration. The hydrogen evolution performance of these Ni-POMs is compared to the structurally identical Ni-based HER catalyst-tetra-nickel polyoxotungstate Ni_4W_{18} under similar reaction conditions. Overall, both the novel Ni-POMs surpass the HER activity produced by the benchmark Ni_4W_{18} catalyst. In this context, the quantum yield of our novel $Ni_{12}W_{30}$ and $Ni_{12}W_{27}$ POMs is 10.42% and 8.36% which greatly exceed the previously reported benchmark Ni_4W_{18} catalyst. However, the overall hydrogen produced is higher for $Ni_{12}W_{30}$ POM possibly due to the greater number of cubane cores directly linked to improved HER efficiency. This suggests that our Ni-POMs are the fastest and the most efficient Ni-based POMs reported so far for hydrogen evolution reaction. Post-catalytic IR, TXRF, and reloading studies account for their stability and show that the Ni-POMs are structurally intact and recyclable. Photoluminescence spectroscopy suggests that both oxidative and reductive quenching mechanisms are possible as the quenching constant calculated for Ni-POMs is higher than the sacrificial donor TEOA. However, due to the much higher concentration of TEOA used as compared to the catalyst under turnover conditions, a reductive quenching mechanism is proposed for the photocatalytic system under investigation. It is noteworthy that despite the stability of the Ni-POMs, the use of degradable organic photosensitizer causes the photosystem to reach saturation which makes it highly unstable. Furthermore, the recovery of the catalyst is quite challenging in homogeneous systems. Therefore, it is required to use an inorganic solid-state oxide material that acts as a support for the catalyst and stabilizes it. Additionally, there is no need for an external photosensitizer and the catalyst can be recovered conveniently.

Therefore, in article #3, I combine the advantages of homogeneous and heterogeneous systems by the deposition of molecular $[Mo_3S_{13}]^{2-}$ (Mo_3) clusters onto titania (TiO_2) nanoparticles (Mo_3/TiO_2) to develop an all inorganic highly stable photosystem for the application of photocatalytic hydrogen evolution reaction (figure 4.1b). It is demonstrated that the clusters strongly bind to the TiO_2 surface by the loss of terminal disulfide ligands, establishing a Mo-O-Ti covalent linkage with the hydroxide moieties of TiO_2 surface. It is further shown that loading different amounts of Mo_3 clusters reached a saturation point at 9 wt.% suggesting a surface-limited adsorption. The Mo_3 cluster, when tested for hydrogen evolution reaction, is proved to be a highly active and stable cocatalyst and its activity is not far from the benchmark platinum cocatalyst. The optimal HER performance is achieved at 2 wt.% loading due to the efficient hole scavenging by the sacrificial donor at lower loadings. Thermal treatments of Mo_3/TiO_2 show that the oxidation of ligands under an oxygen atmosphere and the structural transformation under a nitrogen atmosphere greatly reduce the HER performance. On account of these results, it is evident that the structural integrity of the Mo_3 cluster and the presence of disulfide ligands in its original configuration are the crucial factors affecting the efficiency of reaction. Since most of the terminal disulfide ligands are lost while anchoring, we suggest that the bridging disulfide ligands and the uncoordinated Mo centers are the probable active sites. This study acts as a model system to explore other photosystems employing visible light absorbing supports for photocatalytic hydrogen evolution reaction.

Therefore, in my next project, I aim to utilize such supports to design a heterogeneous photosystem that can be compared directly to the homogeneous system under similar reaction conditions (figure 4.1c). For this reason, in article #4, I utilize graphitic carbon nitride (GCN) as a visible light photosensitizer that is able to bind Mo_3 cluster via electrostatic interaction. I compare the stability, activity, and HER performance of the supported Mo_3 clusters to its homogeneous analog containing $[Ru(bpy)_3]^{2+}$ photosensitizer (Mo_3/Ru). The hydrogen evolution reaction conditions of both the photosystems are optimized using different solvents, sacrificial donors, and Mo_3 loading/concentration. This work demonstrates that the use of solvent and sacrificial donor is critical in Mo_3/Ru system. We know from the literature that Mo_3/Ru all the active sites of the cluster are exploited for the hydrogen evolution reaction. However, in Mo_3/GCN, the maximum loading achieved on GCN surface is 3.9 wt% providing a limited number of catalytic sites to reduce protons. Thus, the HER activity of Mo_3/GCN photosystem is shown to be dependent on the number of catalytic sites present on the GCN surface. These catalytic sites can be surged by loading more clusters onto GCN surface. This is achieved by the protonation of GCN surface (H-GCN) which in turn improves the loading of clusters. The turnover numbers for Mo_3/GCN and Mo_3/H-GCN are identical (0.237 min^{-1} and 0.221 min^{-1} using TEOA sacrificial donor) suggesting that the extraction of charge from GCN is not restricted by the kinetics of interfacial charge transfer from Mo_3 to GCN. Overall, both the photosystems demonstrate similar turnover numbers per thiomolybdate cluster ($TOF_{Mo3/Ru}$ is 0.065 min^{-1} and $TOF_{Mo3/GCN}$ is 0.062 min^{-1}) under identical reaction conditions. I further show that the stability of the homogeneous Mo_3/Ru system is compromised over time due to the potential degradation of the Ru-dye. On the contrary, the Mo_3/GCN system retains its activity over time displaying high stability. Photoluminescence quenching experiments further affirm that the nature of available catalytic sites does not limit the performance of the Mo_3/GCN photosystem, but rather may be limited by the surface area of support and the inefficient charge separation.

Overall, in this dissertation, I present a novel strategy to overcome the limitations of homogeneous and heterogeneous photocatalysis by using metal chalcogenide-based molecular clusters as catalysts/co-catalysts along with light-absorbing functional substrates. My Ph.D. research delves into a comprehensive exploration of the structure-activity relationship, HER performance, identification of active sites, and the underlying mechanism. The outcomes of this

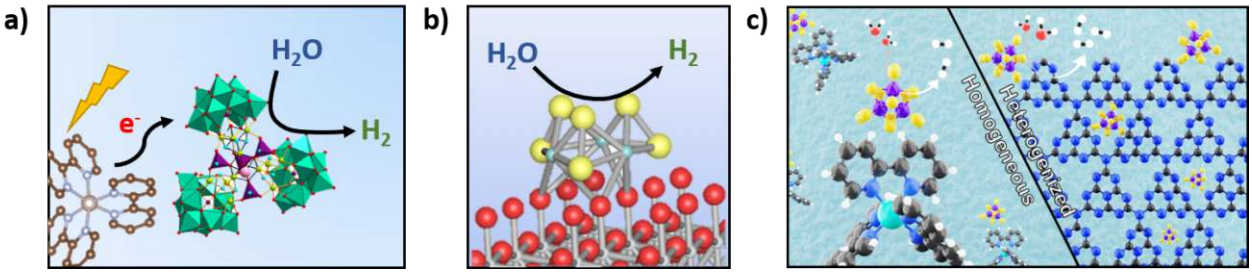

Figure 4.1: Summary of the thesis: a) homogeneous photosystem, b) combination of homogeneous and heterogeneous photocatalytic approaches, c) comparison of homogeneous and heterogeneous photosystems.

thesis lay the foundation to design an analogous photosystem integrating molecular clusters and solid-state materials for visible-light-driven hydrogen evolution reaction and other applications in the realm of solar fuels.

4.2 Published articles

4.2.1 Article #1

"Thiomolybdate Clusters: from Homogeneous Catalysis to Heterogenization and Active Sites"

Samar Batool, Marcel Langer, Stephen Nagaraju Myakala, Magdalena Heiland, Dominik Eder, Carsten Streb, Alexey Cherevan

Advanced Materials, 2023, 2305730
DOI: https://doi.org/10.1002/adma.202305730

My contributions as a first author to this collaborative review article encompass the summary of prominent examples of thiomolybdate-based catalysis along with the comprehensive analysis of their reactivity, active sites, and structure-activity relationship in the context of the hydrogen evolution reaction, both in homogeneous and heterogeneous conditions.

Reprinted with permission from the Advanced Materials[88]

ADVANCED MATERIALS
www.advmat.de

Thiomolybdate Clusters: From Homogeneous Catalysis to Heterogenization and Active Sites

Samar Batool, Marcel Langer, Stephen Nagaraju Myakala, Magdalena Heiland, Dominik Eder, Carsten Streb, and Alexey Cherevan**

Thiomolybdates are molecular molybdenum-sulfide clusters formed from Mo centers and sulfur-based ligands. For decades, they have attracted the interest of synthetic chemists due to their unique structures and their relevance in biological systems, e.g., as reactive sites in enzymes. More recently, thiomolybdates are explored from the catalytic point of view and applied as homogeneous and molecular mimics of heterogeneous molybdenum sulfide catalysts. This review summarizes prominent examples of thiomolybdate-based electro- and photocatalysis and provides a comprehensive analysis of their reactivities under homogeneous and heterogenized conditions. Active sites of thiomolybdates relevant for the hydrogen evolution reaction are examined, aiming to shed light on the link between cluster structure and performance. The shift from solution-phase to surface-supported thiomolybdates is discussed with a focus on applications in electrocatalysis and photocatalysis. The outlook highlights current trends and emerging areas of thiomolybdate research, ending with a summary of challenges and key takeaway messages based on the state-of-the-art research.

1. Introduction

Extraction, processing, and combustion of fossil fuels are the cornerstones of our modern global economy. However, fossil feedstocks are finite, and their use is the main driver of greenhouse gas emissions and climate change. The continuously increasing energy demand poses massive challenges for the global economy and underlines the need to transition from fossil to renewable energy systems. One promising alternative fuel is hydrogen (H_2) as it has a high gravimetric energy density and can be produced from water by chemical, photochemical, and electrochemical means. However, traditional methods of H_2 production, such as steam reforming, need to be replaced with sustainable technologies including water electrolysis or photocatalysis, which enable the direct production of "green", sustainable H_2 using renewable energy. Thus, the development of efficient and robust catalytic systems for the splitting of water is one of the grand current challenges in chemistry. Cooperative and interdisciplinary research efforts are required to design earth-abundant and high-performance electro- and photocatalysts able to perform the hydrogen evolution reaction (HER) with high efficiency, selectivity, and stability.

HER involves the proton-coupled transfer of two electrons and occurs in two steps. The first step of HER is the Volmer reaction, which involves electron transfer to adsorbed H^+ ions to form hydrogen intermediates (H*) bound to the catalyst. After this, the formation of molecular H_2 can occur via two reaction pathways, depending on the surface coverage of H*. If the surface coverage is low, the H_2 formation will proceed by electrochemical hydrogen desorption—termed as Heyrovsky reaction—where a proton-coupled electron transfer (PCET) results in the formation and release of H_2 (**Scheme 1**a). In contrast, if the surface coverage of H* is high, this second step proceeds via the Tafel reaction, where two neighboring surface-bound hydrogen atoms H* are coupled to give dihydrogen (**Scheme** 1b). Independent of the reaction mechanism, it is evident that H* is involved in all reaction steps, hence the Gibbs free energy of hydrogen adsorption (ΔG_{H^*}) becomes an important indicator for an efficient HER catalyst. As postulated in the Sabatier principle,[1] and practically demonstrated by Nørskov et al.[2,3] the bonding strength between the catalyst surface and hydrogen atoms should neither be too weak nor too strong, implying that optimal bonding is a key to achieving optimized HER rates.

Many compounds have demonstrated HER activity, including noble metals, metal oxides, nitrides, and sulfides.[4] In this

S. Batool, S. N. Myakala, D. Eder, A. Cherevan
Institute of Materials Chemistry
TU Wien
Getreidemarkt 9/BC/02, Vienna 1060, Austria
E-mail: alexey.cherevan@tuwien.ac.at
M. Langer, M. Heiland, C. Streb
Institute of Inorganic Chemistry I
Ulm University
Albert-Einstein-Allee 11, 89081 Ulm, Germany
E-mail: carsten.streb@uni-mainz.de
M. Langer, M. Heiland, C. Streb
Department of Chemistry
Johannes Gutenberg University Mainz
Duesbergweg 10-14, 55128 Mainz, Germany

The ORCID identification number(s) for the author(s) of this article can be found under https://doi.org/10.1002/adma.202305730

DOI: 10.1002/adma.202305730

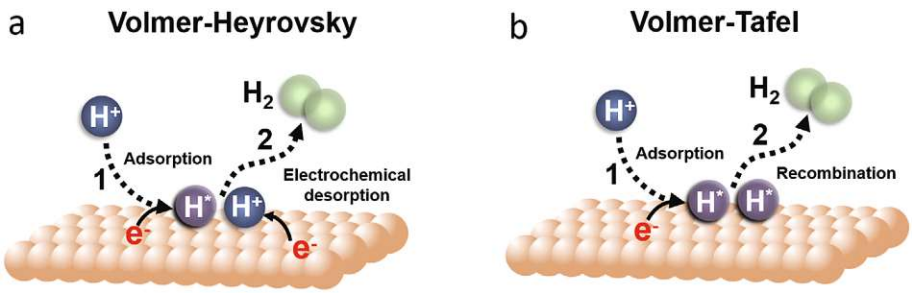

Scheme 1. Simplified HER pathways taking place under acidic conditions. a) Volmer–Heyrovsky mechanism in which H_2 formation proceeds via PCET and electrochemical desorption steps, b) Volmer–Tafel mechanism in which two surface-adsorbed hydrogen atoms (H*) recombine to form H_2.

respect, molybdenum sulfides (MoS_2) have emerged as promising earth-abundant alternatives to the state-of-the-art Pt HER catalysts. MoS_2-based catalysts are long known as a class of industrial catalysts widely used in the world for petroleum refining processes such as hydrodesulfurization (HDS), hydrodeoxygenation (HDO), and hydrodemetallization (HDM) reactions.[5] Importantly, these processes share the dihydrogen activation steps required for the following hydrogenation or hydrogenolysis reactions, which highlights the H_2 activation reactivity of MoS_2 with relevance for HER. Despite these widespread commercial applications of MoS_2-based catalysts, early experiments using bulk crystalline MoS_2 revealed poor HER performance.[6] However, later studies showed that nanostructuring of MoS_2 results in HER activity levels approaching those of Pt.[7] Also, amorphous molybdenum sulfides (a-MoS_x) as well as nonstoichiometric molybdenum sulfides ($MoS_{2\pm x}$) have been shown to exhibit suitable hydrogen adsorption centers and promising HER performance.[8,9] The demonstration that edge-sites of MoS_2 sheets are likely HER active sites[10] triggered further interest in thiomolybdate clusters, which can be seen as molecular analogs of MoS_2. Their well-defined molecular structure and composition make it possible to probe their active centers and study their (de)activation pathways, ultimately delivering atomistic insights on the performance of a variety of MoS_2-based catalysts. This is nicely exemplified by early developments in inorganic molecular thiochemistry, which were stimulated by the needs of the petrochemical industries. In this context, molecular transition metal sulfides have been studied to gain insights into reactions that occur on the surfaces of heterogeneous catalysts. These studies involve the investigation of model feedstock molecules and the activation of dihydrogen with transition metal sulfur sites, shedding light on potential modes of binding for H_2 and thiophenes.[11]

Research progress in thiomolybdate HER activity until 2018 has been summarized by Streb and colleagues in their recent review.[12] The authors pointed out that thiomolybdates can act as models for two proposed active site mechanisms. The "sulfide/disulfide" mechanism proceeds via a Volmer–Heyrovsky process based on protonated sulfide/disulfide ligands. The "molybdenum hydride" mechanism proceeds via the formation of a Mo^V—H moiety, so that Mo-centered redox processes are involved in the hydrogen evolution.[13] It was pointed out that careful design of thiomolybdate complexes can provide crucial information on the active sites and limitations of MoS-based HER catalysis.

Previous reviews and book chapters have already provided a systematic look into the structure and synthesis of thiomolybdates and related inorganic compounds,[14–16] described methodologies that have been used to construct oxothiometalate-based materials[17,18] and reviewed early application of transition-metal complexes with sulfide ligand and thiomolybdate clusters in catalysis[19] and petrochemical industry.[5] This progress report will put a particular focus on the latest developments in thiomolybdate-based electro- and photocatalysts, especially with regard to combined experimental and theoretical studies to shed light on reaction mechanisms, active sites, and possible degradation and repair paths, as well as emerging strategies for heterogenization on functional substrates. Section 2 will introduce thiomolybdates from the perspective of their origin, structural variety and highlight some of the recent developments. Section 3.1 will provide a comprehensive look into the catalytic properties of thiomolybdates under homogeneous conditions in solution. Section 3.2 will examine state-of-the-art research related to the identification of active sites of molecularly dissolved and surface-supported thiomolybdate clusters. Section 4.1 will explore a variety of thiomolybdate compounds, including $[Mo_2S_{12}]^{2-}$, $[Mo_3S_{13}]^{2-}$, $[Mo_3S_4]^{4+}$, their analogs and derivatives, as HER electrocatalysts and will provide insights into the activity comparisons of the clusters compared to other MoS_x-based nanostructures. Section 4.2 will document the successful implementation of basic thiomolybdate clusters as HER co-catalysts by combining them with a range of oxide, nitride, sulfide, and microporous supports exhibiting inorganic, organic as well as hybrid nature. Section 5 will provide a short summary of our findings and present our broad outlook aiming to provide directions for the future research.

1.1. Thiometalates: Structure and Recent Developments

Pioneering work in the field of (poly)thiometalates—all-inorganic molecular metal sulfide clusters formed by several metal centers and sulfur-containing ligands—was in part inspired by bioinorganic studies of the enzymes nitrogenase and hydrogenase, where metal sulfide clusters were identified as active sites.[20,21] This insight has triggered major research into the design of artificial, biomimetic analogs.[22–26] In ground-breaking studies in the late 1970s, Müller and co-workers reported the structure and characterization of the two prototype anions $[Mo^V{}_2S_{12}]^{2-}$ (**Mo_2**)[27] and $[Mo^{IV}{}_3S_{13}]^{2-}$ (**Mo_3**)[28] as the respective ammonium

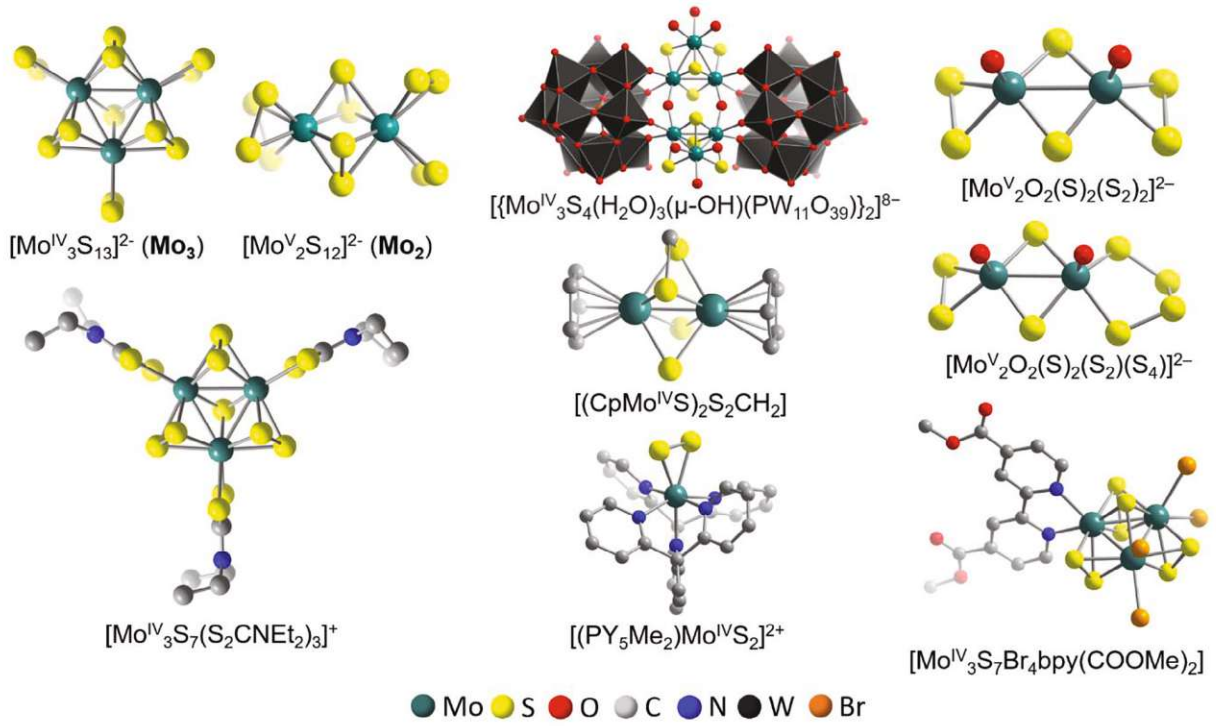

Figure 1. Structure illustrations of the thiomolybdate compounds described in this Review.

salts. Both clusters are formed by reduction of Mo^{VI} precursors (originally, ammonium heptamolybdate, $(NH_4)_6[Mo_7O_{24}]$) in (poly)sulfide-containing aqueous solutions resulting in the isolation of crystalline products. As shown in **Figure 1** (left), $Mo^{V/IV}$ centers in both thiomolybdate anions are coordinated by terminal and bridging disulfide (S_2^{2-}) ligands, however, the **Mo$_3$** cluster also contains an apical μ_3-S^{2-} ligand, which has been shown to allow initial **Mo$_3$** dimerization and stacking on the way to its thermal transformation to the hexagonal MoS_2 lattice.[29] Several extensive reviews published soon after this initial work provide a comprehensive overview of the synthesis, structural archetypes, electronic configurations, and spectroscopic characteristics of these and similar anionic clusters, in particular with a focus on their relevance as bioinspired models for the active sites of nitrogenase and hydrogenase enzymes.[30,31]

Although **Mo$_2$** and **Mo$_3$** can be seen as major representatives of prototypical all-inorganic thiomolybdates, several other groups of Mo-S-related molecular clusters and compounds are of high relevance to this review. As such, thiomolybdates can be modified to introduce O-containing ligands, leading to a larger group of oxothiometalate clusters (Figure 1, right).[32] On the other hand, stable thiometalates with structurally similar tungsten cores, such as $[W_2O_2S_8]^{2-}$ or $[W_3S_9]^{2-}$,[32,33] can be studied to gain deeper understanding of the roles of sulfide/disulfide ligands and metal centers on structural and catalytic aspects of such clusters. In recent years, studies in thiometalate chemistry have moved from individual molecules to extended structures, so that 1D chains,[34] metal–organic frameworks (MOFs),[35] and coordination polymers[36] with exciting reactivity have been reported. This opens new avenues to the design and implementation of more complex thiomolybdate (nano)structures.

Although thiomolybdates and their derivatives have been long-known in the literature, the main interest was initially focused on their synthesis, structure, principal chemistry, and bioinorganic relevance. The in-depth study of their hydrogen evolution activity was only triggered in 2008, when Chorkendorff and colleagues reported the electrochemical HER activity of the cubane-type $[Mo_3S_4(H_2O)_9]^{4+}$.[37,38] These groundbreaking studies have now led to a plethora of research activities, both in homogeneous and heterogeneous catalysis.

2. Catalytic Performance and Active Sites

In this section, we will explore the catalytic performance of prototype thiomolybdates and their derivatives under homogeneous conditions and when deposited as molecular species on heterogeneous supports and discuss proposed active sites of these species. Molecular thiomolybdate systems are ideally suited to deploy a wide range of modern analytical methods, including in situ and operando spectroscopies, to gain atomic-level understanding of active species, reaction mechanisms, and degradation pathways. Over the last decade, pioneering mechanistic studies have utilized thiomolybdates as molecular models able to shed light on the underlying processes which govern reactivity and stability of these and more complex molybdenum sulfide-based nanostructures. Most of these studies were focused on electrochemical or light-driven catalysis by the prototype **Mo$_3$** cluster (Figure 1, left).

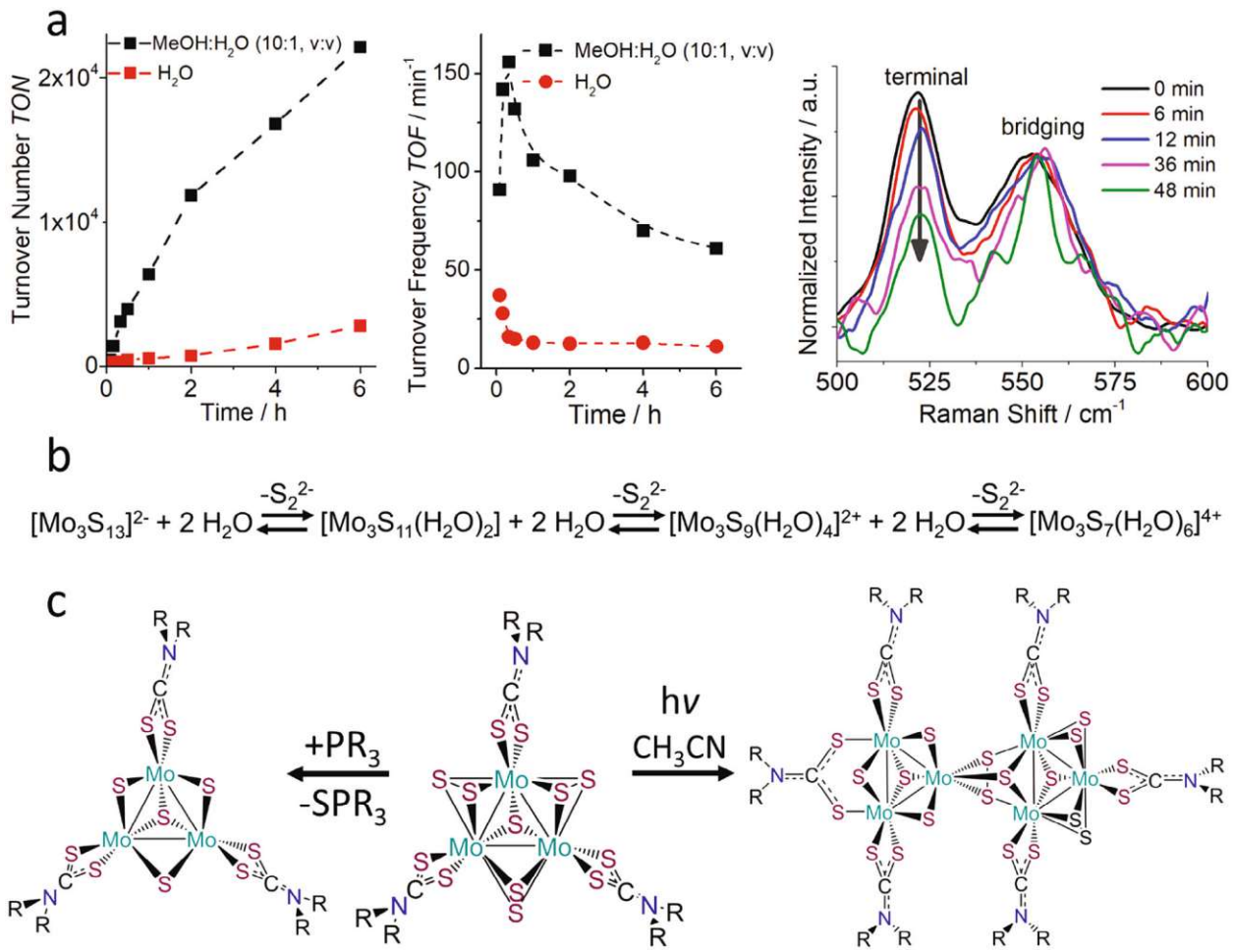

Figure 2. Catalytic performance under homogeneous conditions. a) Effect of solvent mixtures on light-driven HER: turnover numbers (TONs, left) and turnover frequencies (TOFs, center) during HER catalysis indicate faster deactivation of Mo_3 in aqueous conditions and suggest exchange of ligands followed by in situ generation of a catalytically more active species, also confirmed with in situ Raman spectroscopy (right). b) Schematic of disulfide ligand exchange with water ligands. c) Conversion of $\{Mo_3S_7\}$-core to $\{Mo_3S_4\}$-core containing clusters. R: methyl, ethyl, i-butyl, benzyl. (a,b) Reproduced with permission.[40] Copyright 2018, Royal Society of Chemistry. (c) Adapted with permission.[44] Copyright 2019, American Chemical Society.

In the following, we will explore the principal HER reactivity of thiomolybdates in Section 3.1, while active site insights will be discussed in Section 3.2.

2.1. Catalytic Properties

In 2018, the groups of Min[39] and Streb[40] independently reported the first studies into the light-driven HER by **Mo_3** under homogeneous conditions. Both groups observed high catalytic activity when combining **Mo_3** with $[Ru(bpy)_3]^{2+}$ as a photosensitizer (PS) and provided initial mechanistic understanding of the catalyst deactivation. Theoretical modeling of the HER process was used to rationalize the experimental data.

Streb and co-workers focused on understanding the structural changes and deactivation pathways of **Mo_3**. The group used Raman spectroscopy to propose the exchange of the terminal disulfide ligands of **Mo_3** by water ligands when operating in methanol/water ($MeOH/H_2O$) mixtures (**Figure 2**a,b). Catalytic analyses and theoretical calculations indicated that the resulting **Mo_3**-derivatives have different HER activity, depending on the number of water ligands. This insight was used to optimize the water content of the reaction mixture, so that the most active species were stabilized, leading to turnover numbers (TONs) > 20000. The group also observed decreasing TONs with increasing **Mo_3** concentration, which was assigned to ion pairing and colloid formation by aggregation of the anionic **Mo_3** with the cationic PS $[Ru(bpy)_3]^{2+}$. In a follow-up study using the **Mo_3**/$[Ru(bpy)_3]^{2+}$/ascorbic acid solutions, the authors reported an unusual effect of ammonium ions (NH_4^+) in enhancing the overall HER performance of the photosystem.[41] The authors performed a range of mechanistic studies and suggested that NH_4^+ is capable of increasing the lifetime of the photosensitizer excited state. Other contributions, including hydrogen bonding or proton management during HER, were also discussed, and the effect was demonstrated to be more general and

relevant to other PS, HER-catalysts, solvents, and sacrificial electron donors.

At the same time, Min and co-workers analyzed the effects of varying reaction parameters on the catalytic activity of **Mo_3**, including catalyst and photosensitizer concentration and their molar ratio. The authors also screened commonly used sacrificial electron donors such as organic amines or organic carboxylic acids. The highest light-driven HER activity was observed for ascorbic acid, which the authors explained by its dual function as proton and electron donor. Also, the authors reported that exchange of the original PS $[Ru(bpy)_3]^{2+}$ with the organic dye Eosin Y resulted in a complete loss of HER activity, possibly due to weak excited-state interactions of the PS and ascorbic acid, so that no electron transfer between the species occurs. Emission quenching studies demonstrated that ascorbic acid acts as a reductive quencher, while **Mo_3** acts as an oxidative quencher for the excited state of $[Ru(bpy)_3]^{2+}$. In a subsequent study, Min and co-workers combined **Mo_3** with the polyoxometalate (POM) $[H_4SiW_{12}O_{40}]$ as a UV-active photosensitizer.[42] In the presence of ethanol as a sacrificial agent, and under irradiation with UV light, the POM forms a two-electron-reduced species capable of electron transfer to **Mo_3**. Sustained hydrogen evolution over periods of 40 h with maximum TONs of≈6900 was reported for this molecular photosystem.

$[Mo_2S_{12}]^{2-}$ (**Mo_2**) is a smaller pure thiomolybdate cluster structurally closely related to **Mo_3** (Figure 1, left). Streb and co-workers explored the light-driven homogeneous HER of this complex[43] when combined with a PS and a sacrificial electron/proton donor. The group observed that catalyst reactivity is highly dependent on the solvent mixture used. Lower HER activity compared with **Mo_3** was reported, with TONs ≈ 1600. Notably, **Mo_2** shows the highest activity in pure methanol, and HER activity decreases with increasing water content of the solvent. This was rationalized by emission quenching studies which showed that increasing solvent water content leads to a less effective quenching of the $[Ru(bpy)_3]^{2+}$ PS by **Mo_2**. The authors did not observe the exchange of the terminal disulfide ligands of **Mo_2** under reaction conditions, which had been described as a major deactivation path for the reference **Mo_3** cluster. Analysis of the main reasons for the loss of catalytic activity (studied after ca. 6 h of irradiation) showed significant PS degradation, so the addition of a second PS aliquot after the initial irradiation period could be used to re-establish HER activity. These early results emphasize the need for replacing molecular photosensitizers with more redox-stable absorbers—a strategy that will be discussed in Section 3.3.

In addition to studies using pure thiomolybdates such as **Mo_2** and **Mo_3**, other thiomolybdate derivatives have been explored under homogeneous conditions. Donahue, Schmehl and colleagues investigated the light-driven HER activity for dithiocarbamate-functionalized **Mo_3** (Figure 1, left).[44] In these systems, the $\{Mo_3S_4\}$-core of native **Mo_3** is retained, while the terminal disulfides are substituted by dithiocarbamate ligands, e.g., diethyl dithiocarbamate, $NEt_2CS_2^-$. The authors used MALDI mass spectrometry to gain understanding of structural changes during catalysis. Within a few minutes of irradiation, the original species $[Mo_3S_7(S_2CNEt_2)_3]^+$ (Figure 1, left) disappears and a new species, $[Mo_3S_4(S_2CNEt_2)_3]^+$ arises. The authors propose that this new species is formed from the original cluster by exchange of the bridging disulfide ligands (S_2^{2-}) with sulfide ligands (S^{2-}), so that under catalytic conditions, $[Mo_3S_7(S_2CNEt_2)_3]^+$ acts as pre-catalyst, forming $[Mo_3S_4(S_2CNEt_2)_3]^+$ as the initial HER-active species. During catalysis, further speciation is observed, including the formation of dimeric species where a $[Mo_3S_7(S_2CNEt_2)_3]^+$ and a $[Mo_3S_4(S_2CNEt_2)_3]^+$ moiety are linked by a bridging sulfide ligand (Figure 2c). This observation is further evidence of the highly dynamic behavior and coordination chemistry of organo-functionalized thiomolybdates, which has been previously discussed for the parent **Mo_3** (vide supra).[40]

In a related study, Cadot and co-workers used the $\{Mo_3S_4\}$-core as an HER-active site for homogeneous, light-driven hydrogen evolution.[45] The authors stabilized two $[Mo_3S_4(H_2O)_3(\mu\text{-}OH)]^{3+}$ species with two $[PW_{11}O_{39}]^{8-}$ polyoxometalate clusters (Figure 1, middle), and reported the light-driven homogeneous HER of this compound using an Ir-based PS and triethanolamine as sacrificial electron donor. The authors showed that the covalent–coordinate linkage between thiomolybdate and polyoxometalate is required for high HER activity, while physical mixtures of both components only result in low hydrogen evolution. Mechanistic studies based on steady-state and time-resolved optical absorption and emission spectroscopies suggested that the Ir-based PS is reductively quenched by the electron donor and can subsequently transfer electrons to the catalyst at a high rate. Notably, high catalyst concentrations led to decreasing HER activity. The authors propose that the **Mo_3**-derived catalyst can absorb significant amounts of the incident photons, leading to overall suppressed rates of light-driven HER.

These studies document the intrinsic reactivity of a variety of thiomolybdate species towards light-driven HER under strictly homogeneous conditions and provide initial molecular-level insights about their activity and stability. The following chapter will examine mechanistic insights on the type of active sites in thiomolybdate HER catalysts.

2.2. Identification of Active Sites in Thiomolybdates

Mechanistic studies on amorphous materials are notoriously challenging due to a lack of information on the material structure at the atomic level, as well as the possible presence of multiple reactive sites. However, identifying the active site and rationalizing the resulting HER mechanism are critical for advancing catalyst development, as the nature of the active site is a key factor that determines the energetics, kinetics, and stability of a catalyst.

The study of thiomolybdate clusters as molecular models for a-MoS_x catalysts was fueled by a pioneering study by Tran, Artero and colleagues, who proposed that a-MoS_x with high HER activity is composed of polymeric chains of **Mo_3**.[46] This report has led to massive interest in exploring thiomolybdate reactivity and rationalizing HER mechanisms along with the nature of the active sites in molybdenum sulfide hydrogen evolving catalysts. However, even for molecularly well-defined systems such as thiomolybdates, identification of catalytically active sites is not straightforward, as active sites can depend on the reaction conditions applied (e.g., photochemical versus electrochemical processes, type of solvent, pH value, etc.).

In addition, it has been reported that thiomolybdates show highly dynamic behavior and undergo ligand exchange under typical catalytic conditions, so that different species can be

present and the catalyst composition can change as a function of time (vide infra). As a result, different reactivity mechanisms are currently described in the literature based on experimental methods (e.g., spectroscopic investigations), theoretical calculations (e.g., DFT studies) and combinations of both. In the following section, we will discuss recent findings and summarize the current understanding of HER mechanisms and active sites in thiomolybdates. In addition, the summary presented in **Table 1** aims at correlating catalyst type, experimental condition and proposed active site.

2.2.1. Sulfide/Disulfide Mechanisms

Experimental and theoretical evidence highlighting the importance of the disulfide ligands were reported by Fantauzzi, Jacob, Streb and colleagues, who studied the light-driven HER using $\mathbf{Mo_3}$ as a catalyst.[40] The authors showed that under catalytic conditions in the presence of water, partial or complete exchange of terminal disulfide ligands with water ligands leads to several $\mathbf{Mo_3}$ derivatives (which can be described as $[Mo_3S_{13-x}(H_2O)_x]^{(2-x)-}$) that coexist in the reaction solution (Figure 2b). Experimental and theoretical analyses indicated that the number of water ligands in such a cluster controls the HER activity: while the fully exchanged species $[Mo_3S_7(H_2O)_6]^{4+}$ showed only marginal HER activity, Mo_3-core surrounded by a mixture of terminal disulfide and water ligands showed the highest reactivity. The introduction of terminal halide ligands also resulted in species with low HER activity. The study further used DFT calculations to explore the energetics of hydrogen evolution on the different water-substituted $\mathbf{Mo_3}$ species. The authors concluded that the energetics of the Volmer step for hydrogen adsorption at bridging disulfide ligands and for forming Mo-hydride species are similar, suggesting that both mechanistic paths are energetically feasible. These results could be interpreted as a first theoretical indication that $\mathbf{Mo_3}$ species are capable of undergoing sulfide/disulfide as well as molybdenum hydride mechanisms in HER catalysis Section 3.

Supporting evidence for a terminal disulfide ligand exchange mechanism was reported by Ončák and co-workers.[47] The groups combined mass spectrometric collision-induced dissociation (CID) experiments with theoretical DFT calculations to examine possible paths to $\mathbf{Mo_3}$ HER activity. The authors observed that even under low energy CID conditions, a range of sulfur/sulfide fragments could be generated from $\mathbf{Mo_3}$. The authors also note that the $\mathbf{Mo_3}$-based species created by CID show high reactivity with water, as observed by the formation of oxothiomolybdates as secondary species. As the mass spectrometric analyses did not allow unambiguous assignment of the type of sulfide ligands removed, the authors performed a subsequent study employing $\mathbf{Mo_3}$ derivatives where all terminal disulfides were replaced by halides (chloride, bromide, and iodide). Gas-phase fragmentation studies showed that loss of the terminal halides is the energetically most feasible fragmentation route, lending further support to the concept of preferred exchange at the terminal ligand sites.[48] In a follow-up work, Ončák and colleagues further linked thermochemical data calculated by DFT to experimental Fourier-transform ion-cyclotron resonance mass spectrometry (FT-ICR MS) and infrared multiple photon dissociation (IRMPD) spectroscopy data measured for a singly protonated $[HMo_3S_{13}]^-$ species.[49] The authors reported that under their conditions (in the gas phase), only the $\mathbf{Mo_3}$-based species with a singly protonated terminal disulfide ligand is observed. Calculations show that this species is thermochemically significantly more stable (by more than 1 eV) compared with $\mathbf{Mo_3}$ isomers where protonation occurs on the bridging disulfide or the apical sulfide position (**Figure 3**b). This study, therefore, suggests that protonated terminal disulfides are key HER intermediates. However, the authors also point out that these gas-phase studies cannot be directly compared with solution analyses, as many effects in the condensed phase can impact the stability and formation pathways of the intermediate and catalytic species.

In contrast to this series of studies focusing on terminal disulfide-based HER reactivity for thiomolybdate-derived catalysts, Joh and colleagues proposed that bridging sulfur ligands play a key role as HER active sites in heterogeneous systems accessed by thermal treatment of $\mathbf{Mo_3}$.[50] The authors used a combination of thermogravimetric analysis (TGA) and X-ray photoelectron spectroscopy (XPS) to link weight loss under heating to changes of the deconvoluted sulfur XPS signal to differentiate between apical/bridging and terminal sulfur positions. The authors propose that upon heating, first the apical sulfide ligand is removed, followed by the loss of the bridging ligands. Catalytic analyses of the resulting materials (supported on carbon nanotubes [CNTs]) showed that higher thermal treatment leads to lower electrocatalytic HER activity. However, further studies are required to fully appreciate the impact of sulfur removal versus structural/morphological changes caused by the heat treatment. Careful electrochemical studies, e.g., using electrochemical impedance spectroscopy or electrochemically active surface area determinations, could help to shed light on this intriguing result.

Very recently, Cherevan and colleagues reported a one-step deposition of $\mathbf{Mo_3}$ on TiO_2 particles for light-driven HER. The authors assigned the stable attachment to the formation of Mo—O—Ti bonds accompanied by the loss of most of the terminal disulfide ligands of $\mathbf{Mo_3}$.[51] Using XPS and thermal analyses together with pre- and postcatalytic materials comparison, the authors concluded that molybdenum centers with vacant coordination sites, Mo-oxo species or bridging disulfides are likely HER-active sites. In addition, the authors note that under catalytic conditions, polymerization of individual $\mathbf{Mo_3}$ species on the TiO_2 surface is observed, highlighting that operando studies are required to follow the temporal development of these catalysts as the reaction progresses.

Yeo and co-workers used operando Raman spectroelectrochemistry to assess possible active sites in a-MoS_2 films synthesized using $\mathbf{Mo_3}$ as precursor.[52] The group observed a characteristic Raman signal assigned to the S—H stretching of a Mo—S—H moiety. The assignment was supported by H/D isotope labeling and DFT calculations. Furthermore, the authors did not observe any Mo-hydride vibrations, which could be expected for a molybdenum hydride HER mechanism. Following a similar approach, Park and colleagues emphasize the importance of Mo═O intermediates in HER catalysis for a-MoS_x derived from thiomolybdate chains.[53] The heterogeneous material was obtained by simple polymerization of monomeric thiomolybdate $[MoS_4]^{2-}$ species. Resonance Raman spectroscopy and extended

Table 1. Active sites of Mo-sulfides: summary of conditions used and HER mechanisms proposed.

Proposed active sites	Catalyst	Experimental conditions	Year	Ref.
Terminal disulfides				
terminal S_2^{2-} (based on experimental data), possible role of Mo-H mechanism (based on theory)	**Mo_3**	Homogeneous, photochemical	2018	[40]
Terminal S_2^{2-}	**Mo_3** and protonated species ($[HMo_3S_{13}]^-$, $[H_3Mo_3S_{13}]^+$)	Homogeneous, gas-phase CID and FT-ICR MS[47]/IRMPD[49]	2018, 2020	[47,49]
Bridging (di-)sulfides				
Bridging S_2^{2-}	**Mo_3**	Heterogeneous, electrochemical, deposited on O-CNT, low-temperature heat treatment	2018	[50]
Bridging S_2^{2-}, vacant coordination sites at Mo centers	**Mo_3**	Heterogeneous, photochemical, deposited on TiO_2	2022	[51]
Bridging S_2^{2-}	a-MoS_x, Mo-precursor: $(NH_4)_2[MoS_4]$	Heterogeneous, electrochemical, deposited on Mo or GC electrodes	2016	[52]
Bridging $S^{2-}$and Mo═O intermediates	Amorphous MoS_3, Mo-precursor: $(NH_4)_2[MoS_4]$	Heterogeneous, electrochemical, deposited on CP	2020	[53]
Bridging S_2^{2-}	**Mo_2**	Heterogeneous, electrochemical, deposited on FTO or GC electrodes	2015	[54]
Mo-centered				
Mo^{IV}-centered mechanism (Mo-hydride)	a-MoS_x, Mo-precursor: $(NH_4)_2[MoS_4]$	Heterogeneous, electrochemical, deposited on FTO electrodes	2016	[46]
Trapped Mo^{III}-H	Precatalytic a-MoS_x, Mo-precursor: $(NH_4)_2[MoS_4]$	Heterogeneous, electrochemical, deposited on a planar Au[55] or GC[56] electrode	2022	[55,56]
Others				
S_2^{2-}-centered mechanism	$[Mo^{IV}S_2$(2,6-*bis*(1,1-*bis*(2-pyridyl(ethyl)pyridine)$]^{2+}$	Heterogeneous, electrochemical, deposited on GC or Hg drop electrodes	2012	[58]
Protonated S_2^{2-}, Mo═O (as proton relay)	$[Mo^{VI}O(S_2)_2L_2]^-$/$[Mo^{VI}O(S_2)_2L]$ (L = pic[59] pym,[59] bpyR (R = H,[60,61] ^{t}Bu,[60] OMe[60]))	Homogeneous, electrochemical[59]	2016, 2017	[59–61]
Mo^{IV}—H mechanism and neighboring bridging hydrosulfide intermediates	$[Mo_3(\mu_3\text{-}S)(\mu_2\text{-}S_2)_3(S_2CNR_2)_3]I$ (R = Me, Et, ^{t}Bu, $CH_2C_6H_5$)	Homogeneous, photochemical	2019	[44]
S-centered mechanism	$[Mo_2O_2S_y]^{2-}$; $[(H)Mo_2O_2S_x]^-$ ($y = 6, 5$; $x = 6, 5, 4$)	Homogeneous, gas phase CID and FT-ICR MS	2022	[62]
S-centered mechanism, PCET	$[M_2O_2(\mu\text{-}S)_2(S_2)(S_x)_2]^{2-}$ (M = Mo, W; $x = 2, 4$)	Heterogeneous, electrochemical, deposited on GC electrodes	2019	[32]

Notes: PCET: proton-coupled electron transfer; pic: picolinate; pym: pyrimidine-2-carboxylate; bpy: 2,2′-bipyridine; CID: collision-induced dissociation; FT-ICR MS: Fourier transform ion cyclotron resonance mass spectrometry; IRMPD: infrared multiple photon dissociation; O-CNT: oxidized multiwalled carbon nanotubes; GC: glassy carbon; CP: carbon paper; FTO: fluorine-doped tin oxide.

ADVANCED SCIENCE NEWS www.advancedsciencenews.com
ADVANCED MATERIALS www.advmat.de

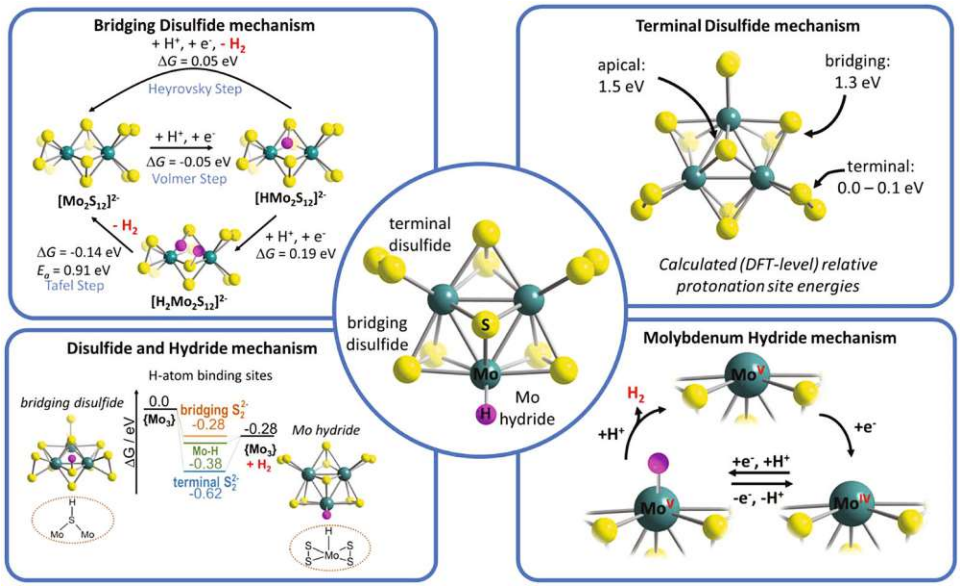

Figure 3. Illustration of possible active sites in the thiomolybdate prototype Mo_3, and proposed mechanisms at these active sites.

X-ray absorption fine structure (EXAFS) analyses showed that under catalytic conditions, formation of $Mo(O)_x$ species ($x = 1, 2$) is observed. The authors suggest that both, the presence of these $Mo(O)_x$ species and the presence of Mo^V units are important for binding and stabilizing protons on the reactive Mo—S site. They propose that the molybdenum-oxo groups could be responsible for proton management, e.g., by stabilizing hydrogen-bound intermediates via hydrogen bonding and by facilitating hydrogen atom transfer to the reactive disulfide ligands.

Chen and co-workers used the small **Mo_2** thiomolybdate as a model HER electrocatalyst by drop-casting **Mo_2** on electrode surfaces.[54] The authors used DFT calculations to study the high HER activity observed for **Mo_2**. Their theoretical analyses show a calculated Gibbs free energy for hydrogen atom adsorption to the bridging disulfide ligands (−0.05 eV), which is close to the thermoneutral optimum of 0 eV. Experimental electrochemistry (Tafel slope analysis) and theoretical calculations both support that H_2 formation proceeds via a Volmer–Heyrovsky mechanism, while high activation barriers are calculated for the alternative Volmer–Tafel mechanism (Figure 3a; Scheme 1).

2.2.2. Mo-Hydride Mechanisms

In contrast to these sulfur-based mechanisms, Tran et al. proposed a Mo-based HER mechanism, based on electrochemistry, resonance Raman spectroscopy, and electron paramagnetic resonance (EPR) spectroscopy as well as DFT calculations.[46] The authors studied samples of **Mo_3** as nanoparticles or a-MoS_x films deposited on electrodes. Based on their results, they propose that under reductive electrochemical conditions, a pre-catalytic electrochemical activation occurs where Mo^{IV} centers with a vacant coordination site are generated on **Mo_3**. These Mo^{IV} centers are reported to represent the catalytically active site (Figure 3d). Theoretical studies support the possibility of Mo^{IV}-hydride moieties as active sites of **Mo_3**-derived amorphous MoS_x films. In addition, the authors reported that during HER electrocatalysis, resonance Raman data show that the signal intensity for bridging disulfide ligands is reduced, and the signal for terminal disulfides is completely lost. Also, the apical sulfide ligand signal is shifted, and the formation of Mo-oxide species is observed. Thus, the authors suggest that the resulting amorphous materials are best described by the formula MoS_{2+x}.

Very recently, Bau et al. reported the presence of Mo^{III} hydride species in **Mo_3**-derived a-MoS_x deposited on electrode surfaces.[55] The authors report the observation of isotropic EPR spectra, which can be interpreted as a Mo^{III}-H species formed by electrochemical reduction starting from Mo^{IV}-based amorphous molybdenum sulfide. In-depth (in situ/operando) analyses, e.g., using X-ray absorption spectroscopy (XAS) methods are expected to provide further evidence for this striking initial hypothesis. The authors built on this work and proposed that Mo^{III} hydrides play an important role in many molybdenum-based HER electrocatalysts. Their hypothesis is based on experimental and theoretical analysis of a range of catalytic systems. The authors propose that (partial) oxidation of the Mo centers is a key deactivation mechanism, since Mo^{III}-oxo species are difficult to reduce to the active Mo^{III}-centers, and oxo ligands also limit proton diffusion to the Mo site.[56]

2.2.3. Organo-Functionalized Thiomolybdate Derivatives

Research has also focused on systems beyond pure molybdenum sulfides. In particular, modification of thiomolybdates with organic ligands has been used to control reactivity. In pioneering work, Appell et al. reported the electrocatalytic homogeneous HER of binuclear $[(CpMoS)_2S_2CH_2]$ and related species at nearly 100% current efficiency and low overpotentials (Figure 1, middle).[57] In mechanistic studies, the author team proposed

that the rate-determining step appears to be the elimination of dihydrogen which can occur via neighboring hydrosulfide ligands or mixed hydrosulfido/Mo-hydride species.

Chang and co-workers explored the electrocatalytic homogeneous HER activity of the complex $[(PY_5Me_2)Mo^{IV}S_2]^{2+}$ (PY_5Me_2 = 2,6-*bis*(1,1-*bis*(2-pyridyl)ethyl)pyridine), which is a molecular model for the terminal Mo-disulfide moiety (Figure 1, middle).[58] The authors observed that the complex can be reduced by at least two electrons. In the presence of protons under reductive electrochemical conditions, a strong catalytic wave, and H_2 evolution at nearly 100% Faradaic efficiency is observed. Voltammetric analyses show that the first reduction of the complex is proton-coupled, allowing the authors to propose that this process corresponds either to the formation of a protonated, one-electron-reduced Mo-disulfide species, or the breaking of a Mo—S bond between the molybdenum center and the disulfide ligand. Notably, reference experiments with the species $[(PY_5Me_2)MoO]^{2+}$ where the disulfide ligand is replaced with a terminal oxo group show much lower HER activity, highlighting the importance of the disulfide ligand, either as an active site or as a modulator to facilitate reduction of the complex.

A different, elegant model system has been reported by Wu and co-workers.[59–61] The group developed a mononuclear species, $[Mo^{IV}O(S_2)_2L]$ (L = organic ligand, e.g., picolinate,[59] pyrimidine-2-carboxylate or 2,2′-bipyridine-derivatives[60,61]), as an active-site model for a-MoS_x. For the 2,2-bipyridine-derivative, the authors propose an electrocatalytic Volmer-Heyrovsky type HER mechanism, which proceeds by two-electron reduction and protonation of a disulfide (to yield a sulfide, S^{2-} and a hydrosulfide, HS^-).[61] The hydrosulfide ligand acts as a "hydride" mimic and reacts with a second proton in a Mo-oxo-mediated Heyrovsky step, resulting in H_2 evolution and regeneration of the original catalyst. In a subsequent study, the group demonstrated the importance of the organic 2,2-bipyridine (bpy) ligand. Modification of the electronic structure of the ligand by attaching electron donating groups had a direct impact on the nucleophilicity of the disulfide ligands on the Mo center. This, in turn, modulated the protonation affinity of the disulfides, which affected the HER performance. The authors also demonstrate that the disulfide ligands are the redox-active sites in this system, while the molybdenum center retains its oxidation state (+IV) even under highly reductive conditions. This could be explained by the presence of the electronegative oxo ligand, which prevents further Mo reduction.

Schmehl and colleagues studied a **Mo_3** derivative, in which the three terminal disulfide ligands were selectively replaced with organic dithiocarbamates (Figure 2c).[44] This model compound is well suited to explore light-driven homogeneous HER activity in the absence of terminal disulfides. The authors used mass spectrometry to follow changes in the catalyst composition under turnover conditions and observed that the actual catalytic species is formed by conversion of the bridging disulfides to sulfide ligands. Catalyst "poisoning" experiments using strongly coordinating solvents such as DMF showed that at least one vacant coordination site at a Mo center is required for HER to proceed. Based on this observation and DFT calculations, the authors propose a species featuring a Mo^{IV} hydride and adjacent bridging hydrosulfide as the most likely intermediate formed before H_2 release.

2.2.4. Mixed Oxothiomolybdates

The introduction of oxo-ligands in thiomolybdates has a major impact on the reactivity of the resulting oxothiomolybdates (vide supra),[47,51,53] which led to seminal studies exploring their HER-function. Following the suggestion that protonated terminal disulfides are important HER intermediates for **Mo_3**, Ončák and colleagues used theoretical calculations to study potential H atom binding sites to $[Mo_2O_2S_x]^{n-}$ in different charge states together with H_2 elimination pathways. The authors identified several H atom adsorption sites as well as energetically favored H_2 elimination pathways. This flexibility, combined with the ease of electron attachment and removal, appears to be the crucial property that makes molybdenum oxysulfides such good HER catalysts.[62] Miras and co-workers reported the electrocatalytic HER activity of the dinuclear compounds $[Mo_2O_2(S)_2(S_2)(S_x)]^{2-}$ (x = 2, 4; Figure 1) when deposited on GC electrodes.[32] Computational analysis of the systems suggested a Volmer–Heyrovsky mechanism where proton-coupled two-electron-reduction leads to a reductive cleavage of a disulfide ligand and the formation of two hydrosulfides. The authors note that the exact mechanism of the Heyrovsky step in these models is still not fully understood, so a complete rationalization of the H_2 release requires further studies. In addition, DFT calculations suggest that the oxo ligand plays an important role in stabilizing the reduced catalyst species by accepting negative charge density due to the high electronegativity of the oxygen atom. In addition, Nadjo and co-workers explored the electrocatalytic homogeneous HER activity of mixed oxothiomolybdate rings, such as $[Mo_8S_8O_8(OH)_8(oxalate)]^{2-}$.[63] The group reported electrochemical studies where catalytic hydrogen evolution was observed under reducing conditions in DMF solution in the presence of strong as well as weak acids.

As shown in Table 1, when summarizing the findings from Section 3.2, there is a general trend that under homogeneous conditions, most reports favor terminal disulfide active sites, while under heterogenized conditions, bridging disulfides are mainly discussed as active sites. Mo-hydride species are most often described when amorphous a-MoS_x is studied, while for thiomolybdates featuring organic ligands, a variety of possible active sites have been reported. While each individual study provides a huge contribution to improve the general understanding of underlying mechanistic processes, stability and identification of catalytically active sites, many of the studies seem contradictory, and there is no general consensus in the field in terms of the true reaction mechanism (or mechanisms). This is due to the fact that the molybdenum sulfide HER mechanism is highly dependent on the exact reaction conditions, the type of support used, and on the exact structure of the cluster. Hence, further work including the design of suitable model systems, as well as combined experimental and theoretical studies—ideally involving in situ and operando investigations—are required to fully understand the complex mechanisms involved in hydrogen evolution by thiomolybdates.

2.3. Heterogenization of Thiometalates

In this section, we will pick up on initial discussions from Sections 3.1 and 3.2 concerning the prospects and benefits of

thiometalate heterogenization. In this context, heterogenization describes either the anchoring of individual thiometalate clusters on the surface of solid-state supports, the incorporation of thiometalates within (micro)porous matrices or the deposition of clusters followed by their chemical conversion into nanostructured amorphous or crystalline particles. Similar to the case of other molecular inorganics such as polyoxometalates,[64] surface-anchoring of thiometalate clusters can rely on electrostatic (due to their ionic charge), covalent (due to exchange of the sulfide/disulfide ligands), or weaker noncovalent interactions between cluster and the support surface. From the synthetic point of view, heterogenization can be achieved using a range of immobilization techniques including dip-coating, solvothermal deposition, layer-by-layer assembly, and electrodeposition.[64] Note that depending on the deposition methods and conditions used, the conversion of molecular thiomolybdates into more complex nanostructures—often a-MoS_x—is possible and should be critically assessed when studying and reporting thiomolybdate-based electrocatalysts.

Heterogenization of thiomolybdates is a fast-moving research direction due to several reasons: deposition of thiomolybdates on electrically conductive substrates or semiconductors facilitates their use in (photo)electrochemical HER as heterogeneous materials, which is an advantage for scaling and technological processing. Furthermore, heterogenization could lead to a stabilization of the thiomolybdate clusters, e.g., by preventing fast ligand exchange or providing structural stabilization during the catalytic redox cycles. In addition, molecule–support interactions could be used to further fine-tune reactivity and stability of thiomolybdates, e.g., by utilizing the supports for managing proton and/or electron transfer. Finally, the use of semiconductors as supports opens new avenues to combine heterogenization and photosensitization in one material, making the traditional use of noble metal-based photosensitizers (e.g., $[Ru(bpy)_3]^{2+}$) obsolete. These and other aspects of thiomolybdate heterogenization will be next discussed from the application point of view in Section 4.

3. Applications of Heterogenized Thiomolybdate Clusters

This section aims to scrutinize the applications of surface-anchored thiomolybdate clusters. The analysis focuses on the catalytic performance as well as on details of the surface-anchoring, the stability of the resulting system, and the fate of the cluster, from deposition through to catalysis. In particular, we highlight the emerging use of in situ/operando analyses as well as the combination of experiment and theory to rationalize the observed reactivity trends. In Section 3.1, we focus on electrocatalysis, while Section 3.2 describes selected examples of photocatalytic deployment. In Section 3.3, recent examples where heterogenized thiomolybdates were used for reactions and processes other than HER are summarized.

3.1. Electrocatalysis

Solid-state molybdenum sulfides are well known for their excellent electrocatalytic HER performance and are discussed as replacements for platinum-based HER catalysts. In particular, MoS_{2+x} systems with an S-to-Mo ratio higher than two have been reported to be excellent electrocatalysts for the HER.[65] This section explores how thiomolybdate-based heterogeneous materials are designed, tuned and deployed as high-performance HER electrocatalysts.

Along with TONs that are indicative of the catalyst stability, turnover frequencies (TOFs)—a measure of the rate of catalysis per active site—are key figure of merits for the HER performance and will be used throughout this section as an indicator for the intrinsic HER activity measured for the thiomolybdate clusters. Note that for most of the heterogenized catalysts discussed here, the calculation of TOFs and TONs assumes that every cluster present in the catalyst is available for the reaction. Thus, the use of TON and TOF—particularly in heterogenized systems, requires careful thought and critical analysis of the system studied.[66–68] Also note that all potentials mentioned throughout this chapter (and those in **Table 2**) are reported versus the reversible hydrogen electrode (RHE) and all overpotentials are reported at the current density of 10 mA cm^{-2} unless stated otherwise. Nevertheless, we strongly advise the reader to always be aware of the substrate used for the electrode, as different supporting materials can have varied electrochemical surface areas for the same geometric surface area, thus affecting the reported performance indicators. The challenges of benchmarking electrocatalytic reactions have been comprehensively reviewed by Jaramillo and co-workers.[69]

Further, throughout this section we will use Tafel slope analysis as a tool to gain insights into the rate-limiting steps in electrocatalytic HER. For example, a Tafel slope below 30 mV dec^{-1} is indicative of the Tafel reaction (H* recombination) to be the rate-limiting step. Similarly, a Tafel slope around 40 or 120 mV dec^{-1} suggests Heyrovsky (electrochemical H_2 desorption) or Volmer (discharge) step be the rate-limiting step, respectively (Scheme 1).[70]

3.1.1. Electrocatalytic HER Activity of Heterogenized Thiomolybdates

This section summarizes the initial reports on molecular mimics of MoS_2 electroactive toward HER, along with factors affecting their performance. Chorkendorff and co-workers were the first to test cubane-type $[Mo_3S_4]^{4+}$ clusters supported on carbon materials (Vulcan xc72 and highly oriented pyrolytic graphite [HOPG]) for the electrocatalytic HER.[38] For $[Mo_3S_4]^{4+}$/Vulcan system, the authors reported a low HER onset potential of ≈150 mV, similar to that of nanoparticulate MoS_2. However, the authors observed drops in current density upon multiple scans without any change in onset potential, which they attribute to possible dissolution of the clusters. Further investigation using scanning tunneling microscopic (STM) imaging was conducted for the drop-cast $[Mo_3S_4]^{4+}$/HOPG system revealing agglomeration mounds—possibly corresponding to cluster deposits or products of its degradation—which the authors related to the weak interactions between the clusters and the substrate surface. This assumption was further strengthened based on postcatalytic XPS analysis of $[Mo_3S_4]^{4+}$/HOPG, which revealed almost no peaks corresponding to the Mo 3d of the pristine cluster suggesting

Table 2. Supported thiomolybdates in electrocatalytic HER: summary table showing prominent examples of thiomolybdate clusters implementation, along with the supports used, deposition applied, and HER performance indicators including Tafel slopes, overpotentials, TOF values as well as major experimental conditions.

Cluster	Support	Deposition technique	Experimental conditions	Tafel slope [mV dec^{-1}]	Overpotential at 10 mA cm^{-2} vs RHE [mV]	TOF at 200 mV [s^{-1}]	Year	Ref.
MoS_2								
MoS_2 NPs	Au(111)	PVD of Mo in H_2S background	H_2SO_4, pH 0.2	55	–	0.02	2007	[10]
MoS_2	rGO | GCE	Drop casting	0.5 M H_2SO_4	41	–	–	2011	[85]
Monodispersed MoS_2	$Au^{[110]}$	Incubation	0.5 M H_2SO_4	69	180–190	–	2013	[86]
		Drop casting		100	–		2013	[86]
Mo_xS_4								
$[Mo_3S_4]^{4+}$	C-xc72	Drop casting	0.5 M H_2SO_4, pH 0.4	120	200	0.07	2008	[38]
$CuMoS_4$	GCE	Drop casting	0.1 M H_3PO_4, pH 7	–	–	–	2012	[87]
$Mo_2/Mo_3/W_2$								
Mo_3	GP/HOPG	Drop casting	0.5 M H_2SO_4	40/57	180	1	2014	[71]
Mo_3	Au | GC	Spray coating	0.1 M $HClO_4$	58	–	0.47	2017	[72]
Mo_3	Ag | GC			48	–	0.27	2017	[72]
Mo_3	GC			45	–	0.15	2017	[72]
Mo_3	Cu | GC			66	–	0.045	2017	[72]
Mo_3	rGO-CNTs	Solvothermal	0.5 M H_2SO_4	67.4	179	–	2017	[76]
Mo_3	HOPG	Electrodeposition	0.5 M H_2SO_4	37	200	–	2017	[78]
Mo_3	O-CNTs	Physical mixture	0.5 M H_2SO_4	40	137	2.5	2018	[50]
						at 250 mV		
Mo_2	FTO	Drop casting	0.5 M H_2SO_4	39	161	1.6	2015	[54]
$[Mo_2O_2S_6]^{2-}$	GCE	Drop casting	1 M H_2SO_4	52	114	0.12	2019	[32]
$[Mo_2O_2S_8]^{2-}$			1 M H_2SO_4	55	116	0.12	2019	[32]
$[W_2O_2S_8]^{2-}$			1 M H_2SO_4	100	227	0.13	2019	[32]
MoS_3								
a-MoS_3-Mo_1-derived	Carbon paper	Drop casting	0.5 M H_2SO_4	46	167	0.01	2020	[53]
a-MoS_3-Mo_2-derived			0.5 M H_2SO_4	47	170	0.004	2020	[53]
a-MoS_3-Mo_3-derived			0.5 M H_2SO_4	52	196	0.0006	2020	[53]
MoS_3	FTO	Spray casting	1 M H_2SO_4	45	190	–	2011	[88]
MoS_3	FTO	Drop casting	1 M H_2SO_4, pH 0	61	200	–	2011	[88]
MoS_3	GCE	Drop casting	1 M H_2SO_4	50	200	–	2011	[88]
Others/composites								
bachera-MoS_2/MWCNT	Ag	Drop casting + in situ reduction of MoS_3	1 M H_2SO_4	40	–	–	2013	[89]
Ni-P/MoS_x	FTO	Electrodeposition	1 M KOH	64	140	–	2017	[90]
MoS_x	FTO	Electrodeposition	1 M KOH	140	260	–	2017	[90]
MoS_x/MWCNT	GCE	Drop casting	0.5 M H_2SO_4	62	–	–	2016	[91]
MoS_x/GO	GCE	Drop casting	0.5 M H_2SO_4	60	180	0.94 at 220 mV	2016	[92]
Pd-MoS_2/MWCNT	GCE	Drop casting	0.5 M H_2SO_4	54	120	0.05 at 30 mV	2017	[93]
MoS_2/CN_x	GCE	Drop casting	0.5 M H_2SO_4	52	158	–	2017	[94]

Notes: NPs: nanoparticles; PVD: physical vapor deposition; rGO: reduced graphene oxide; GCE: glassy carbon electrode; C-xc72: vulcan carbon; GP: graphite paper; HOPG: highly oriented pyrolytic graphite; O-CNTs: oxidized carbon nanotubes; FTO: fluorine-doped tin oxide; MWCNT: multiwalled carbon nanotubes.

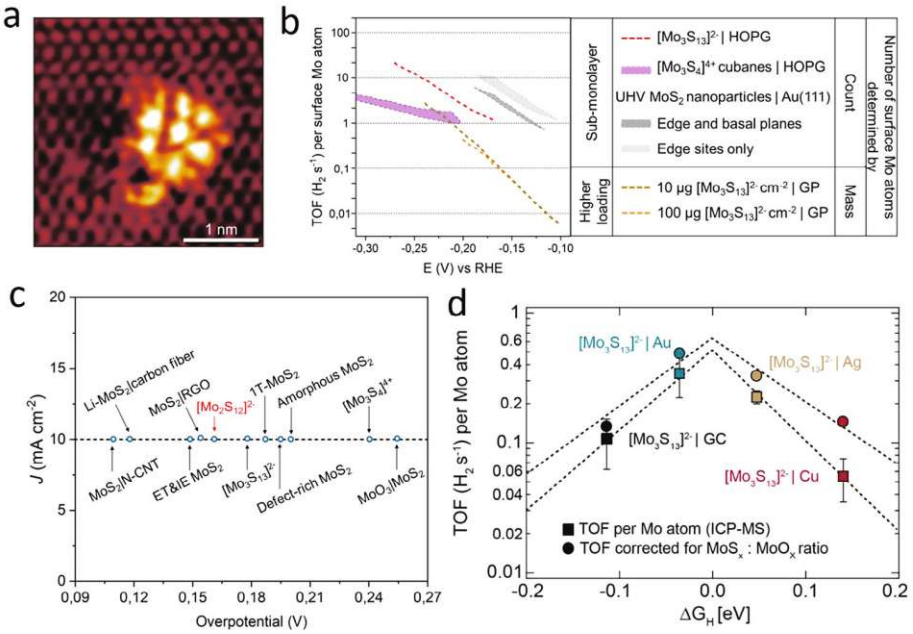

Figure 4. Supported thiometalates in electrocatalysis. a) Scanning tunneling microscopy (STM) image of a single Mo_3 cluster on HOPG support. b) TOF plot comparing electrochemical HER performance of Mo_3/HOPG and Mo_3/GP with other MoS_x catalysts. c) Overpotential comparison between various Mo—S based catalysts. d) HER volcano plot showing TOF_{MoOx} corrected using ICP-MS. (a,b) Reproduced and adapted with permission.[71] Copyright 2014, Nature Chemistry. (c) Adapted with permission.[54] Copyright 2015, Wiley-VCH GmbH. (d) Reproduced with permission.[72] Copyright 2017, American Chemical Society.

unstable nature of its attachment. To circumvent this issue, HOPG surface was activated by electrochemical oxidation to introduce —OH and —COOH groups able to act as anchoring sites for $[Mo_3S_4]^{4+}$ cations. Combining this strategy with STM imaging to reveal the surface density of the clusters, the authors reached a TOF of 0.07 s^{-1} per $[Mo_3S_4]^{4+}$ molecule, as compared to 0.02 s^{-1} (per edge site determined via STM imaging) measured for the reference MoS_2 sample.

Almost half a decade later, Besenbacher and co-workers reported excellent electrocatalytic performance by **Mo_3** which was drop-cast onto an anodized HOPG surface (**Figure 4**a). XPS analysis confirmed stable attachment of the clusters onto the surface without any transformation.[71] **Mo_3** dispersed over HOPG exhibited a low overpotential of ≈180 mV and a Tafel slope of ≈57 mV dec^{-1}, indicating H* recombination to be the rate-determining step (Scheme 1). However, to obtain a better comparison to reported literature, the authors loaded the clusters onto graphite paper (GP) increasing the loading from 10 to 100 µg cm^{-2}. They observed all Tafel slopes to be around 38–40 mV dec^{-1}, which indicates the Heyrovsky (desorption) step to be rate limiting. To further elucidate the reason for the change in HER mechanism and avoid any effects due to the change in support, the authors measured the Tafel slopes of different loadings of clusters onto a single support, glassy carbon (GC). They observed a Tafel slope of 40 mV dec^{-1} at higher loadings whereas a Tafel slope of ≈60 mV dec^{-1} was observed for very low loadings similar to the case of HOPG. Therefore, the authors suggested this change in the mechanism is independent of the support and rather could be due to closer packing of the cluster (and thus active sites) which affects the H-adsorption and chemical rearrangement of the intermediate steps during HER. As to the intrinsic HER activity of the clusters, the authors reported a high TOF of 3 s^{-1} per Mo atom (i.e., 1 s^{-1} per **Mo_3**) at −200 mV for the **Mo_3**/HOPG architecture (Figure 4b). However, they did observe a fivefold lower TOF when depositing higher loadings of the clusters onto GP, which they attributed to shielding of the catalytic sites due to cluster agglomeration. As an important contrast to the $[Mo_3S_4]^{4+}$ work conducted by Chorkendorff and co-workers,[38] here the authors observed no loss in catalytic performance, which suggests a more stable binding of **Mo_3** to anodized HOPG compared with $[Mo_3S_4]^{4+}$. As a consequence, upon accelerated HER testing (1000 cyclic voltammetry (CV) cycles between −0.3 and +0.2 V), the **Mo_3**/HOPG composite showed only a slight decrease in current density and a small increase in total impedance.

Building on these results, Wu and co-workers explored the electrochemical performance of the dimeric **Mo_2** deposited onto FTO substrate via layer-by-layer assembly (involving positively charged polyquaternium-6 interlayer) and drop-casting, aiming for sub-monolayers and higher catalyst loading, respectively.[54] They reported an even higher TOF of 3.2 s^{-1} per Mo atom (which could be translated to 1.6 s^{-1} per **Mo_2** cluster based on total **Mo_2** loading) at −200 mV, while the overpotential required to reach a current density of 10 mA cm^{-2} for **Mo_2** was found to be only 161 mV, outcompeting both previously mentioned $[Mo_3S_4]^{4+}$ and **Mo_3** that showed an overpotential of 240 and 180 mV, respectively, when deposited on HOPG (Figure 4c). To explain this difference in performance, the authors theoretically modeled H adsorption on the unsupported clusters in question. They calculated the change in free energy for **Mo_2** and **Mo_3** as −0.05 and

−0.08 eV, respectively: these values are significantly closer to the theoretical optimum (0.0 eV) compared with data reported earlier for $[Mo_3S_4]^{4+}$ (0.4 eV).[54] Therefore, based on these initial works, dimeric **Mo_2** seems to outperform the previously reported MoS_x-based HER electrocatalysts due to favourable adsorption-desorption thermodynamics. However, more studies and direct comparison between **Mo_2** and **Mo_3** under identical experimental conditions is necessary to identify their active HER sites and unravel structural features which control their HER performance.

3.1.2. Catalyst–Support Interactions

The choice of the substrate is essential for providing robust anchoring and improved electronic coupling between catalyst and substrate. A bulk of earlier work on supported MoS_2-based catalytic phases for HDS, HDO and HDM catalysis already demonstrated a synergistic effect between the two components and importance of the support choice.[73,74] In this section, we discuss the current understanding of how the choice of substrates affects the stability and electrocatalytic performance of heterogenized thiomolybdates.

Building on their earlier studies on **Mo_3**, Jaramillo and co-workers carried out a follow up study correlating the HER activity of **Mo_3** with the type of support material used.[72] The group studied electrocatalytic HER performance of a thin layer of cluster deposited on four substrates, i.e., pristine glassy carbon (GC), Cu on GC (Cu/GC), Ag on GC (Ag/GC), and Au on GC (Au/GC). The authors deliberately kept the catalyst loading low to be able to observe the effects of the catalyst–support interactions as these tend to have a short range.[75] By keeping the catalyst loading low the authors also avoided any detrimental effects related to cluster aggregation. The results of XPS analyses of the supported catalysts were virtually identical to the pure **Mo_3** precursors, suggesting that the heterogenization did not majorly affect the structure of the deposited **Mo_3**. Tafel slope analyses for all samples were in the range of 40 to 60 mV dec^{-1}, so that no clear insights into the difference in underlying rate-determining steps were possible. In contrast, a marked impact of the substrate on the TOF was observed, and the resulting TOF values at −200 mV were measured to be 0.47 s^{-1} (Au/GC), 0.27 s^{-1} (Ag/GC), 0.15 s^{-1} (GC), and 0.045 s^{-1} (Cu/GC), respectively (Figure 4d). The authors carried out DFT calculations considering long range van der Waals forces to account for the effect of the strength of the cluster adhesion on the support on its activity.[75] They correlate the observed TOFs to changes in Gibbs free energy for hydrogen adsorption on the cluster (for each support) and arrived at the conclusion that the relationship between the two follows a volcano-plot trend well known for other HER electrocatalysts.[2]

Following similar concepts, Gao and co-workers reported an increase in electrocatalytic HER performance at low catalyst loadings when immobilizing **Mo_3** onto highly conductive reduced graphene oxide (rGO)–CNT aerogels (**Figure 5**a),[76] reporting an HER overpotential of 179 mV. Attachment of the clusters to the aerogels was demonstrated using multiple techniques including EDS mapping and Raman spectroscopy. The authors reported a low Tafel slope of 60–70 mV dec^{-1}, similar to the case reported by Jaramillo and co-workers in the best-performing **Mo_3** on Au/GC and Cu/GC.[72] The authors employed zeta potential measurements and XPS analyses to gain insights into the immobilization mechanism. Zeta potential measurements revealed a negatively charged rGO-CNT surface, which—considering the anionic **Mo_3** clusters in solution—renders electrostatic attachment unlikely. XPS analysis showed a characteristic S—O binding peak allowing the authors to suggest strong cluster attachment via covalent linkage to the O-containing functional groups on the nanocarbon surface. However, we note that molybdenum sulfides and thiomolybdates can feature oxidized sulfur species (e.g., sulfate) left from the synthesis or formed during catalysis.[77] Thus, care must be taken when interpreting the origin of any S—O signals, e.g., in XPS. Thus, further studies might be required to fully appreciate the type of attachment present in the **Mo_3**/rGO-CNT composites. For example, an alternative attachment scenario could take place via the **Mo_3** ligand exchange mechanism discussed in Section 3, which shows that charge-neutral or even cationic cluster species could be accessed. As to the electrocatalytic performance of the **Mo_3**/rGO-CNT composite, although the authors did not report the TOF values, the small Tafel slope, low charge transfer, and dispersion resistances indicate a fast reaction rate corresponding to efficient HER performance and low overpotentials. Moreover, the authors report a negligible change in activities even after 1000 CV cycles, further confirming the robust nature of the **Mo_3**/rGO-CNT electrocatalyst (Figure 5a).

Li and co-workers took a different approach to strengthen the linkage between the cluster and substrate.[78] Contrary to using drop-casting or impregnation methods, they electrodeposited **Mo_3** onto HOGP in the form of flakes of varying thicknesses by changing the deposition times. Note that under mild electrodeposition conditions, anionic **Mo_3** clusters can transform into an amorphous MoS-like structure that is largely made up of the original $\{Mo_3S_7\}$ subunits.[79] In line with this, XPS analysis complemented by atomic emission spectroscopy and XAS measurements, confirmed the structural integrity of the cluster after deposition. At optimized film thicknesses (beyond 1500 s when through-film resistance starts dominating the process), the as-derived **Mo_3**/HOPG attained an onset potential of 130 mV with a Tafel slope of 37 mV dec^{-1} and showed no signs of Mo leaching even after 3000 CV cycles, thereby confirming the durability of the supported electrocatalyst. Compared to simple drop-cast films, electrodeposited **Mo_3**/HOPG electrodes showed a much lower charge transfer resistance demonstrating remarkable electron transport.

In addition, Assaud and co-workers reported an interesting study demonstrating the effect of thiomolybdate cluster interactions with carbon-based supports commonly used in PEM water electrolysis.[80] They observed a strong decrease in onset potential from −439 to −124 mV when moving from graphene- to Vulcan-supported $[Mo_3S_4]^{4+}$-based clusters. Furthermore, the authors also reported a much lower overpotential required for $[Mo_3S_4]^{4+}$/Vulcan as compared to $[Mo_3S_4]^{4+}$/graphene to reach a current density of 30 mA cm^{-2}. Since these overpotentials already consider surface roughness characteristics of the two supports and the current densities were already normalized per electrochemically active surface area, the authors proposed that this difference in performance is due to stronger physisorption of $[Mo_3S_4]^{4+}$ on the Vulcan surface.

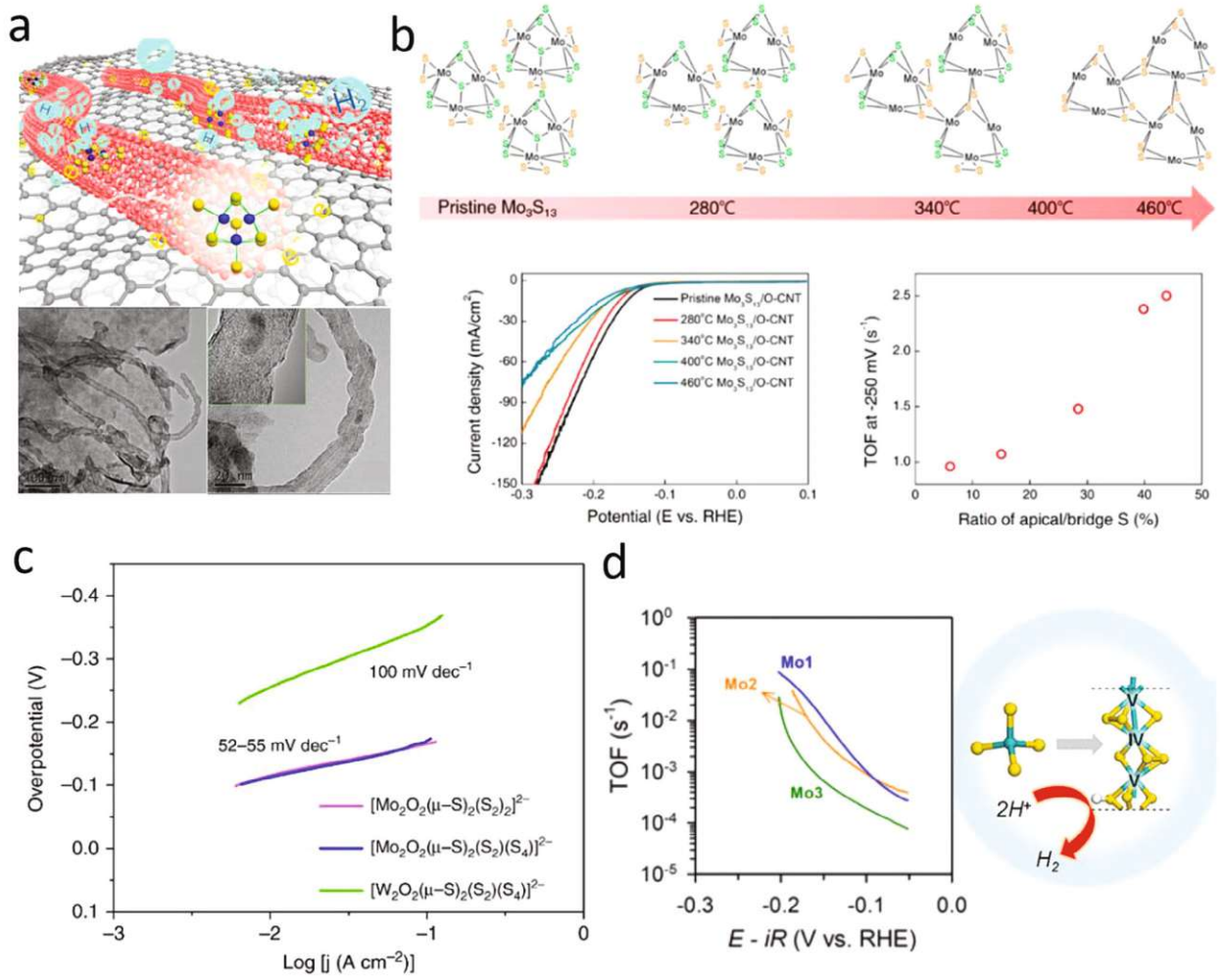

Figure 5. Supported thiometalates in electrocatalysis. a) Schematic representation of the Mo_3/rGO-CNTs composite structure with TEM images of Mo_3/rGO-CNT taken after 1000 HER cycles. b) Proposed structural evolution and electrochemical HER performance with TOFs of thermally annealed Mo_3/CNT composites at 280, 340, 400, and 460 °C. c) Tafel plots of different Mo- and W-based oxothiometalate clusters. d) TOFs of Mo_1-, Mo_2-, and Mo_3-derived MoS_3 (its model on the right). (a) Reproduced with permission.[76] Copyright 2017, American Chemical Society. (b) Reproduced with permission.[50] Copyright 2018, American Chemical Society. (c) Reproduced with permission.[32] Copyright 2019, Nature Communications. (d) Reproduced with permission.[53] Copyright 2020, American Chemical Society.

3.1.3. Role of Cluster Structure

Finally, this section outlines the studies performed to gain an in-depth understanding of how the composition, structure, and origin of the thiomolybdate species can be linked to their HER performance.

Traditionally, **Mo_3** clusters have been synthesized from $(NH_4)_6[Mo_7O_{24}]$ precursor via a method reported by Müller and co-workers.[27,28,81] However, there are several other synthetic methods of **Mo_3** formation using molybdenum trisulfide (MoS_3) as proposed by Müller and Weber.[82,83] Building on this, Joh and co-workers investigated electrochemical HER activity of MoS_3-derived **Mo_3** by supporting it onto oxidized multiwalled carbon nanotubes.[50] The authors observe an overpotential of 137 mV and a Tafel slope of 40 mV dec^{-1}. To further understand the role of each component they next explored the possibility of **Mo_3** cluster polymerization by studying the effect of thermally assisted conversion of **Mo_3**. The authors demonstrated that heat-treatment of **Mo_3** at different temperatures up to 460 °C results in materials which show variable TOFs in the electrocatalytic HER reaction (Figure 5b). Based on these catalytic data and complemented by DFT studies, the authors proposed bridging disulfide ligands to be the likely active HER site, as was detailed in Section 3.2.1. We note that the authors propose that the heat treatment at specific temperatures can be used to trigger selective structural changes (e.g., loss of the apical sulfide ligands). However, this level of assignment requires further detailed analysis, e.g., by vibrational spectroscopy or mass spectrometry to verify this hypothesis. Alternative processes might include (partial) cluster degradation and conversion into amorphous molybdenum sulfides.

In another prominent work, Miras and co-workers investigated the impact of the structural and stoichiometric ratio of the chalcogen to transition metal on HER performance by examining a broader set of oxothiometalate clusters.[32] Focusing specifically on the thiomolybdates, the authors compared $[Mo_2O_2(S)_2(S_2)_2]^{2-}$ and $[Mo_2O_2(S)_2(S_2)(S_4)]^{2-}$ (Figure 1, right) drop-cast onto GC electrodes. Both clusters exhibited similar Tafel slopes in the range of 52–54 mV dec^{-1} and a low overpotential of about 114 mV, which demonstrates a negligible effect of the terminal sulfide groups in the cluster on the HER mechanism and performance (Figure 5c). On contrary to this conclusion, the authors estimated a TOF of 0.12 s^{-1} for both oxothiometalates. This value is significantly lower as compared to TOFs reported for other similar clusters (Table 2), thus still leaving an open question to the stability and potential transformation of oxothiometalates under turnover conditions.

Joo and co-workers explored the effect of Mo oxidation state in the MoS_x family of clusters on the overall HER.[53] They prepared amorphous MoS_3 polymeric chains using $[MoS_4]^{2-}$, **Mo_2**, and **Mo_3** as monoatomic, diatomic, and triatomic Mo precursors, respectively. The electrodes were prepared by drop casting the precursors onto carbon paper, followed by thermal treatment at 120 °C to initiate polymerization. The samples were labeled as Mo_1-, Mo_2-, and Mo_3-derived MoS_3, depending on the precursor chemistry. After the synthesis, Mo_1-derived films showed the lowest overpotential of 167 mV, closely followed by 170 mV for Mo_2-derived and the highest overpotential of 196 mV for Mo_3-derived electrocatalysts. However, Tafel slopes for each of them was within the range of 46–52 mV dec^{-1}. Further characterization revealed that Mo_1-derived MoS_3 had a higher electrochemical active surface area as compared to other electrocatalysts, thus justifying its superior HER performance amongst the three (Figure 5d). Since both **Mo_2** and **Mo_3** clusters have been used as precatalysts (precursors) in this work, no further conclusion about the impact of thiomolybdate molecular structure on HER activity could be drawn from the results. However, this work demonstrates that thiomolybdates can be used as precursors which allow to obtain a variety of structurally different MoS_x electrocatalysts.

Overall, Table 2 highlights, that the HER performance of thiomolybdates depends strongly on the type of the cluster and type of the support used with overpotential values reported in the range between 120 and 200 mV (at 10 mA cm^{-2} current density). This range is generally higher when compared to molybdenum carbides or phosphides; however, MoS_2-based nanostructures are known for higher intrinsic activity (i.e., TOF values)[84] still making thiomolybdates and their derivatives attractive.

3.2. Photocatalysis

Soon after the first studies on thiomolybdate HER electrocatalysis, the light-driven catalysis community started exploring these cluster species as molecular co-catalysts. Starting with the most common UV-active TiO_2 as a photoactive support, a range of narrow-band semiconductors and (micro)porous hosts have been employed to design efficient and robust heterogeneous photoactive composites (**Figure 6**a). Section 4.2.1 discusses these studies with a focus on photocatalytic HER by thiomolybdate anchored on TiO_2 semiconductors, while Section 4.2.2 focuses on visible-light-active semiconductor supports. In Section 4.2.3, the photoreactivity of thiomolybdates heterogenized in porous matrices is discussed.

3.2.1. Thiomolybdate Clusters as HER Co-Catalysts

Several prominent works have been reported over the past years, in which heterogenized thiomolybdates have been used for light-driven HER. In 2014, Llusar and co-workers reported the use of $[Mo_3S_7]^{4+}$ fragments which were heterogenized onto TiO_2 to act as a co-catalyst for photocatalytic HER.[95] To facilitate covalent anchoring of the cluster on the oxide surface, the authors employed the $\{Mo_3S_7\}$-core-containing complex $[Mo_3S_7Br_4bpy(CO_2Me)_2]$, ($bpy(CO_2Me)_2$ = 4,4′-dimethyldicarboxylate-2,2′-bipyridine, see Figure 1, right). Based on electrochemical and spectroscopic measurements, the authors suggest that the molecular species serves as a precatalyst and is reductively converted to a more active catalyst species when in contact with sulfite/sulfide species in the reaction solution. The nature of these reduced species was unraveled by XPS analysis, according to which the final electroactive material is composed of Mo^{IV} atoms coordinated to S^{2-} moieties, suggesting a MoS_2-based compound. The resulting MoS_2/TiO_2 composite showed promising visible light-driven HER with no performance loss even after 8 h of operation (Figure 6b).

More recently, Cherevan and colleagues investigated the attachment modes and loading-dependent photocatalytic HER performance of the non-modified **Mo_3** cluster which was anchored onto TiO_2.[51] The authors proposed that **Mo_3** deposition follows a monolayer adsorption and involves the formation of Mo—O—Ti coordinative bonds while maintaining the overall molecular structure of **Mo_3**. The authors further explored the photocatalytic HER performance of **Mo_3**/TiO_2 composites with different cluster loadings revealing optimal activity at around 3 wt% of **Mo_3** (Figure 6c). As revealed by radical-trapping photoluminescence (PL) spectroscopy, the drop for higher loading values is related to the availability of the support-solution interface required for the efficient hole scavenging. The authors also performed long-term HER studies which showed stable photocatalytic H_2 evolution rates. These results are in strong contrast to the work discussed previously[95] and suggest that native thiomolybdates without any organo-functionalization are able to undergo direct binding with oxide-based supports and further act as structurally stable co-catalysts for HER.

In related studies, Du and colleagues explored the surface attachment, optical properties, photocatalytic HER performance and stability of **Mo_2** as a co-catalyst when deposited onto anatase-type TiO_2.[97] XPS analyses indicated that **Mo_2** attaches covalently to the TiO_2 support by replacement of the terminal S_2^{2-} ligands. Optimum HER activity was achieved at 3 wt% loading. The authors additionally reported PL data for **Mo_2**/TiO_2 composites, which documented improvement in charge separation (low PL intensity and higher excited state lifetime when compared to pure TiO_2), while complementary photoelectrochemical measurements showed higher photocurrent for the optimum **Mo_2**/TiO_2 composite, which further confirms improved charge

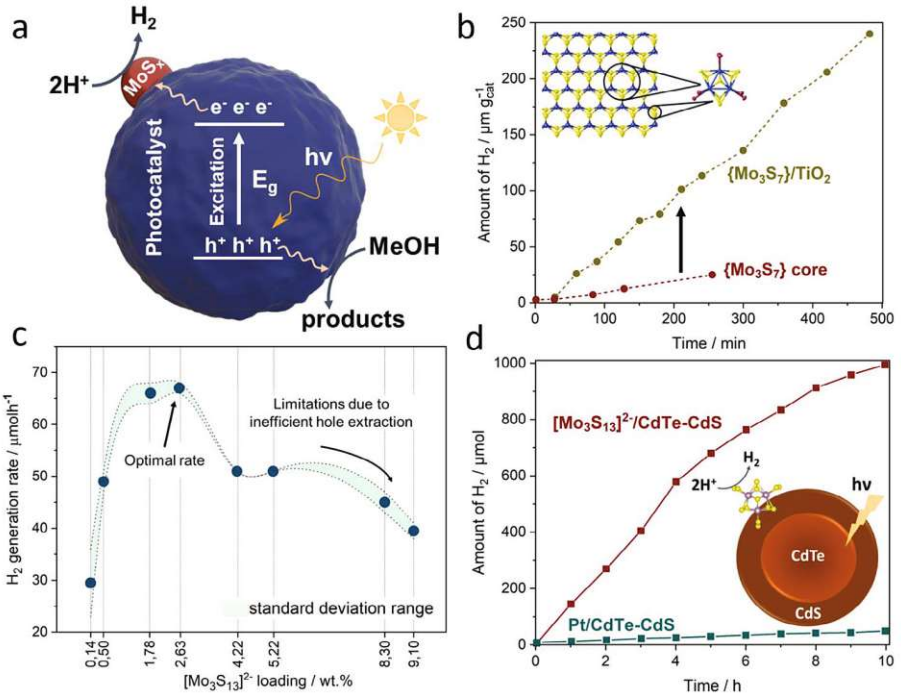

Figure 6. Supported thiometalates in photocatalysis. a) Illustration of charge transfer from photocatalyst to the thiometalate co-catalyst upon light illumination. E_g: energy bandgap; MoS_x: any thiometalate cluster. b) Hydrogen generation profiles of heterogenized $\{Mo_3S_7\}/TiO_2$ (5 wt% cluster loading, 1 g L^{-1}) and $\{Mo_3S_7\}$-core containing complex (homogeneous, 0.31 g L^{-1}) in acetone/H_2O mixture obtained in the presence of 0.1 M Na_2S and 0.02 M Na_2SO_3. c) Hydrogen evolution rate plotted against the Mo_3 cluster loading on TiO_2: volcano type profile is highlighted. d) Amount of hydrogen produced by Mo_3/CdTe@CdS (Mo_3 concentration: 4.6×10^{-6} M) and Pt/CdTe-CdS under optimal reaction conditions of pH = 2.5 from 20 mg mL^{-1} ascorbic acid aqueous solution (20 mL). (b) Adapted with permission.[95] Copyright 2015, Wiley-VCH. (c) Reproduced with permission.[51] Copyright 2022, American Chemical Society. (d) Adapted with permission.[96] Copyright 2016, American Chemical Society.

separation dynamics and suggests efficient charge extraction by the surface-bound **Mo_2** species.

3.2.2. Extension to Visible-Light-Active Supports

For light-driven HER, it is crucial to investigate support materials that can maximize the absorption of solar light.[98] One of the most promising classes to this end are semiconducting CdX (X = S, Se, Te) quantum dots (QDs), as their light absorption properties can be fine-tuned by modulating their dimensions and composition. Zhao and co-workers employed CdTe/CdS core/shell QDs as support for **Mo_3** and verified the cluster anchoring by a combination of high-resolution transmission electron microscopy (HRTEM) and XPS analyses.[96] The authors proposed that the adsorption of **Mo_3** occurs via the Cd-terminated faces as well as surface defects, including Cd adatoms and S vacancies of QDs. The HER activity of **Mo_3**/CdTe-CdS composite was almost constant over more than 10 h of illumination. The authors also report the HER performance to be significantly higher compared with a benchmark Pt co-catalyst loaded on CdTe-CdS QDs (Figure 6d). However, the team also emphasized that the **Mo_3**/CdTe-CdS composites were not stable below the optimal pH of 2.5 triggered by the precipitation of QDs and the weakened interaction between the two components. Also, the study reports that increasing **Mo_3** loading above a certain level results in the drop of HER activity, most likely due to light blocking by the catalyst.

Carbon nitride (CN_x) is another promising narrow band gap semiconductor often used by the community as an efficient metal-free heterogeneous light absorber. Driven by the idea to utilize the anionic charge of **Mo_3** for the attachment, Wang and co-workers used melon-derived mesoporous CN_x—that was rendered positively charged via facile protonation[99]—as a support for the attachment.[100] The **Mo_3**/CN_x composite was characterized using TEM and XPS measurements, which confirmed the monodispersed nature of the clusters. Similar to the works discussed above, the authors found **Mo_3** to act as efficient HER co-catalyst (**Figure 7**a): (a) when supported on insulating SiO_2, **Mo_3** was unable to generate any H_2 and (b) when neat (uncharged) CN_x was used as a support, much lower HER activities were recorded. These data correlate well with the conclusions drawn in Section 4.1 and strongly suggest the importance of strong (electrostatic) interaction between catalyst and support, which is critical to achieve optimal HER performance.

While many photosystems have demonstrated that **Mo_3** can act as co-catalysts for light-driven HER, Streb and colleagues provided a unique perspective on the electrostatically assembled **Mo_3**/CN_x—using amorphous carbon nitride support—aiming to shed light on the charge transfer dynamics between the

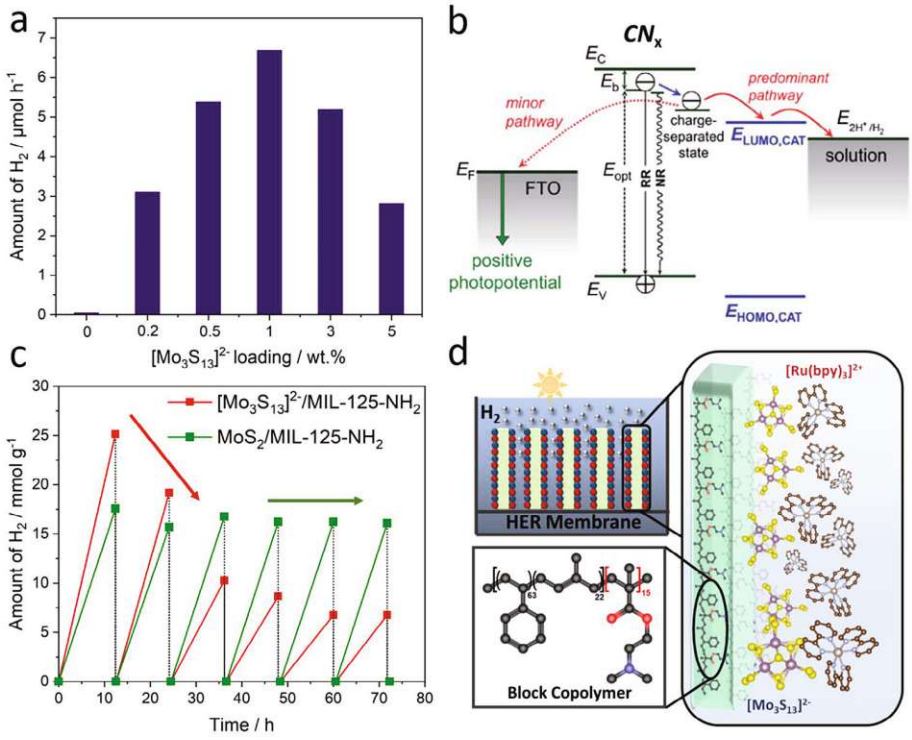

Figure 7. Supported thiometalates in photocatalysis. a) Effect of different loadings of Mo_3 in Mo_3/CN_x composite on the amount of hydrogen produced. b) Scheme showing the change in photopotential at FTO/CN_x photoelectrode surface in the presence of Mo_3 catalyst. E_C: conduction band edge; and E_V: valence band edge; RR: radiative recombination from emissive (band-edge) states; NR: nonradiative recombination from nonemissive (shallow-trap) excitonic states; E_{opt}: optical bandgap of CN_x; E_b: exciton binding energy; CAT: Mo_3 catalyst. c) Comparison of Mo_3/MIL-125-NH_2 and MoS_2/MIL-125-NH_2 in terms of their stability under HER experimental conditions. d) Design of photocatalytic hydrogen evolution system based on nanoporous block copolymer membrane that is electrostatically co-anchoring Mo_3 catalyst and $[Ru(bpy)_3]^{2+}$ photosensitizer. (a) Adapted with permission.[100] Copyright 2017, Royal Society of Chemistry. (b) Reproduced with permission.[101] Copyright 2020, Royal Society of Chemistry. (c) Adapted with permission.[102] Copyright 2018, American Chemical Society. (d) Adapted with permission.[77] Copyright 2020, Royal Society of Chemistry.

two components as well as unravel the reaction kinetics under turnover conditions.[101] The authors utilized steady-state and time-resolved PL spectroscopy to reveal that increasing cluster loading in **Mo_3**/CN_x composites leads to enhanced charge separation at the interface. As such, for smaller cluster loadings, **Mo_3** seems to selectively bind to the amine groups. As these are associated with shallow trap states, this binding tends to repopulate the emissive excitonic states, thereby increasing the PL intensity and lifetime. Higher cluster loadings, on the other hand, increase the nonradiative decay, which dissociates the shallow trapped excitons into charge carriers and leads to improved charge separation, causing the PL emission intensity and lifetime to decrease. These findings provide a valuable perspective to explain the loading-dependent HER performance observed in this and other works. The second relevant observation was delivered by the transient photopotential measurements able to elaborate the effect of **Mo_3** co-catalyst on the charge separation extent. As shown in Figure 7b, the photopotential is negative for the FTO-supported CN_x, which the authors attributed to its insulating behavior and the poor electrical connection between CN_x and FTO. Conversely, a positive photopotential was recorded when **Mo_3** was attached to the CN_x surface, suggesting the efficient extraction of photoexcited electrons by the cluster. These data suggest that surface-anchored **Mo_3** strongly affects the exciton dissociation and mediates the transfer of trapped electrons from CN_x to the reactants. However, as the addition of **Mo_3** had no impact on the ultrafast (sub-ns) photoinduced kinetics in the CN_x, the authors also note that the electron extraction to **Mo_3** occurs on a relatively longer (ns-s) time scale.

3.2.3. Thiomolybdates within Porous Hosts

Metal–organic frameworks (MOFs) have recently attracted the attention of the community as organic–inorganic hybrid materials comprised of metal ions or metal-oxo clusters linked by bridging organic ligands to form multidimensional solid-state networks. Their modular assembly and tunable pore structure and pore size makes them ideally suited for heterogenization of thiomolybdate HER catalysts.[103] This principle has been explored by Stylianou and colleagues who used the visible-light-active MIL-125-NH_2 MOF as a support to compare (co-)catalytic HER performance of **Mo_3** and 1T-MoS_2 nanoparticles (Figure 7c).[102] Their data suggest **Mo_3**/MOF to be more active compared to MoS_2/MOF when similar co-catalyst loadings were used. The authors attributed this observation to the improved interaction of molecular

clusters with the MOF surface along with their inherently higher catalytic activity discussed previously in Section 4.1. However, the authors also found $\mathbf{Mo_3}$/MOF to be less stable in long-term photocatalytic tests compared to 1T-MoS_2/MOF composites, which could be attributed to structural instability of the $\mathbf{Mo_3}$ under alkaline pH conditions.[100,101] More investigations are required to elaborate on this important issue.

In another prominent example, Streb and co-workers were the first to use soft-matter-based nanoporous block copolymer membranes with cationic surface groups as heterogeneous supports for electrostatic anchoring of $\mathbf{Mo_3}$ catalyst and $[Ru(bpy)_3]^{2+}$ photosensitizer for light-driven HER (Figure 7d).[77] The functionalized polymer membranes were analyzed using scanning electron microscopy (SEM), energy dispersive X-ray spectroscopy (EDX), and XPS analyses, which suggest that one of the terminal S_2^{2-} ligands is replaced with a water ligand after attachment to the membrane, in line with the behavior observed previously.[40] The copolymer-supported $\mathbf{Mo_3}$/$[Ru(bpy)_3]^{2+}$ photosystem generated H_2 for at least 20 h of illumination. However, the authors also observed that a considerable amount of H_2 was stored in the pores of the polymer membrane and could be recovered after the catalytic process. The authors further reported that $\mathbf{Mo_3}$ did not leach from the membrane; however, they noted significant loss of the photosensitizer after 10 h of irradiation. Their data suggest that even at low Ru-photosensitizer loadings, the membrane is able to preserve its HER activity, possibly by mediating the electron transfer between photosensitizer and catalyst within the membrane.

3.3. Other Applications

Apart from electrocatalytic and photocatalytic applications involving thiometalates, most recent works have been exploring the heterogenized clusters in thermal catalysis, and selective ion capture. As such, Zhang and co-workers have immobilized $\mathbf{Mo_2}$ and $\mathbf{Mo_3}$ on mesoporous SiO_2 (SBA-15) and applied the composites for thiophene hydrodesulfurization (HDS), a process used to remove sulfur-containing compounds from petroleum.[104] The results showed that both thiomolybdates can be successfully deposited on SBA-15, while maintaining their structure. The stability of the supported catalysts was assessed through TGA, which revealed that $\mathbf{Mo_2}$/$\mathbf{Mo_3}$ are likely to retain their sulfur ligands during catalysis. The composites were also tested for hydrogen adsorption using temperature-programmed reduction, which indicated the hydrogenation of terminal and bridging sulfur species to be the likely intermediate step of the HDS process. Overall, the study demonstrates the successful loading and effective catalytic performance of the thiomolybdates in HDS. The findings further provide insights into the role of sulfur species in the catalytic process and contribute to the development of supported thiometalate clusters for other catalytic applications.

In another outstanding study, Ma, Kanatzidis and colleagues used $\mathbf{Mo_3}$ to prepare composites for the selective extraction of silver from copper-rich minerals.[105] The authors incorporated $\mathbf{Mo_3}$ into the matrix of a conjugated polypyrrole (ppy) backbone by ion-exchange reaction and demonstrated exceptional selectivity and high efficiency of the resulting $\mathbf{Mo_3}$/ppy in capturing Ag^+ and Hg^{2+} ions at concentration levels <1 ppb. The mechanism for silver removal involves two synergistic pathways: direct binding and in situ reduction. In the former, the $\mathbf{Mo_3}$ clusters release S^{2-} ions, which bind with Ag ions to form Ag_2S complexes, effectively removing Ag from the solution. In the latter, the Mo^{IV} ions in Mo_3 act as reducing agents, converting Ag^+ ions to metallic silver while being oxidized to Mo^{VI}. This reduction reaction occurs alongside the binding of Ag^+ ions to S^{2-} ions, resulting in the deposition of silver crystals on the $\mathbf{Mo_3}$/ppy composite surface. The results suggest that composites based on $\mathbf{Mo_3}$—and, potentially, other thiometalates—can offer a promising approach for selective silver extraction and removal of toxic metal ions from complex aqueous environments.

Parallel to the implementation of thiometalates as reduction co-catalysts for HER, several works have employed composites containing such clusters to promote various oxidation reactions. In an early set of studies, $\mathbf{Mo_3}$ was employed as co-catalyst for photocatalytic dye degradation using visible-light-active BiOBr and Bi_2WO_6 substrates prepared through a hydrothermal method. Both nanocomposites demonstrated excellent photocatalytic activity—comparable to state-of-the-art Pt co-catalysts—which was primarily attributed to the ability of $\mathbf{Mo_3}$ to efficiently promote the extraction of photoexcited electrons thus indirectly affecting the lifetimes of electron-hole pairs and hole utilization efficiency.[106,107] In addition to this, the authors highlighted that, compared to commonly used Pt, $\mathbf{Mo_3}$ shows enhanced sulfur tolerance and can thus be used effectively in processes involving sulfur species, such as in desulfurization or sulfur-containing wastewater remediation.

In a more recent example of thiomolybdate application, Xufang and co-workers fabricated a novel $\mathbf{Mo_3}$/TiO_2 photocatalyst for the oxidation of acetone to CO_2.[108] The CO_2 production was investigated with $\mathbf{Mo_3}$/TiO_2 composites containing different loadings of $\mathbf{Mo_3}$: 0.6, 1.1, 1.7, and 3.4 wt%. The authors found that among these composites, the highest amount of CO_2 was produced with 1.7$\mathbf{Mo_3}$/TiO_2, which was ascribed to the optimal loading of clusters over titania surface promoting better photoinduced charge separation. Importantly for benchmarking, the 1.7$\mathbf{Mo_3}$/TiO_2 photocatalyst was found to be more active for acetone mineralization compared to the benchmark Pt/TiO_2 photocatalyst exhibiting a similar co-catalyst loading value. In addition, the solution of 1.7$\mathbf{Mo_3}$$TiO_2$ composite sprayed onto polypropylene nonwoven fabric produced higher CO_2 amounts compared to the pristine TiO_2/fabric, which one more time highlights the effect of $\mathbf{Mo_3}$ in the structure. These polypropylene-coated nonwoven fabrics coated with $\mathbf{Mo_3}$/TiO_2 composite have been used as an efficient photocatalyst for indoor air purification.

4. Conclusions and Outlook

This review placed special emphasis on recent developments in thiomolybdate catalysis, particularly with respect to combined experimental and theoretical studies that shed light on reaction mechanisms, active sites and potential degradation pathways, as well as on new strategies for thiometalate heterogenization on functional substrates and their emerging applications. Two comprehensive summary Tables were provided to highlight the current state-of-the-art: Table 1 examines active sites of thiomolybdate clusters, Table 2 documents that heterogenized thiomolybdates are highly active, structurally versatile HER promoters and

that their molecular nature can be used as a tool to tune their activity.

Despite a number of proof-of-concept demonstrations and promising results that are already been recorded, the authors of this perspective have identified a list of critical points that will hopefully help shaping future research directions in the field:

We suggest that more in-depth mechanistic studies are required to fully understand how thiomolybdates are anchored to heterogeneous supports, and to explore the role of catalyst–support interactions for electrocatalytic and photocatalytic HER. Also, understanding the physical and electronic structure of the catalytically active state of the clusters under turnover conditions is critical for a knowledge-based development of the field. These themes have been the focus of two recent studies which used time-resolved methods to gain further insights into thiomolybdate reactivity: Ha-Thi and colleagues revealed the mechanism of light-driven catalysis of a $\{Mo_3S_4\}$-core containing cluster in solutions,[45] while Streb and co-workers provided important insights into the charge transfer dynamics of surface-supported **Mo_3**.[101] In another pioneering example, Bozheyev and colleagues used transient surface photovoltage spectroscopy to unravel the electronic properties of WSe_2-anchored **Mo_3** heterostructures.[109]

Another critical aspect when considering thiomolybdate heterogenization is the stability and fate of the molecules under deposition and reaction conditions. Many studies deliberately use thiomolybdates as molecular precursors for the preparation of MoS_x nanostructures or films. However, in other cases, this molecule-to-solid-state compound conversion might occur unintentionally. In both cases, the resulting material needs to be thoroughly characterized, and clear evidence must be provided if the respective manuscript claims that the material used for catalysis is still a molecular species. This can be challenging, particularly when the conversion occurs in situ, under catalytic conditions. Thus, comprehensive pre- and postcatalytic analyses—ideally supported by in situ/operando studies—are required to assess the complex processes occurring in this compound class. Key aspects to be focused on are ligand loss/exchange, chemical interaction with the surface, oligo- and polymerization of individual clusters and formation of MoS_x fragments. As outlined in Sections 2 and 3, there is still much room to explore these questions and provide more insights into improvement when analyzing and reporting these aspects.

In addition to the chemical and structural considerations outlined above, there is an urgent need to provide fundamental insights into the differences in reactivity of different thiomolybdate prototypes, particularly when deposited on identical supports. This would allow the research community to engage in knowledge-based advanced materials design, based on a full understanding of the underlying reaction and stability mechanisms.

Apart from these critical notes, the authors of this perspective would like to suggest directions of future research:

A current limitation in the field is that most HER research has been focused on the use of a limited number of prototype thiomolybdates, mainly **Mo_2** and **Mo_3**. While these studies have provided ground-breaking new insights and materials, we propose expanding the compound base and exploring the reactivity of advanced cluster types. This includes research on other types of thiometalates, such as thiotungstates,[33] mixed-ligand clusters, e.g., featuring oxo- or organic ligands in addition to thio groups,[17] as well as selenide-containing derivatives.[110] While these areas are highly promising, they have thus far not received the attention to allow us to draw any final conclusions on the component suitability for HER studies.

State-of-the-art thiomolybdate catalysis research is mainly focused on electrocatalytic or light-driven HER. However, based on earlier research and on selected recent publications, we suggest that other (thermal) catalytic processes including reductions, oxidations and small molecule activations are intriguing areas to be explored using thiometalates. In a recent example, Llusar and colleagues have combined experimental and theoretical methods to explore the catalytic hydrogenation of azobenzene using cuboidal $\{Mo_3S_4\}$-containing clusters.[111] The results suggest a mechanism involving homolytic activation of hydrogen at bridging sulfur atoms in the cluster, followed by consecutive hydrogen transfers to azobenzene, resulting in the formation of aniline. The authors also explored the effects of different organic ligands on the catalytic activity of the clusters and provided evidence supporting the sulfur-centered mechanism, which contributes strongly to a better understanding of the catalytic properties of these and structurally similar thiomolybdates. Along similar lines, mechanistic comparison between HER and hydrodesulfurization catalysis studies can offer a new insight into the function of thiomolybdates. In one example, Suman and co-workers studied an oxothiomolybdate complex $[(Mo_2O_2S_4)(en)(dmf)]$ and suggested an oxidative addition/reductive elimination mechanism or a ligand-based insertion reaction—in which sulfur inserts either into the terminal S—S bond or into the Mo—S bond—as possible reaction pathways.[112]

Finally, the merging of thiomolybdates with functional support materials such as polymers, MOFs, and narrow bandgap semiconductors is also an area which can lead to advanced composites. In one example, Chane-Ching and colleagues recently immobilized **Mo_2** derivatives on 2D WS_2 photoelectrodes to drive photoelectrocatalytic water splitting.[113] In MOF-chemistry, Yaghi and co-workers were able to build thiomolybdate-based porous frameworks and demonstrate the HER performance of these pioneering materials.[35] We believe that many more functional molecular, hybrid, and solid-state materials could be realized using thiometalates and their derivatives.

Acknowledgements

S.B. and M.L. contributed equally to the work. The authors gratefully acknowledge financial support by the Austrian Science Fund (FWF, Project No. P32801 and Cluster of Excellence MECS) and Deutsche Forschungsgemeinschaft [Project No. 364549901 (TRR 234 CataLight, Project Nos. A4, A5, and B3)]. M.H. gratefully acknowledges the Alexander von Humboldt Foundation for a postdoctoral fellowship. C.S. gratefully acknowledges financial support by Johannes Gutenberg University Mainz, the Gutenberg Research College GRC, and the state of Rheinland-Pfalz (top-level research area SusInnoScience, and "Spitzenforscher" funds).

Open access funding enabled and organized by Projekt DEAL.

Conflict of Interest

The authors declare no conflict of interest.

Keywords

electrocatalysis, heterogenization, hydrogen evolution, molybdenum sulfide, photocatalysis, thiomolybdate

Received: June 14, 2023
Revised: October 9, 2023
Published online:

[1] H. Ooka, J. Huang, K. S. Exner, *Front. Energy Res.* **2021**, *9*, 654460.
[2] J. K. Nørskov, T. Bligaard, A. Logadottir, J. R. Kitchin, J. G. Chen, S. Pandelov, U. Stimming, *J. Electrochem. Soc.* **2005**, *152*, 1.
[3] Z. W. Seh, J. Kibsgaard, C. F. Dickens, I. Chorkendorff, J. K. Nørskov, T. F. Jaramillo, *Science* **2017**, *355*, 4998.
[4] M. G. Walter, E. L. Warren, J. R. Mckone, S. W. Boettcher, Q. Mi, E. A. Santori, N. S. Lewis, *Chem. Rev.* **2010**, *110*, 6446.
[5] E. I. Stiefel, *Transition Metal Sulfur Chemistry*, American Chemical Society, Washington, DC, pp. 2–38.
[6] H. Tributsch, J. C. Bennett, *J. Electroanal. Chem. Interfacial Electrochem.* **1977**, *81*, 97.
[7] B. Hinnemann, P. G. Moses, J. Bonde, K. P. Jørgensen, J. H. Nielsen, S. Horch, I. Chorkendorff, J. K. Nørskov, *J. Am. Chem. Soc.* **2005**, *127*, 5308.
[8] C. G. Morales-Guio, X. Hu, *Acc. Chem. Res.* **2014**, *47*, 2671.
[9] H. Li, C. Tsai, A. L. Koh, L. Cai, A. W. Contryman, A. H. Fragapane, J. Zhao, H. S. Han, H. C. Manoharan, F. Abild-Pedersen, J. K. Nørskov, X. Zheng, *Nat. Mater.* **2016**, *15*, 364.
[10] T. F. Jaramillo, K. P. Jørgensen, J. Bonde, J. H. Nielsen, S. Horch, I. Chorkendorff, *Science* **2007**, *317*, 100.
[11] K. Herbst, M. Monari, M. Brorson, *Inorg. Chem.* **2002**, *41*, 1336.
[12] M.-L. Grutza, A. Rajagopal, C. Streb, P. Kurz, *Sustainable Energy Fuels* **2018**, *2*, 1893.
[13] B. Seo, S. H. Joo, *Nano Convergence* **2017**, *4*, 19.
[14] T. Shibahara, *Coord. Chem. Rev.* **1993**, *123*, 73.
[15] M. G. Kanatzidis, S.-P. Huang, *Coord. Chem. Rev.* **1994**, *130*, 509.
[16] E. Cadot, M. N. Sokolov, V. P. Fedin, C. Simonnet-Jégat, S. Floquet, F. Sécheresse, *Chem. Soc. Rev.* **2012**, *41*, 7335.
[17] F. Sécheresse, E. Cadot, *World Scientific Series in Nanoscience and Nanotechnology*, World Scientific, Singapore **2013**, pp. 243–304.
[18] A. Elliott, H. N. Miras, *J. Coord. Chem.* **2022**, *75*, 1467.
[19] M. R. Dubois, *Chem. Rev.* **1989**, *89*, 1.
[20] R. Hernández-Molina, A. G. Sykes, *J. Chem. Soc., Dalton Trans.* **1999**, 3137.
[21] R. Hernandez-Molina, M. N. Sokolov, A. G. Sykes, *Acc. Chem. Res.* **2001**, *34*, 223.
[22] A. Mcskimming, D. L. M. Suess, *Nat. Chem.* **2021**, *13*, 666.
[23] Y. Ohki, K. Munakata, Y. Matsuoka, R. Hara, M. Kachi, K. Uchida, M. Tada, R. E. Cramer, W. M. C. Sameera, T. Takayama, Y. Sakai, S. Kuriyama, Y. Nishibayashi, K. Tanifuji, *Nature* **2022**, *607*, 86.
[24] Y. Hou, B. L. Abrams, P. C. K. Vesborg, M. E. Björketun, K. Herbst, L. Bech, A. M. Setti, C. D. Damsgaard, T. Pedersen, O. Hansen, J. Rossmeisl, S. Dahl, J. K. Nørskov, I. Chorkendorff, *Nat. Mater.* **2011**, *10*, 434.
[25] M. G. Basallote, M. J. Fernández-Trujillo, J. Á. Pino-Chamorro, T. F. Beltrán, C. Corao, R. Llusar, M. Sokolov, C. Vicent, *Inorg. Chem.* **2012**, *51*, 6794.
[26] S. W. Seo, S. Park, H.-Y. Jeong, S. H. Kim, U.k Sim, C. W. Lee, K. T. Nam, K. S. Hong, *Chem. Commun.* **2012**, *48*, 10452.
[27] A. Müller, W.-O. Nolte, B. Krebs, *Angew. Chem., Int. Ed. Engl.* **1978**, *17*, 279.
[28] A. Müller, S. Sarkar, R. G. Bhattacharyya, S. Pohl, M. Dartmann, *Angew. Chem., Int. Ed. Engl.* **1978**, *17*, 535.
[29] E. Diemann, A. Müller, P. J. Aymonino, *Z. Anorg. Allg. Chem.* **1981**, *479*, 191.
[30] A. Müller, R. Jostes, F. A. Cotton, *Angew. Chem., Int. Ed. Engl.* **1980**, *19*, 875.
[31] A. Müller, E. Diemann, R. Jostes, H. Bögge, *Angew. Chem., Int. Ed. Engl.* **1981**, *20*, 934.
[32] J. Mcallister, N. A. G. Bandeira, J. C. Mcglynn, A. Y. Ganin, Y.-F. Song, C. Bo, H. N. Miras, *Nat. Commun.* **2019**, *10*, 370.
[33] E. Königer-Ahlborn, A. Müller, *Angew. Chem.* **1975**, *87*, 598.
[34] N. E. Horwitz, J. Xie, A. S. Filatov, R. J. Papoular, W. E. Shepard, D. Z. Zee, M. P. Grahn, C. Gilder, J. S. Anderson, *J. Am. Chem. Soc.* **2019**, *141*, 3940.
[35] Z. Ji, C. Trickett, X. Pei, O. M. Yaghi, *J. Am. Chem. Soc.* **2018**, *140*, 13618.
[36] J. Xie, L. Wang, J. S. Anderson, *Chem. Sci.* **2020**, *11*, 8350.
[37] T. Shibahara, H. Kuroya, *Polyhedron* **1986**, *5*, 357.
[38] T. F. Jaramillo, J. Bonde, J. Zhang, B.-L. Ooi, K. Andersson, J. Ulstrup, I. Chorkendorff, *J. Phys. Chem. C* **2008**, *112*, 17492.
[39] Y. Lei, M. Yang, J. Hou, F. Wang, E. Cui, C. Kong, S. Min, *Chem. Commun.* **2018**, *54*, 603.
[40] M. Dave, A. Rajagopal, M. Damm-Ruttensperger, B. Schwarz, F. Nägele, L. Daccache, D. Fantauzzi, T. Jacob, C. Streb, *Sustainable Energy Fuels* **2018**, *2*, 1020.
[41] M. Heiland, R. De, S. Rau, B. Dietzek-Ivansic, C. Streb, *Chem. Commun.* **2022**, *58*, 4603.
[42] W. Li, S. Min, F. Wang, Z. Zhang, D. Gao, *Chem. Commun.* **2021**, *57*, 1121.
[43] A. Rajagopal, F. Venter, T. Jacob, L. Petermann, S. Rau, S. Tschierlei, C. Streb, *Sustainable Energy Fuels* **2018**, *3*, 92.
[44] P. R. Fontenot, B. Shan, B.o Wang, S. Simpson, G. Ragunathan, A. F. Greene, A. Obanda, L. A. Hunt, N. I. Hammer, C. E. Webster, J. T. Mague, R. H. Schmehl, J. P. Donahue, *Inorg. Chem.* **2019**, *58*, 16458.
[45] Y. Smortsova, C. Falaise, A. Fatima, M.-H. Ha-Thi, R. Méallet-Renault, K. Steenkeste, S. Al-Bacha, T. Chaib, L. Assaud, M. Lepeltier, M. Haouas, N. Leclerc, T. Pino, E. Cadot, *Chemistry* **2021**, *27*, 17094.
[46] P. D. Tran, T. V. Tran, M. Orio, S. Torelli, Q. D. Truong, K. Nayuki, Y. Sasaki, S. Y. Chiam, R. Yi, I. Honma, J. Barber, V. Artero, *Nat. Mater.* **2016**, *15*, 640.
[47] A. Baloglou, M. OncK, M.-L. Grutza, C. Van Der Linde, P. Kurz, M. K. Beyer, *J. Phys. Chem. C* **2019**, *123*, 8177.
[48] M. Pritzi, T. F. Pascher, M.-L. Grutza, P. Kurz, M. OncK, M. K. Beyer, *J. Am. Soc. Mass Spectrom.* **2022**, *33*, 1753.
[49] A. Baloglou, M. Plattner, M. OncK, M.-L. Grutza, P. Kurz, M. K. Beyer, *Angew. Chem., Int. Ed.* **2021**, *60*, 5074.
[50] C.-H. Lee, S. Lee, Y.-K. Lee, Y. C. Jung, Y.-I. Ko, D. C. Lee, H.-I. Joh, *ACS Catal.* **2018**, *8*, 5221.
[51] S. Batool, S. P. Nandan, S. N. Myakala, A. Rajagopal, J. S. Schubert, P. Ayala, S. Naghdi, H. Saito, J. Bernardi, C. Streb, A. Cherevan, D. Eder, *ACS Catal.* **2022**, *12*, 6641.
[52] Y. Deng, L. R. L. Ting, P. H. L. Neo, Y.-J. Zhang, A. A. Peterson, B. S. Yeo, *ACS Catal.* **2016**, *6*, 7790.
[53] B. Seo, G. Y. Jung, S. J. Lee, D. S. Baek, Y. J. Sa, H. W. Ban, J. S. Son, K. Park, S. K. Kwak, S. H. Joo, *ACS Catal.* **2020**, *10*, 652.
[54] Z. Huang, W. Luo, L. Ma, M. Yu, X. Ren, M. He, S. Polen, K. Click, B. Garrett, J. Lu, K. Amine, C. Hadad, W. Chen, A. Asthagiri, Y. Wu, *Angew. Chem., Int. Ed.* **2015**, *54*, 15181.
[55] J. A. Bau, A.-H. Emwas, P. Nikolaienko, A. A. Aljarb, V. Tung, M. Rueping, *Nat. Catal.* **2022**, *5*, 397.
[56] J. A. Bau, R. Ahmad, L. Cavallo, M. Rueping, *ACS Energy Lett.* **2022**, *7*, 3695.
[57] A. M. Appel, D. L. Dubois, M. R. Dubois, *J. Am. Chem. Soc.* **2005**, *127*, 12717.

[58] H. I. Karunadasa, E. Montalvo, Y. Sun, M. Majda, J. R. Long, C. J. Chang, *Science* **2012**, *335*, 698.
[59] B. R. Garrett, K. A. Click, C. B. Durr, C. M. Hadad, Y. Wu, *J. Am. Chem. Soc.* **2016**, *138*, 13726.
[60] B. R. Garrett, S. M. Polen, K. A. Click, M. He, Z. Huang, C. M. Hadad, Y. Wu, *Inorg. Chem.* **2016**, *55*, 3960.
[61] B. R. Garrett, S. M. Polen, M. Pimplikar, C. M. Hadad, Y. Wu, *J. Am. Chem. Soc.* **2017**, *139*, 4342.
[62] M. Pritzi, T. F. Pascher, M.-L. Grutza, P. Kurz, M. OncK, M. K. Beyer, *Phys. Chem. Chem. Phys.* **2022**, *24*, 16576.
[63] B. Keita, S. Floquet, J.-F. Lemonnier, E. Cadot, A. Kachmar, M. Bénard, M.-M. Rohmer, L. Nadjo, *J. Phys. Chem. C* **2008**, *112*, 1109.
[64] A. S. Cherevan, S. P. Nandan, I. Roger, R. Liu, C. Streb, D. Eder, *Adv. Sci.* **2020**, *7*, 1903511.
[65] T. Wang, J. Zhuo, K. Du, B. Chen, Z. Zhu, Y. Shao, M. Li, *Adv. Mater.* **2014**, *26*, 3761.
[66] S. Kozuch, J. M. L. Martin, *ACS Catal.* **2012**, *2*, 2787.
[67] T. Bligaard, R. M. Bullock, C. T. Campbell, J. G. Chen, B. C. Gates, R. J. Gorte, C. W. Jones, W. D. Jones, J. R. Kitchin, S. L. Scott, *ACS Catal.* **2016**, *6*, 2590.
[68] D. Ziegenbalg, A. Pannwitz, S. Rau, B. Dietzek-Ivansic, C. Streb, *Angew. Chem., Int. Ed.* **2022**, *61*, e202114106.
[69] J. D. Benck, T. R. Hellstern, J. Kibsgaard, P. Chakthranont, T. F. Jaramillo, *ACS Catal.* **2014**, *4*, 3957.
[70] S. Anantharaj, S. Noda, *Mater. Today Energy* **2022**, *29*, 101123.
[71] J. Kibsgaard, T. F. Jaramillo, F. Besenbacher, *Nat. Chem.* **2014**, *6*, 248.
[72] T. R. Hellstern, J. Kibsgaard, C. Tsai, D. W. Palm, L. A. King, F. Abild-Pedersen, T. F. Jaramillo, *ACS Catal.* **2017**, *7*, 7126.
[73] P. Faye, E. Payen, D. Bougeard, in *Hydrotreatment and Hydrocracking of Oil Fractions* (Eds: G. F. Froment, B. Delmon, P. Grange), Elsevier, Amsterdam **1997**, pp. 281–292.
[74] M. A. Domínguez-Crespo, E. M. Arce-Estrada, A. M. Torres-Huerta, L. Díaz-García, M. T. Cortez De La Paz, *Mater. Charact.* **2007**, *58*, 864.
[75] C. Tsai, F. Abild-Pedersen, J. K. Nørskov, *Nano Lett.* **2014**, *14*, 1381.
[76] Y. Shang, X. Xu, B. Gao, Z. Ren, *ACS Sustainable Chem. Eng.* **2017**, *5*, 8908.
[77] I. Romanenko, A. Rajagopal, C. Neumann, A. Turchanin, C. Streb, F. H. Schacher, *J. Mater. Chem. A* **2020**, *8*, 6238.
[78] K. Du, L. Zheng, T. Wang, J. Zhuo, Z. Zhu, Y. Shao, M. Li, *ACS Appl. Mater. Interfaces* **2017**, *9*, 18675.
[79] O. Mabayoje, Y. Liu, M. Wang, A. Shoola, A. M. Ebrahim, A. I. Frenkel, C. B. Mullins, *ACS Appl. Mater. Interfaces* **2019**, *11*, 32879.
[80] J. A.l Cheikh, R. Zakari, A. C. Bhosale, A. Villagra, N. Leclerc, S. Floquet, P. C. Ghosh, A. Ranjbari, E. Cadot, P. Millet, L. Assaud, *Mater. Adv.* **2020**, *1*, 430.
[81] A. Müller, S. Pohl, M. Dartmann, J. P. Cohen, J. M. Bennett, R. M. Kirchner, *Z. Naturforschung, B* **1979**, *34*, 434.
[82] A. Müller, E. Diemann, E. Krickemeyer, H. J. Walberg, H. Bögge, A. Armatage, *Eur. J. Solid State Inorg. Chem.* **1993**, *30*, 565.
[83] T. Weber, J. C. Muijsers, J. W. Niemantsverdriet, *J. Phys. Chem.* **1995**, *99*, 9194.
[84] J. N. Hansen, H. Prats, K. K. Toudahl, N. Mørch Secher, K. Chan, J. Kibsgaard, I. Chorkendorff, *ACS Energy Lett.* **2021**, *6*, 1175.
[85] Y. Li, H. Wang, L. Xie, Y. Liang, G. Hong, H. Dai, *J. Am. Chem. Soc.* **2011**, *133*, 7296.
[86] T. Wang, L. Liu, Z. Zhu, P. Papakonstantinou, J. Hu, H. Liu, M. Li, *Energy Environ. Sci.* **2013**, *6*, 625.
[87] P. D. Tran, M. Nguyen, S. S. Pramana, A. Bhattacharjee, S. Y. Chiam, J. Fize, M. J. Field, V. Artero, L. H. Wong, J. Loo, J. Barber, *Energy Environ. Sci.* **2012**, *5*, 8912.
[88] H. Vrubel, D. Merki, X. Hu, *Energy Environ. Sci.* **2012**, *5*, 6136.
[89] T.-W. Lin, C.-J. Liu, J.-Y. Lin, *Appl. Catal., B* **2013**, *134*, 75.
[90] G.-Q. Han, X. Li, J. Xue, B. Dong, X. Shang, W.-H. Hu, Y.-R. Liu, J.-Q. Chi, K.-L. Yan, Y.-M. Chai, C.-G. Liu, *Int. J. Hydrogen Energy* **2017**, *42*, 2952.
[91] S. Reddy, R. Du, L. Kang, N. Mao, J. Zhang, *Appl. Catal., B* **2016**, *194*, 16.
[92] W.-H. Hu, X. Shang, G.-Q. Han, B. Dong, Y.-R. Liu, X. Li, Y.-M. Chai, Y.-Q. Liu, C.-G. Liu, *Carbon* **2016**, *100*, 236.
[93] E. Heydari-Bafrooei, S. Askari, *Int. J. Hydrogen Energy* **2017**, *42*, 2961.
[94] X. Zhang, P. Ding, Y. Sun, Y. Wang, J. Li, J. Guo, *Mater. Lett.* **2017**, *197*, 41.
[95] D. Recatalá, R. Llusar, A. L. Gushchin, E. A. Kozlova, Y. A. Laricheva, P. A. Abramov, M. N. Sokolov, R. Gómez, T. Lana-Villarreal, *ChemSusChem* **2015**, *8*, 148.
[96] D. Yue, X. Qian, Z. Zhang, M. Kan, M. Ren, Y. Zhao, *ACS Sustainable Chem. Eng.* **2016**, *4*, 6653.
[97] R. Zhang, K. Gong, F. Du, S. Cao, *Int. J. Hydrogen Energy* **2022**, *47*, 19570.
[98] Z. Wang, C. Li, K. Domen, *Chem. Soc. Rev.* **2019**, *48*, 2109.
[99] Y. Zhang, A. Thomas, M. Antonietti, X. Wang, *J. Am. Chem. Soc.* **2009**, *131*, 50.
[100] F. Guo, Y. Hou, A. M. Asiri, X. Wang, *Chem. Commun.* **2017**, *53*, 13221.
[101] A. Rajagopal, E. Akbarzadeh, C. Li, D. Mitoraj, I. Krivtsov, C. Adler, T. Diemant, J. Biskupek, U. Kaiser, C. Im, M. Heiland, T. Jacob, C. Streb, B. Dietzek, R. Beranek, *Sustainable Energy Fuels* **2020**, *4*, 6085.
[102] T.u N. Nguyen, S. Kampouri, B. Valizadeh, W. Luo, D. Ongari, O. M. Planes, A. Züttel, B. Smit, K. C. Stylianou, *ACS Appl. Mater. Interfaces* **2018**, *10*, 30035.
[103] J. Wang, A. S. Cherevan, C. Hannecart, S. Naghdi, S. P. Nandan, T. Gupta, D. Eder, *Appl. Catal., B* **2021**, *283*, 119626.
[104] Z. Xin, J.-L. Liu, W. Wei, A.-Q. Jia, Q.-F. Zhang, *Inorg. Nano-Met. Chem.* **2021**, https://www.tandfonline.com/doi/full/10.1080/24701556.2021.1988975.
[105] M. Yuan, H. Yao, L. Xie, X. Liu, H. Wang, S. M. Islam, K. Shi, Z. Yu, G. Sun, H. Li, S. Ma, M. G. Kanatzidis, *J. Am. Chem. Soc.* **2020**, *142*, 1574.
[106] D. Yue, T. Zhang, M. Kan, X. Qian, Y. Zhao, *Appl. Catal., B* **2016**, *183*, 1.
[107] D. Yue, Z. Zhang, Z. Tian, T. Zhang, M. Kan, X. Qian, Y. Zhao, *Catal. Today* **2016**, *274*, 22.
[108] Y.u Han, D. Yue, M. Kan, Y. Wu, J. Zeng, Z. Bian, Y. Zhao, X. Qian, *Appl. Catal., B* **2019**, *245*, 190.
[109] F. Bozheyev, S. Fengler, J. Kollmann, T. Klassen, M. Schieda, *ACS Appl. Mater. Interfaces* **2022**, *14*, 22071.
[110] A. Elliott, J. Mcallister, L. Masaityte, M. Segado-Centellas, D.-L. Long, A. Y. Ganin, Y.-F. Song, C. Bo, H. N. Miras, *Chem. Commun.* **2022**, *58*, 6906.
[111] E. Guillamón, M. Oliva, J. Andrés, R. Llusar, E. Pedrajas, V. S. Safont, A. G. Algarra, M. G. Basallote, *ACS Catal.* **2021**, *11*, 608.
[112] B. O. Birgisson, L. J. Monger, K. K. Damodaran, S. G. Suman, *Inorg. Chim. Acta* **2020**, *501*, 119272.
[113] J. Barros Barbosa, P. L. Taberna, V. Bourdon, I. C. Gerber, R. Poteau, A. Balocchi, X. Marie, J. Esvan, P. Puech, A. Barnabé, L. Da Gama Fernandes Vieira, I.-T. Moraru, J. Y. Chane-Ching, *Appl. Catal., B* **2020**, *278*, 119288.

Samar Batool received her bachelor's degree in 2017 from Quaid-I-Azam University Islamabad, Pakistan. The same year she was awarded a scholarship from the Graduate School of Science and Engineering of Bilkent University and moved to Turkey to pursue her master's degree in chemistry, which she completed in 2020. She was then offered a Ph.D. fellowship from Vienna University of Technology, Austria, where she currently works as project assistant at the Institute of Materials Chemistry. Her research interests involve the combination of solid-state (heterogeneous) photocatalysts with molecular-sized artificial homogeneous photosystems.

Marcel Langer received his bachelor's degree from the University of Ulm in 2017. During his master's, which he completed in 2020, he worked in the group of Johan Boman in Gothenburg, Sweden, in the field of analytical chemistry. Marcel is currently a Ph.D. student in the Streb group at Johannes Gutenberg University Mainz, and—at the time of writing this Review—on a research visit to the group of Alina Schimpf at University of California San Diego. He is interested in embedding light-driven molecular catalysts for water oxidation and hydrogen evolution in soft matter membranes to harness synergistic reactivity.

Carsten Streb is professor of inorganic chemistry at Johannes Gutenberg University Mainz. His current research is focused on designing functional molecular and nanoscale materials and composites to address global chemical challenges with a focus on energy conversion and energy storage. He is interested in using in situ/operando methods to study reactivity and stability of homogeneous and heterogeneous catalysts.

Alexey Cherevan is an assistant professor and subgroup leader at the Institute of Materials Chemistry, TU Wien, Austria. He received his master's degree from Moscow State University in 2010 and a Ph.D. from the University of Münster in 2014. Joining TU Wien in 2015, he specializes in materials chemistry, particularly functional inorganic nanomaterials for energy applications. He develops innovative tools that combine heterogeneous and homogeneous branches of photocatalysis. As of 2023, he holds a tenure track assistant professor position and is a PI of the FWF Cluster of Excellence "Materials for Energy Conversion and Storage."

4.2.2 Article #2

"Ni_{12} tetracubane cores with slow relaxation of magnetization and efficient charge utilization for photocatalytic hydrogen evolution"

Elias Tanuhadi, Joan Cano, Samar Batool, Alexey Cherevan, Dominik Eder, Annette Rompel

J. Mater. Chem. C, 2022, 10, 17048-17052
DOI: https://doi.org/10.1039/D2TC03508A

My contributions to this collaborative project encompass the development of photocatalytic protocols for HER activity evaluation, benchmark and baseline measurements, concentration-dependent studies as well as post-catalytic characterization of the photosystem.

The corresponding Supplementary information of the article can be found on page 63. For the purpose of clarity and highlighting my contribution to this paper, I modified the electronic supplementary information (ESI) and removed sections 1-12 (Synthesis, material characterization, and magnetism) from the ESI. To see the full version of ESI, please refer to the ESI stored online.[89]

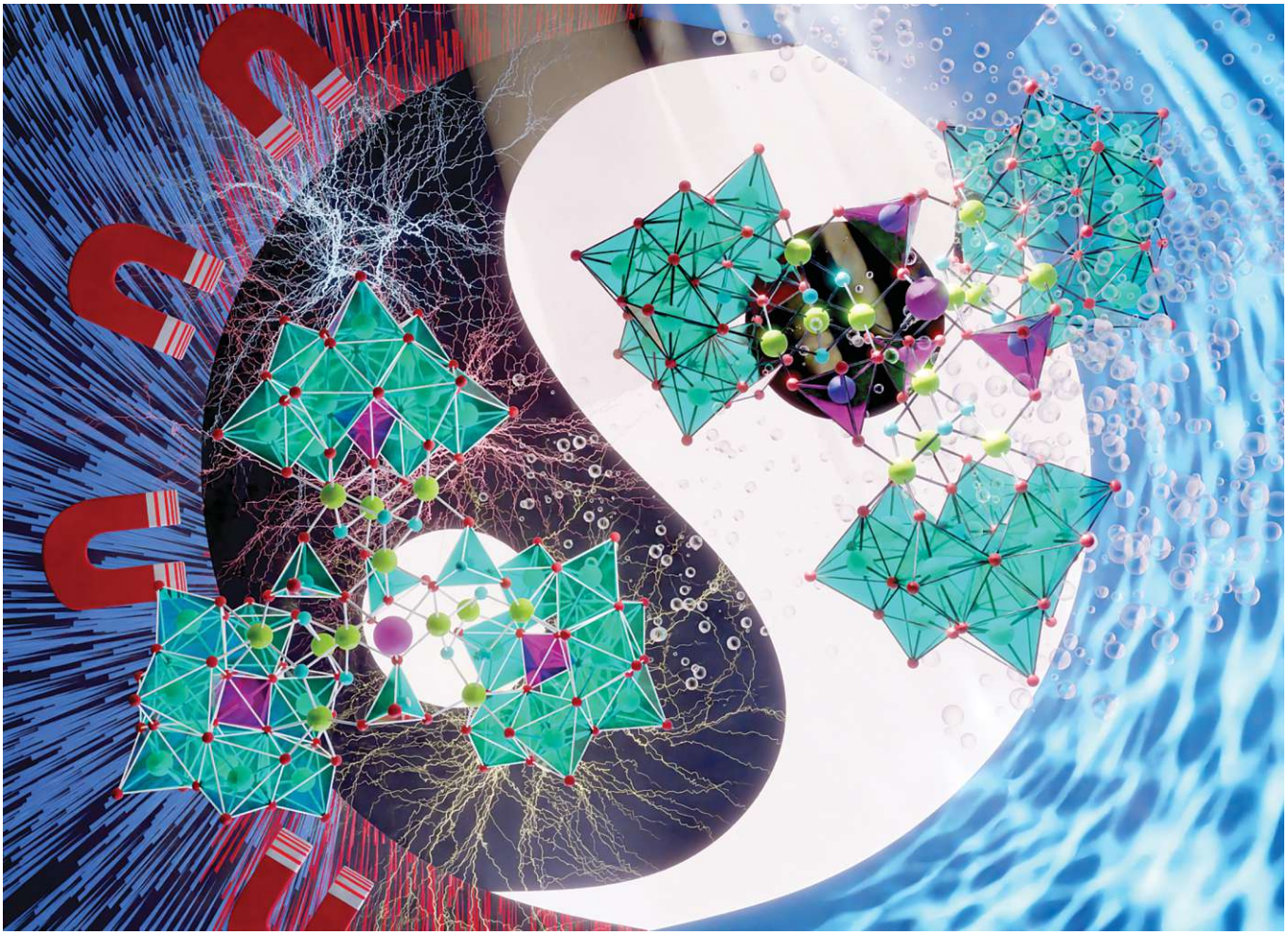

Showcasing collaborative research from Universität Wien (Austria), TU Wien (Austria), and Universitat de València (Spain).

Ni_{12} tetracubane cores with slow relaxation of magnetization and efficient charge utilization for photocatalytic hydrogen evolution

Two Ni_{12} – multicubane topologies were encapsulated in the polyanions $\{Ni_{12}W_{30}\}$ and $\{Ni_{12}W_{27}\}$. SMM behavior arising from excited spin states as well as high quantum yields (>10%) clearly distinguish $\{Ni_{12}W_{30}\}$ and $\{Ni_{12}W_{27}\}$ magnetically and photocatalytically as hydrogen evolution catalysts (HECs) from conventional Ni_4 cubanes. These findings pave the way towards advanced spintronics and photovoltaic devices. Cover design by Elias Tanuhadi and Stephen Myakala.

As featured in:

See Alexey Cherevan, Annette Rompel *et al.*, *J. Mater. Chem. C*, 2022, **10**, 17048.

ROYAL SOCIETY OF CHEMISTRY

rsc.li/materials-c

Registered charity number: 207890

Journal of Materials Chemistry C

COMMUNICATION

Cite this: J. Mater. Chem. C, 2022, 10, 17048

Received 19th August 2022,
Accepted 17th October 2022

DOI: 10.1039/d2tc03508a

rsc.li/materials-c

Ni_{12} tetracubane cores with slow relaxation of magnetization and efficient charge utilization for photocatalytic hydrogen evolution†

Elias Tanuhadi, [a] Joan Cano, [b] Samar Batool, [c] Alexey Cherevan, *[c] Dominik Eder [c] and Annette Rompel *[a]

We report two Ni_{12} multicubane topologies enclosed in the polyanions $[Ni_{12}(OH)_9(WO_4)_3(PO_4)(B\text{-}\alpha\text{-}PW_9O_{34})_3]^{21-}$ $\{Ni_{12}W_{30}\}$ and $[Ni_{12}(OH)_9(HPO_4)_3(PO_4)(B\text{-}\alpha\text{-}PW_9O_{34})(A\text{-}\alpha\text{-}PW_9O_{34})_2]^{21-}$ $\{Ni_{12}W_{27}\}$ that magnetically behave as Ni_{12} units clearly distinguishing them from typical Ni_4 cubanes as shown by magnetic studies together with high field and frequency electron paramagnetic resonance (HFEPR). Beyond the unprecedented static properties, $\{Ni_{12}W_{30}\}$ shows the unusual coexistence of slow relaxation of the magnetization and a diamagnetic ground state (S = 0), providing the unique opportunity of studying the essentially elusive magnetic relaxation behavior in excited states. The cubane-topology dependent activity of $\{Ni_{12}W_{30}\}$ and $\{Ni_{12}W_{27}\}$ as homogeneous HER photocatalysts unveils the structural key features significant for the design of photocatalysts with efficient charge utilization exemplified by high quantum yields (QY) of 10.42% and 8.36% for $\{Ni_{12}W_{30}\}$ and $\{Ni_{12}W_{27}\}$, respectively.

The compound class of transition metal (TM) based cubane clusters with the general formulation $\{TM_4L_4\}$ (TM = Co^{II}, Ni^{II}, Fe^{III}, $Mn^{II/III/IV}$ and L = O, S, N)[1] exhibits unique structural and electronic properties. Consequently, cubane-based materials have been subjected to magnetic studies.[2] In solution, the structural reminiscence of enzyme active sites such as the oxygen evolving complex (OEC) $\{Mn_4O_5Ca\}$[3] in photosystem II (PS II)[4,5] and the $\{Fe_4S_4\}$ cubane cluster in hydrogenases[6] encouraged studies on cubane-based metal oxide nanoparticle catalysts.[7] From a synthetic point of view, recent attention has been given to lacunary polyoxometalates (POMs).[8,9] Being generated upon the removal of one or several MO_6 (M = Mo^{VI}, W^{VI}) units from their parental architectures such as the Keggin[10] or Wells–Dawson types[11], lacunary POMs can act as strong inorganic, diamagnetic, multidentate O-donor ligands towards electrophiles. This multidentate nature allows the construction of mono- or multinuclear transition metal substituted POMs.[12] Considering the lacunary POMs' rigidity, bulkiness, and diamagnetic nature, cubane-motif incorporating POM representatives were shown to exhibit interesting magnetic properties such as single molecule magnet (SMM) behavior as a result of large spin ground state (S) values.[13a] POMs generally exhibit a facile photoexcitation *via* near-visible or UV-light generating photoexcited species with enhanced oxidizing (higher electron affinity E_{ea}) and reducing (lower ionization energy E_I) properties.[13b] Their multicentered nature allows POMs to undergo multi-redox events. In addition to their versatile redox properties, the inherent water solubility of POMs and stability encouraged researchers to employ cubane-motif incorporating POMs as homogeneous photocatalysts for the water reduction catalysis (WRC)[14] and oxidation catalysis (WOC)[15] reactions, respectively.

Despite the variety of existing POM-stabilized cubane motifs (Fig. S2, ESI†) that have been subjected to magnetic and/or (photo)-catalytic studies (Table S1, ESI†), there are no studies exploring the correlation between a (multi)cubane-topology and its magnetic properties. Hence, advanced magnetic studies of, *e.g.*, magnetic relaxation arising from excited states that might pave the way towards advanced spintronics remain widely elusive. While significant advances have been made in studying the cubane-dependent HER photocatalytic activity of POMs[14] (Fig. S3 and Table S2, ESI†), the underlying structural features that may grant taking full advantage of photogenerated charge carriers as a key for improving the activity of photocatalysts remain essentially unexplored.[16]

Herein, we employ phosphotungstates as rigid, all-inorganic multidentate ligands together with the simple inorganic templates PO_4^{3-} or CO_3^{2-} for the template-dependent stabilization

[a] Universität Wien, Fakultät für Chemie, Institut für Biophysikalische Chemie, Josef-Holaubek-Platz-2, Wien 1090, Austria. E-mail: annette.rompel@univie.ac.at; Web: https://www.bpc.univie.ac.at
[b] Department of Química Inorgànica/Instituto de Ciencia Molecular (ICMol), Facultat de Química, Universitat de València, C/Catedrático Jose Beltrán 2, Paterna 46980, València, Spain
[c] TU Wien, Institute of Materials Chemistry, Getreidemarkt 9, Vienna 1060, Austria. E-mail: alexey.cherevan@tuwien.ac.at; Web: https://www.imc.tuwien.ac.at/division_molecular_materials_chemistry/

† Electronic supplementary information (ESI) available. CCDC 2102166 and 2102167. For ESI and crystallographic data in CIF or other electronic format see DOI: https://doi.org/10.1039/d2tc03508a

of two tetracubane Ni_{12} topologies enclosed in the polyanions $[Ni_{12}(OH)_9(WO_4)_3(PO_4)(B\text{-}\alpha\text{-}PW_9O_{34})_3]^{21-}$ **{$Ni_{12}W_{30}$}** and $[Ni_{12}(OH)_9(HPO_4)_3(PO_4)(B\text{-}\alpha\text{-}PW_9O_{34})(A\text{-}\alpha\text{-}PW_9O_{34})_2]^{21-}$ **{$Ni_{12}W_{27}$}**. Given the identical number of incorporated Ni metal centers and their same net charge, **{$Ni_{12}W_{30}$}** and **{$Ni_{12}W_{27}$}** only differ in the type of POM-stabilized multicubane topology, thereby representing ideal candidates to study the topology dependent magnetic and photocatalytic behavior in the solid and solution states, respectively.

{$Ni_{12}W_{30}$} and **{$Ni_{12}W_{27}$}** were prepared employing a template dependent synthetic approach.[17a] To an aqueous reaction mixture containing the $K_{14}[P_2W_{19}O_{69}(H_2O)]\cdot 24H_2O$[17b] **{$P_2W_{19}$}** lacunary precursor, three equivalents of $NiCl_2$ were added following the adjustment of the pH value to 9.1 *via* CO_3^{2-} or PO_4^{3-} and subsequent heating of the reaction mixture at 80 °C for 10 min. Depending on the inorganic template used for the solution's basification, **{$Ni_{12}W_{30}$}** (CO_3^{2-}) or **{$Ni_{12}W_{27}$}** (PO_4^{3-}) is obtained (Fig. 1, ESI†) upon slow evaporation of the solution for two weeks at 25 °C leading to yellow-plate shaped crystals of **{$Ni_{12}W_{27}$}** or light-green rod-shaped crystals of **{$Ni_{12}W_{30}$}**, respectively. When this paper was under preparation, a crystal structure with the identical anion of **{$Ni_{12}W_{30}$}** was reported.[17c] Note that for the synthesis of **{$Ni_{12}W_{30}$}**, different routes have been used by Lian *et al.* and our group (see Synthesis procedure†). The template dependent synthetic system reported in this work ultimately leads to the isolation of the novel polyanion **{$Ni_{12}W_{27}$}**.

Single crystal X-ray diffraction (SXRD) was performed (Tables S5–S9, ESI†) revealing that **{$Ni_{12}W_{27}$}** and **{$Ni_{12}W_{30}$}** both incorporate a Ni_{12} metal-oxo core that differs in the type of connectivity, and resulting in multicubane topology (Fig. 1) leading to the stabilization of three full **{Ni_4O_4}** cubane units in **{$Ni_{12}W_{30}$}** while **{$Ni_{12}W_{27}$}** comprises one full **{Ni_4O_4}** and two defect $\{Ni_4O_3\}$ cubane motifs (Fig. 1, Fig. S14 and Tables S10, S11, ESI†). The compound's elemental composition and homogeneity were determined in the solid state by elemental analysis, IR spectroscopy (Fig. S4–S9 and Table S3, ESI†), thermogravimetric analyses (TGA) (Fig. S10–S13 and Table S4, ESI†), diffuse reflectance spectroscopy (DRS) (Fig. S17–S22, ESI†), and powder X-ray diffraction (PXRD) (Fig. S15 and S16, ESI†) as well as in solution by UV/vis spectroscopy (Fig. S31, ESI†) and cyclic voltammetry (Fig. S26–S30, ESI†).

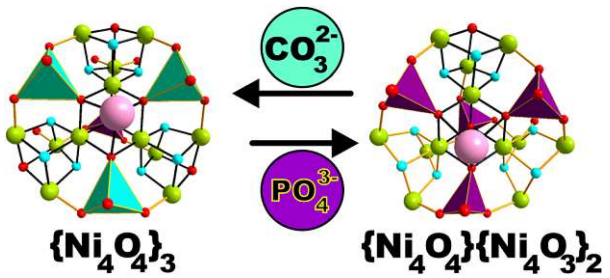

Fig. 1 Schematic representation showing the template-dependent stabilization of the multicubane scaffolds **{Ni_4O_4}$_3$** (in **{$Ni_{12}W_{30}$}** *via* CO_3^{2-}) and **{Ni_4O_4}{Ni_4O_3}$_2$** (in **{$Ni_{12}W_{27}$}** *via* PO_4^{3-}. Color code, polyhedra: turquoise for $\{WO_4\}$ and purple for $\{PO_4\}$. Balls: red for oxygen lime green for Ni^{II} and sky-blue for OH^- ions, respectively.

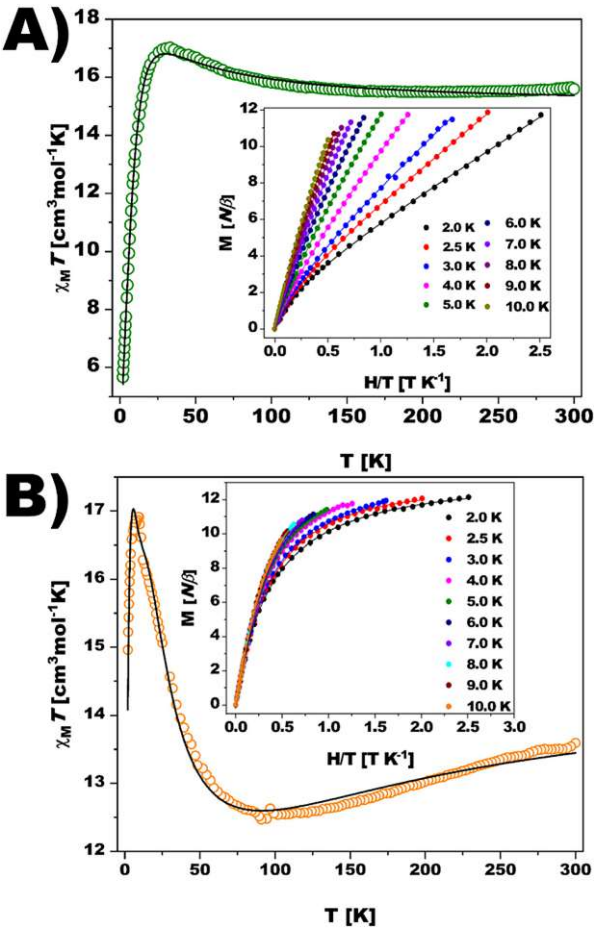

Fig. 2 Temperature dependence of $\chi_M T$ and reduced magnetization curves (inset) for (A) **{$Ni_{12}W_{30}$}** and (B) **{$Ni_{12}W_{27}$}**. Solid lines are the best-fit curve and a guide to the eye for $\chi_M T$ and M.

The magnetic properties of **{$Ni_{12}W_{30}$}** and **{$Ni_{12}W_{27}$}** were studied in the solid state (Fig. 2) and solution (Fig. S42, ESI†). Plots of $\chi_M T$ (χ_M being the magnetic susceptibility per Ni_{12} unit) *vs.* T for **{$Ni_{12}W_{30}$}** and **{$Ni_{12}W_{27}$}** are displayed in Fig. 2. At 300 K, after removing the temperature-independent paramagnetism in subsequent fits (TIP = 4211×10^{-6} and 2756×10^{-6} cm^3 mol^{-1} for **{$Ni_{12}W_{30}$}** and **{$Ni_{12}W_{27}$}**, respectively), their $\chi_M T$ values are *ca.* 15.6 (**{$Ni_{12}W_{30}$}**) and 13.6 cm^3 mol^{-1} K (**{$Ni_{12}W_{27}$}**). These values are larger and smaller, respectively, than the spin-only value expected (*ca.* 14.5 cm^3 mol^{-1} K, with g = 2.2) for twelve magnetically non-interacting high-spin Ni^{II} ions (S = 1). Hence, ferromagnetic (F) interactions are suggested to be predominant in **{$Ni_{12}W_{30}$}** as supported by the continuous increase of the compound's $\chi_M T$ upon lowering the temperature. In contrast to **{$Ni_{12}W_{30}$}**, a continuous decrease of $\chi_M T$ starting at room temperature (300 K) and reaching a minimum at 95 K accompanied by a subsequent increase is observed for **{$Ni_{12}W_{27}$}**.

These features support the coexistence of F and antiferromagnetic (AF) interactions, with the latter being predominant. At 31 K ({**Ni$_{12}$W$_{30}$**}, Fig. 2A) and 17 K ({**Ni$_{12}$W$_{27}$**}, Fig. 2B), $\chi_M T$ shows maxima followed by an abrupt downturn to reach values of 5.7 and 15.0 cm^3 mol^{-1} K at 2.0 K, respectively. Usually, zero-field splitting (zfs) could be the responsible factor for the observed decrease, as shown by the values of the local axial and rhombic zfs parameters (Table S14, see ESI,† Magnetism). The sharp downturn observed for {**Ni$_{12}$W$_{30}$**} (Fig. 2A) and {**Ni$_{12}$W$_{27}$**} (Fig. 2B) suggests additional factors apart from conventional zfs to be related to the AF inter- or intramolecular interactions. The shapes of the magnetization (M) *vs.* H plot at 2.0 K for both compounds (see insets of Fig. 2) show values largely below that expected for a ferromagnetic S = 12 spin ground state (26.4 $N\beta$, with g = 2.2). In the case of {**Ni$_{12}$W$_{27}$**}, weak or moderate H cancel the intermolecular magnetic interaction between two Ni$_{12}$ units, and M tends to a saturation value of *ca* 12 $N\beta$, which is close to that expected for an S = 6 ground state. In contrast, a gentle increase of M for {**Ni$_{12}$W$_{30}$**} is observed at low fields without any trend for reaching saturation, supporting the close presence of many excited states of higher spin multiplicity that are partially populated upon increasing the magnetic field or the temperature. An estimation of the coupling constants (J_i values) obtained from DFT calculations guides the analysis of the observed magnetic behavior of both compounds suggesting a diamagnetic spin ground state S = 0 for {**Ni$_{12}$W$_{30}$**} with an energetically close excited state S = 1 (0.4 cm^{-1}) and a ground state S = 6 with close excited states S = 5 and S = 4 at 2.0 and 10.1 cm^{-1} for {**Ni$_{12}$W$_{27}$**} (Fig. S32–S37 and Tables S12, S13, ESI,† see Magnetism).

Alternating current (ac) magnetic susceptibility studies of {**Ni$_{12}$W$_{30}$**} and {**Ni$_{12}$W$_{27}$**} were performed to explore their magnetic relaxation properties. Out-of-phase (χ_M'') signals were observed both in the absence and under applied dc magnetic fields (H_{dc}) (Fig. S38 and S39, ESI†), typical for SMMs with energy barriers (E_a) risen from a $D < 0$ for low rhombicity ($E/D \approx 0$).[18,19] The occurrence of only incipient χ_M'' signals without maxima in the $\chi_M'' - T$ plots in both compounds precludes a correct treatment of the experimental data. Hence, a semiquantitative estimation of the E_a values was extracted from the $\ln(\chi_M''/\chi_M')$ *vs.* $1/T$ plots for each frequency.[18] According to the relationship $\ln(\chi_M''/\chi_M') = \ln(2\pi\nu\tau_0) + E_a/kT$ valid for a system with a single relaxation process, a collection of parallel straight lines is expected (Fig. S40 and S41, ESI†).[18,19] The value of E_a would be obtained from their slope, giving E_a values of 18.1(7) and 25.0(3) cm^{-1} for {**Ni$_{12}$W$_{30}$**} and {**Ni$_{12}$W$_{27}$**}, respectively, with the E_a value for {**Ni$_{12}$W$_{30}$**} being close to that estimated (17.3 cm^{-1}, the largest value between the round-trip paths) from the values of D (−15.2 cm^{-1}) and E (0.14) proposed from the theoretical study for the first excited state S = 1. Since the negative sign of D enables a magnetic energy barrier and the good agreement between experimental and theoretical values of E_a, it can be concluded that a two-phonon Orbach mechanism governs the relaxation of the magnetization. The magnetization relaxation in {**Ni$_{12}$W$_{27}$**} occurs in the S = 6 ground state and is controlled through the energy barrier promoted by the zfs, whereas the diamagnetic singlet ground state S = 0 in {**Ni$_{12}$W$_{30}$**} suggests the observed slow relaxation of magnetization to arise from the close first excited state (S = 1, 0.4 cm^{-1}, Fig. S36, ESI†).[20a,b] This excited triplet state S = 1 is only partially populated at the lowest experimental temperature being the cause of the weak χ_M'' signals and precluding the data analysis in the absence of H_{dc}. These assumptions are additionally reinforced by high-frequency and high-field electron paramagnetic resonance (HFEPR) studies, which show an EPR-silent spectrum for {**Ni$_{12}$W$_{30}$**} in accordance with the proposed singlet ground state S = 0 (Fig. S43, ESI†), whereas HFEPR studies on {**Ni$_{12}$W$_{27}$**} reveal a weak signal at 6.6 T (Fig. S44 and S45, ESI†) further supporting the presence of a paramagnetic ground state and dipolar AF interactions arising from the {**Ni$_{12}$W$_{27}$**}$_2$ supradimers, according to the DFT study and the crystal structure (Fig. S46, ESI,† DFT studies. Section 10.1). The observed topology-dependent magnetic behaviour and electronic properties distinguish the isolated Ni$_{12}$ scaffolds from typical {**Ni$_4$O$_4$**} single-cubane motifs.

A careful inspection of the 236 GHz EPR spectrum of {**Ni$_{12}$W$_{30}$**} allows for identifying of two almost muted signals at 4.0 and 6.9 T resulting from a very close excited state (Fig. S43, ESI†). These signals do not change as the temperature increases, and their intensity decreases when using a frequency of 400 GHz. This surprising result must be attributed to several excited states very close to the ground one, as shown in Figure S36 (ESI†) from the theoretical study. A triplet spin state and a D value comparable to that proposed by CASSCF calculations (≈−15 cm^{-1}) could reproduce the signal at 6.9 T. However, the low-field signal must appear due to a notable rhombicity in the zfs tensor ($E/D \neq 0$), which agrees well with the theoretical study (0.14) and the weakness of these signals (page 59 in the ESI†).

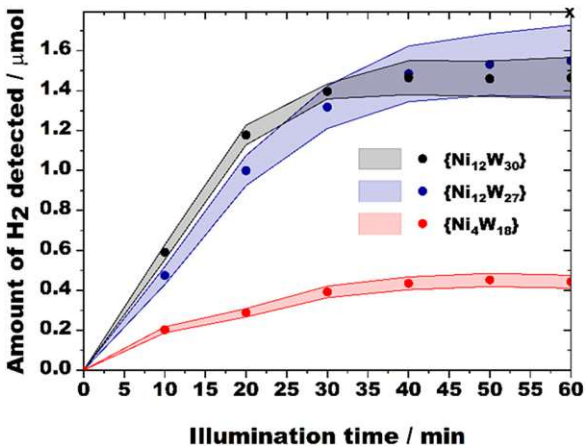

Fig. 3 H_2 evolution profiles for {**Ni$_{12}$W$_{30}$**}, {**Ni$_{12}$W$_{27}$**}, and the benchmark {**Ni$_4$W$_{18}$**} obtained using 20 μM catalyst concentrations. Data points represent average values obtained from multiple measurements, and colored areas indicate standard deviations for each compound and data point. Each measurement was conducted for 60 min until H_2 saturation was reached (point *x*).

The EPR spectrum at 236 GHz of **{Ni$_{12}$W$_{27}$}** shows five attenuated signals at 3.6, 6.2, 6.6, 7.0 and 8.0 T, which move to higher fields when increasing the frequency to 388 GHz but do not substantially modify their intensity (Fig. S45, ESI†). This pattern resembles that observed in a previous double-cubane Ni_7 cluster,[20c] which, like **{Ni$_{12}$W$_{27}$}**, exhibits an $S = 6$ ground state, supporting our conclusions. The analysis of the EPR spectra of Ni_7 required a nearby $S = 7$ excited state. However, according to our theoretical study, an analogous procedure in **{Ni$_{12}$W$_{27}$}** should consider an $S = 5$ rather than an $S = 7$ excited state. Unfortunately, the weakness of the signals on **{Ni$_{12}$W$_{27}$}** prevents further investigation.

Following earlier reports on structurally relevant Ni-containing POM hydrogen evolution catalysts (HECs)[21] the TBA salts of **{Ni$_{12}$W$_{30}$}** and **{Ni$_{12}$W$_{27}$}** were evaluated towards the visible-light-driven hydrogen evolution reaction (HER) employing $[Ir(dtbbpy)(ppy)_2]^+$ (dtbbpy = 4,4′-di-*tert*-butyl-2,2′-dipyridyl, ppy = 2-phenylpyridine) as the photosensitizer (PS), triethanolamine (TEOA) as an electron donor and 11 : 33 : 4 vol% CH_3CN/DMF/H_2O as a solvent mixture (see Hydrogen evolution (HER) experiments, Fig. S47 and S48, ESI†). A compositionally relevant tetra-nickel polyoxotungstate reported by Hill *et al.*[21c] referred to as **{Ni$_4$W$_{18}$}** was prepared, characterized (Fig. S1, ESI†), and tested under identical experimental conditions as a benchmark HEC following a comprehensive set of pre-catalytic studies employing time-dependent UV/vis studies (Fig. S31, ESI†) that demonstrated pre-catalytic stability of **{Ni$_{12}$W$_{30}$}** and **{Ni$_{12}$W$_{27}$}** as shown by the compounds' virtually unchanged spectra over a time period of 60 min relevant to the catalytic experiment (see Section S12.1, ESI†).

Table 1 contains the values of the turnover frequencies (TOFs) calculated after 10 minutes of each HER experiment. Depending on the concentrations of **{Ni$_{12}$W$_{30}$}** and **{Ni$_{12}$W$_{27}$}**, their HER TOFs lie in the range between 19.8 and 145.7 (expressed in 10^{-3} s^{-1}). To allow for a valid comparison to relevant catalysts, the HER quantum yields (QYs, see General information†) were calculated (Table 1) and amount to 10.42 and 8.36% for **{Ni$_{12}$W$_{30}$}** and **{Ni$_{12}$W$_{27}$}**, respectively. These QYs greatly surpass values previously reported for Ni-containing POMs[14,16] (Table S2, ESI†) and – considering that HER QY values already include absorption and recombination losses (*e.g.*, contributions by PS-POM charge transfer) – they indicate extremely high efficiency of charge utilization for **{Ni$_{12}$W$_{30}$}** and **{Ni$_{12}$W$_{27}$}** suggesting **{Ni$_{12}$W$_{30}$}** and **{Ni$_{12}$W$_{27}$}** to be the fastest **Ni-PT** based HECs reported so far (Table S2, ESI†).

Table 1 Average values (standard deviations 3–6%) of turnover number (TON) and turnover frequency (TOF) values towards H_2 generation for **{Ni$_{12}$W$_{30}$}**, **{Ni$_{12}$W$_{27}$}**, the benchmark **{Ni$_4$W$_{18}$}** and **Ni(NO$_3$)$_2$** along with quantum yields (QYs) (2–20 μM). TONs were extracted after H_2 evolution saturation point (point *x* at 60 min), initial TOFs and QYs were extracted after 10 min (Fig. 3)

Ni-POT	*c*/μM	H_2/μmol	TON	TOF/10^{-3} s^{-1}	QY/%
{Ni$_{12}$W$_{30}$}	2	0.56	140.9	145.7	6.15
	5	0.82	81.6	84.4	8.90
	10	1.11	55.4	39.2	8.26
	20	1.47	36.7	24.7	10.42
{Ni$_{12}$W$_{27}$}	2	0.52	130.0	106.3	4.49
	5	0.81	81.0	56.1	5.92
	10	1.12	56.2	37.4	7.89
	20	1.55	38.8	19.8	8.36
{Ni$_4$W$_{18}$}	20	0.45	11.4	8.8	3.72
Ni(NO$_3$)$_2$	20	0.35	8.7	6.9	

Post-catalytic studies (see the ESI† section Post-catalytic studies) featuring IR-spectroscopy demonstrated the post-catalytic bulk stability of **{Ni$_{12}$W$_{30}$}** and **{Ni$_{12}$W$_{27}$}** (Fig. S49, ESI†), which was subsequently assessed quantitatively employing X-ray fluorescence (XRF) (Table S15, ESI†). A series of reloading experiments demonstrated the recyclability of **{Ni$_{12}$W$_{30}$}** and **{Ni$_{12}$W$_{27}$}** as homogeneous HECs (Fig. S50, ESI†).

A careful analysis of the TOF values allows for structure–activity relationship (SAR) correlations between **{Ni$_{12}$W$_{30}$}** and **{Ni$_{12}$W$_{27}$}** that both feature $\{Ni^{II}_4O_4\}$ quasi-cubanes. While higher catalyst concentrations (10 and 20 μM) yield similar TOFs, a significantly higher HER performance of **{Ni$_{12}$W$_{30}$}** over **{Ni$_{12}$W$_{27}$}** can be observed for 2 and 5 μM catalyst solutions at which the catalytic role of the elsewise isostructural **Ni-PT**s – that both display the same net charge of −21 – is more pronounced. One contribution to the superior activity of **{Ni$_{12}$W$_{30}$}** over **{Ni$_{12}$W$_{27}$}** can be related to the higher number of $\{Ni^{II}_4O(OH)_3\}$ cubanes incorporated in the POT framework as compared to **{Ni$_{12}$W$_{27}$}**, which is in accordance with the findings reported by Wang and co-workers (Fig. S3, ESI†).[14]

To further explore the origin of the higher HER activity of **{Ni$_{12}$W$_{30}$}**, photoluminescence (PL) emission studies (Fig. S52 and S53, Section S14, ESI†) elucidating the HEC mechanism were conducted. Both steady-state and time-resolved data propose reductive quenching to dominate under the turnover conditions (Scheme S1, ESI†), which suggests that the reversible reduction of the corresponding **Ni-PT** (Scheme S2, ESI,† step III) – which consecutively reduces H^+ upon H_2 formation may represent a rate-limiting step in the HER. Based on CV studies on **{Ni$_{12}$W$_{27}$}** (Fig. S25, ESI†), **{Ni$_{12}$W$_{30}$}** (Fig. S24, ESI†), and **{Ni$_4$W$_{18}$}** (Fig. S23, ESI†), the onset reduction of the **Ni-PT**s occurs at more positive potentials in the order **{Ni$_4$W$_{18}$}** (−0.66 V) < **{Ni$_{12}$W$_{27}$}** (−0.25 V) < **{Ni$_{12}$W$_{30}$}** (−0.12 V). Hence, the observed activity trend can be explained by the increased tendency of **{Ni$_{12}$W$_{30}$}** to be reduced, which is additionally reflected by a substantially higher (50%) quenching rate K_q for **{Ni$_{12}$W$_{30}$}** ($K_q = 13.2 \times 10^9$ M^{-1} s^{-1}) compared to that of **{Ni$_{12}$W$_{27}$}** ($K_q = 8.9 \times 10^9$ M^{-1} s^{-1}) (Fig. S53, ESI†) illustrating its more efficient redox shuttling. A template-dependent change in the topology of the Ni_{12} metal-oxo core resulted in an increased number of $\{Ni^{II}_4O(OH)_3\}$ cubanes present in **{Ni$_{12}$W$_{30}$}** and provided this **Ni-PT** with an enhanced charge-utilization expressed by the tuned redox-activity and increased photocatalytic HER performance as compared to **{Ni$_{12}$W$_{27}$}** and **{Ni$_4$W$_{18}$}**.

Conclusions

Our results highlight that a diamagnetic ground state does not necessarily preclude SMM behavior in compounds that exhibit

energetically closely located paramagnetic excited spin states. Moreover, incorporating a tandem ground and nearby excited states, behaving both as SMMs or qubits, allows for envisaging advanced spintronics and quantum computing. Structure–activity studies on $\{Ni_{12}W_{30}\}$ and $\{Ni_{12}W_{27}\}$ probing their photocatalytic HEC activity revealed high charge utilization for $\{Ni_{12}W_{30}\}$ and $\{Ni_{12}W_{27}\}$. The topology modulation of the tetracubane scaffold employing simple inorganic anionic templates represents a key to tuning their functional HEC properties upon modulating the corresponding Ni-PT's redox properties as exemplified by the high quantum yield of $\{Ni_{12}W_{30}\}$.

Conflicts of interest

There are no conflicts to declare.

Acknowledgements

This research was funded by the Austrian Science Fund (FWF): P33089 (to A. R.) and P32801 (to A. C.), the University of Vienna, the Spanish MINECO (Project PID2019-109735GB-I00 and Unidad de Excelencia María de Maeztu CEX2019-000919-M), and Generalitat Valenciana (AICO/2020/183 and AICO/2021/295). E. T. and A. R. acknowledge the University of Vienna for awarding a Uni:docs fellowship to E.T. The authors thank Nadiia I. Gumerova, PhD for support with ESI-MS experiments, Pablo Ayala, MSc for TXRF measurements, and Dr Heiko Geisler for assisting in CV experiments. Photoluminescence (PL) emission and lifetime measurements were performed by Sreejith P. Nandan, MSc. The authors thank Ing. Dipl.-Ing. (FH) Alexander Prado-Roller (X-ray Structure Analysis Center, Faculty of Chemistry, University of Vienna) and ao. Univ.-Prof. Mag. Dr Gerald Giester (Department of Mineralogy and Crystallography, University of Vienna) for support and valuable discussions with single crystal X-ray crystallographic measurements and data analyses. Lastly, the authors wish to thank Dipl.-Ing. Dr techn. Andreas Mautner, Privatdoz and Mag. Johannes Theiner (Mikroanalytisches Laboratorium Universität Wien) for elemental analyses. The high-field EPR spectra were recorded by Andrew Ozarowski, PhD, at the National High Magnetic Field Laboratory, which is supported by the National Science Foundation Cooperative Agreement No. DMR-1644779 and the State of Florida.

Notes and references

1 F. G. Mann, D. Purdie and A. F. Wells, *J. Chem. Soc.*, 1936, 1503–1513.
2 (*a*) J. E. Andrew and A. B. Blake, *J. Chem. Soc. A*, 1969, 1456–1461; (*b*) A. P. Ginsberg, J. A. Bertrand, R. I. Kaplan, C. E. Kirkwood, R. L. Martin and R. C. Sherwood, *Inorg. Chem.*, 1971, **10**, 240–246.
3 R. M. Cinco, J. H. Robblee, A. Rompel, C. Fernandez, V. K. Yachandra, K. Sauer and M. P. Klein, *J. Phys. Chem. B*, 1998, **102**, 8248–8256.
4 J. Yano and V. K. Yachandra, *Chem. Rev.*, 2014, **114**, 4175–4205.
5 M. L. Helm, M. P. Stewart, R. M. Bullock, M. R. DuBois and D. L. DuBois, *Science*, 2011, **333**, 863–866.
6 J. Liu, S. Chakraborty, P. Hosseinzadeh, Y. Yu, S. Tian, I. Petrik, A. Bhagi and Y. Lu, *Chem. Rev.*, 2014, **114**, 4366–4469.
7 (*a*) S. Berardi, G. La Ganga, M. Natali, I. Bazzan, F. Puntoriero, A. Sartorel, F. Scandola, S. Campagna and M. Bonchio, *J. Am. Chem. Soc.*, 2012, **134**, 11104–11107; (*b*) B. Zhang, F. Li, F. Yu, X. Wang, X. Zhou, H. Li, Y. Jiang and L. Sun, *ACS Catal.*, 2014, **4**, 804–809.
8 M. T. Pope, *Heteropoly and Isopoly Oxometalates*, Springer Verlag, Berlin, 1983, vol. **2**, pp. 10–26.
9 N. I. Gumerova and A. Rompel, *Chem. Soc. Rev.*, 2020, **49**, 7568–7601.
10 G. L. Miessler and D. A. Tarr, *Inorganic Chemistry*, Pearson Prentice Hall, Upper Saddle River, N.J., 3rd edn, Internat. edn, 2004.
11 L. Briand and H. J. Thomas, *Appl. Catal., A*, 2003, **256**, 37–50.
12 Z.-J. Liu, X.-L. Wang, C. Qin, Z.-M. Zhang, Y.-G. Li, W.-L. Chen and E.-B. Wang, *Coord. Chem. Rev.*, 2016, **313**, 94–110.
13 (*a*) M. Ibrahim, Y. Lan, B. S. Bassil, Y. Xiang, A. Suchopar, A. K. Powell and U. Kortz, *Angew. Chem., Int. Ed.*, 2011, **50**, 4708–4711; (*b*) C. Streb, K. Kastner and J. Tucher, *Phys. Sci. Rev.*, 2019, **4**, 368–378.
14 X.-B. Han, C. Qin, X.-L. Wang, Y.-Z. Tan, X.-J. Zhao and E.-B. Wang, *Appl. Catal., B*, 2017, **211**, 349–356.
15 X.-B. Han, Y.-G. Li, Z.-M. Zhang, H.-Q. Tan, Y. Lu and E.-B. Wang, *J. Am. Chem. Soc.*, 2015, **137**, 5486–5493.
16 P. Zhang, T. Wang, X. Chang and J. Gong, *Acc. Chem. Res.*, 2016, **49**, 911–921.
17 (*a*) S. Li, H. Wang, H. Su, H. Chen, M. Du, L. Long, X. Kong and L. Zheng, *Small Methods*, 2021, **5**, 2000777; (*b*) C. M. Tourné and G. F. Tourné, *J. Chem. Soc., Dalton Trans.*, 1988, **9**, 2411–2420; (*c*) C. Lian, H.-L. Li and G.-Y. Yang, *Inorg. Chem.*, 2022, **61**, 11335–11341.
18 F. Luis, J. Bartolomé, J. F. Fernández, J. Tejada, J. M. Hernández, X. X. Zhang and R. Ziolo, *Phys. Rev. B: Condens. Matter Mater. Phys.*, 1997, **55**, 11448–11456.
19 A. Pascual-Álvarez, J. Vallejo, E. Pardo, M. Julve, F. Lloret, J. Krzystek, D. Armentano, W. Wernsdorfer and J. Cano, *Chem. – Eur. J.*, 2015, **21**, 17299–17307.
20 (*a*) D. Cabrosi, C. Cruz, V. Paredes-García and P. Alborés, *Dalton Trans.*, 2021, **50**, 1402–1412; (*b*) J. Tang, I. Hewitt, N. T. Madhu, G. Chastanet, W. Wernsdorfer, C. E. Anson, C. Benelli, R. Sessoli and A. K. Powell, *Angew. Chem., Int. Ed.*, 2006, **45**, 1729–1733; (*c*) S. Petit, P. Neugebauer, G. Pilet, G. Chastanet, A.-L. Barra, A. B. Antunes, W. Wernsdorfer and D. Luneau, *Inorg. Chem.*, 2012, **51**, 6645–6654.
21 (*a*) H. Lv, Y. Chi, J. van Leusen, P. Kögerler, Z. Chen, J. Bacsa, Y. V. Geletii, W. Guo, T. Lian and C. L. Hill, *Chem. – Eur. J.*, 2015, **21**, 17363–17370; (*b*) W. Guo, H. Lv, J. Bacsa, Y. Gao, J. S. Lee and C. L. Hill, *Inorg. Chem.*, 2016, **55**, 461–466; (*c*) H. Lv, W. Guo, K. Wu, Z. Chen, J. Bacsa, D. G. Musaev, Y. V. Geletii, S. M. Lauinger, T. Lian and C. L. Hill, *J. Am. Chem. Soc.*, 2014, **136**, 14015–14018.

ELECTRONIC SUPPLEMENTARY INFORMATION

Ni_{12} - tetracubane cores with slow relaxation of magnetization and efficient charge utilization for photocatalytic hydrogen evolution

Elias Tanuhadi[†], Joan Cano[‖], Samar Batool[‡], Alexey Cherevan[*,‡], Dominik Eder[‡], and Annette Rompel[*,†]

*correspondence to: annette.rompel@univie.ac.at, alexey.cherevan@tuwien.ac.at

[†] Universität Wien, Fakultät für Chemie, Institut für Biophysikalische Chemie, Josef-Holaubek-Platz 2, 1090 Wien, Austria; www.bpc.univie.ac.at

[‖] Department of Química Inorgànica/Instituto de Ciencia Molecular (ICMol), Facultat de Quimica de la Universitat de València, C/Catedrático Jose Beltrán 2, 46980 Paterna, València, Spain

[‡] TU Wien Institute of Materials Chemistry, Getreidemarkt 9, Vienna, 1060, Austria; https://www.tuwien.at/en/tch/mmc

Content

1. Hydrogen Evolution (HER) experiments

1.1. Pre-catalytic stability study.

To probe the solution stability of **{$Ni_{12}W_{30}$}** and **{$Ni_{12}W_{27}$}**, time-dependent UV-vis spectra were recorded in 11:33:4:2 vol. % CH_3CN/DMF/H_2O/TEOA solvent mixtures. The UV-vis spectra of TBA-**{$Ni_{12}W_{30}$}** and TBA-**{$Ni_{12}W_{27}$}** (TBA = tetrabutylammonium) display absorption maxima at 285 nm (**{$Ni_{12}W_{30}$}**, **Figure S31 A**) and 265 nm (**{$Ni_{12}W_{27}$}**, **Figure S31 B**) corresponding to the O→W ligand−to−metal charge−transfer (LMCT)[1] as well as the d-d transitions typical for octahedrally coordinated NiII metal centers at 688 nm (**{$Ni_{12}W_{30}$}**, **Figure S31 C**) and 700 nm (**{$Ni_{12}W_{27}$}**, **Figure S31 D**), respectively.[2] All observed peaks remain unchanged for at least 60 min, mimicking the photocatalytic conditions and thereby suggesting pre-catalytic stability of **{$Ni_{12}W_{30}$}** and **{$Ni_{12}W_{27}$}** until H_2 saturation is reached in the HER experiments (**Figure 3**).

1.2. HER – activity studies on $TBA_{13}Na_8$-**{$Ni_{12}W_{30}$}** and $TBA_{13}Na_8$-**{$Ni_{12}W_{27}$}**.

Figure 3 shows HER profiles for **{$Ni_{12}W_{30}$}** and **{$Ni_{12}W_{27}$}** obtained from 20 µM catalytic solutions. In both cases, the H_2 evolution follows a sigmoidal profile and reaches saturation after around 60 minutes of illumination. Control experiments with longer light exposure confirmed that no additional H_2 can be generated after this point. Note that only negligible HER (2-3 % of the Ni-PT-catalyzed reaction) could be detected in absence of any catalyst due to direct PS* reduction (**Figure S47**). Moreover, significantly lower H_2 amounts were detected when using 20 µM $Ni(NO_3)_2$ solutions (**Figure S47**), which confirms the catalytic role of the studied **Ni-PT**s. No H_2 was generated in the absence of TEOA or sensitizer (**Figure S47**), demonstrating the validity of the experimental setup.

The amounts of H_2 measured at HER saturation level were translated into turnover numbers (TONs) and yield 36.7 and 38.8 for **{$Ni_{12}W_{30}$}** and **{$Ni_{12}W_{27}$}** (at 20 µM), respectively (**Table 1**). These similar values suggest that the structural differences between **{$Ni_{12}W_{30}$}** and **{$Ni_{12}W_{27}$}** (type of capping ligands, core connectivity) do not contribute to their WRC performance at the investigated catalyst concentration. Importantly, the measured TON values are significantly higher than that of **{Ni_4W_{18}}** (11.4), which manifests the superior performance of the reported **Ni-PT**s over the benchmark WRC even when normalized to the number of Ni-centers. This activity trend is further in line with electronic structure elucidation carried out using diffuse reflectance spectroscopy (DRS) for band gap values (**Figures S17-S22**) and cyclic voltammetry for the values of lowest unoccupied and highest occupied molecular orbitals (LUMO/HOMO) of all three compounds (**Figures S23-S25**).

HER performance of **{$Ni_{12}W_{30}$}** and **{$Ni_{12}W_{27}$}** was subsequently evaluated as a function of **Ni-PT** concentration in the lower range between 2 and 10 µM. **Figure S48** indicates that the obtained HER profiles are similar to those from 20 µM experiments shown in **Figure 3**. However, the lower concentrations of **{$Ni_{12}W_{30}$}** and **{$Ni_{12}W_{27}$}** did not yield proportionally lower H_2 amounts considering that the decrease from 20 to 2 µM only resulted in a 2.6 and 3-fold HER drop for **{$Ni_{12}W_{30}$}** and **{$Ni_{12}W_{27}$}**, respectively. This indicates that catalyst concentration is not the limiting factor for the investigated systems and hence suggests limiting contributions by the sensitizer or TEOA concentration.

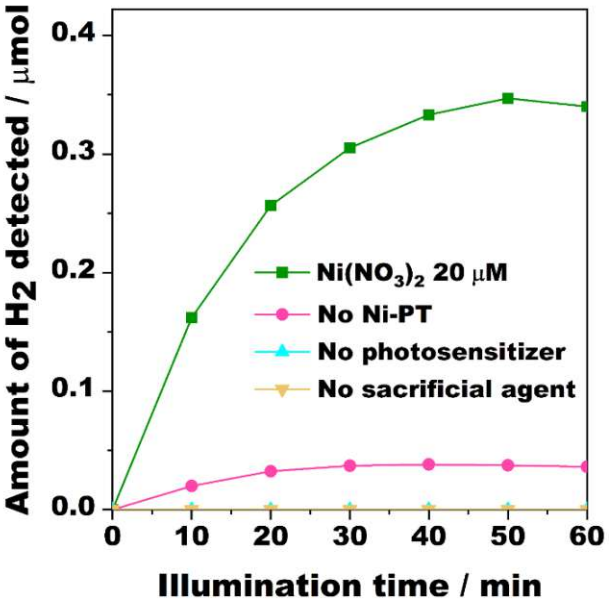

Figure S47. Control experiments aiming to verify the importance of the 3-component system and reveal the potential HER activity due to Ni-leaching. Experiments performed in the absence of any catalyst (*i.e.* only PS, SA, and solvent), sensitizer (*i.e.* only $TBA_{13}Na_8$-**{$Ni_{12}W_{30}$}**, SA and solvent) and sacrificial proton donor (*i.e.* only $TBA_{13}Na_8$-**{$Ni_{12}W_{30}$}**, PS and solvent), as well as the reference HER experiment, performed using 20 µM $Ni(NO_3)_2$ solution charged with the PS and SA. PT = phosphotungstate.

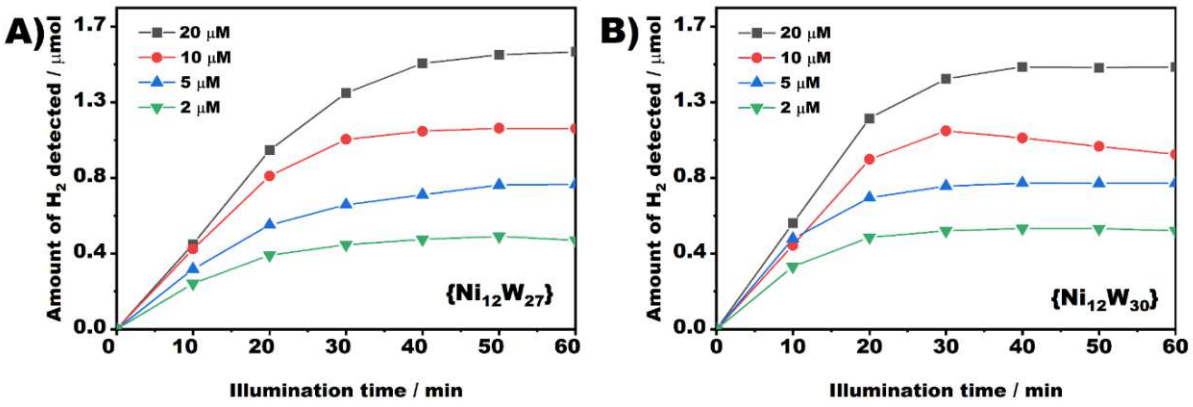

Figure S48. Concentration-dependent HER trends. H_2 evolution profiles for **(A)** $TBA_{13}Na_8$-**{$Ni_{12}W_{30}$}** and **(B)** $TBA_{13}Na_8$-**{$Ni_{12}W_{27}$}** obtained from 2-20 µM catalytic solutions. The slight drop of H_2 amount detected for the 10 µM **{$Ni_{12}W_{30}$}** sample is related to the sampling procedure which removes a part of the H_2 from the reactor headspace volume (details in the description of the photocatalytic setup given under General Information).

2. POM - HER activity and integrity

13.1 Post-catalytic studies

Post-catalytic studies and re-loading experiments were performed to elucidate the POTs' stability under photocatalytic conditions. First, the catalytic solution of **{$Ni_{12}W_{30}$}** or **{$Ni_{12}W_{27}$}** after the first HER cycle (point x in **Figure 3**) was re-loaded with a sensitizer-TEOA mixture. This second illumination cycle resulted in renewed H_2 evolution, whose extent and profile matched those from the first HER run (**Figure S49 A**). In contrast, the addition of exclusively TEOA yielded only 25% of the original activity (**Figure S49 B**). This proves that the H_2 saturation shown in **Figure 3** is not a result of sole Ni-PT-deactivation but can instead be related to the sensitizer degradation or TEOA depletion. Second, following the completion of HER (point x, **Figure 3**), **{$Ni_{12}W_{30}$}** and **{$Ni_{12}W_{27}$}** were selectively precipitated from the catalytic solution using CsCl.[3] ATR spectra of the isolated Cs-salts match well with the initially recorded tungsten fingerprint areas in the range from 1000-300 cm^{-1} (**Figures S49 A, B**), suggesting structural integrity of both polyanions under turnover conditions. To provide a quantitative assessment of the Ni-PT integrity, the remaining solutions after separating the POT Cs-salts were further analyzed with X-ray fluorescence (XRF) concerning their Ni and W contents (**Table S15**). Elemental data obtained for **{$Ni_{12}W_{30}$}** and **{$Ni_{12}W_{27}$}** show that the catalytic cycle resulted in minor leaching of both Ni and W; however, it can only account for 3 to 10 % of the Ni-PT dissociation, while more than 90 % of the polyanions stayed intact after the catalytic HER cycle. This partial degradation under catalytic conditions have been reported before for similar compounds.[4] Nevertheless, considering the effectiveness of the PS reloading tests in **Figure S50**, the observed Ni-PT degradation seems insignificant compared to the effect of sensitizer instability.

13.2 Post-catalytic precipitation of $TBA_{13}Na_8$-**{$Ni_{12}W_{30}$}** and $TBA_{13}Na_8$-**{$Ni_{12}W_{27}$}**

The photocatalytic reaction was carried out with 100 µM of the corresponding catalyst to obtain the POM in sufficient quantity for post-analysis. After 30 min of illumination, 0.5 mL of a [0.5 M] solution of cesium chloride in a mixture of acetonitrile/H_2O (2:1) was added resulting in the immediate formation of precipitates. The precipitate was centrifuged at 2500 rpm for 5 min and completeness of the precipitation was insured by adding a few drops of the cesium chloride solution to the supernatant. The precipitates were air dried and displayed to IR-spectroscopic analysis (**Figure S49**).

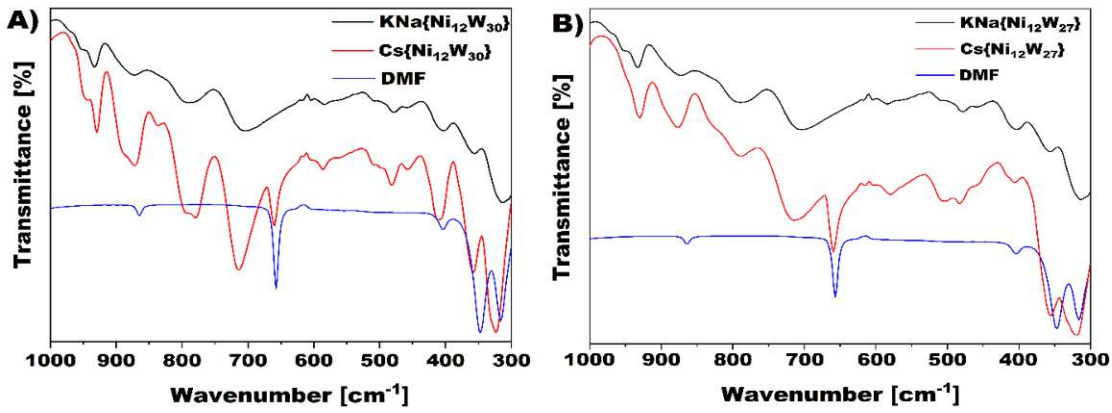

Figure S49. ATR-IR spectra showing the superimposed tungsten fingerprint areas (1000-300 cm^{-1}) of **A)** $K_{11}Na_{10}$-**{$Ni_{12}W_{30}$}** and the precipitated cesium salt Cs**{$Ni_{12}W_{30}$}** as well as **B)** $K_{14}Na_7$-**{$Ni_{12}W_{27}$}** and the precipitated cesium salt Cs**{$Ni_{12}W_{27}$}**. A dominant band at ~660 cm^{-}

[1] in the precipitated Cs-salts arises from residual DMF as shown by the IR spectrum of pure DMF.

13.3 Reloading experiments

To investigate the recyclability of $TBA_{13}Na_8$-**{$Ni_{12}W_{27}$}** and $TBA_{13}Na_8$-**{$Ni_{12}W_{30}$}**, a solution containing $[Ir(ppy)_2(dtbbpy)]^+$ photosensitizer (0.2 mM), TEOA proton donor (0.25 M), and the corresponding POT-WRC (20 µM) in 2 mL of 11:33:4 CH_3CN/DMF/H_2O solvent mixture was irradiated and the H_2 evolution was followed by GC until saturation was reached, indicated by a plateau. The reaction solution was reloaded with 100 µL of a freshly prepared solution of $[Ir(ppy)_2(dtbbpy)]^+$ photosensitizer (3.99 mM) in acetonitrile, 80 µL H_2O and 40 µL TEOA to yield 2.22 mL of a reloaded reaction mixture with 180 µM $[Ir(ppy)_2(dtbbpy)]^+$ photosensitizer, ~137 mM TEOA and 18 µM POT, thereby resembling the initial POT/PS molar ratios of the first reaction cycle. Subsequently, sealing of the reloaded reaction mixture, de-gassing and irradiation initiated the second reaction cycle (**Figure S50**).

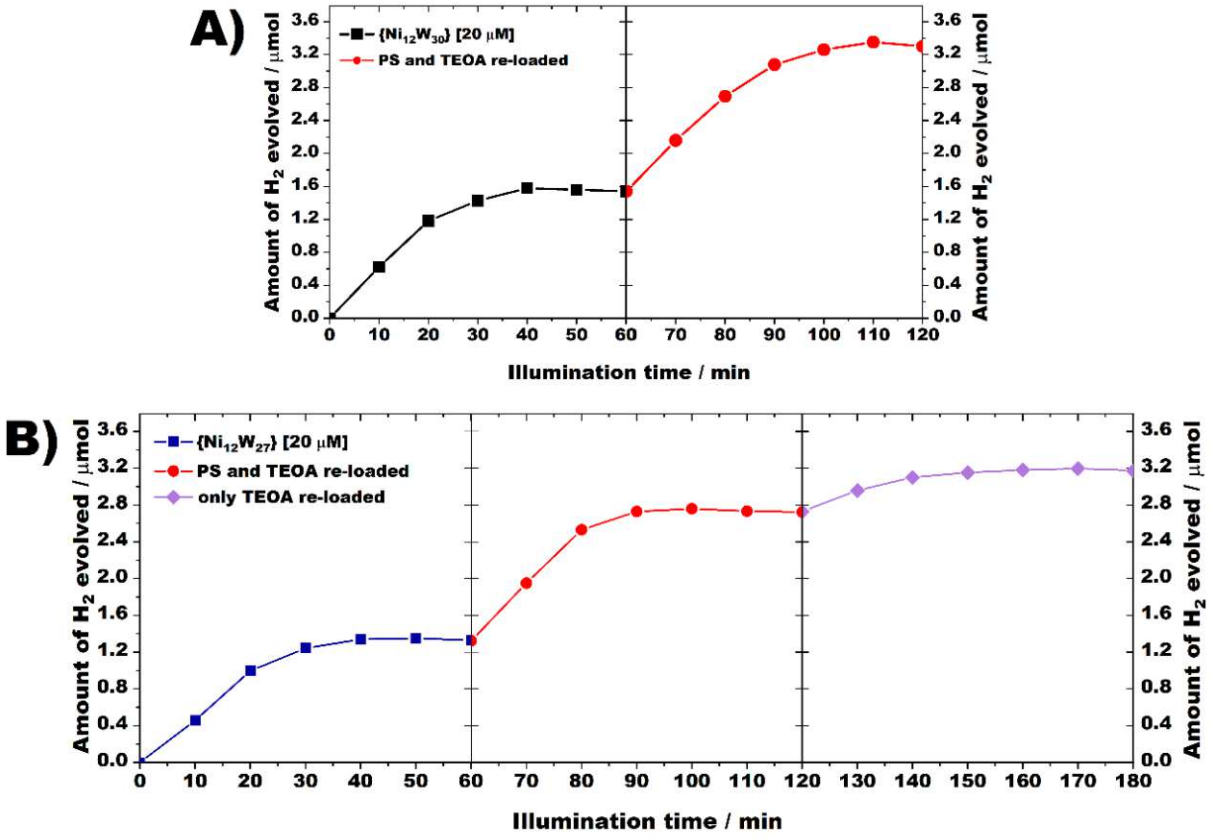

Figure S50. Re-loading experiments aiming to reveal the impact of catalytic solution components on HER performance. For 20 µM **(A)** $TBA_{13}Na_8$-**{$Ni_{12}W_{30}$}** and **(B)** $TBA_{13}Na_8$-**{$Ni_{12}W_{27}$}** after the first 60 min HER cycle (left panels), the reaction volumes were re-charged with a photosensitizer/TEOA/CH_3CN/DMF/water solution (as described above). After degassing, the second photocatalytic run (red curves) yielded significant H_2 evolution close to that of the first HER cycle for both compounds. When only TEOA was re-loaded (lila curve in **B)**, the amount of generated H_2 only accounted to around a quarter of the original activity value.

13.4 Total X-ray fluorescence (TXRF) experiments

Following the post-catalytic precipitation experiments (see subsection 13.1. Post-catalytic precipitation of $TBA_{13}Na_8$-**{$Ni_{12}W_{30}$}** and $TBA_{13}Na_8$-**{$Ni_{12}W_{27}$}**), TXRF analyses of the Ni and W contents present in the isolated supernatants of the corresponding **Ni-PT** solutions were conducted to elucidate on potential leaching and provide a quantitative assessment of the **Ni-PT**s' post-catalytic stability (see General

Information section *X-ray fluorescence*). The TXRF results are summarized in the following **Table S15**: The detected Ni/W contents before (**2**, in ppm) and after HER cycle (**4**, in ppm) were evaluated with regard to the theoretical amounts of Ni/W in case complete **Ni-PT** dissociation/decomposition would take place (**1**, in ppm). The part of the **Ni-PT** that underwent dissociation/leaching before (**3**, in %) and after the HER cycle (**5**, in %) provides a quantitative measure for PT stability. Expressing the Ni/W amounts found by TXRF in % (consideration of mol. % or wt. % would give identical results) of the total amounts of Ni/W present in the original catalytic solutions allows to evaluate instability of the **Ni-PT**s under the turnover condition.

Results. A detectable amount of Ni and W could be measured in the supernatants before photocatalysis (3.1% Ni and 5.4% W for $TBA_{13}Na_8$-**{$Ni_{12}W_{27}$}**; 4.7% Ni and 4.5% W for $TBA_{13}Na_8$-**{$Ni_{12}W_{30}$}**). Considering the precatalytic stability experiments (see sections 8 Cyclic Voltammetry and 9 UV-vis spectroscopy), which suggested long-term stability of both **Ni-PT**s, the observed Ni- and W contents in the solution before HER indicate incomplete precipitation of the anions during the extraction. Hence, the observed pre-catalytic Ni/W contents (**3**, in %) were subtracted from the determined post-catalytic contents (**5**, in %) to assess for the degree of **Ni-PT** leaching/decomposition (**6**, in %). **Table S15** shows (see column **6**) contents of 6.5% for Ni and 10.3% for W for $TBA_{13}Na_8$-**{$Ni_{12}W_{27}$}** as well as 5.0% for Ni and 3.6% for W for $TBA_{13}Na_8$-**{$Ni_{12}W_{30}$}** indicating that not more than ~10% of the Ni/W was leached over the course of the HER cycle. This implies that ~90 % of the polyanions stayed intact allowing for the long-term photocatalytic stability shown in **Figure S50A**.

Table S15. Summary of the TXRF results for $TBA_{13}Na_8$-**{$Ni_{12}W_{27}$}** and $TBA_{13}Na_8$-**{$Ni_{12}W_{30}$}**.

Ni-PT	detected contents	1 [ppm]	2 [ppm]	3 [%]	4 [ppm]	5 [%]	6 [%]
{$Ni_{12}W_{27}$}	*Ni*	*12.83*	*0.3975 ± 0.176*	*3.1*	*1.2295 ± 0.193*	*9.6%*	***6.5***
	W	*90.45*	*4.902 ± 0.442*	*5.4*	*14.1605 ± 0.571*	*15.7%*	***10.3***
{$Ni_{12}W_{30}$}	*Ni*	*12.83*	*0.5985 ± 0.108*	*4.7*	*1.239 ± 0.179*	*9.7%*	***5.0***
	W	*100.50*	*4.4725 ± 0.269*	*4.5*	*8.1145 ± 0.47*	*8.1%*	***3.6***

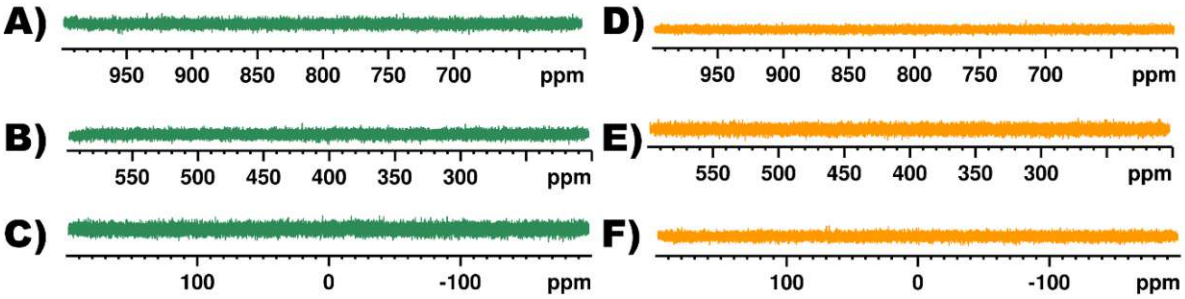

Figure S51. ^{31}P NMR spectra of $TBA_{13}Na_8$-**{$Ni_{12}W_{30}$}** in the range from 1000 to -200 ppm (**A** – **C**) and $TBA_{13}Na_8$-**{$Ni_{12}W_{27}$}** from 1000 to -200 ppm (**D** – **F**). The absence of signals can be attributed to the presence of paramagnetic Ni(II) and the comparably low number of incorporated P centers.

3. Photoluminescence (PL) emission spectroscopy

To explore the photocatalytic mechanism of hydrogen evolution reaction (HER), and to understand the electron transfer kinetics between the reaction solution components, photoluminescence (PL) emission spectroscopy was employed. The PL properties of $[Ir(ppy)_2(dtbbpy)]^+$ in N_2-deaerated CH_3CN:DMF:H_2O (11:33:4) solution were observed using a light excitation at 445 nm. **Figure S52** demonstrates that the photosensitizer's PL emission is quenched by TEOA, $TBA_{13}Na_8$-**{$Ni_{12}W_{30}$}** and $TBA_{13}Na_8$-**{$Ni_{12}W_{27}$}** in a linear Stern–Volmer behavior depending on the quencher's concentrations (**Figure S52**).

The linear fitting of the Stern-Volmer plot demonstrates that the rate constant for reductive quenching by TEOA is deduced to be 2.7 x 10^7 M^{-1} s^{-1}, whereas rate constants of 8.9 x 10^9 M^{-1} s^{-1} ($TBA_{13}Na_8$-**{$Ni_{12}W_{27}$}**) and 13.2 x 10^9 M^{-1} s^{-1} ($TBA_{13}Na_8$-**{$Ni_{12}W_{30}$}**) were calculated for the oxidative quenching by the corresponding Ni-PT suggesting that $[Ir(ppy)_2(dtbbpy)]^{+*}$ can undergo both reductive and oxidative quenching if TEOA and the corresponding Ni-PT are present in equimolar concentrations (**Scheme S1**). Considering the 12.5 – fold higher concentration of TEOA (250 µM) as compared to the highest investigated Ni-PT concentration (20 µM) under turnover conditions, a reductive quenching mechanism is proposed for the investigated reaction system. This conclusion is further supported by time-resolved PL experiments allowing to explore the decay kinetics of $[Ir(ppy)_2(dtbbpy)]^{+*}$. The PL decay of $[Ir(ppy)_2(dtbbpy)]^+$ fitted using a biexponential function gives an excited state lifetime of ~117 ns, which decreases in the presence of TEOA, $TBA_{13}Na_8$-**{$Ni_{12}W_{27}$}** and $TBA_{13}Na_8$-**{$Ni_{12}W_{30}$}** to yield lifetimes of 70.4, 107.6 and 108.1 ns, respectively, further illustrating that TEOA accelerates the quenching kinetics of $[Ir(ppy)_2(dtbbpy)]^+$ most effectively out of the investigated quenchers and additionally supporting the proposed reductive quenching pathway.

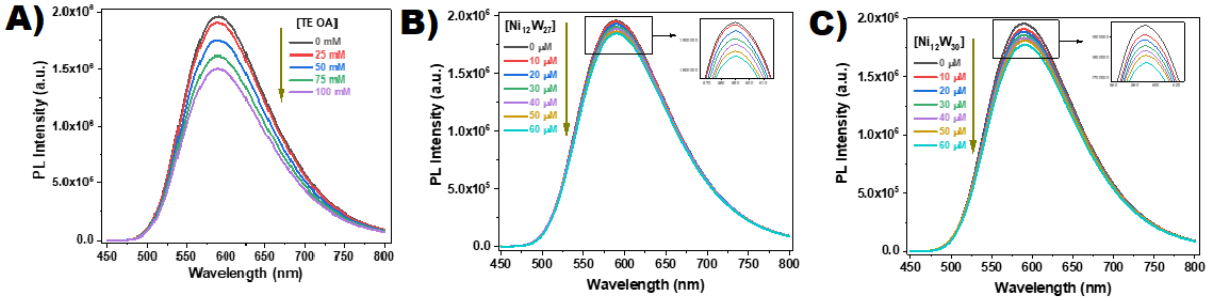

Figure S52. PL emission of $[Ir(ppy)_2(dtbbpy)]^+$ (0.2 mM) excited at 445 nm with the addition of different amounts of **A)** TEOA (0-100 mM), **B)** $TBA_{13}Na_8$-**{$Ni_{12}W_{27}$}** (0-60 µM) and **C)** $TBA_{13}Na_8$-**{$Ni_{12}W_{30}$}** (0-60 µM). K_q values calculated from linear fitting of Stern-Volmer plots are (**A**) 2.7 x 10^7 M^{-1} s^{-1}, (**B**) 8.9 x 10^9 M^{-1} s^{-1} and (**C**) 13.2 x 10^9 M^{-1} s^{-1}, respectively (**Figure S53**).

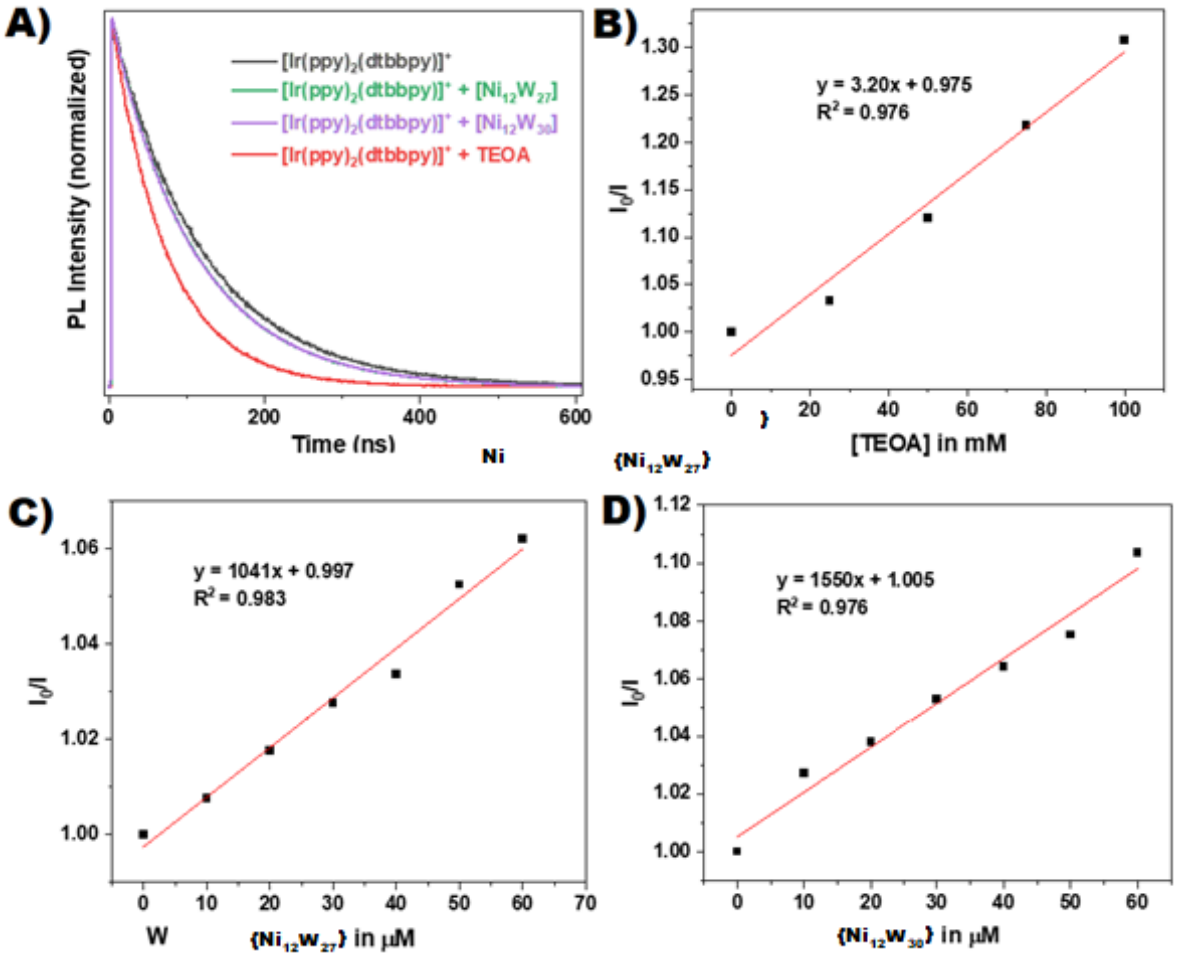

Figure S53. Superimposed time-resolved PL spectra of **A)** $[Ir(ppy)_2(dtbbpy)]^+$ [0.2 mM] without added quencher and after addition of TEOA [0.25 M], $TBA_{13}Na_8$-**{$Ni_{12}W_{27}$}** [20 µM], or $TBA_{13}Na_8$-**{$Ni_{12}W_{30}$}** [20 µM] detected at 590 nm, excited with a laser (λ = 377 nm); Stern-Volmer plots and linear fits for the emission of $[Ir(ppy)_2(dtbbpy)]^+$ [20 µM] quenched by **B)** TEOA, **C)** $TBA_{13}Na_8$-**{$Ni_{12}W_{27}$}** and **D)** $TBA_{13}Na_8$-**{$Ni_{12}W_{30}$}**.

Scheme S2. Proposed mechanism for visible-light-driven hydrogen evolution catalyzed by $TBA_{13}Na_8$-**{$Ni_{12}W_{27}$}** and $TBA_{13}Na_8$-**{$Ni_{12}W_{30}$}**. Upon visible-light driven excitation (**I.**) $[Ir(ppy)(dtbbpy)]^+$ is excited to $[Ir(ppy)(dtbbpy)]^{*+}$. The excited photosensitizer can undergo both reductive and oxidative quenching. Oxidative quenching: In a subsequent step, $[Ir(ppy)(dtbbpy)]^{*+}$ is oxidized to $[Ir(ppy)(dtbbpy)]^{2+}$ (**II.**) upon reduction of the corresponding Ni-PT, which is re-oxidized to the initial species by reducing H^+ and forming H_2 (**III.**). The oxidized photosensitizer $[Ir(ppy)(dtbbpy)]^{2+}$ is consecutively reduced to $[Ir(ppy)(dtbbpy)]^+$ by the sacrificial agent TEOA (**IV.**). Reductive quenching: The excited $[Ir(ppy)(dtbbpy)]^{*+}$ is quenched upon reduction by TEOA to give $[Ir(ppy)(dtbbpy)]$ (**II.**). In a consecutive **III.** step, $[Ir(ppy)(dtbbpy)]$ is re-oxidized to $[Ir(ppy)(dtbbpy)]^+$ by the corresponding Ni-PT which reduces H^+ to ultimately form H_2 (**IV.**).

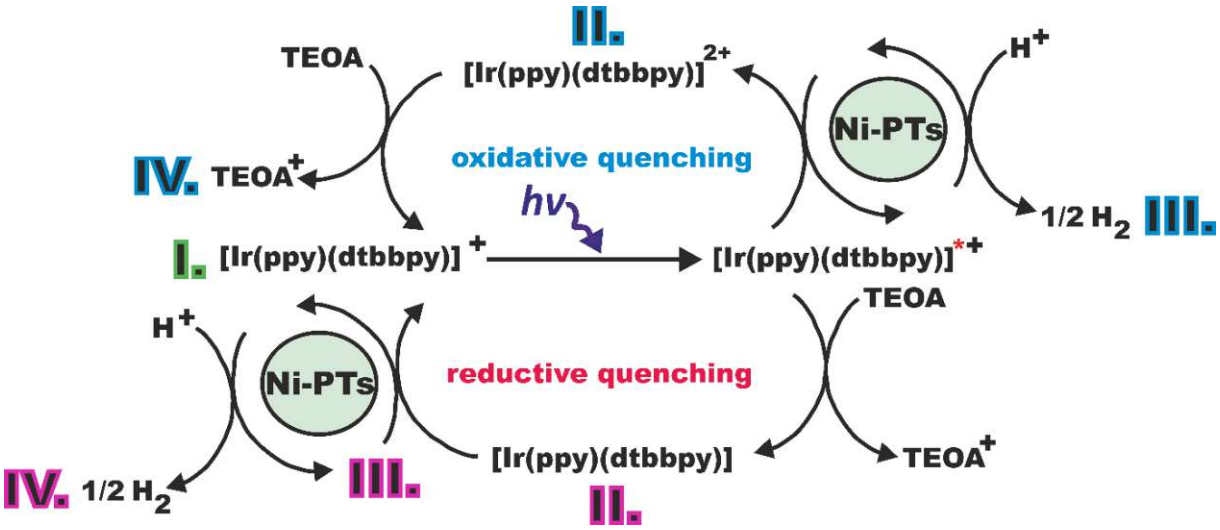

4. References

1 L.-H. Bi, B. Li, L.-X. Wu and Y.-Y. Bao, *Inorg. Chim. Acta*, 2009, **362**, 3309–3313.
2 A. Haider, B. S. Bassil, Z. Lin, X. Ma, P. J. Haferl, J. K. Bindra, J. Kinyon, G. Zhang, B. Keita, N. S. Dalal and U. Kortz, *Dalton Trans.*, 2021, **50**, 3923–3930.
3 E. Al-Sayed, S. P. Nandan, E. Tanuhadi, G. Giester, M. Arrigoni, G. K. H. Madsen, A. Cherevan, D. Eder and A. Rompel, *ChemSusChem*, 2021, **14**, 2529–2536.
4 a) J. J. Stracke and R. G. Finke, *ACS Catal.*, 2013, **3**, 1209–1219, b) S. J. Folkman and R. G. Finke, *ACS Catal.*, 2017, **7**, 7–16, c) S. J. Folkman, J. Soriano-Lopez, J. R. Galán-Mascarós and R. G. Finke, *J. Am. Chem. Soc.*, 2018, **140**, 12040–12055.

4.2.3 Article #3

"Surface Anchoring and Active Sites of $[Mo_3S_{13}]^{2-}$ Clusters as Co-Catalysts for Photocatalytic Hydrogen Evolution"

Samar Batool, Sreejith P. Nandan, Stephen Nagaraju Myakala, Ashwene Rajagopal, Jasmin S. Schubert, Pablo Ayala, Shaghayegh Naghdi, Hikaru Saito, Johannes Bernardi, Carsten Streb, Alexey Cherevan, Dominik Eder

ACS Catalysis, 2022, 12, 11, 6641–6650
DOI: https://doi.org/10.1021/acscatal.2c00972

My contributions as the first author of this work involve conceptualization of the cluster deposition, development of the synthetic methodology (cluster synthesis, attachment, post-treatments), and numerous investigations (FTIR, XPS, PL, HER) as well as data curation, plotting and writing of the article draft.

The corresponding Supplementary information of the article can be found on page 86.

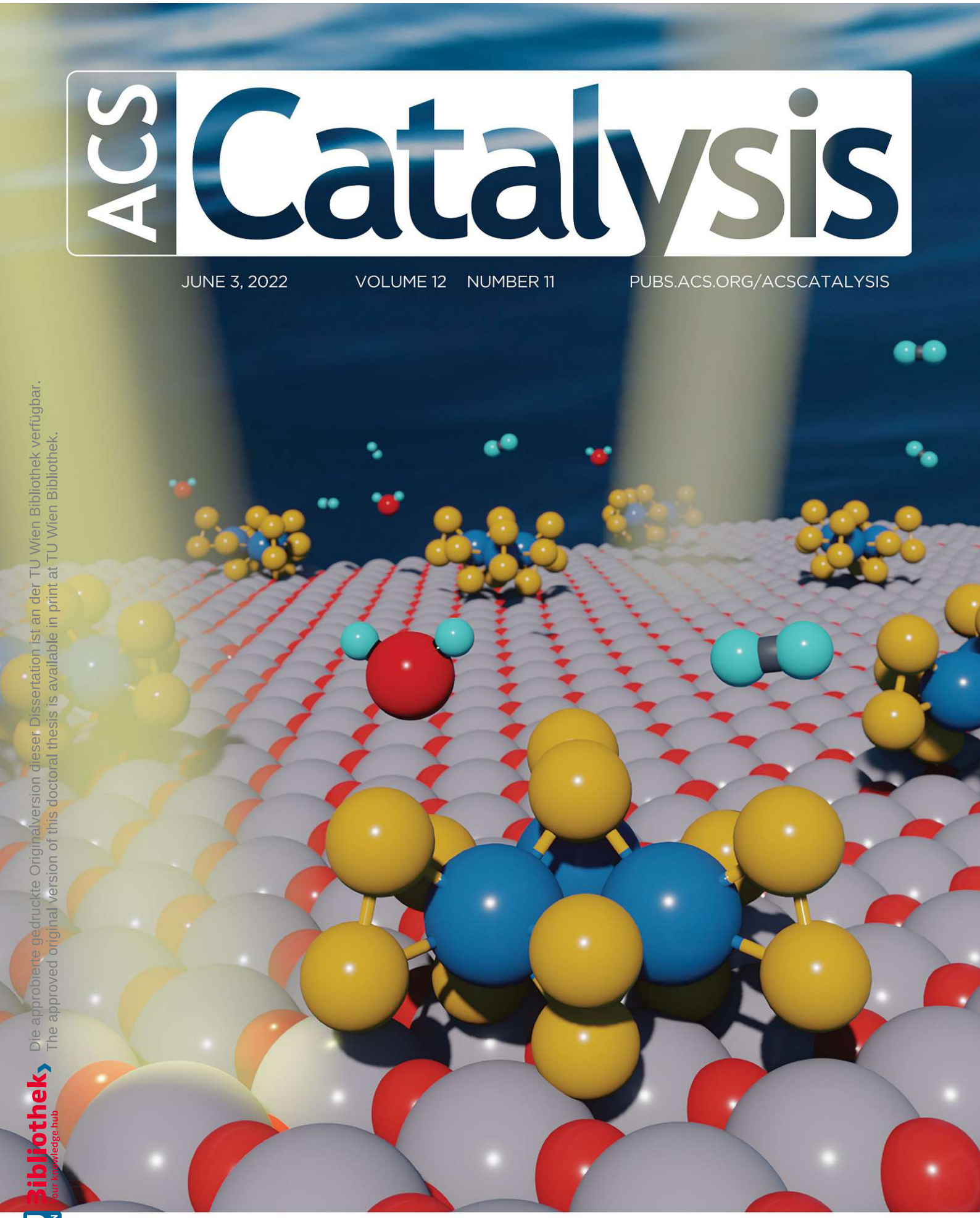

ACS Catalysis

JUNE 3, 2022 VOLUME 12 NUMBER 11 PUBS.ACS.ORG/ACSCATALYSIS

ACS Publications
Most Trusted. Most Cited. Most Read.
www.acs.org

ACS Catalysis

pubs.acs.org/acscatalysis Research Article

Surface Anchoring and Active Sites of $[Mo_3S_{13}]^{2-}$ Clusters as Co-Catalysts for Photocatalytic Hydrogen Evolution

Samar Batool,[⊥] Sreejith P. Nandan,[⊥] Stephen Nagaraju Myakala, Ashwene Rajagopal, Jasmin S. Schubert, Pablo Ayala, Shaghayegh Naghdi, Hikaru Saito, Johannes Bernardi, Carsten Streb, Alexey Cherevan,* and Dominik Eder

Cite This: *ACS Catal.* 2022, 12, 6641−6650 Read Online

ACCESS | Metrics & More | Article Recommendations | Supporting Information

ABSTRACT: Achieving light-driven splitting of water with high efficiency remains a challenging task on the way to solar fuel exploration. In this work, to combine the advantages of heterogeneous and homogeneous photosystems, we covalently anchor noble-metal- and carbon-free thiomolybdate $[Mo_3S_{13}]^{2-}$ clusters onto photoactive metal oxide supports to act as molecular co-catalysts for photocatalytic water splitting. We demonstrate that strong and surface-limited binding of the $[Mo_3S_{13}]^{2-}$ to the oxide surfaces takes place. The attachment involves the loss of the majority of the terminal S_2^{2-} groups, upon which Mo−O−Ti bonds with the hydroxylated TiO_2 surface are established. The heterogenized $[Mo_3S_{13}]^{2-}$ clusters are active and stable co-catalysts for the light-driven hydrogen evolution reaction (HER) with performance close to the level of the benchmark Pt. Optimal HER rates are achieved for 2 wt % cluster loadings, which we relate to the accessibility of the TiO_2 surface required for efficient hole scavenging. We further elucidate the active HER sites by applying thermal post-treatments in air and N_2. Our data demonstrate the importance of the trinuclear core of the $[Mo_3S_{13}]^{2-}$ cluster and suggest bridging S_2^{2-} and vacant coordination sites at the Mo centers as likely HER active sites. This work provides a prime example for the successful heterogenization of an inorganic molecular cluster as a co-catalyst for light-driven HER and gives the incentive to explore other thio(oxo)metalates.

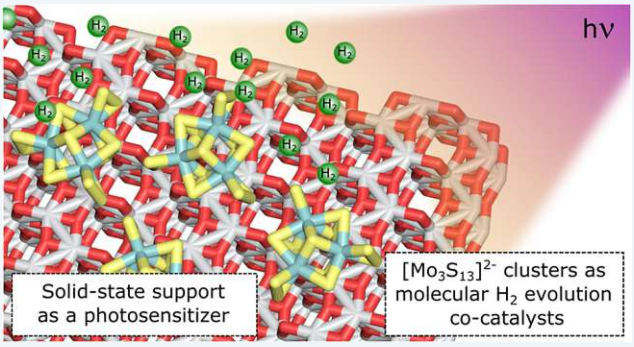

KEYWORDS: *thiometalates, metal sulfides, heterogenization, water splitting, photocatalysis*

1. INTRODUCTION

The ever-increasing energy consumption by our society leads to the unprecedented need for green and renewable fuels.[1] With its high energy density, hydrogen can be seen as a suitable alternative to gasoline and natural gas;[2] however, still today it is mostly generated from fossil fuels by steam reforming. Since the ratification of the Paris Agreement, alternative methods of hydrogen generation from water have attracted unprecedented attention including those through electrolysis using solar or nuclear power (*i.e.*, yellow and pink hydrogen). Among others, photocatalysis is seen as an ultimate sustainable solution that allows direct generation of hydrogen from renewable sources, such as water and sunlight. However, the efficiencies of contemporary heterogeneous photocatalytic systems are still far from the level to contribute substantially to the world energy demand.[3] One important issue that requires urgent attention is the design of earth-abundant and high-performance co-catalyst able to facilitate the desired redox reaction at the photocatalyst surface.

Among various alternatives to noble-metal-based hydrogen evolution reaction (HER) catalytic systems,[4,5] transition-metal chalcogenides—especially those from the MoS_2 family—have shown excellent promise for electrochemical H_2 production due to the presence of suitable adsorption and catalytic sites.[6] After the realization that the basal planes of MoS_2 are mostly inactive toward HER,[7−9] a class of molecular thiomolybdate clusters[10,11] that mimic the edge sites of MoS_2 has gained interest for the applications in energy conversion. Over the past decade, $[Mo_3S_4]^{4+}$,[12,13] $[Mo_3S_{13}]^{2-}$,[14−16] $[Mo_2S_{12}]^{2-}$,[17] and their analogues[18−20] have demonstrated exceptional electrochemical H_2 generation (in terms of stability and low overpotentials) associated with the presence of abundant and accessible sulfur sites in their molecular structure. Compared to typical inorganic catalysts reported elsewhere,[21] such

Received: February 24, 2022
Revised: March 31, 2022
Published: May 20, 2022

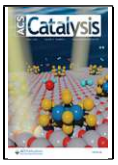

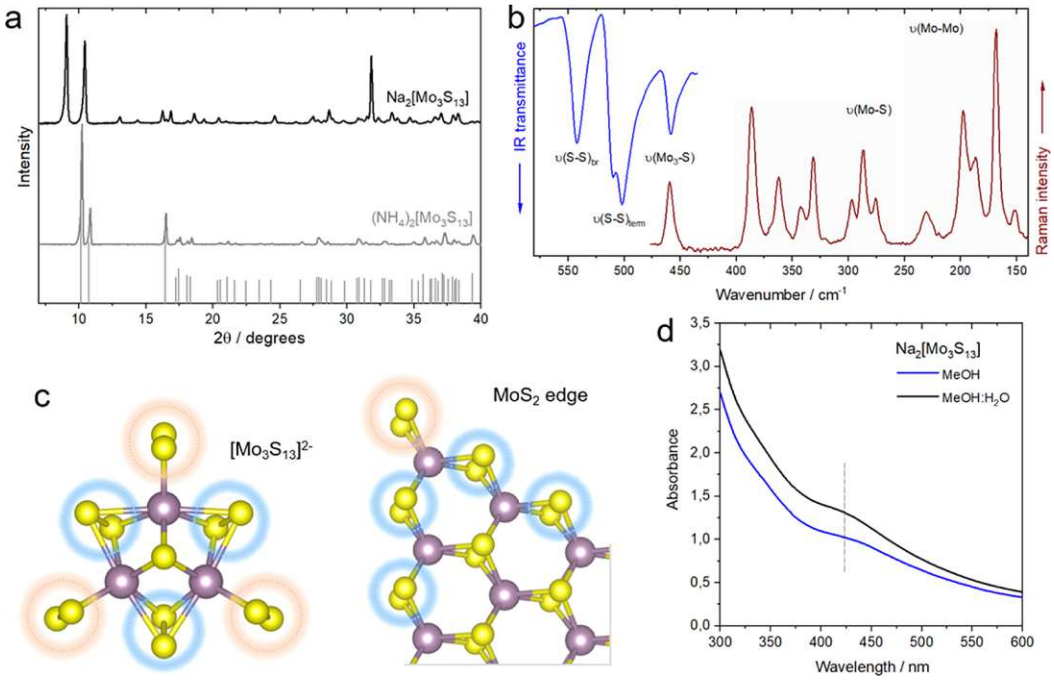

Figure 1. Cluster structure. (a) Powder XRD pattern of the $Na_2[Mo_3S_{13}]$ and $(NH_4)_2[Mo_3S_{13}]$ along with the ICDD 04-021-7028 reference pattern of the ammonium salt, (b) overlayed ATR-FTIR and Raman spectra of the $Na_2[Mo_3S_{13}]$ powder featuring characteristic molecular vibrations and the corresponding ranges, (c) molecular model of the $[Mo_3S_{13}]^{2-}$ compared to the edge structure of the MoS_2 sheet, similar bonding motifs are highlighted; and (d) UV−Vis absorption spectrum of the 0.025 mM $Na_2[Mo_3S_{13}]$ solution in water and water/methanol featuring a characteristic absorption band.

clusters feature well-defined molecular structures, compositions, and geometries, which may further allow for in-depth studies and understanding of the active sites, reaction mechanisms, and dynamic nature of the (photo)catalytic processes.[22] The implementation of these clusters in photocatalytic applications has so far been limited to several examples. On one hand, parallel to each other, two groups unraveled activity of $[Mo_2S_{12}]^{2-}$ and $[Mo_3S_{13}]^{2-}$ toward HER under strictly homogeneous conditions, when photosensitized by a molecular $[Ru(bpy)_3]^{2+}$ dye.[23,24] On the other hand, two early studies have explored composites of $[Mo_3S_{13}]^{2-}$ on Bi_2WO_6 and TiO_2 for the application in light-driven degradation of methylene blue and acetone, respectively.[25,26] Only a few studies so far have employed $[Mo_3S_{13}]^{2-}$ as a dedicated HER co-catalyst in a combination with non-oxide supports,[27−29] however, mainly relying on weak electrostatic interactions between the two components. To the best of our knowledge, none of these studies present detailed insights into the support/cluster attachment modes, structural modifications and, most importantly, the catalytic sites of these HER-relevant clusters after immobilization. Beside this, in light of the most recent record-breaking solar-to-hydrogen conversion efficiencies achieved on oxide-based semiconductors,[30−32] exploration of the thiomolybdate−oxide interface and binding constitutes a highly relevant yet underexplored research subject.

Motivated by these factors, here we construct and investigate a set of promising earth-abundant photocatalysts comprising various photoactive oxide supports and $[Mo_3S_{13}]^{2-}$ as a model HER co-catalyst. We show that the clusters undergo strong and irreversible covalent binding to the model TiO_2 surface *via* Mo−O−Ti bond formation with the surface-hydroxyl groups, and that this surface anchoring is limited to monolayer formation and involves oligomerization of the cluster cores at high $[Mo_3S_{13}]^{2-}$ surface density. We demonstrate a stable photocatalytic performance of the heterogenized $[Mo_3S_{13}]^{2-}$ toward HER as a function of the loading with an optimal value of around 2 wt %, unravel factors limiting the performance at higher $[Mo_3S_{13}]^{2-}$ coverage, and elaborate on the active state of the $[Mo_3S_{13}]^{2-}$ under turnover conditions. Finally, we investigate the impact of the cluster structure and integrity on photocatalytic activity by subjecting it to dedicated heat treatments. Our results show that both the molecular structure of the Mo_3 core and the presence of the bridging S_2^{2-} ligands are key factors, enabling these clusters to act as efficient HER co-catalysts.

2. RESULTS AND DISCUSSION

2.1. Cluster Preparation. $(NH_4)_2[Mo_3S_{13}]$ and $Na_2[Mo_3S_{13}]$ were synthesized following reported procedures with minor modifications (see details in the experimental section). Their molecular and crystal structures were verified by a combination of spectroscopic, elemental, and morphological analyses (see details in Supporting Information, Section 1). X-ray diffraction (XRD) patterns of the as-prepared thiomolybdate salts indicate high crystallinity compounds (Figure 1a) and match well with the database and the data reported previously.[29] SEM of the $Na_2[Mo_3S_{13}]$ shows rodlike crystals, typical of the sodium salt (Figure S1). ATR-FTIR spectroscopy reveals signature peaks centered at 542 cm^{-1}, 505 (510/501 doublet) cm^{-1}, and 458 cm^{-1}, corresponding to bridging, terminal, and apical sulfur ligands, respectively (Figures 1b and S2).[29] Complementary Raman spectra (Figure 1b) indicate additional peaks in 400−250 and 210−150 cm^{-1} ranges, which are characteristic of Mo−S and Mo−Mo vibrations of the $[Mo_3S_{13}]^{2-}$ anion.[33,34] The presence of Mo−Mo bonding is in line with the relatively short

https://doi.org/10.1021/acscatal.2c00972
ACS Catal. 2022, 12, 6641−6650

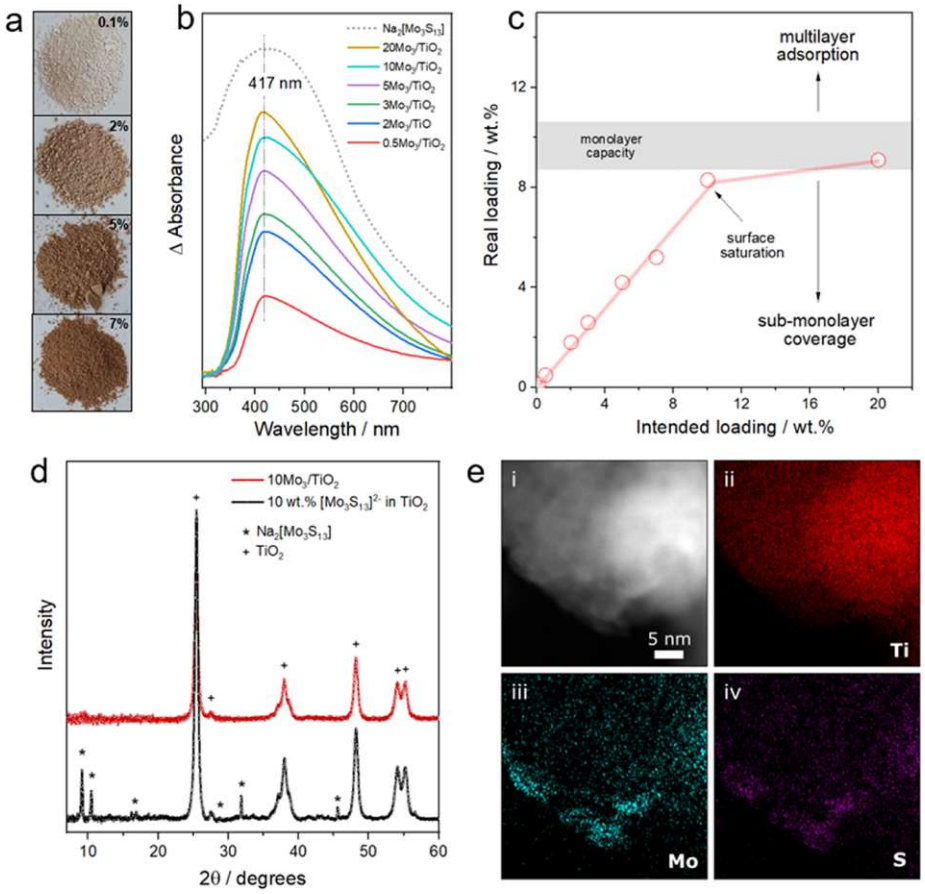

Figure 2. Cluster immobilization. (a) Digital photographs of the xMo$_3$/TiO$_2$ samples with 0.1, 2, 5, and 7 wt % cluster loadings, (b) difference DRS spectra of the Mo$_3$/TiO$_2$ composites with different cluster loadings (0.1−20 wt %) subtracted from TiO$_2$ absorption (see details in Supporting Information, methods) along with the DRS spectrum of Na$_2$[Mo$_3$S$_{13}$] (dashed line), (c) real *vs* intended loading plot depicting the range of theoretical monolayer capacity (see details in Supporting Information, Section 6), a linear increase between the real and intended loadings for loadings <9 wt % and its saturation at higher loadings. (d) XRD pattern of Mo$_3$/TiO$_2$ composites (10 wt % loading) and of a physical mixture of Na$_2$[Mo$_3$S$_{13}$] and TiO$_2$ (1:9 wt %), (e) EDS-derived elemental mappings of Ti (ii), Mo (iii), and S (iv) in an exemplary 3Mo$_3$/TiO$_2$ composite.

intermetallic distances in the cluster.[10] Overall, the data confirm the trinuclear nature of the $[Mo_3S_{13}]^{2-}$ and the presence of S^{2-}/S_2^{2-} ligands that make it structurally reminiscent of the MoS_2-bonding motif (Figure 1c).

Ion exchange from NH_4^+ to Na^+ (see the experimental section) renders the compound water and alcohol soluble (see details in Supporting Information, methods), which allows circumventing the high-boiling point dimethylformamide for further deposition and application in water splitting reactions. UV−vis spectra of Na$_2$[Mo$_3$S$_{13}$] aqueous solution (0.025 mM) reveal an absorption centered at 417 nm (Figure 1d) corresponding to that of the powdered sample evaluated by diffuse-reflectance spectroscopy (DRS) in the solid state (Figure S3). Based on the electronic structure of the ammonium salt[35] and the disappearance of this absorption band after oxidation (Figure S3), this characteristic absorption can be assigned to the $(S_2^{2-})_{term} \rightarrow$ d (Mo) ligand-to-metal charge transfer (LMCT) transitions within the Mo-(S_2) moiety.

2.2. Cluster Anchoring. After confirming the structure of the targeted Na$_2$[Mo$_3$S$_{13}$] compound, we proceeded with cluster immobilization onto the model photocatalytic TiO$_2$ surface following a wet-impregnation route (details in Experimental Section). A set of $[Mo_3S_{13}]/TiO_2$ composites further denoted as xMo$_3$/TiO$_2$ was prepared with x—nominal cluster loading—ranging from 0.1 to 20 wt %.

2.2.1. Loading and Dispersion. The color of the Mo$_3$/TiO$_2$ composite series corresponds well to the increasing mass fraction of the $[Mo_3S_{13}]^{2-}$ used for the synthesis (Figure 2a). DRS of the samples allows for a quantitative assessment and—after subtracting TiO$_2$ spectra—shows a gradual increase of the characteristic LMCT band for higher cluster loadings (Figure 2b). However, a certain non-linearity of the trend can be seen at higher nominal loading values (Figure S4), which suggests an adsorption-limited process. Since our synthetic protocol involves extensive washing steps to remove loosely attached clusters, total reflection X-ray fluorescence (TXRF) spectroscopy was used to unravel the real $[Mo_3S_{13}]^{2-}$ loadings in the composites.

The data (Table 1) reveal a close-to-linear increase in the cluster content (*i.e.*, real loadings correspond well to the nominal loadings) up to around 9 wt % at which saturation is achieved (Figure 2c). Based on the cluster footprint and surface area of the used TiO$_2$ (116 m^2/g, Figure S5), we estimate the theoretical adsorption capacity of our support (corresponding to a dense monolayer) to be around 9.6 wt % (see details in Supporting Information, Section 6). This value is close to that obtained experimentally, which strongly suggests that $[Mo_3S_{13}]^{2-}$ cluster adsorption follows a

https://doi.org/10.1021/acscatal.2c00972
ACS Catal. 2022, 12, 6641−6650

Table 1. Comparison between Intended (Nominal) $[Mo_3S_{13}]^{2-}$ Loadings and Those Found in the As-Prepared $[Mo_3S_{13}]/TiO_2$ Samples by Means of TXRF Quantification of Mo Content

nominal $[Mo_3S_{13}]^{2-}$ loadings (wt %)	real $[Mo_3S_{13}]^{2-}$ loadings (wt %)
0.1	0.14 ± 0.01
0.5	0.50 ± 0.05
2.0	1.78 ± 0.18
3.0	2.63 ± 0.26
5.0	4.22 ± 0.42
7.0	5.22 ± 0.52
10.0	8.30 ± 0.83
20.0	9.10 ± 0.91

monolayer formation and is thus limited by the surface area of the support. The complementary XRD pattern of the $10Mo_3/TiO_2$ powder shows no sign of $[Mo_3S_{13}]^{2-}$ compound (Figure 2d), which corroborates the molecular dispersion of the clusters on the support surface and excludes strong cluster aggregation (Figure S6 and Supporting Information, Section 7).

Elemental maps acquired on the nanoscale through energy-dispersive X-ray spectroscopy (EDS) further confirm the homogeneous dispersion of Mo and S elements over the TiO_2 surface (Figure 2e); however, some areas with locally higher Mo/S concentration can also be observed (Figure S7). Close examination of the Mo_3/TiO_2 composites with high-resolution transmission electron microscopy (HRTEM, Figure S8) reveals that while the majority of TiO_2 surfaces seem to be smooth and intact, the areas of higher Mo and S content display structural ordering (up to a few layers), which may correspond to a certain degree of stacking or polymerization of the $[Mo_3S_{13}]^{2-}$ clusters due to their proximity and dense packing at higher loading values.

2.2.2. Surface Structuring. Aberration-corrected high-angle annular dark-field scanning transmission electron microscopy (HAADF-STEM) was employed to provide an atomistic view on the surface-anchored clusters. Figure 3a shows a high-resolution micrograph of the $3Mo_3/TiO_2$ sample and reveals a collection of bright spots distributed over the edge of an individual support nanoparticle. Based on the Z-contrast difference between Ti and Mo, along with the observed spot size smaller than 1 Å, each spot likely corresponds to an individual Mo atom, wherein the Mo−Mo distance of 2.8 Å and less (due to the tilted position of the clusters on the surface) could be measured, in line with that within the $[Mo_3S_{13}]^{2-}$ cluster core (2.72 Å). Depending on the orientation of the supported clusters (insets are shown in Figure 3a), we can identify a number of triangular formations, which suggests the intact structure of the $\{Mo_3\}$ cluster cores upon binding, in line with their high structural stability.[36] Figure 3b shows a high-resolution image of an area with relatively higher Mo/S concentrations according to EDS signal. It reveals an assembly of bright spots organized in chain-like meta-structures, as highlighted by circled regions in the filtered

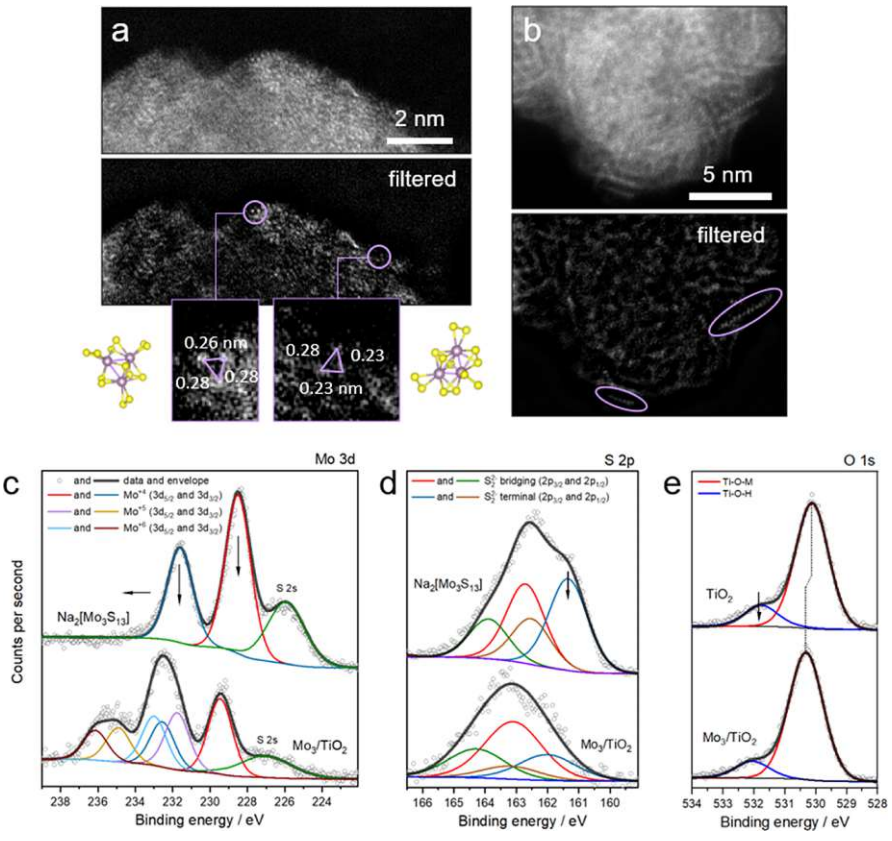

Figure 3. Cluster attachment. (a,b) HAADF-STEM images of $3Mo_3/TiO_2$ composites; Fourier filtered images are shown in the bottom panels; examples of detected $\{Mo_3\}$ cores are circled and magnified in the insets in (a), where they are compared with the model of tilted $[Mo_3S_{13}]^{2-}$ cluster cores, (c−e) XPS spectra of the $Na_2[Mo_3S_{13}]$ and the clusters after attachment to the TiO_2 surface (c) Mo 3d region, (d) S 2p, and (e) O 1s regions with corresponding fits; real $[Mo_3S_{13}]^{2-}$ loading is derived *via* TXRF to be 2 wt %.

https://doi.org/10.1021/acscatal.2c00972
ACS Catal. 2022, 12, 6641−6650

image. The estimated distance between the spots of 2.7 ± 0.4 Å strongly suggests that the chains correspond to oligomers made of Mo atoms originated from the {Mo_3} cores. Similar to the formation of two-dimensional MoS_x nanostructures from $[Mo_3S_{13}]^{2-}$ on graphite reported previously,[18] our HAADF-STEM data thus suggest that cluster polymerization—likely *via* partial loss and sharing of terminal disulfide ligands—takes place also in the case of the oxide support, however only at high cluster densities. The restructuring to chain-like structures shows the tendency of the clusters to organize in a highly disordered MoS_2-like motif similar to that described recently.[37]

2.2.3. Adsorption Model. To elucidate the specificity and strength of the cluster anchoring, we set up a series of impregnation experiments using concentrated $Na_2[Mo_3S_{13}]$ solutions and a range of alternative substrates including anatase TiO_2 with a significantly larger particle size and rutile TiO_2 and $BiVO_4$ powders (see details in Supporting Information, Section 10). Figure S9 plots real cluster loadings (quantified through TXRF) and surface areas of the supports used (Table S1). The trend reveals a strong dependency between the two parameters: while only 0.19 wt % of $[Mo_3S_{13}]^{2-}$ anchored onto low-surface area $BiVO_4$ (1.11 m^2/g), 5.14 wt % of $[Mo_3S_{13}]^{2-}$ could be accommodated by the surface of rutile nanopowder (27 m^2/g). Based on these data, the surface-limited $[Mo_3S_{13}]^{2-}$ deposition seems to be independent of the composition of the chosen oxides, which allows us to suggest that the formation of $[Mo_3S_{13}]^{2-}$ monolayer involves irreversible chemical bonding (chemisorption) with the support surface. The high strength and durability of the $[Mo_3S_{13}]^{2-}$ anchoring were further corroborated in a set of leaching experiments (see details in Supporting Information, Section 11), which overall strongly suggests that other semiconducting oxide-based materials will also act as suitable supports for the cluster deposition.

2.2.4. Binding Modes. The data conclusively show that the attachment of $[Mo_3S_{13}]^{2-}$ onto oxide surfaces is irreversible and surface-limited. For the series of Mo_3/TiO_2 composites based on anatase nanoparticles (116 m^2/g), the maximum achieved $[Mo_3S_{13}]^{2-}$ loadings of 9.1 wt % thus correspond to a dense monolayer coverage. Confirmation of the cluster integrity after immobilization *via* Raman/ATR-FTIR, however, renders challenging as only a weak set of characteristic Mo−S, S−S, and Mo−Mo vibrations could be seen in the 20Mo_3/TiO_2 sample, that is, with the highest cluster loading (Figure S10).

Therefore, we employed surface-sensitive X-ray photoelectron spectroscopy (XPS) to verify the cluster structure and elucidate their binding modes to the oxide support (see details in Supporting Information, methods). Quantification of the relative Mo-to-S ratios from survey spectra (Figure S11) reveals a strong relative loss of S (around 50%) upon anchoring (Tables S2 and S3), which provides a first hint for the binding scenario. Detailed analyses of the Mo 3d edge (Figure 3c) show that partial oxidation of Mo (original oxidation state +4) to a mixture of +5/+6 takes place, while the change in the S 2p edge profile (Figure 3d) implies that terminal disulfide ligands are mostly affected by the anchoring process. Considering the additional shift of Mo signals to higher binding energy, the overall data suggest that $[Mo_3S_{13}]^{2-}$ loses more labile terminal ligands and establishes a covalent binding with the strong electron-withdrawing hydroxyl groups of the oxide surface, likely forming Mo−O−Ti bonds. In line with this assumption, XPS data of the O 1s edge (Figure 3e) indicate a noticeable shift of the prime O signal (Ti−O−Ti) to higher binding energies (530.1 eV for TiO_2 to 530.3 eV for Mo_3/TiO_2) accompanied by a decrease in surface-hydroxyl groups by 5% (see details in Supporting Information, Section 13.2). Both observations corroborate the transformation of Ti−OH groups into Ti−O−Mo. Observed shifts in binding energy values further indicate that a considerable degree of electron density flows from the $[Mo_3S_{13}]^{2-}$ to the titania support, as expected from the anionic charge of the clusters (see details in Supporting Information, Section 13.2). Overall, XPS data show that terminal S_2^{2-} groups get replaced upon anchoring to allow for covalent binding with TiO_2. Although most of the clusters lose their original $[Mo_3S\text{-}(S_2)_3^{term}(S_2)_3^{bridg}]^{2-}$ composition, the integrity of their trinuclear {$Mo_3(\mu\text{-}S_2)_3$} cores can be confirmed.[38] A certain degree of oligomerization of the {Mo_3} cores *via* remaining terminal disulfides, however, cannot be excluded based on our STEM data.

2.3. Photocatalytic Performance. The set of the prepared xMo_3/TiO_2 composites allows us to evaluate the prospected co-catalytic function of the $[Mo_3S_{13}]^{2-}$ clusters toward HER and—considering the structural changes upon binding—can further provide relevant information regarding their active sites. Several reports have attempted to identify catalytic HER sites of thiometalate clusters by examining their electrocatalytic HER performance. Based on DFT calculations and experimental evidence, the groups of Joh,[16] Miras,[19] and Beyer[39,40] agree that terminal sulfides are the preferred sites for hydrogen adsorption and the most favorable catalytic sites for electrochemical HER. In contrast to this, the group of Artero observed a loss of terminal disulfides under the turnover conditions and thus suggested the unsaturated Mo centers to act as catalytic sites.[18] Joo and colleagues corroborated this idea and identified Mo-oxo species to play a key role in generating effective hydrogen adsorption sites.[20] Complementary to these, the group of Streb recently examined the photocatalytic performance of the $[Mo_3S_{13}]^{2-}$ under homogeneous conditions.[22] They revealed a dynamic structure of the cluster that involves the partial exchange of terminal disulfides with aqua ligands under turnover conditions. All three groups, however, agree that the formation Mo−H or Mo═O intermediate could be possible when Mo centers with undercoordinated sites are present in the system, which is the case for our attachment model.

2.3.1. Clusters as HER Co-Catalysts. The as-obtained short-term H_2 evolution profiles of the Mo_3/TiO_2 composites are shown in Figure S12a (experimental section for setup and reactor description and Figure S12b for reproducibility). Figure 4a plots the extracted HER rates against cluster loading (real values from Table 1 are considered) and surface area coverage (theoretical values assuming monolayer adsorption are considered). Interestingly, from the point of view of the proposed monolayer adsorption model, the HER performance of the Mo_3/TiO_2 photocatalysts follows a volcano trend: the rate of H_2 evolution peaks at around 2 wt % value and drops gradually for higher cluster loadings. We can exclude a significant contribution of the $[Mo_3S_{13}]^{2-}$ parasitic absorption[29] to the HER decline (Figure 2b) based on the sufficiently high light flux used in our experiments (Figure S13). However, this HER trend can be explained by considering the overall redox cycle: while higher $[Mo_3S_{13}]^{2-}$ loadings correspond to more active HER sites, they may diminish the extent of the available TiO_2/solution interface necessary for an efficient hole

https://doi.org/10.1021/acscatal.2c00972
ACS Catal. 2022, 12, 6641−6650

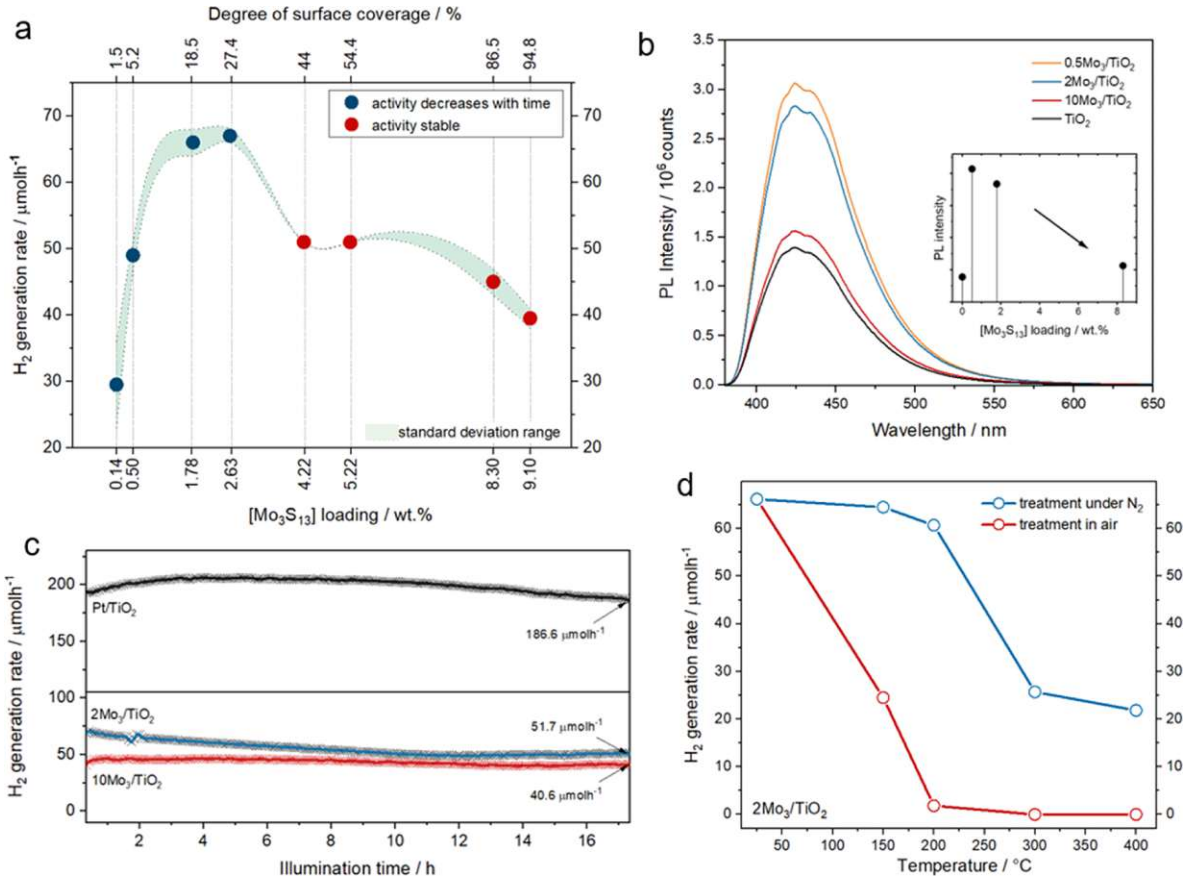

Figure 4. Photocatalytic performance and active sites. (a) Hydrogen evolution rates plotted against the $[Mo_3S_{13}]^{2-}$ cluster content and the degree of surface coverage in %; green area shows the standard deviation of hydrogen evolution rate values obtained from multiple measurements for each loading value, (b) PL spectra obtained from the catalyst solutions containing TA as OH trap after UV pre-illumination; inset shows intensities of the peak maximum (*ca.* 425 nm corresponding to hydroxyterephthalic acid emission) plotted against the real $[Mo_3S_{13}]^{2-}$ loadings, (c) long-term photocatalytic hydrogen evolution experiments of Mo_3/TiO_2 composites with 2 and 10 wt % loadings and their comparison with Pt/TiO_2 in terms of HER stability, (d) comparison of the hydrogen generation rate of Mo_3/TiO_2 composites heat-treated (25−400 °C) under air and the N_2 atmosphere; full HER profiles are shown in Figures S12 and S19.

scavenging.[41] A set of radical trapping photoluminescence (PL) experiments using terephthalic acid (TA) as a probe molecule were performed to elaborate on this point (see details in the experimental section). As depicted in Figure 4b, compared to neat TiO_2, we observe a significant increase in OH radical generation on Mo_3/TiO_2 samples, especially at lower cluster contents. This result corresponds to the enhanced separation of photogenerated charge carriers and manifests the ability of the thiomolybdate clusters to extract the electrons from the support, in line with their role as HER co-catalysts. The inset in Figure 4b, however, illustrates that higher cluster loadings (*i.e.*, $10Mo_3/TiO_2$) restrict the ability of Mo_3/TiO_2 to form OH radicals. As a consequence, the inefficient utilization of photogenerated holes leads to the acceleration of the recombination rates. These data validate our assumption and confirm that the extent of the available TiO_2/solution interface becomes a factor that limits the overall HER performance at higher cluster loading values.

In addition to the overall HER trend, Figure 4a reveals that the composites with the cluster content below 3 wt % show mild deactivation (*i.e.*, decrease in the H_2 evolution rate with time, Figure S12a) over the first 60 min of illumination, while those with the $[Mo_3S_{13}]^{2-}$ content above 3 wt % exhibit stable HER performance. This result hints toward a coverage-dependent stabilization of $\{Mo_3S_6\}$ cores and their active sites, which may be related to the oligomerization of the closely packed clusters under turnover conditions.[18] Lastly, both types of composites feature robust H_2 evolution over a long-term reaction (Figure 4c). The performance of $10Mo_3/TiO_2$ can even be compared to the benchmark HER photocatalyst couple of Pt on TiO_2 tested under identical conditions (see details in Supporting Information, methods), which manifests these thiomolybdate clusters as efficient and stable noble-metal-free HER co-catalysts. The catalytic nature of H_2 evolution can be further confirmed by comparing the number of H_2 molecules generated (0.88 mmol) with the number of Mo atoms present in the exemplary $2Mo_3/TiO_2$ photosystem (0.75 μmol).[42]

Post-catalytic characterization of the Mo_3/TiO_2 composites uncovers several key points. As revealed by EDS mapping (Figure S14a) and TXRF (Figure S14b) of the catalyst recovered after HER, we observe neither change in Mo distribution nor leaching of the Mo content from the TiO_2 surface. This is in strong agreement with the stable HER rates discussed before. Detailed XPS spectra, however, show that a mild transformation of the clusters upon turnover conditions takes place: following the oxidation of Mo centers and the loss of terminal S_2^{2-} upon cluster anchoring (see previous

https://doi.org/10.1021/acscatal.2c00972
ACS Catal. 2022, 12, 6641−6650

discussions), even more of the Mo^{4+} turns into $Mo^{5+/6+}$ (Figure S15a), while a part of bridging S_2^{2-} disappears from the structure (Figure S15b). Both changes can be indicative of the active HER state of the clusters and are in line with the dynamic exchange of the disulfide ligands with aqua/hydroxo ligands under catalytic conditions.[22]

2.3.2. Active Sites. In order to verify the impact of the molecular composition and structure of $[Mo_3S_{13}]^{2-}$ on its HER activity, we subjected the as-prepared Mo_3/TiO_2 photocatalysts to a series of heat treatments. Thermogravimetric analysis (TGA, Figure S16) performed in air and N_2 reveal that the clusters undergo structural changes in the temperature range of 250−450 °C. Earlier reports suggested that apical S^{2-} is most thermolabile,[36] while terminal and bridging disulfides require higher temperature for decomposition/restructuring.[16] Moreover, according to *in situ* XRD, heating of $[Mo_3S_{13}]^{2-}$ in N_2 yields 2H−MoS_2 (Figure S17),[43] while calcination under ambient air ultimately results in the formation of MoO_3 (Figure S18). Importantly, for the following discussion, heat treatments in air tend to degrade the clusters more rapidly (*i.e.*, at lower temperatures) due to facilitated ligand oxidation.

HER tests were performed on $2Mo_3/TiO_2$ after respective heat treatments in air and N_2 up to 400 °C (full HER profiles in Figure S19). Figure 4d shows that the H_2 evolution rates start to decline in both cases after a certain temperature is reached. Importantly, for the treatments in air, the activity drops sharply—close to zero—already at 200 °C, which is likely related to the oxidation (ligand cleavage) of the $\{Mo_3(\mu\text{-}S_2)_3\}$ cores facilitated by the O-rich support surface *via* the Mars-van Krevelen mechanism.[44,45] In the case of N_2-treated samples, the activity is unaffected at 200 °C but drops strongly—by 60%—when 300 °C treatment is applied. Both trends conclusively show that the molecular composition of the cluster and the presence of sulfur ligands in its original structure are crucial structural factors that allow for high HER performance.

In conjunction with our observation that the majority of terminal S_2^{2-} ligands tend to be displaced upon $[Mo_3S_{13}]^{2-}$ attachment, these activity trends correlate well with previous reports,[18,20,22] suggesting that both accessible Mo centers (either undercoordinated or oxo species) and bridging S_2^{2-} ligands constitute essential structural motifs, rendering these clusters as high-performance and stable HER co-catalysts.[46] The contribution of the remaining terminal S_2^{2-} as proton adsorption or catalytic HER sites can, however, not be entirely excluded considering their persistent presence in the Mo_3/TiO_2 catalyst before and after catalysis. Finally, in light of our post-catalytic studies, the active HER state of the $[Mo_3S_{13}]^{2-}$ formed under turnover conditions seem to involve a more complex and dynamic interplay between available Mo sites, partially replaced ligands, and oligomerized $\{Mo_3\}$ cores; dedicated operando studies will be required to unravel individual contributions of these factors.

3. CONCLUSIONS

In this contribution, we demonstrate the immobilization of an all-inorganic thiomolybdate $[Mo_3S_{13}]^{2-}$ cluster on various metal oxide surfaces and investigate its function as a co-catalyst for photocatalytic HER. The results indicate that the attachment of the $[Mo_3S_{13}]^{2-}$ on TiO_2 is strong and irreversible and that it follows monolayer adsorption, whereas the surface coverage is directly proportional to the cluster loadings. Elemental mappings confirm that the majority of the $[Mo_3S_{13}]^{2-}$ species distribute homogeneously over the support surface. STEM-HAADF images allow us to resolve individual $\{Mo_3\}$ cores attached to the surface and also indicate the formation of chain-like structures presumably made of oligomerized cluster cores. Detailed XPS analyses show that the attachment involves partial oxidation of Mo centers and partial loss of the terminal S_2^{2-} ligands, which we assign to the formation of covalent Ti−O−Mo bonds at the support−cluster interface. We further demonstrate stable, loading-depended HER performance of the prepared Mo_3/TiO_2 photocatalysis, which reaches an optimum at around 2−3 wt % cluster loading—value limited by the hole utilization efficiency. Post-catalytic studies confirm no leaching of the Mo species (in line with strong bonding) but strongly indicate a further milder transformation of the clusters upon turnover conditions involving ligand exchange. Finally, by subjecting our composites to stepwise thermal decomposition, we demonstrate that both the molecular structure of the Mo_3 cores and the presence of the bridging S_2^{2-} ligands in the parent structure are responsible for the excellent HER performance. This work serves as an important example of the implementation of $[Mo_3S_{13}]^{2-}$ clusters as co-catalysts for photocatalytic applications and provides insights into their active states and structures, which will be of interest to other molecular systems and applications. Exploration of visible-light active supports and other all-inorganic clusters such as polyoxometalates[47] is envisioned to develop tunable photosystems for efficient sunlight-driven generation of H_2 and other solar fuels.

4. EXPERIMENTAL SECTION

A detailed overview of the used chemicals, analytical instrumentation, characterization methods, supplementary figures, and discussions are provided in the Supporting Information. Synthetic protocols and photocatalytic activity measurements are detailed below.

4.1. Synthesis of $(NH_4)_2[Mo_3(\mu_3\text{-}S^{2-})(\mu,\eta^2\text{-}S_2^{2-})_3(\eta^2\text{-}S_2^{2-})_3]\cdot H_2O$. The precursor for the synthesis of $Na_2[Mo_3S_{13}]\cdot H_2O$ was prepared using a modified procedure reported by Müller *et al.*[48] A solution of $(NH_4)_2[Mo_7O_{24}]\cdot H_2O$ (3.2 mmol) was prepared in water (20 mL) in a round-bottom flask followed by the addition of $(NH_4)_2S_x$ (25 wt %, 120 mL). The resulting red-colored solution was heated at 96 °C for 5 days under continuous stirring. The dark red colored product was obtained by filtration and thoroughly washed with water, ethanol, carbon disulfide, and diethyl ether. The product was dried at 60 °C in the air (yield: 90%).

4.2. Synthesis of $Na_2[Mo_3(\mu_3\text{-}S^{2-})(\mu,\eta^2\text{-}S_2^{2-})_3(\eta^2\text{-}S_2^{2-})_3]\cdot H_2O$. The sodium salt was synthesized following a reported method by Weber *et al.*[33] Briefly, 250 mg of $(NH_4)_2[Mo_3S_{13}]\cdot H_2O$ was added to a 1% NaOH solution (40 mL) followed by stirring under vacuum for 2 h. The mixture was then filtered in 10% NaCl solution and kept for 12 h in order to precipitate out the desired $Na_2[Mo_3S_{13}]\cdot H_2O$ (yield: 70%).

4.3. Synthesis of $Na_2[Mo_3(\mu_3\text{-}S^{2-})(\mu,\eta^2\text{-}S_2^{2-})_3(\eta^2\text{-}S_2^{2-})_3]\cdot H_2O/TiO_2$ Composites. The $Na_2[Mo_3S_{13}]\cdot H_2O/TiO_2$ composites having different weight contents (0.1, 0.5, 2, 3, 5, 7, 10, and 20%) of thiomolybdate clusters were synthesized. TiO_2 powder was dispersed in MeOH (100 mg in 28 mL) by ultrasonication for 10 min. The clusters (amount corresponding to the nominal loading) were dissolved in methanol, added to the TiO_2 suspension, and again sonicated for 15 min. The mixture was then kept on stirring for 24 h to allow for

https://doi.org/10.1021/acscatal.2c00972
ACS Catal. 2022, 12, 6641−6650

adsorption, followed by filtration and repeated washing with methanol to remove unattached clusters and those attached loosely (*e.g.*, in a layer-by-layer fashion). Filtration and washing of the powders with lower intended cluster loadings (*e.g.*, below 10 wt % for TiO_2) resulted in colorless filtrates. Filtration of the powders with higher intended loadings (*e.g.*, above 10 wt % for TiO_2) gave colored filtrates, while washing was repeated until the filtrates turned colorless to ensure the removal of excess clusters. The final powders were dried at 60 °C and are denoted as $x Mo_3/TiO_2$ throughout the manuscript, where x stands for the nominal (intended) mass content of the clusters.

4.4. Photocatalytic Experiments. The hydrogen evolution experiments were carried out using a top-down irradiation gas-flow slurry type custom-built reactor (total volume of 100 mL) equipped with a monochromatic UV LED light source with an incident light intensity of 0.49 W centered at 365 ± 6 nm (196 mW/cm^2, Thorlabs SOLIS). In the reaction setup, 10 mg of the powdered photocatalyst was introduced into the reactor containing 40 mL of 1:1 vol % MeOH/H_2O mixture (activity *vs* catalyst mass curves are presented in Figure S13). The reaction mixture was dispersed evenly by ultrasonication for 10 s. During the experiment, the reactor was continuously purged with argon carrier gas at a flow rate of 30 mL min^{-1}, which is controlled by a mass flow controller (MCC-instruments); the reaction solution was stirred at 500 rpm. The gaseous H_2 was detected directly in the stream by an online gas analyzer (X-stream, Emerson Process Management) equipped with a thermal conductivity detector. H_2 concentrations were deduced based on a multilevel calibration. The temperature of the reactor was maintained at 15 °C using a water-cooling system (Lauda). In a single experiment, the reaction mixture was stirred for 20 min before starting the illumination to attain a stable signal baseline, followed by a 60 min light-on cycle and a 40 min resting in the dark. A typical H_2 evolution profile (*e.g.*, as shown in Figure S12) obtained with our flow reactor includes an "induction" period (increasing H_2 evolution rate during the first 5−10 min) that is due to the fact the H_2 gas first needs to fill the dead volume (*e.g.*, reactor volume and tubing volume) to reach the detector. After this "induction," H_2 evolution reaches a stable rate, which speaks for stable HER performance. In contrast, when the rate changes over time, (de)activation of the photocatalytic system can be deduced.[49,50] When the illumination is stopped, the signal returns to its baseline.

4.5. PL Measurements. The photocatalytic mechanism was investigated using radical-trapping PL emission spectroscopy employing TA as an OH radical scavenger following earlier reports.[51] In a single experiment, 1 mg/mL aqueous suspension of the catalyst (TiO_2 and Mo_3/TiO_2 composites) was prepared and diluted with 3×10^{-3} M TA solution in 0.01 M NaOH. The suspension was illuminated for 40 min with UV light (for conditions, see above), followed by centrifugation at 5600 rpm for 30 min to separate the catalyst from the solution. PL emission of this solution was probed with an excitation wavelength of 315 nm (see details in Supporting Information, methods). According to the method, photoexcited holes generated during the illumination of the photocatalyst suspensions form OH radicals at the catalyst/solution interface; the OH radicals in the solution can be next effectively scavenged by the TA molecules, resulting in the formation of 2-hydroxyterephthalic acid (TA-OH). As TA-OH is highly fluorescent, PL can be used to quantify the amount of so-generated OH radicals and thus can be used to assess the extent of electron−hole separation and the effectiveness of hole utilization.

■ ASSOCIATED CONTENT

Supporting Information

The Supporting Information is available free of charge at https://pubs.acs.org/doi/10.1021/acscatal.2c00972.

Extended experimental section, SEM images of $Na_2[Mo_3S_{13}]$, additional ATR-FTIR and DRS spectra, physisorption data, estimation of the theoretical surface coverage, extended XRD patterns and additional EDX maps and (S)TEM images of the Mo_3/TiO_2 samples, discussion of the alternative supports, cluster leaching experiments, Raman spectra, XPS data (quantification) along with the discussion of the cluster binding and interfacial charge transfer, photocatalytic data (HER profiles, reproducibility, and optimization), post-catalytic characterization of the Mo_3/TiO_2 photocatalysts (TXRF, EDS, and XPS), and thermal analyses of the $[Mo_3S_{13}]^{2-}$ salts (TGA, *in situ* XRD) (PDF)

■ AUTHOR INFORMATION

Corresponding Author

Alexey Cherevan − *Institute of Materials Chemistry, TU Wien, 1060 Vienna, Austria;* orcid.org/0000-0001-8934-6371; Email: alexey.cherevan@tuwien.ac.at

Authors

Samar Batool − *Institute of Materials Chemistry, TU Wien, 1060 Vienna, Austria;* orcid.org/0000-0003-0314-9903

Sreejith P. Nandan − *Institute of Materials Chemistry, TU Wien, 1060 Vienna, Austria;* orcid.org/0000-0002-1605-501X

Stephen Nagaraju Myakala − *Institute of Materials Chemistry, TU Wien, 1060 Vienna, Austria;* orcid.org/0000-0001-7234-6252

Ashwene Rajagopal − *Institute of Inorganic Chemistry I, Ulm University, 89081 Ulm, Germany*

Jasmin S. Schubert − *Institute of Materials Chemistry, TU Wien, 1060 Vienna, Austria;* orcid.org/0000-0002-1292-8485

Pablo Ayala − *Institute of Materials Chemistry, TU Wien, 1060 Vienna, Austria;* orcid.org/0000-0002-2569-4438

Shaghayegh Naghdi − *Institute of Materials Chemistry, TU Wien, 1060 Vienna, Austria*

Hikaru Saito − *Institute for Materials Chemistry and Engineering, Kyushu University, Kasuga, Fukuoka 816-8580, Japan;* orcid.org/0000-0001-9578-1433

Johannes Bernardi − *University Service Centre for Transmission Electron Microscopy (USTEM), TU Wien, 1040 Vienna, Austria*

Carsten Streb − *Institute of Inorganic Chemistry I, Ulm University, 89081 Ulm, Germany; Department of Chemistry, Johannes Gutenberg University Mainz, 55128 Mainz, Germany*

Dominik Eder − *Institute of Materials Chemistry, TU Wien, 1060 Vienna, Austria;* orcid.org/0000-0002-5395-564X

Complete contact information is available at: https://pubs.acs.org/10.1021/acscatal.2c00972

Author Contributions

⊥S.B. and S.P.N. contributed equally. Conceptualization: S.P.N. and A.C.; methodology: S.B., S.P.N., S.N.M., and A.C.; investigation: S.B., S.P.N., S.N.M., A.R., J.S.S., P.A., S.N., J.B., and H.S.; resources: C.S., A.C., and D.E.; data curation: S.B., S.P.N., and A.C.; writing—original draft preparation: S.B.; writing—review and editing: C.S., A.C., and D.E.; visualization, supervision, project administration, and funding acquisition: A.C. All authors have read and agreed to the published version of the manuscript.

Funding

This research was funded in whole, or in part, by the Austrian Science Fund (FWF) (grant number P32801-N). Open Access is funded by the Austrian Science Fund (FWF).

Notes

The authors declare no competing financial interest.

■ ACKNOWLEDGMENTS

The authors would like to acknowledge the facilities of the Technische Universität Wien (TU Wien) for technical support and fruitful discussions: X-Ray Center (XRC, especially Werner Artner); Analytical Instrumentation Center (AIC, especially Markus Sauer and Annette Foelske), Electron Microscopy Center (USTEM), and TU Wien Atominstitute. We are grateful to Georg Ramer and Bernhard Lendl for conducting and enabling Raman measurements and acknowledge Peter Weinberger for providing access to the IR spectrometer.

■ REFERENCES

(1) Welsby, D.; Price, J.; Pye, S.; Ekins, P. Unextractable fossil fuels in a 1.5 °C world. *Nature* **2021**, *597*, 230−234.
(2) Bičáková, O.; Straka, P. Production of Hydrogen from Renewable Resources and Its Effectiveness. *Int. J. Hydrogen Energy* **2012**, *37*, 11563−11578.
(3) Chen, S.; Takata, T.; Domen, K. Particulate Photocatalysts for Overall Water Splitting. *Nat. Rev. Mater.* **2017**, *2*, 1−17.
(4) Conway, B. E.; Tilak, B. V. Interfacial Processes Involving Electrocatalytic Evolution and Oxidation of H2, and the Role of Chemisorbed H. *Electrochim. Acta* **2002**, *47*, 3571−3594.
(5) Li, C.; Baek, J.-B. Recent Advances in Noble Metal (Pt, Ru, and Ir)-Based Electrocatalysts for Efficient Hydrogen Evolution Reaction. *ACS Omega* **2020**, *5*, 31−40.
(6) Chianelli, R. R.; Siadati, M. H.; De la Rosa, M. P.; Berhault, G.; Wilcoxon, J. P.; Bearden, R.; Abrams, B. L. Catalytic Properties of Single Layers of Transition Metal Sulfide Catalytic Materials. *Catal. Rev.* **2006**, *48*, 1−41.
(7) Raybaud, P.; Hafner, J.; Kresse, G.; Kasztelan, S.; Toulhoat, H. Ab Initio Study of the H2-H2S/MoS2 Gas-Solid Interface: The Nature of the Catalytically Active Sites. *J. Catal.* **2000**, *189*, 129−146.
(8) Hinnemann, B.; Moses, P. G.; Bonde, J.; Jørgensen, K. P.; Nielsen, J. H.; Horch, S.; Chorkendorff, I.; Nørskov, J. K. Biomimetic Hydrogen Evolution: MoS2 Nanoparticles as Catalyst for Hydrogen Evolution. *J. Am. Chem. Soc.* **2005**, *127*, 5308−5309.
(9) Jaramillo, T. F.; Jørgensen, K. P.; Bonde, J.; Nielsen, J. H.; Horch, S.; Chorkendorff, I. Identification of Active Edge Sites for Electrochemical H 2 Evolution from MoS 2 Nanocatalysts. *Science* **2007**, *317*, 100−102.
(10) Müller, A.; Jostes, R.; Cotton, F. A. Trinuclear Clusters of the Early Transition Elements. *Angew. Chem., Int. Ed. Engl.* **1980**, *19*, 875−882.
(11) Müller, A.; Diemann, E.; Jostes, R.; Bögge, H. Transition Metal Thiometalates: Properties and Significance in Complex and Bioinorganic Chemistry. *Angew. Chem., Int. Ed. Engl.* **1981**, *20*, 934−955.
(12) Jaramillo, T. F.; Bonde, J.; Zhang, J.; Ooi, B.-L.; Andersson, K.; Ulstrup, J.; Chorkendorff, I. Hydrogen Evolution on Supported Incomplete Cubane-Type [Mo3S4]4+ Electrocatalysts. *J. Phys. Chem. C* **2008**, *112*, 17492−17498.
(13) Hou, Y.; Abrams, B. L.; Vesborg, P. C. K.; Björketun, M. E.; Herbst, K.; Bech, L.; Setti, A. M.; Damsgaard, C. D.; Pedersen, T.; Hansen, O.; Rossmeisl, J.; Dahl, S.; Nørskov, J. K.; Chorkendorff, I. Bioinspired Molecular Co-Catalysts Bonded to a Silicon Photocathode for Solar Hydrogen Evolution. *Nat. Mater.* **2011**, *10*, 434−438.
(14) Kibsgaard, J.; Jaramillo, T. F.; Besenbacher, F. Building an appropriate active-site motif into a hydrogen-evolution catalyst with thiomolybdate [Mo3S13]2− clusters. *Nat. Chem.* **2014**, *6*, 248−253.
(15) Recatalá, D.; Llusar, R.; Gushchin, A. L.; Kozlova, E. A.; Laricheva, Y. A.; Abramov, P. A.; Sokolov, M. N.; Gómez, R.; Lana-Villarreal, T. Photogeneration of Hydrogen from Water by Hybrid Molybdenum Sulfide Clusters Immobilized on Titania. *ChemSusChem* **2015**, *8*, 148−157.
(16) Lee, C.-H.; Lee, S.; Lee, Y.-K.; Jung, Y. C.; Ko, Y.-I.; Lee, D. C.; Joh, H.-I. Understanding the Origin of Formation and Active Sites for Thiomolybdate [Mo3S13]2- Clusters as Hydrogen Evolution Catalyst through the Selective Control of Sulfur Atoms. *ACS Catal.* **2018**, *8*, 5221−5227.
(17) Huang, Z.; Luo, W.; Ma, L.; Yu, M.; Ren, X.; He, M.; Polen, S.; Click, K.; Garrett, B.; Lu, J.; Amine, K.; Hadad, C.; Chen, W.; Asthagiri, A.; Wu, Y. Dimeric [Mo2S12]2−Cluster: A Molecular Analogue of MoS2Edges for Superior Hydrogen-Evolution Electrocatalysis. *Angew. Chem., Int. Ed.* **2015**, *54*, 15181−15185.
(18) Tran, P. D.; Tran, T. V.; Orio, M.; Torelli, S.; Truong, Q. D.; Nayuki, K.; Sasaki, Y.; Chiam, S. Y.; Yi, R.; Honma, I.; Barber, J.; Artero, V. Coordination Polymer Structure and Revisited Hydrogen Evolution Catalytic Mechanism for Amorphous Molybdenum Sulfide. *Nat. Mater.* **2016**, *15*, 640−646.
(19) McAllister, J.; Bandeira, N. A. G.; McGlynn, J. C.; Ganin, A. Y.; Song, Y.-F.; Bo, C.; Miras, H. N. Tuning and Mechanistic Insights of Metal Chalcogenide Molecular Catalysts for the Hydrogen-Evolution Reaction. *Nat. Commun.* **2019**, *10*, 370.
(20) Seo, B.; Jung, G. Y.; Lee, S. J.; Baek, D. S.; Sa, Y. J.; Ban, H. W.; Son, J. S.; Park, K.; Kwak, S. K.; Joo, S. H. Monomeric MoS42–Derived Polymeric Chains with Active Molecular Units for Efficient Hydrogen Evolution Reaction. *ACS Catal.* **2020**, *10*, 652−662.
(21) Wang, Z.; Li, C.; Domen, K. Recent Developments in Heterogeneous Photocatalysts for Solar-Driven Overall Water Splitting. *Chem. Soc. Rev.* **2019**, *48*, 2109−2125.
(22) Dave, M.; Rajagopal, A.; Damm-Ruttensperger, M.; Schwarz, B.; Nägele, F.; Daccache, L.; Fantauzzi, D.; Jacob, T.; Streb, C. Understanding Homogeneous Hydrogen Evolution Reactivity and Deactivation Pathways of Molecular Molybdenum Sulfide Catalysts. *Sustain. Energy Fuels* **2018**, *2*, 1020−1026.
(23) Lei, Y.; Yang, M.; Hou, J.; Wang, F.; Cui, E.; Kong, C.; Min, S. Thiomolybdate [Mo3S13]2−nanocluster: a molecular mimic of MoS2active sites for highly efficient photocatalytic hydrogen evolution. *Chem. Commun.* **2018**, *54*, 603−606.
(24) Rajagopal, A.; Venter, F.; Jacob, T.; Petermann, L.; Rau, S.; Tschierlei, S.; Streb, C. Homogeneous visible light-driven hydrogen evolution by the molecular molybdenum sulfide model [Mo2S12]2−. *Sustain. Energy Fuels* **2018**, *3*, 92−95.
(25) Yue, D.; Zhang, Z.; Tian, Z.; Zhang, T.; Kan, M.; Qian, X.; Zhao, Y. Highly photocatalytic active thiomolybdate [Mo 3 S 13] 2− clusters/Bi 2 WO 6 nanocomposites. *Catal. Today* **2016**, *274*, 22−27.
(26) Han, Y.; Yue, D.; Kan, M.; Wu, Y.; Zeng, J.; Bian, Z.; Zhao, Y.; Qian, X. [Mo3S13]2− modified TiO2 coating on non-woven fabric for efficient photocatalytic mineralization of acetone. *Appl. Catal., B* **2019**, *245*, 190−196.
(27) Yue, D.; Qian, X.; Zhang, Z.; Kan, M.; Ren, M.; Zhao, Y. CdTe/CdS Core/Shell Quantum Dots Cocatalyzed by Sulfur Tolerant [Mo3S13]2- Nanoclusters for Efficient Visible-Light-Driven Hydrogen Evolution. *ACS Sustain. Chem. Eng.* **2016**, *4*, 6653−6658.

https://doi.org/10.1021/acscatal.2c00972
ACS Catal. 2022, 12, 6641−6650

(28) Guo, F.; Hou, Y.; Asiri, A. M.; Wang, X. Assembly of protonated mesoporous carbon nitrides with co-catalytic [Mo3S13]2− clusters for photocatalytic hydrogen production. *Chem. Commun.* **2017**, *53*, 13221−13224.
(29) Rajagopal, A.; Akbarzadeh, E.; Li, C.; Mitoraj, D.; Krivtsov, I.; Adler, C.; Diemant, T.; Biskupek, J.; Kaiser, U.; Im, C.; Heiland, M.; Jacob, T.; Streb, C.; Dietzek, B.; Beranek, R. Polymeric Carbon Nitride Coupled with a Molecular Thiomolybdate Catalyst: Exciton and Charge Dynamics in Light-Driven Hydrogen Evolution. *Sustain. Energy Fuels* **2020**, *4*, 6085−6095.
(30) Nishiyama, H.; Yamada, T.; Nakabayashi, M.; Maehara, Y.; Yamaguchi, M.; Kuromiya, Y.; Nagatsuma, Y.; Tokudome, H.; Akiyama, S.; Watanabe, T.; Narushima, R.; Okunaka, S.; Shibata, N.; Takata, T.; Hisatomi, T.; Domen, K. Photocatalytic Solar Hydrogen Production from Water on a 100-M2 Scale. *Nature* **2021**, *598*, 304−307.
(31) Qi, Y.; Zhang, J.; Kong, Y.; Zhao, Y.; Chen, S.; Li, D.; Liu, W.; Chen, Y.; Xie, T.; Cui, J.; Li, C.; Domen, K.; Zhang, F. Unraveling of Cocatalysts Photodeposited Selectively on Facets of BiVO4 to Boost Solar Water Splitting. *Nat. Commun.* **2022**, *13*, 484.
(32) Li, Y.; Wang, Z.; Wang, Y.; Kovács, A.; Foo, C.; Dunin-Borkowski, R. E.; Lu, Y.; Taylor, R. A.; Wu, C.; Tsang, S. C. E. Local Magnetic Spin Mismatch Promoting Photocatalytic Overall Water Splitting with Exceptional Solar-to-Hydrogen Efficiency. *Energy Environ. Sci.* **2022**, *15*, 265−277.
(33) Fedin, V. P.; Czyzniewska, J.; Prins, R.; Weber, T. Supported molybdenum-sulfur cluster compounds as precursors for HDS catalysts. *Appl. Catal. Gen.* **2001**, *213*, 123−132.
(34) Müller, A.; Wittneben, V.; Krickemeyer, E.; Bögge, H.; Lemke, M. Studies on the triangular cluster [Mo3S13]2?: Electronic structure (X? calculations, XPS), crystal structure of (Ph4As)2[Mo3S13]. 2CH3CN and a refinement of the crystal structure of (NH4)2-[Mo3s13] H2O. *Z. Anorg. Allg. Chem.* **1991**, *605*, 175−188.
(35) Müller, A.; Jostes, R.; Jaegermann, W.; Bhattacharyya, R. Spectroscopic investigation on the molecular and electronic structure of [Mo3S13]2−, a discrete binary transition metal sulfur cluster. *Inorg. Chim. Acta.* **1980**, *41*, 259−263.
(36) Hibble, S. J.; Feaviour, M. R. An in situ structural study of the thermal decomposition reactions of the ammonium thiomolybdates, (NH4)2Mo2S12·2H2O and (NH4)2Mo3S13·2H2O. *J. Mater. Chem.* **2001**, *11*, 2607−2614.
(37) Ronge, E.; Hildebrandt, S.; Grutza, M.-L.; Klein, H.; Kurz, P.; Jooss, C. Structure of Nanocrystalline, Partially Disordered MoS2+δ Derived from HRTEM-An Abundant Material for Efficient HER Catalysis. *Catalysts* **2020**, *10*, 856.
(38) Müller, A.; Sarkar, S.; Bhattacharyya, R. G.; Pohl, S.; Dartmann, M. Directed Synthesis of[Mo3S13]2−, an Isolated Cluster Containing Sulfur Atoms in Three Different States of Bonding. *Angew. Chem., Int. Ed. Engl.* **1978**, *17*, 535.
(39) Baloglou, A.; Ončák, M.; Grutza, M.-L.; van der Linde, C.; Kurz, P.; Beyer, M. K. Structural Properties of Gas Phase Molybdenum Sulfide Clusters [Mo3S13]2-, [HMo3S13]−, and [H3Mo3S13]+ as Model Systems of a Promising Hydrogen Evolution Catalyst. *J. Phys. Chem. C* **2019**, *123*, 8177−8186.
(40) Baloglou, A.; Plattner, M.; Ončák, M.; Grutza, M. L.; Kurz, P.; Beyer, M. K. [Mo 3 S 13] 2− as a Model System for Hydrogen Evolution Catalysis by MoS x : Probing Protonation Sites in the Gas Phase by Infrared Multiple Photon Dissociation Spectroscopy. *Angew. Chem., Int. Ed.* **2021**, *60*, 5074−5077.
(41) Zhang, J.; Nosaka, Y. Photocatalytic Oxidation Mechanism of Methanol and the Other Reactants in Irradiated TiO2 Aqueous Suspension Investigated by OH Radical Detection. *Appl. Catal., B* **2015**, *166−167*, 32−36.
(42) Allgeier, A. M.; Mirkin, C. A. Ligand Design for Electrochemically Controlling Stoichiometric and Catalytic Reactivity of Transition Metals. *Angew. Chem., Int. Ed.* **1998**, *37*, 894−908.
(43) Islam, S. M.; Cain, J. D.; Shi, F.; He, Y.; Peng, L.; Banerjee, A.; Subrahmanyam, K. S.; Li, Y.; Ma, S.; Dravid, V. P.; Grayson, M.; Kanatzidis, M. G. Conversion of Single Crystal (NH4)2Mo3S13·H2O to Isomorphic Pseudocrystals of MoS2 Nanoparticles. *Chem. Mater.* **2018**, *30*, 3847−3853.
(44) Mars, P.; van Krevelen, D. W. Oxidations Carried out by Means of Vanadium Oxide Catalysts. *Chem. Eng. Sci.* **1954**, *3*, 41−59.
(45) Doornkamp, C.; Ponec, V. The Universal Character of the Mars and Van Krevelen Mechanism. *J. Mol. Catal. A: Chem.* **2000**, *162*, 19−32.
(46) Grutza, M.-L.; Rajagopal, A.; Streb, C.; Kurz, P. Hydrogen evolution catalysis by molybdenum sulfides (MoSx): are thiomolybdate clusters like [Mo3S13]2− suitable active site models? *Sustain. Energy Fuels* **2018**, *2*, 1893−1904.
(47) Cherevan, A. S.; Nandan, S. P.; Roger, I.; Liu, R.; Streb, C.; Eder, D. Polyoxometalates on Functional Substrates: Concepts, Synergies, and Future Perspectives. *Adv. Sci.* **2020**, *7*, 1903511.
(48) Müller, A.; Pohl, S.; Dartmann, M.; Cohen, J. P.; Bennett, J. M.; Kirchner, R. M. Crystal Structure of (NH4)2[Mo3S(S2)6] Containing the Novel Isolated Cluster [MO3S13]2-. *Z. Naturforsch. B* **1979**, *34*, 434−436.
(49) Haselmann, G. M.; Eder, D. Early-Stage Deactivation of Platinum-Loaded TiO2 Using In Situ Photodeposition during Photocatalytic Hydrogen Evolution. *ACS Catal.* **2017**, *7*, 4668−4675.
(50) Schubert, J. S.; Popovic, J.; Haselmann, G. M.; Nandan, S. P.; Wang, J.; Giesriegl, A.; Cherevan, A. S.; Eder, D. Immobilization of Co, Mn, Ni and Fe Oxide Co-Catalysts on TiO2 for Photocatalytic Water Splitting Reactions. *J. Mater. Chem. A* **2019**, *7*, 18568−18579.
(51) Ishibashi, K.-i.; Fujishima, A.; Watanabe, T.; Hashimoto, K. Detection of Active Oxidative Species in TiO2 Photocatalysis Using the Fluorescence Technique. *Electrochem. Commun.* **2000**, *2*, 207−210.

https://doi.org/10.1021/acscatal.2c00972
ACS Catal. 2022, 12, 6641−6650

Supporting Information (SI)

Surface-Anchoring and Active Sites of $[Mo_3S_{13}]^{2-}$ Clusters as Co-Catalysts for Photocatalytic Hydrogen Evolution

Samar Batool[1]†, Sreejith P. Nandan[1]†, Stephen Nagaraju Myakala[1], Ashwene Rajagopal[2], Jasmin S. Schubert[1], Pablo Ayala[1], Shaghayegh Naghdi[1], Hikaru Saito[3], Johannes Bernardi[4], Carsten Streb[2,5], Alexey Cherevan[1,] and Dominik Eder[1]*

[1] TU Wien, Institute of Materials Chemistry, Getreidemarkt 9/BC/02, 1040, Vienna, Austria

[2] Ulm University, Institute of Inorganic Chemistry I, Albert-Einstein-Allee 11, 89081 Ulm, Germany

[3] Institute for Materials Chemistry and Engineering, Kyushu University, 6-1 Kasugakoen, Kasuga, Fukuoka 816-8580, Japan

[4] TU Wien, University Service Centre for Transmission Electron Microscopy (USTEM), Wiedner Hauptstraße 8-10, 1040, Vienna, Austria

[5] Department of Chemistry, Johannes Gutenberg University Mainz, Duesbergweg 10-14, 55128 Mainz, Germany

† these authors contributed equally

* corresponding author

correspondence to alexey.cherevan@tuwien.ac.at

Content

1. List of chemicals and methods

Chemicals

All the chemicals used for the synthesis were purchased from commercial suppliers and include ammonium molybdate tetrahydrate ($(NH_4)_6[Mo_7O_{24}]\cdot 4H_2O$, Sigma-Aldrich, 99.98% trace metals basis), ammonium sulfide solution ($(NH_4)_2S_x$, Sigma-Aldrich, 20 wt.% in H_2O), carbon disulfide (CS_2, Sigma-Aldrich, 99.9%), sodium chloride (NaCl, Carl Roth), sodium hydroxide (NaOH, Carl Roth), ammonium metavanadate (NH_4VO_3, Carl Roth, 99.8%), bismuth (III) nitrate pentahydrate ($Bi(NO_3)_3\cdot 5H_2O$, Riedel de Haen, 98%), titanium (IV) oxide anatase nanopowder (TiO_2, Sigma-Aldrich, 99.7%, <25 nm particle size) and titanium (IV) oxide rutile nanopowder (TiO_2, Sigma-Aldrich, 99.7%, <100 nm particle size). The solvents used for the synthesis were deionized water, ethanol (EtOH, from Chem-Lab NV), HPLC-gradient grade methanol (MeOH, from VWR), diethyl ether (from Sigma-Aldrich), N,N-dimethylformamide (DMF, from Acros Organics, 99.8%, extra dry over the molecular sieve, acroseal).

Characterization techniques

UV-Vis spectroscopy was performed on a Jasco V670 UV-Vis spectrometer. The samples were prepared in methanol and aqueous methanol (1:1 vol.) solution with a concentration of 0.025 mM; UV-Vis spectra were recorded in absorbance mode. Absorption spectra of powdered samples were measured in solid-state via diffuse-reflectance spectroscopy (DRS) using $MgSO_4$ as a reference. The Mo_3/TiO_2 composite samples were measured using TiO_2 as a background.

ATR-FTIR spectra of the samples were recorded via PerkinElmer FTIR Spectral UATR-TWO with a spectrum two Universal ATR (Single Reflection Diamond) instrument. Powdered samples were directly loaded onto the sample holder and the spectra were recorded in the region of 4000-400 wavenumbers (cm^{-1}). Raman measurements were performed with a WITec alpha 300 RSA+ Raman microscope equipped with a 632 nm excitation laser maintaining the laser intensity at 1 mW.

The quantitative elemental analysis of the samples was performed with X-ray photoelectron spectroscopy (XPS) using a custom-built SPECS XPS-spectrometer equipped with a monochromatized Al-K_α X-ray source (μ 350) and a hemispherical WAL-150 analyzer (acceptance angle: 60°). To improve the sensitivity of the measurements, Mo_3/TiO_2 samples were prepared and investigated in the form of thin-films (see Additional Methods in SI). This was followed by wet impregnation of the $Na_2[Mo_3S_{13}]$ clusters from methanolic solutions. For a single XPS measurement, a slide containing the sample film was placed on the sample holder using a conductive clip. Pass energies of 100 eV and 30 eV and energy resolutions of 1 eV and 100 meV were used for survey and detail spectra, respectively (excitation energy: 1486.6 eV, beam energy and spot size: 70 W onto 400 μm, angle: 51° to sample surface normal, base pressure: 5×10^{-10} mbar, pressure during measurements: 2×10^{-9} mbar). Data analysis was performed using CASA XPS software, employing transmission corrections (as per the instrument vendor's specifications), Shirley and Sh Tougaard backgrounds and Scofield sensitivity factors. Charge correction was applied so the adventitious carbon peak (C–C peak) was shifted to 284.8 eV binding energy (BE). All content values shown are in units of relative atomic percent (at.%), where the detection limit in survey measurements usually lies around 0.1–1 at.%, depending on the element.

Quantitative determination of the $[Mo_3S_{13}]^{2-}$ cluster loadings was performed by X-ray fluorescence spectroscopy in total reflection geometry (TXRF) using an ATOMIKA 8030C X-ray fluorescence analyzer (Atomika Instruments GmbH, Oberschleissheim, Munich, Germany). The excitation source employed was a Wolfram X-ray tube (continuous spectrum)

at 50 kV and 47 mA. The samples were excited for 100 s and a Si(Li)-detector was used for X-rays acquisition. The samples were prepared by fixating 200 µg of the powders at the center of polished quartz glass reflectors with 5 µL of a 1 % polyvinyl alcohol (PVA) solution and drying on a hot plate for 5 min. Quantification of Mo (in wt.%) was done relative to Ti. The real loadings of $[Mo_3S_{13}]^{2-}$ on TiO_2 were determined considering the stoichiometry of the clusters and the support.

Scanning electron microscopy (SEM) images were acquired using a FEI Quanta 250 FEG scanning electron microscope to obtain visual information on the morphology of the samples. Typically acceleration voltage of 10 kV and secondary electron detection mode were used. High-resolution transmission electron microscopy (HRTEM) images were obtained using FEI TECNAI F20 transmission electron microscope equipped with a field emission gun in bright field mode using 200 kV acceleration voltage. The sample was prepared from powdered samples directly on a copper holey carbon-coated grid (Plano, 200 mesh). Energy-dispersive X-ray spectroscopy (EDS) was performed using scanning TEM (STEM) mode to obtain elemental maps.

High-angle annular dark field (HAADF) STEM imaging and energy dispersive X-ray spectroscopy (EDS) were performed by using Titan Cubed G2 60-300 (TEM/STEM, FEI Co., now Thermo Fisher Scientific) operated at 300 kV. This microscope has an aberration corrector for STEM (DCOR, CEOS), four-quadrant windowless super-X SDD (silicon drift detector) system. The probe current was ~60 pA for STEM observation as well as EDS. The convergence semi-angle of the electron probe was 18 mrad. The typical probe diameter was less than 0.1 nm. Forward scattered electrons of an angular range from 38 to 184 mrad were detected by a HAADF detector for STEM imaging.

Thermogravimetric analysis (TGA) was carried out with a PerkinElmer Thermogravimetric Analyzer TGA 8000. The samples were loaded onto Al_2O_3 crucibles and heated at the rate of 5°C min^{-1} under air and N_2 atmosphere from 25-600°C.

Powder X-ray diffraction (XRD) was performed using an XPERT II: PANalytical XPert Pro MPD (Θ–Θ Diffractometer) for the *ex situ* experiments, and an XPERT III: PANalytical XPert Pro MPD (Θ–Θ Diffractometer) for the *in situ* XRD experiments. The sample was placed on a Si sample holder and irradiated with a Cu X-ray source (8.04 keV, 1.5406 Å). The signals were then acquired with Bragg–Brentano Θ/Θ-diffractometer geometry ranging from 5° to 80° degrees using a semiconductor X'Celerator (2.1°) detector. The *in situ* XRD experiments were performed from 5° to 45° degrees under N_2/air flow through the sample holder, and temperatures ranging from 25 to 800°C.

The physisorption measurements were carried out on a Micromeritics ASAP 2010 by Micromeritics GmbH. The degassing procedure was set to 150-200°C overnight and the isotherms were obtained at 77K using nitrogen as the adsorbate. Surface areas of the supports have been estimated based on the Brunauer–Emmett–Teller (BET) theory.

Steady state photoluminescence (PL) measurements were performed using PicoQuant FluoTime 300 spectrophotometer. Xe arc lamp (300 W power) was the excitation source, coupled with a double-grating monochromator. The detection system comprised of a PMA Hybrid 07 detector along with a high-resolution double monochromator. The excitation wavelength utilized for all the steady state measurements was 315 nm (3.94 eV photon energy). The data was collected and later fitted using EasyTau2 software.

Additional methods

Solubility of the $Na_2[Mo_3S_{13}]$ was checked by preparing 1 mg/mL solutions in water, methanol, ethanol, isopropanol, 1-butanol and phenol. Assisted by light ultrasonication, stable molecular solutions could be obtained in every of these solvent, but 1-butanol and phenol.

$BiVO_4$ was synthesized according to the following procedure. 1 mmol of $Bi(NO_3)3.5H_2O$ were added to 2.5 ml of water, followed by the addition of 100 µl of HNO_3 (67%) – noted as solution A. 1 mmol of NH_4VO_3 were dissolved in 2.5 ml of boiling water– noted as solution B. Solution B was then added dropwise to solution A, forming an orangish-yellow suspension. The pH of the solution was then adjusted to 0.8 using ammonia solution, followed by 15 min of stirring. The suspension was transferred to a 30 ml microwave vial and treated at 150°C for 30 min. After the microwave treatment, the product was washed 3 times with distilled water and ethanol followed by drying at 60°C overnight. XRD confirmed the formation of $BiVO_4$.

Thin-film models systems have been developed on a par with the investigations of powdered Mo_3/TiO_2 samples. For this, original anatase TiO_2 powders were filmed through spin-coating. In a single preparation, 400 mg of TiO_2 was added to a mixture of 2 g of 10 wt.% ethanolic solution of ethyl-cellulose and 1.75 ml of terpineol. The mixture was then sonicated for 30 min followed by stirring for 6 h to obtain a homogenous suspension. 500 µl of this suspension was spin-coated onto a 1 x 3 cm FTO glass at 1500 rpm for 30 sec. The spin-coated samples were then annealed at 550°C for 30 min yielding pure anatase films. The films were then immersed in $Na_2[Mo_3S_{13}]$ solutions overnight following by thorough washing to obtain Mo_3/TiO_2 films. Cluster loading was verified with TXRF (see Characterization techniques in SI) to be 2 wt.%.

Reference Pt/TiO_2 HER experiment was performed by using Pt photodeposition method.[1] While the general HER procedure described in Methods was followed (i.e. 10 mg of TiO_2 was taken as a photocatalyst), the reaction solution was additionally loaded with H_2PtCl_6 aqueous solution to account for 10 wt.% of Pt with regard to the TiO_2 amount to allow for a comparison with the $10Mo_3/TiO_2$ sample.

2. SEM images

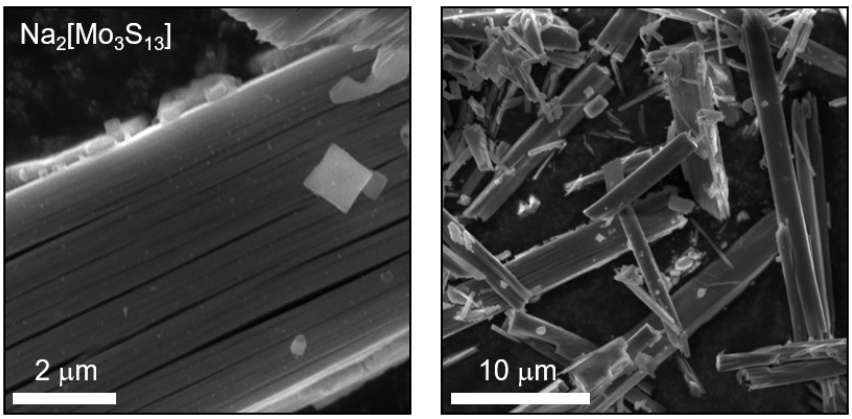

Fig. S1 | Representative SEM images of $Na_2[Mo_3S_{13}]$ powder showing the typical morphology.

3. Additional ATR-FTIR spectra

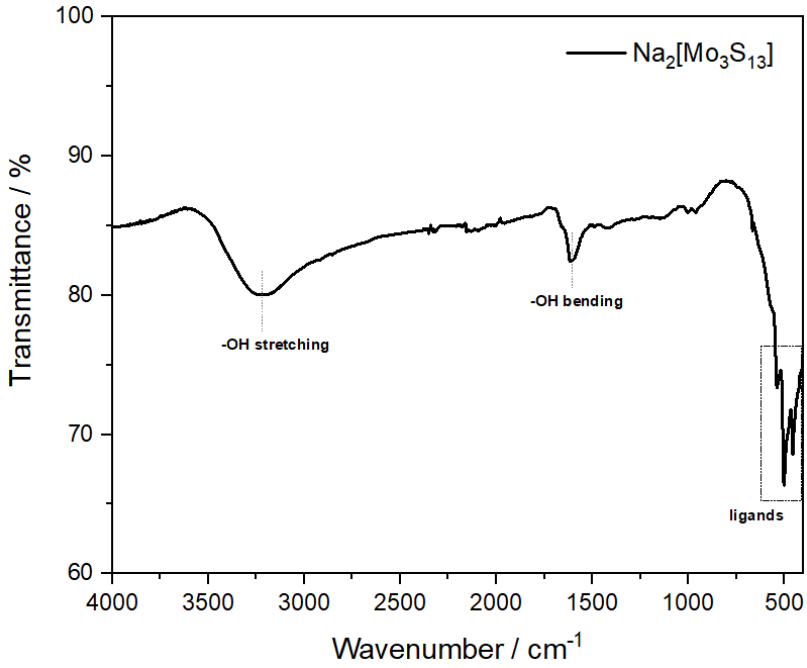

Fig. S2 | ATR-FTIR spectra of the $Na_2[Mo_3S_{13}]\cdot H_2O$ featuring OH bending and stretching vibrations of the water of crystallization. The boxed region containing characteristic S-ligand bands is described in the main text.

4. Additional DRS spectra and analysis

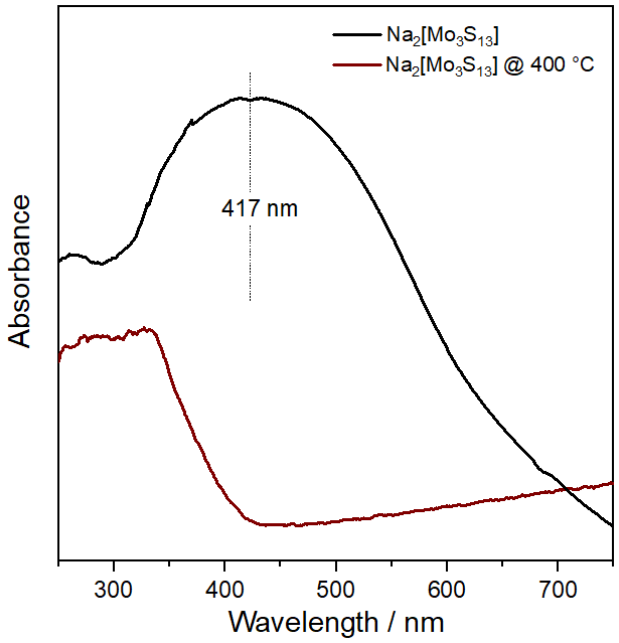

Fig. S3 | DRS spectra of the $Na_2[Mo_3S_{13}]$ and the product of its oxidation in ambient air at 400 °C. The latter product is likely MoO_x featuring an absorption edge corresponding to its band gap. The characteristic $[Mo_3S_{13}]^{2-}$ absorption feature at 417 nm vanishes after oxidation.

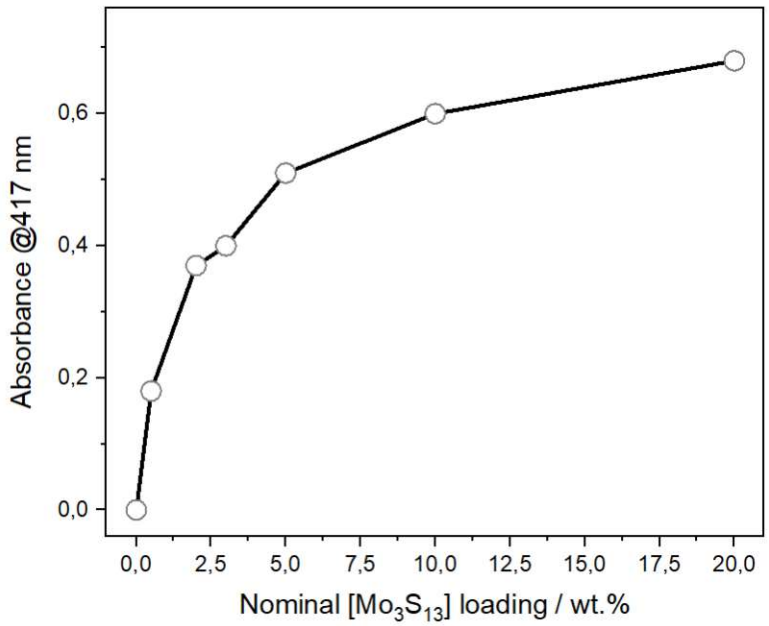

Fig. S4 | Absorption of the Mo_3/TiO_2 composites at 417 nm (after subtracting absorption of TiO_2) plotted against the intended (nominal) cluster loadings. The data correspond to Figure 2b.

5. BET measurements

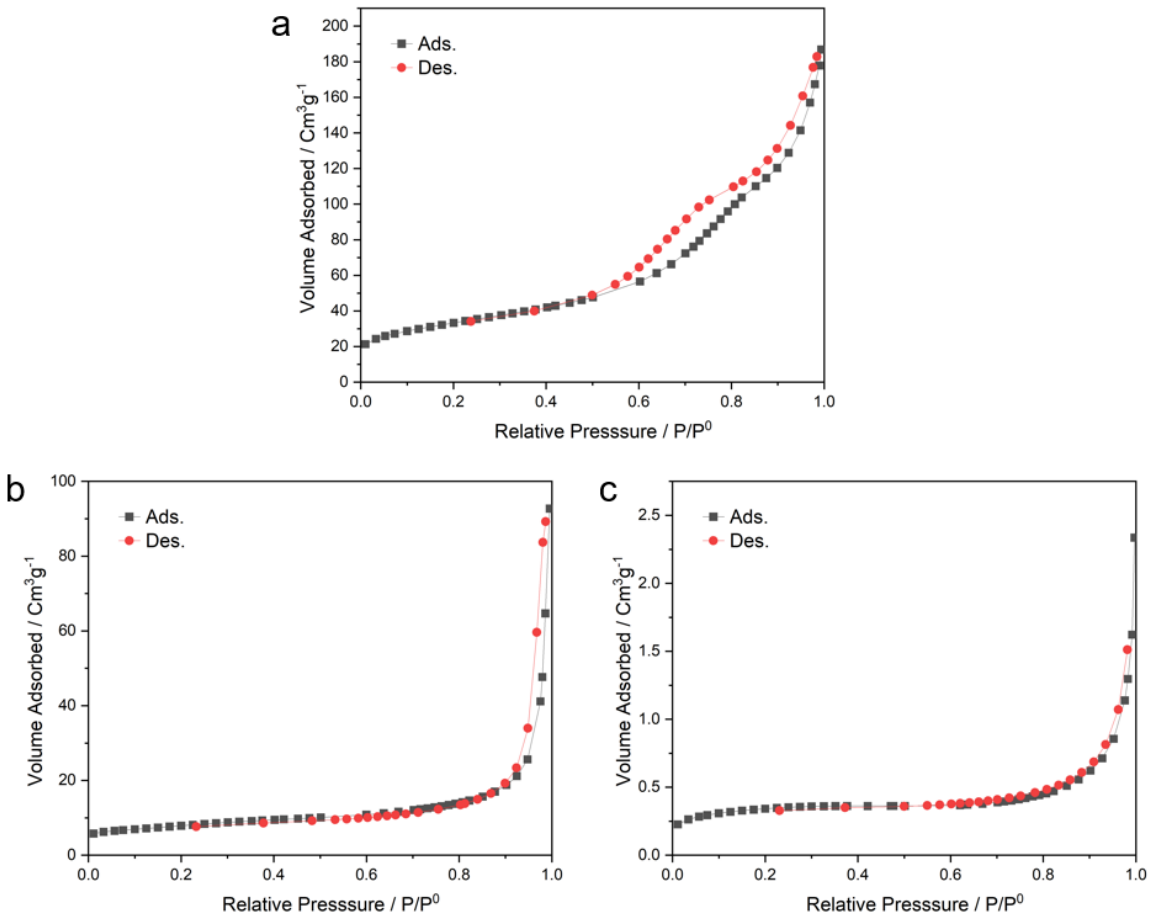

Fig. S5 | N_2 adsorption-desorption isotherms measured for the **(a)** TiO_2 anatase sample originally used as a support, **(b)** commercial rutile TiO_2 and **(c)** home-made $BiVO_4$ powder. Details on the supports are in SI sections of Methods and Chemicals. Values of the BET surface areas for the samples are presented in Table S1.

6. Estimation of the theoretical surface coverage

Using STM analysis, Besenbacher *et al.*[2] found the $\{Mo_3S_{13}\}$ footprint to be ~ 0.7 nm^2 for a single cluster adsorbed onto the flat surface of highly-oriented pyrolytic graphite. However, this value only corresponds to the geometric area that a free-standing cluster occupies on a flat surface. Based on the solid-state crystal structure of the $(NH_4)[Mo_3S_{13}]$ salt, a single $[Mo_3S_{13}]^{2-}$ cluster in a close-packed lattice takes up around 0.96 nm^2 (see scheme below).

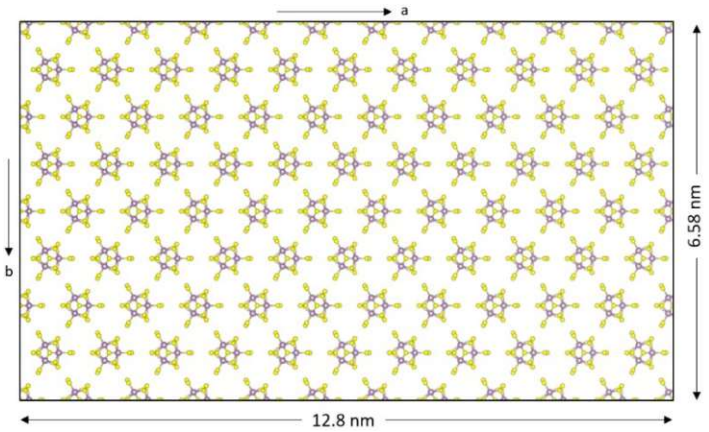

In the case of high coverages of the clusters over the TiO_2 surface in our composites, however, steric and coulombic repulsions of the anionic $[Mo_3S_{13}]^{2-}$ species will contribute to a further spread of the clusters attached to the surface. We estimate the average surface area occupied by a single cluster to increase to around 1.2-1.5 nm^2. From the physisorption data of TiO_2, the BET surface area of the support is around 116 m^2/g. The ratio of the two values gives us the maximum number of clusters that could be loaded onto the TiO_2 surface considering dense monolayer adsorption. Further dividing this value with the Avogadro's number and multiplying by the molecular weight of the cluster (only the anion is considered) gives us the cluster loading (i.e. weight of the cluster on 1 g of TiO_2).

The final calculation yields a loading value range of 8.7 to 10.6 wt.% (average is 9.6 wt.%). This range represents a more realistic scenario when a dense monolayer of $[Mo_3S_{13}]^{2-}$ clusters the entire support surface.

7. Extended XRD patterns

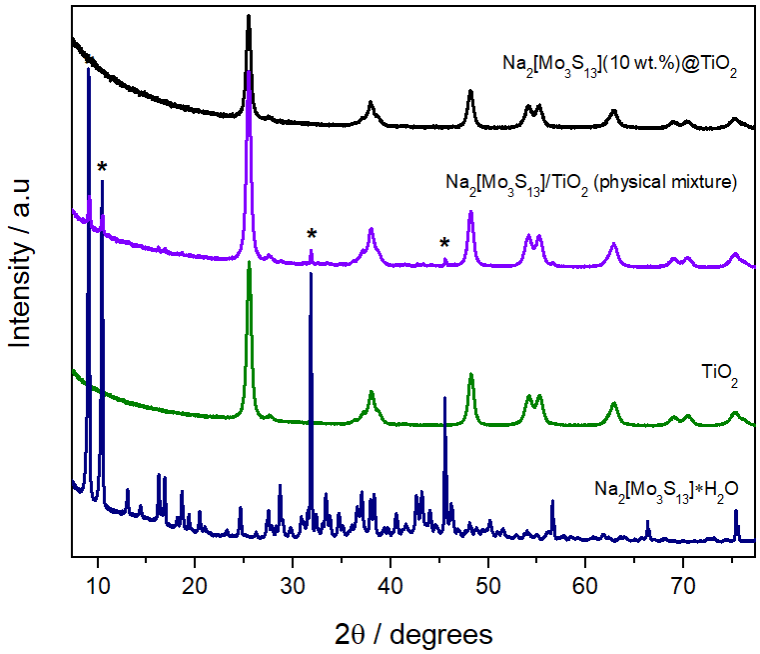

Fig. S6 | Powder XRD patterns of $Na_2[Mo_3S_{13}]$ clusters, anatase-TiO_2, physical mixture of clusters and titania, and Mo_3/TiO_2 composite synthesized by the wet impregnation method.

To elucidate on the state of the $[Mo_3S_{13}]^{2-}$ inside the Mo_3/TiO_2 composites, we performed powder XRD of the $10Mo_3/TiO_2$ sample (real cluster loading of 8.3 wt.%) and compared it to that of a relevant physical mixture of the $Na_2[Mo_3S_{13}]\cdot H_2O$ and TiO_2 (1:9 wt.%).

As Figure S6 shows, XRD spectra of the physical mixture of $Na_2[Mo_3S_{13}]\cdot H_2O$ clusters and TiO_2 exhibits some of the peaks overlapping with the XRD pattern of pure $Na_2[Mo_3S_{13}]$. This corresponds to the presence of thiomolybdate crystals or agglomerates of clusters on the surface of the titania support. Contrary to this, the $10Mo_3/TiO_2$ composite prepared via impregnation shows no peaks corresponding to the XRD pattern of pure $Na_2[Mo_3S_{13}]$. All of the peaks observed are matching well to the XRD pattern of anatase TiO_2 suggesting a good dispersion of the $[Mo_3S_{13}]^{2-}$ clusters over the support surface and the absence of larger cluster aggregates.

8. Additional EDS maps

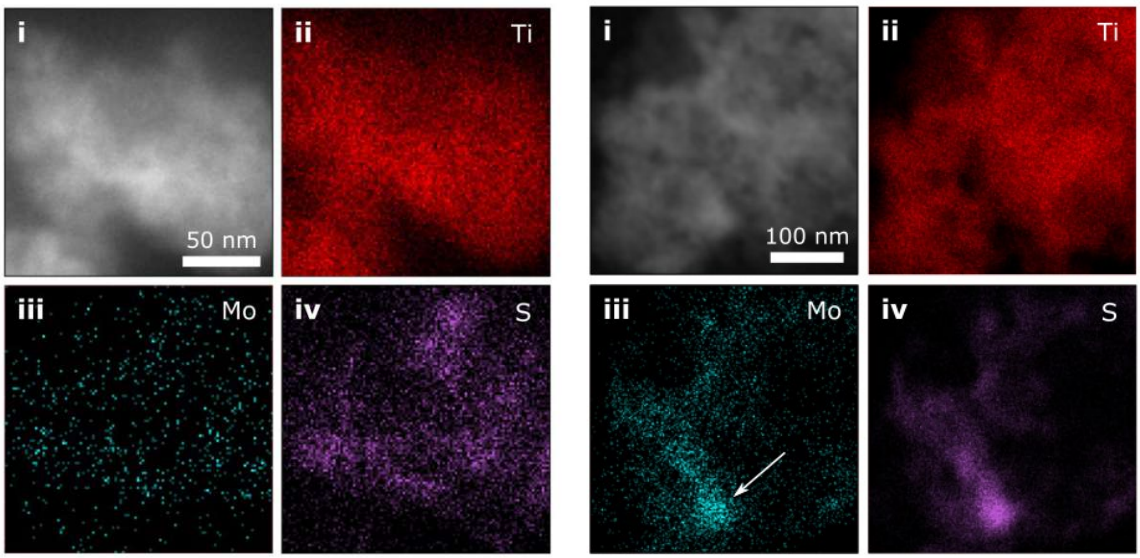

Fig. S7 | Large-area EDS elemental mappings of Ti (ii), Mo (iii) and S (iv) in an exemplary $10Mo_3/TiO_2$ composite. The arrow highlights an area of higher Mo/S concentration. Judging from the lower Ti signal arriving from the area, it can be assumed that the surface of TiO_2 is covered with the MoS_x species.

9. TEM images

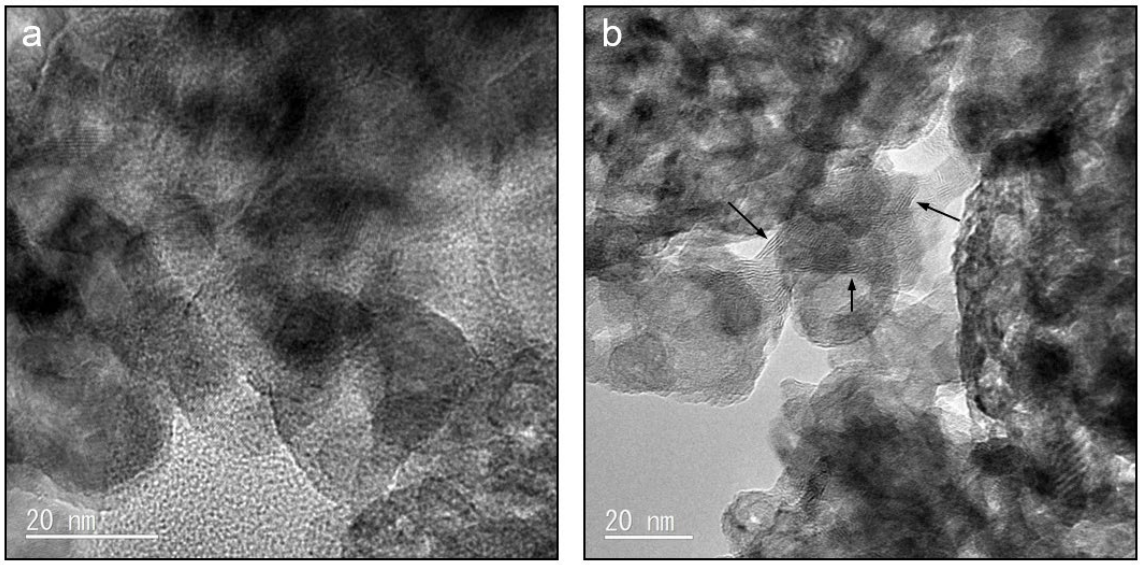

Fig. S8 | HRTEM images of the exemplary $3Mo_3/TiO_2$ composite. (a) A collection of TiO_2 nanoparticles corresponding to the original anatase powder (average size between 20 and 30 nm) can be visible, typically no surface aggregates can be observed, **(b)** arrows indicate seldom areas that feature the formation of ordered/layered nanostructures. These areas also correspond to higher elemental contents of S and Mo, suggesting a certain degree of multilayer adsorption and layering. The average interlayer distance is measured to be around 0.7 nm. It is substantially larger of that found in bulk MoS_2 (0.615 nm) and corresponds well to the size of a single $\{Mo_3S_{13}\}$ anion.

10. Deposition of $[Mo_3S_{13}]^{2-}$ on alternative supports

In order to verify the assumption that the cluster deposition follows a monolayer adsorption model (i.e. the maximum loading values are limited by the surface area of the support) and to further elucidate whether this model is only applicable to anatase TiO_2 (i.e. it is specific to its surface chemistry and charge), we performed similar wet-impregnation of three alternative nano- (faceted TiO_2 and rutile TiO_2) and micron-sized ($BiVO_4$) powders using concentrated $Na_2[Mo_3S_{13}]$ solutions that corresponded to 20 wt. % cluster loadings (i.e. mimicking the preparation of $20Mo_3/TiO_2$ described in the main text). In all three cases, after allowing for 24 h adsorption and equilibrium, first washing resulted in strongly red-coloured filtrates, which indicated that a big portion of the original $[Mo_3S_{13}]^{2-}$ clusters has not been anchored strongly to the support surface. TXRF allowed to quantify real $[Mo_3S_{13}]^{2-}$ loadings and revealed support-dependent values in the range between 0.19 and 5.14 wt.% (Table S1). According to BET measurements (Figure S5), all three supports feature low surface areas in the range between 2 and 27 m^2/g (Table S1). When real loadings are plotted against the BET area (Figure S9), a clear trend can be seen. The result is thus in good agreement with the proposed attachment model.

Table S1. Alternative oxide supports used for impregnation, their BET surface areas and the corresponding $[Mo_3S_{13}]^{2-}$ derived from TXRF measurements.

Sample	Maximum $[Mo_3S_{13}]^{2-}$ loading measured by TXRF / wt.%	BET surface area *
$BiVO_4$	0.19	1.11
faceted TiO_2	3.14	13.42 [3]
rutile TiO_2	5.14	27.03

* N_2 physisorption isotherms are presented in Figure S5

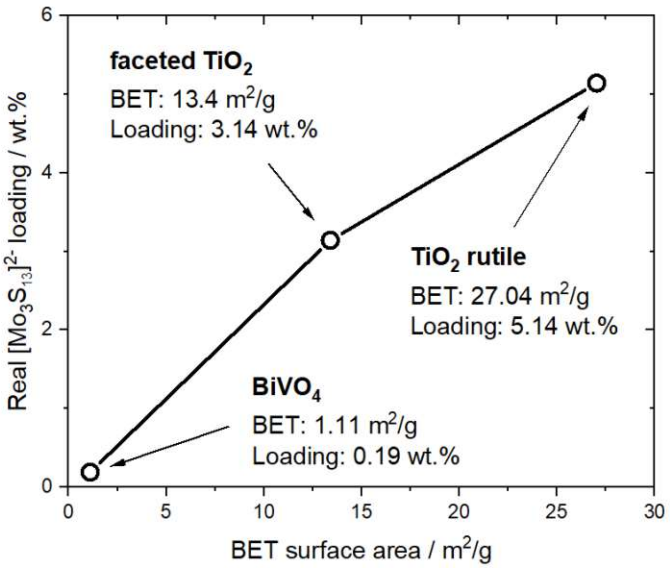

Fig. S9 | Correlation between BET surface areas and maximum cluster loadings achieved for a series of oxide supports.

11. Leaching experiments

The irreversible attachment of $[Mo_3S_{13}]^{2-}$ clusters onto TiO_2 and their stability towards turnover conditions were confirmed by HER leaching experiment. In a single experiment, as-obtained Mo_3/TiO_2 composite was dispersed in methanol/water (1/1) solvent by ultrasonication for 15 seconds. The resulting cloudy solution was then filtered and the filtrate was collected. In order to verify if the filtrate contained any $[Mo_3S_{13}]^{2-}$ detached from the original Mo_3/TiO_2 composite upon ultrasonication, the filtrate solution was charged with 10 mg of anatase TiO_2 nanoparticles. This solution was then stirred for 1 hour to allow for equilibrium (adsorption) and tested for photocatalytic hydrogen evolution reaction using the same procedure followed for normal HER experiments (see Methods section in the main text). The hydrogen evolution performance of so-obtained solution was similar as obtained for bare anatase TiO_2, which suggests that only a negligible amount of $[Mo_3S_{13}]^{2-}$ clusters (< 1 % of the initial amount loaded) leached from Mo_3/TiO_2. This result was further confirmed by analyzing $[Mo_3S_{13}]^{2-}$ loadings of the Mo_3/TiO_2 samples before and after conducting HER tests. Negligible change in Mo contents could be detected.

12. Additional Raman spectra

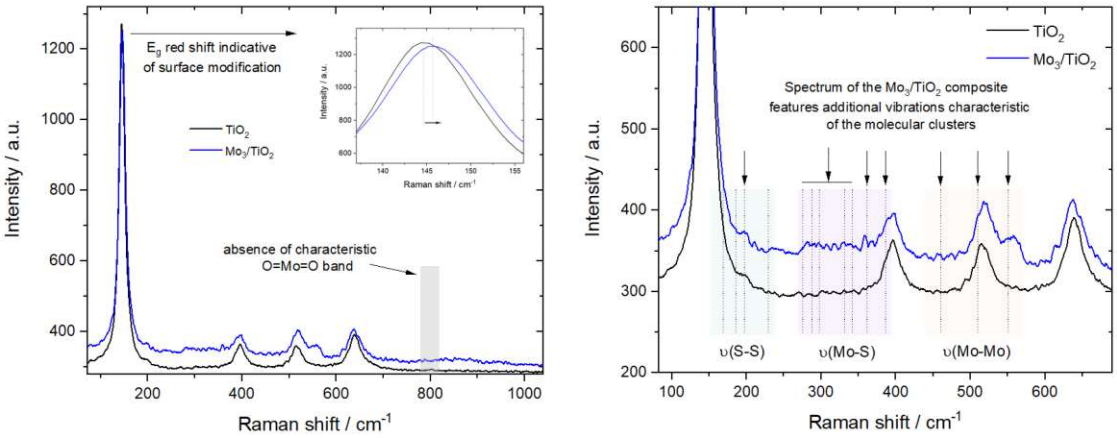

Fig. S10 | **(a)** Raman spectra of 20Mo_3/TiO_2 composite as well as anatase TiO_2 along with the magnified plot from showing the shift of the TiO_2 E_g band; the absence of Mo=O vibration around 800 cm^{-1} suggests that no oxidation of clusters occurred upon attachment. **(b)** Zoomed-in data with arrows highlighting the features characteristic of the $[Mo_3S_{13}]^{2-}$ cluster.

13. XPS discussion

13.1 XPS quantification

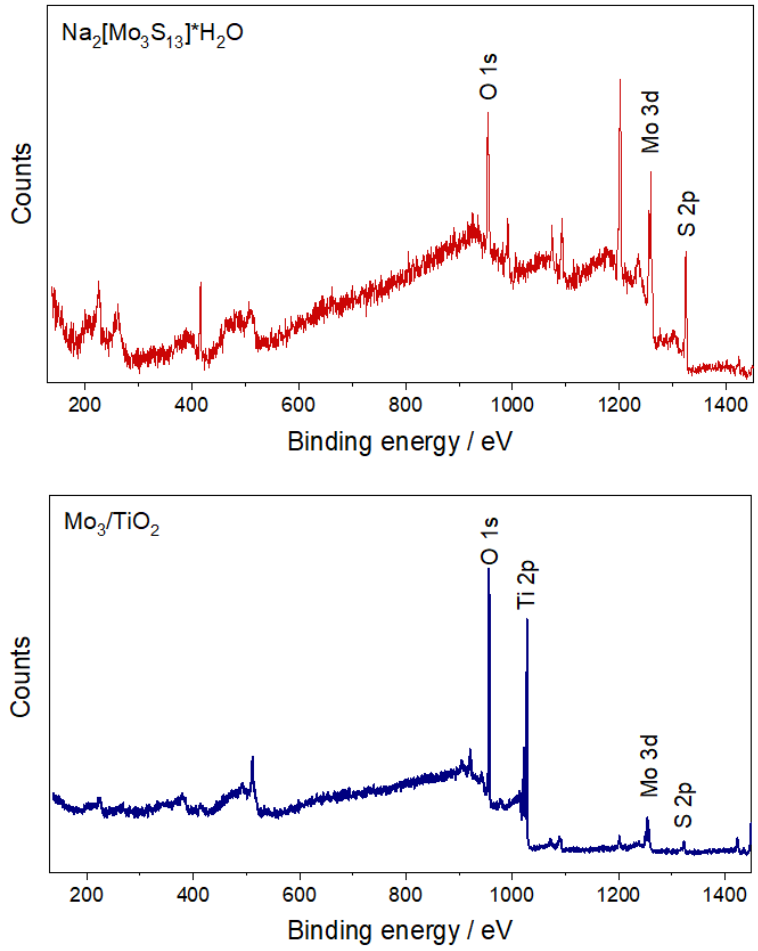

Fig. S11 | XPS survey spectra of **(a)** $Na_2[Mo_3S_{13}]\cdot H_2O$ powder and **(b)** Mo_3/TiO_2 composite (real cluster loading of 2 wt.%) prepared as a thin film, see Methods in SI.

Table S2. Survey quantifications of $Na_2[Mo_3S_{13}]\cdot H_2O$ and Mo_3/TiO_2 samples. Values indicate at.% of the elements derived from the survey spectra quantification.

Samples	Mo 3d	S 2p	C 1s	O 1s	Na 1s	Ti 2p
$Na_2[Mo_3S_{13}]\cdot H_2O$	**6.4**	**17.0**	59.6	15.1	2.0	-
Mo_3/TiO_2	**5.0**	**6.5**	53.9	9.9	0.9	23.8

Table S3. Atomic % of S:Mo ratio calculated from XPS data.

Samples	S:Mo
$Na_2[Mo_3S_{13}]\cdot H_2O$	**2.7**
Mo_3/TiO_2	**1.3**

13.2 XPS discussion

O 1s peak undergoes a considerable shift to higher binding energies upon $[Mo_3S_{13}]^{-2}$ attachment (Figure 3e). This shift is related to the main O component (often called "oxide" component of the "surface bulk" TiO_2, red fitted line) and originally corresponds to Ti-O-Ti binding motif of the titania. Upon the $[Mo_3S_{13}]^{-2}$ attachment, Mo binds to some of the Ti-OH groups forming Ti-O-Mo bonds at the cluster/TiO_2 interface. This results in a new minor "oxide" component (Ti-O-Mo) contributing to the O 1s peak after attachment, which shifts the major Ti-O-Ti peak to higher binding energies due to the higher electronegativity (i.e. lower ability to donate elections) of Mo (2.16) compared to Ti (1.54). Experimentally, we observe a 0.18 eV shift, which aligns well with the surface sensitivity of XPS.

In addition to the Ti-O-M (M stands for Ti or Mo) peak shift, O 1s XPS data also shows a significant drop in the amount of surface-hydroxyls (Figure 3e, blue fitted line) that takes place upon cluster deposition. This observation goes in line with the proposed attachment model, which involves surface Ti-OH groups to covalently bind Mo centers by displacing terminal S_2^{2-} ligands (see discussion in the main text). The decrease of the Ti-O-H signal (ca. 5% based on the relative peak area) corresponds well to their conversion into Ti-O-Mo groups.

Detailed analysis of the XPS data further allows us to clarify the process of charge transfer at the $[Mo_3S_{13}]^{-2}/TiO_2$ interface. The primary evidence for the electron flow is based on Mo 3d XPS data, which suggest that a part of Mo centers get oxidized upon the attachment. We believe that one or two out of three of the Mo atoms in each of the $[Mo_3S_{13}]^{-2}$ clusters – primarily those that undergo covalent binding with O atoms of the surface – change their oxidation state from +4 to +5/+6 depending on the binding scenario. This oxidation implies electron flow across the interface i.e. charge transfer. Besides this, a consistent strong (ca. 1 eV) shift of Mo XPS peaks to higher binding energy (Figure 3c) also implies a general displacement of electron density from the cluster. This may be related to the overall negative charge of the $[Mo_3S_{13}]^{-2}$ anion, which in this case acts as a strong electron donor. What is interesting, however, we do not observe any simultaneous XPS shift of Ti 2p or O 1s to lower binding energy. In contrary, as discussed before, O 1s shifts to higher binding energy (although, to a far lower extent, 0.18 eV) the reason for which was discussed above. Overall, this situation allows us to conclude that the charge transfer from the cluster to the support is in place, however, the transferred electrons do not localize at the (sub-)surface of TiO_2, but rather tend to dissipate into the bulk.

14. Supplementary photocatalytic performance data

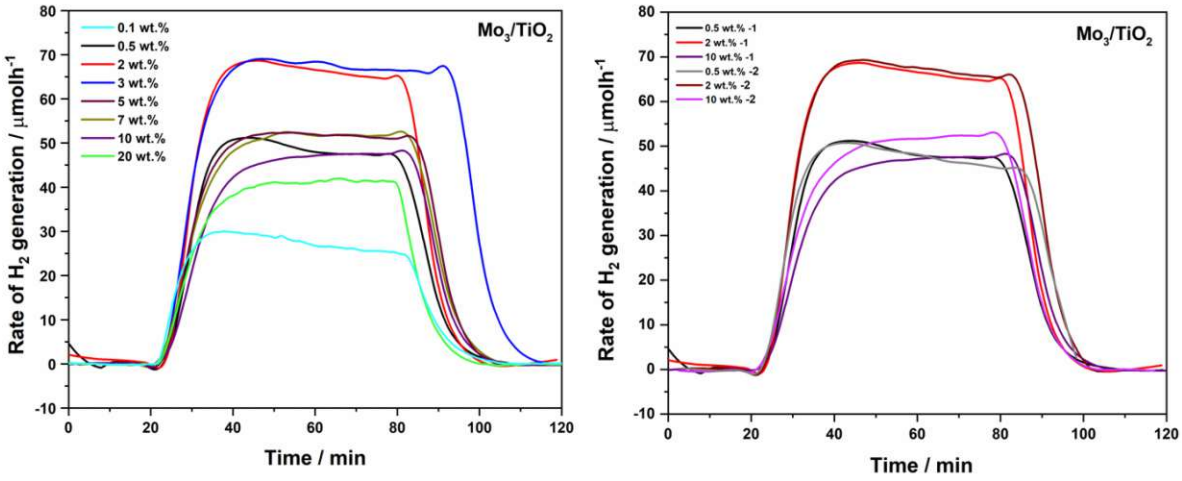

Fig. S12 | **(a)** The rate of hydrogen generation in µmol/h displayed by Mo_3/TiO_2 composites with 0.1-20 wt.% of cluster loading, **(b)** Reproducibility test for photocatalytic HER performance of Mo_3/TiO_2 composites with 0.5, 2, and 10 wt.% of cluster loading. Conditions: 0.25 mg/mL photocatalyst in MeOH:H_2O (1:1) illuminated by 365 nm LED source for 1 hour; see Methods for details. The photocatalytic performance plot in the main manuscript was constructed using the activity value reached after 60 minutes of light illumination.

In order to validate our photocatalytic setup, we performed blank and reference experiments, including those without light, without Mo_3/TiO_2 catalyst, using neat TiO_2 and neat $[Mo_3S_{13}]^{-2}$ cluster solution. In all the cases, we observed no H_2 evolution, which demonstrates that Mo_3/TiO_2 serves as an active HER photocatalyst.

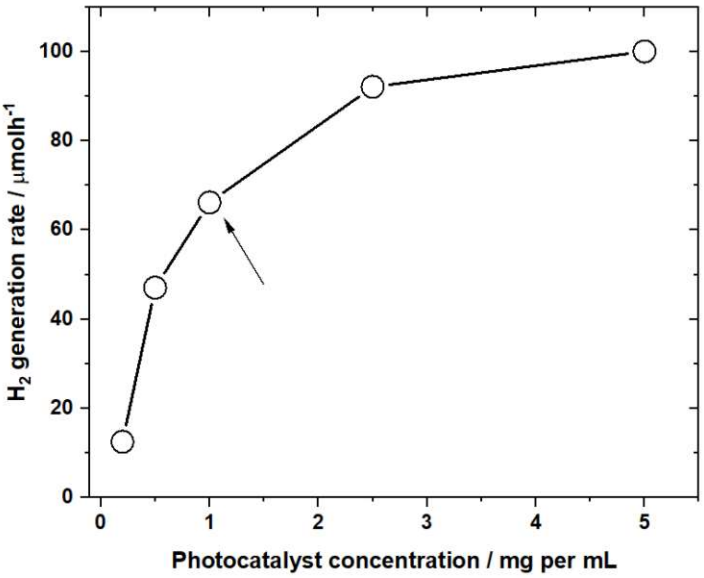

Fig. S13 | The rate of H_2 evolution plotted as a function of photocatalyst amount used.[4] Standard conditions used in this work correspond to 1 mg/mL suspensions of the $2Mo_3/TiO_2$ powders (details in Methods section of the main text). At this concentration, we ensure that sufficient photon flux is available for the absorption by the TiO_2, which allows minimizing the impact of $[Mo_3S_{13}]^{2-}$ parasitic absorption on the obtained H_2 generation rates.

15. Post-catalytic characterization

15.1 TXRF and EDS data

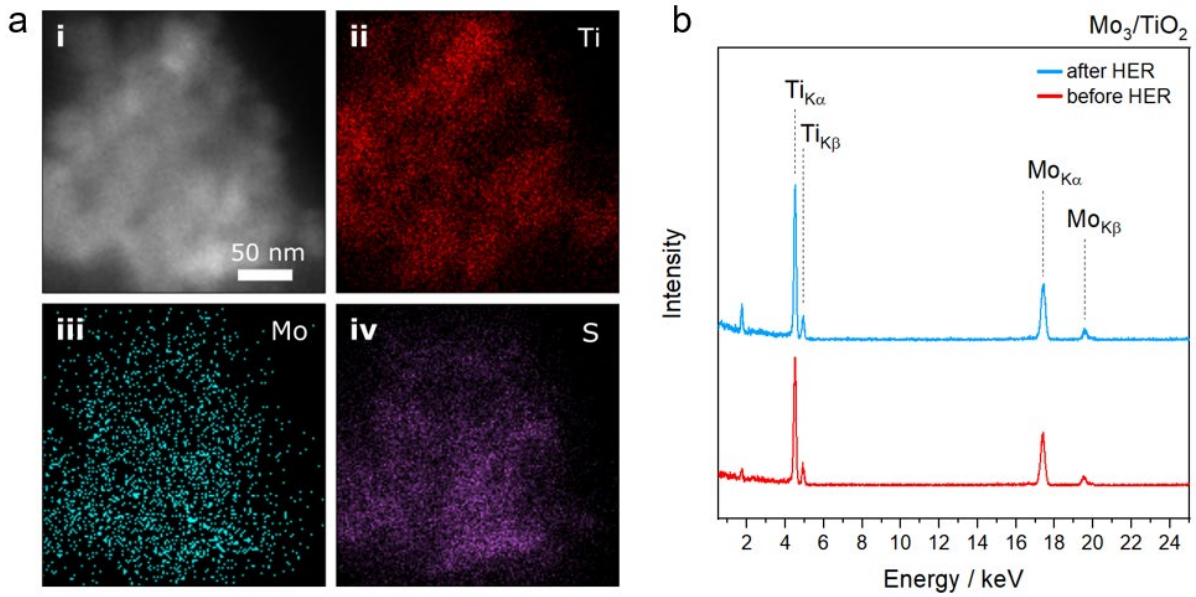

Fig. S14 | **(a)** EDS elemental mappings of Ti (ii), Mo (iii) and S (iv) of an exemplary $3Mo_3/TiO_2$ composite after the HER run showing the presence and homogeneous distribution of the relevant elements. **(b)** TXRF spectra of the Mo_3/TiO_2 before and after HER run showing the unchanged content of Mo.

Quantification of the TXRF data (see SI section Characterization techniques) and relative Ti:Mo ratios reveals cluster loading values of 5.06 wt.% (before reaction) and 4.90 wt.% (after reaction), which suggest that only a minor amount of leaching took place over the course of the photocatalytic reaction.

15.2 XPS data

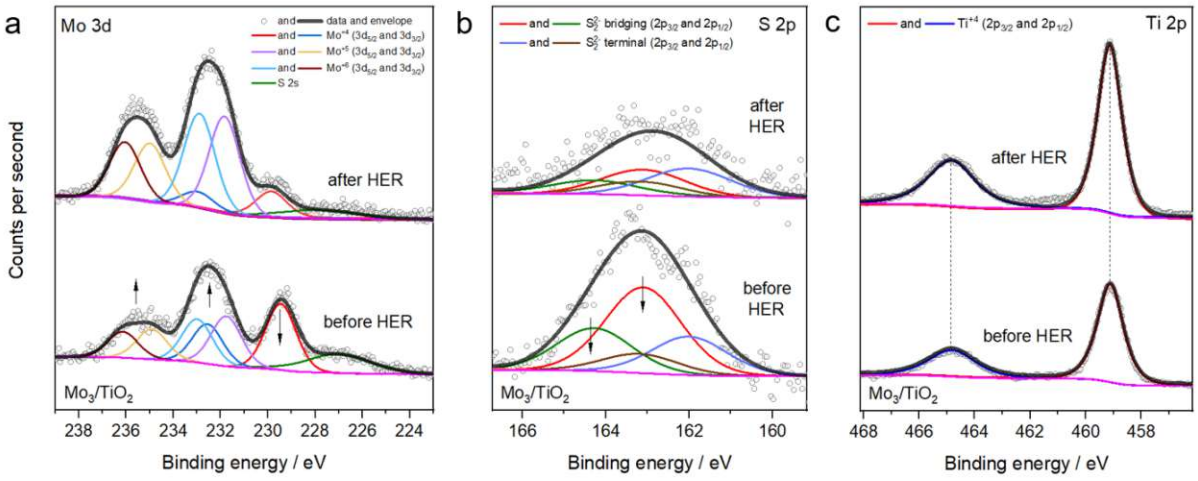

Fig. S15 | XPS spectra of the Mo_3/TiO_2 composites before and after HER run showing **(a)** Mo 3d, **(b)** S 2p and **(c)** Ti 2p regions with relevant fits.

16. Thermal treatments (TGA and *in situ* XRD) and HER performance

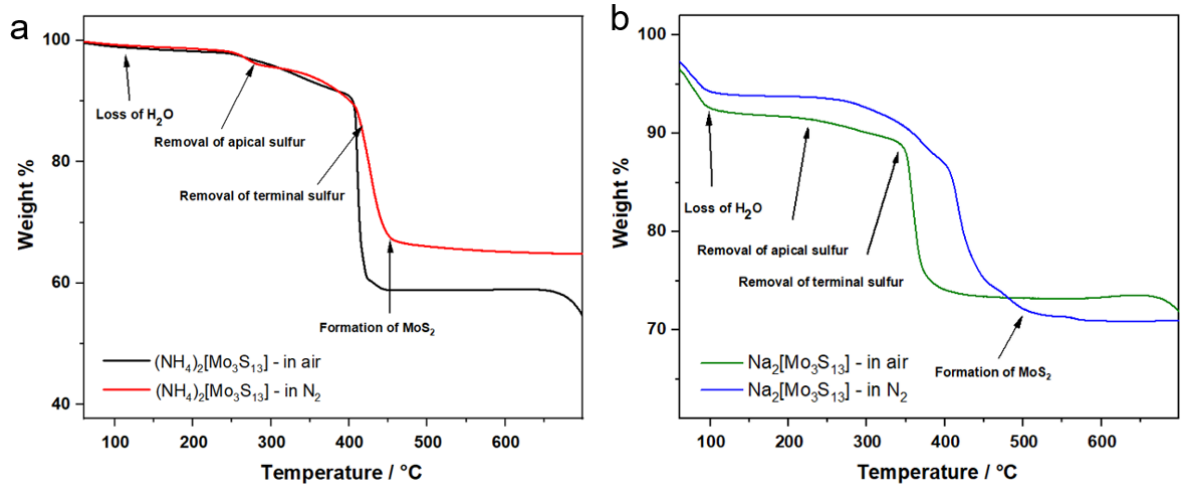

Fig. S16 | TGA profiles of **(a)** $(NH_4)_2[Mo_3S_{13}]$ and **(b)** $Na_2[Mo_3S_{13}]$ powders – used here to represent the behavior of $[Mo_3S_{13}]^{2-}$ anion – obtained under air (black and green) and N_2 (red and blue). Oxidation (in air) or transformation (in N_2) of the $[Mo_3S_{13}]^{2-}$ clusters take place in the temperature window of 250-450 °C. Decomposition of the cluster is facilitated in air compared to N_2.

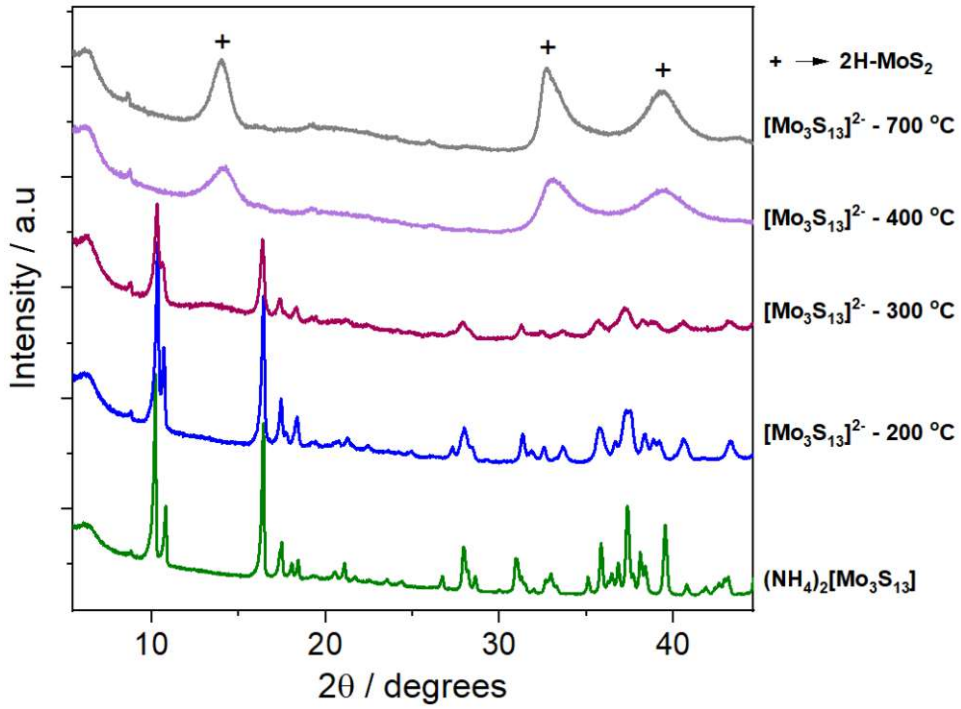

Fig. S17 | *in situ* XRD patterns obtained upon $(NH_4)_2[Mo_3S_{13}]$ – used here to represent the behavior of $[Mo_3S_{13}]^{2-}$ anion – heating under inert N_2 atmosphere (see Characterization techniques). The intact structure of the $[Mo_3S_{13}]^{2-}$ can be observed till at least 300 °C. Transformation to MoS_2-like pattern (broad peaks indicate small areas of structural order) takes place within the temperature window of 300-400 °C. Note: in situ XRD datasets of the $Na_2[Mo_3S_{13}]$ are more convoluted and were thus omitted for clarity.

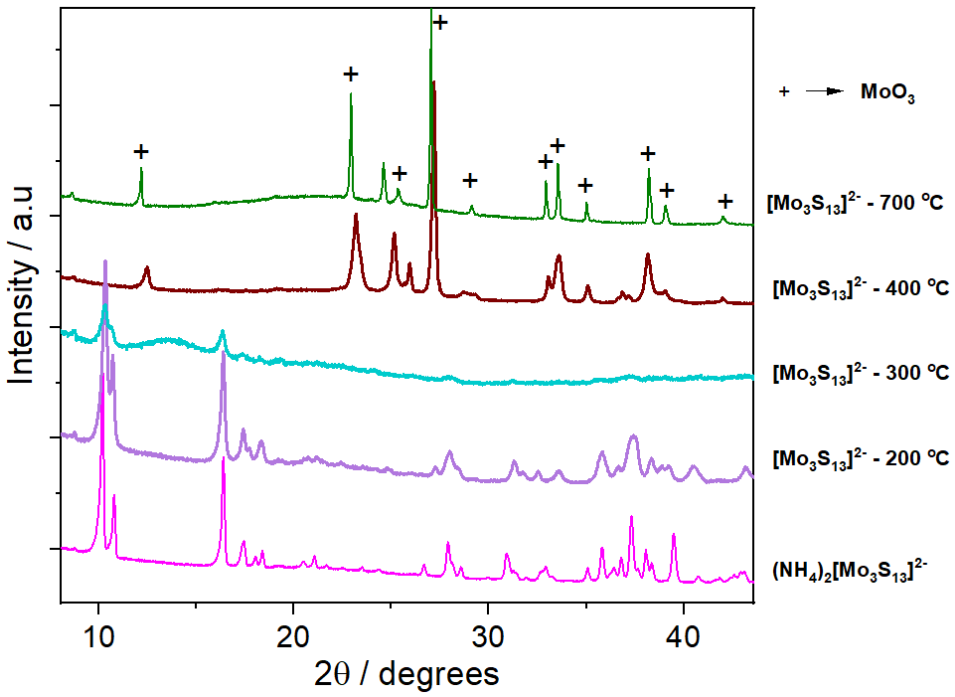

Fig. S18 | *in situ* XRD patterns obtained upon $(NH_4)_2[Mo_3S_{13}]$ heating under ambient air. The intact structure of the $[Mo_3S_{13}]^{2-}$ can be detected till at least 200 °C. In contrast to the treatment in N_2 (see above), XRD pattern at 300 °C manifests a strong loss of crystallinity, likely related to the facilitated oxidation and transformation of the original structure. The appearance of MoO_3 pattern takes place within the temperature window of 300-400 °C.

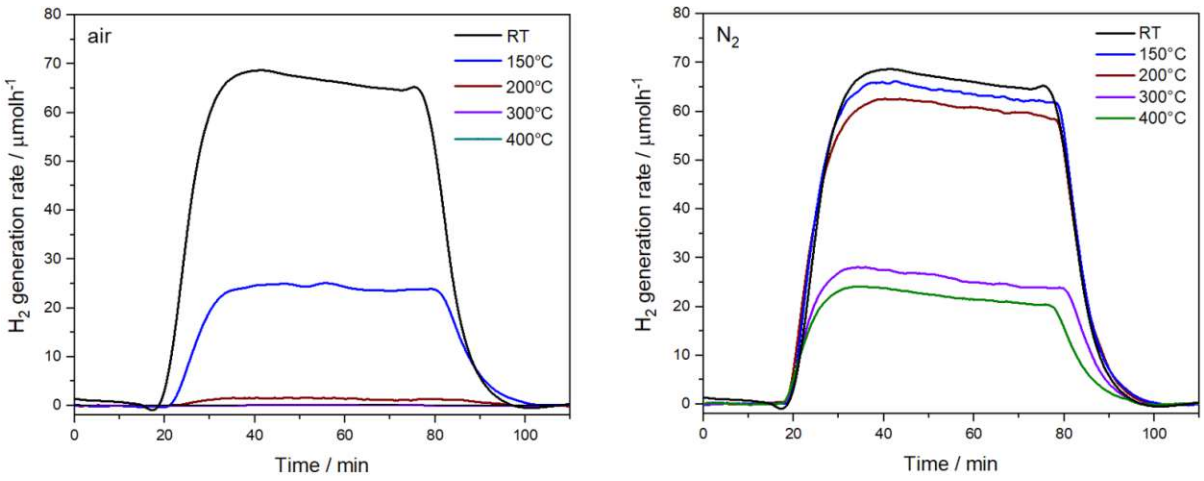

Fig. S19 | The hydrogen evolution rate in µmol/h displayed by $2Mo_3/TiO_2$ photocatalyst heat-treated at different temperatures (150-400 °C) in **(a)** air and **(b)** N_2.

17. List of references

(1) Wenderich, K.; Mul, G. Methods, Mechanism, and Applications of Photodeposition in Photocatalysis: A Review. *Chem. Rev.* **2016**, *116* (23), 14587–14619. https://doi.org/10.1021/acs.chemrev.6b00327.

(2) Kibsgaard, J.; Jaramillo, T. F.; Besenbacher, F. Building an Appropriate Active-Site Motif into a Hydrogen-Evolution Catalyst with Thiomolybdate $[Mo_3S_{13}]^{2-}$ Clusters. *Nat. Chem.* **2014**, *6* (3), 248–253. https://doi.org/10.1038/nchem.1853.

(3) Kashiwaya, S.; Olivier, C.; Majimel, J.; Klein, A.; Jaegermann, W.; Toupance, T. Nickel Oxide Selectively Deposited on the {101} Facet of Anatase TiO2 Nanocrystal Bipyramids for Enhanced Photocatalysis. *ACS Appl. Nano Mater.* **2019**, *2* (8), 4793–4803. https://doi.org/10.1021/acsanm.9b00729.

(4) Qureshi, M.; Takanabe, K. Insights on Measuring and Reporting Heterogeneous Photocatalysis: Efficiency Definitions and Setup Examples. *Chem. Mater.* **2017**, *29* (1), 158–167. https://doi.org/10.1021/acs.chemmater.6b02907.

4.2.4 Article #4

"Thiomolybdate Cluster for Visible-Light Driven Hydrogen Evolution: Comparison of Homogeneous and Heterogeneous Approaches"

Samar Batool, Jasmin S. Schubert, Pablo Ayala, Hikaru Saito, Maria J. Sampaio, Eliana S. Da Silva, Cláudia G. Silva, Joaquim L. Faria, Dominik Eder, Alexey Cherevan

Sustainable Energy & Fuels, Accepted
DOI: https://doi.org/10.1039/D3SE01658G

As the primary author of this work, my contributions concentrate on optimizing the conditions for the hydrogen evolution reaction involving thiomolybdate clusters in both homogeneous and heterogeneous phases. Additionally, I conducted extensive investigations, including FTIR, XPS, PL, and HER analyses, and was responsible for data curation, plot generation, and drafting of the article.

The corresponding Supplementary information of the article can be found on page 126.

Sustainable Energy & Fuels

Interdisciplinary research for the development of sustainable energy technologies

Accepted Manuscript

This article can be cited before page numbers have been issued, to do this please use: S. Batool, J. S. Schubert, P. Ayala, H. Saito, M. J. Sampaio, E. S. Da Silva, C. Gomes Silva, J. Faria, D. Eder and A. S. Cherevan, *Sustainable Energy Fuels*, 2024, DOI: 10.1039/D3SE01658G.

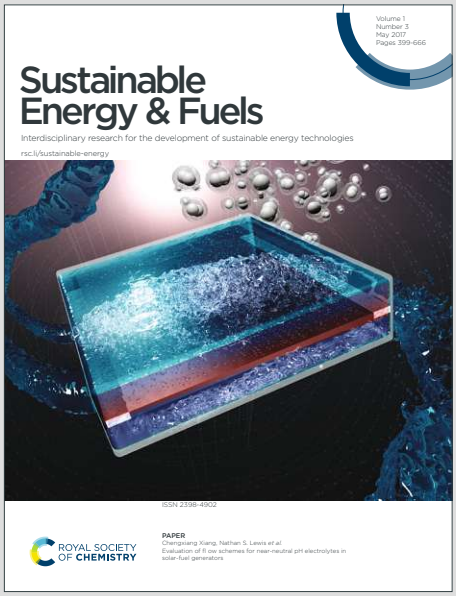

ROYAL SOCIETY OF CHEMISTRY

rsc.li/sustainable-energy

View Article Online
DOI: 10.1039/D3SE01658G

Thiomolybdate Cluster for Visible-Light Driven Hydrogen Evolution: Comparison of Homogeneous and Heterogeneous Approaches

Samar Batool[1], Jasmin S. Schubert[1], Pablo Ayala[1], Hikaru Saito[2], Maria J. Sampaio[3,4], Eliana S. Da Silva[3,4], Cláudia G. Silva[3,4], Joaquim L. Faria[3], Dominik Eder[1], Alexey Cherevan[1]*

[1] TU Wien, Institute of Materials Chemistry, Getreidemarkt 9/BC/02, 1060, Vienna, Austria

[2] Institute for Materials Chemistry and Engineering, Kyushu University, 6-1 Kasugakoen, Kasuga, Fukuoka 816-8580, Japan

[3] LSRE-LCM – Laboratory of Separation and Reaction Engineering – Laboratory of Catalysis and Materials, Faculty of Engineering, University of Porto, Rua Dr. Roberto Frias, 4200-465 Porto, Portugal

[4] ALiCE – Associate Laboratory in Chemical Engineering, Faculty of Engineering, University of Porto, Rua Dr. Roberto Frias, 4200-465 Porto, Portugal

Abstract:

This study investigates the hydrogen evolution reaction (HER) efficiency of two photosystems incorporating an all-inorganic molecular thiomolybdate $[Mo_3S_{13}]^{2-}$ cluster as HER catalyst. First, we delve into the performance of a homogeneous $[Mo_3S_{13}]^{2-}$/$[Ru(bpy)_3]^{2+}$ (Mo_3/Ru), dyad which demonstrates high turnover frequency (TOFs) and apparent quantum yields (AQYs) at 445 nm approaching the level of 0.5%, yet its performance is marked by pronounced deactivation. In contrast, a heterogeneous approach involves anchoring $[Mo_3S_{13}]^{2-}$ onto graphitic carbon nitride (GCN) nanosheets through weak electrostatic association with its triazine/heptazine scaffold. The $[Mo_3S_{13}]^{2-}$/GCN (Mo_3/GCN) displays effective H_2 generation under visible light, with TOF metrics on par with its homogeneous analog. Although substantial leaching of $[Mo_3S_{13}]^{2-}$ species from the Mo_3/GCN surface occurs, the remaining {Mo_3}-based centers demonstrate impressive stability, leading to enduring HER performance, starkly distinguishing it from the homogeneous Mo_3/Ru photosystem. Photoluminescence (PL) quenching experiments confirm that the performance of the Mo_3/GCN is not limited by the quality of the inorganic interface, but could be optimized by using higher surface area supports or higher concentration of $[Mo_3S_{13}]^{2-}$ sites. Our findings showcase complexities underlying the evaluation and comparison of photosystems comprising well-defined catalytic centers and pave the way for developing analogous surface-supported (photo)catalysts with broad use in energy applications.

Keywords*:* cluster, charge transfer, interface, thiometalate, single-site

1. Introduction

Photocatalysis is often cited as one of the most sustainable and straightforward methods for producing solar fuels from renewable energy resources. Despite decades of research,[1] however, only a limited number of efficient and stable photosystems for water splitting have been identified,[2,3] indicating that the path towards developing high-performance photocatalysts is far from straightforward.[4] As a result, the scientific community continues to search for a set of comprehensive design principles that can guide the synthesis of selective and stable photocatalysts, enabling the efficient conversion of solar energy into chemical energy.[5–8]

Direct capture of sunlight energy and its use to facilitate the desired chemical reaction can be accomplished using either a homogeneous or heterogeneous photosystem that by definition bear pronounced differences in terms of their structure (molecules vs. solids), composition (mostly organic vs. mostly inorganic), solubility characteristics (molecular solutions vs.

View Article Online
DOI: 10.1039/D3SE01658G

suspensions), underlying charge transfer and separation processes as well as the nature of the catalytic sites. Many homogeneous photocatalytic systems enjoy high turnover frequencies (TOFs), however – compared to their heterogeneous counterparts – often suffer from low turnover numbers (TONs) on account of photosensitizer degradation, catalyst self-aggregation, or formation of colloidal oxide species. Heterogeneous photocatalysts, on the other hand, benefit from adjustable absorption characteristics and superior stability towards harsh redox conditions of the photocatalytic reaction but face complications associated with their poorly defined catalytic surface, which limit the degree of control over the processes of charge extraction and interfacial charge transfer.

In light of these challenges and prospects, a hybrid approach that combines the advantages of both homogeneous and heterogeneous photocatalytic systems emerges as a promising solution. Several important avenues of this combination have been explored by the community over the past decades. One example involves single-metal-site and single-metal-atom catalysts which allow the creation of robust all-inorganic photosystems with unparalleled atom-utilization efficiency.[9–11] Another strategy exploits stabilization of the well-defined molecular catalysts on the surface of solid-state (photoactive) supports, such as in the case of Co-based (Co_4O_4) water oxidation catalyst (WOC) recently embedded within the pores of a rigid coordination network,[12] or in the field of surface organometallic chemistry which relies on the immobilization of complexes onto structurally-controlled inorganics surfaces.[13,14] Additionally, metal-organic frameworks (MOFs) can be regarded as a promising hybrid photosystem due to their ability to merge molecular units (ligands and metal nodes) into a crystalline solid-state material, thus incorporating the benefits of both molecular and inorganic approaches to (photo)catalysis.[15] Despite these and many other combinations of the molecular and solid-state photosystems have been explored, only rare studies were able to directly compare the photocatalytic performance of similar photocatalytic systems under homogeneous and heterogeneous conditions.[16] Nevertheless, by investigating the effects of molecular catalyst immobilization, one can gain insights into the factors that contribute to or restrict the performance of the heterogenized catalysts. This type of investigation enables a more comprehensive understanding of the underlying mechanisms and provides valuable information for the design and optimization of highly efficient and stable hybrid photosystems.

Aiming to complement this knowledge gap, we turned our attention to an inorganic thiometalate cluster $[Mo_3S_{13}]^{2-}$, which recently emerged as promising noble-metal-free catalysts for hydrogen evolution reaction (HER).[17] This trinuclear cluster features all the advantages of a molecular catalyst – including the defined geometry, structure and composition – which together allow to shed light on its active sites and elucidate the reaction mechanisms.[18–20] Over the past years, examples of $[Mo_3S_{13}]^{2-}$ immobilization onto visible-light-active carbon nitride have been reported confirming the ability of surface-attached $[Mo_3S_{13}]^{2-}$ to act as a HER co-catalyst.[21,22] Additionally, two recent works reported that the encapsulation of $[Mo_3S_{13}]^{2-}$ clusters into porous heterogeneous scaffolds – such as covalent organic frameworks (COFs)[23] and MOFs[24] – yield stable photocatalytic systems, which further emphasizes the benefits of the heterogenization strategy. Most recently, our group reported surface-anchoring of $[Mo_3S_{13}]^{2-}$ on a carbon-free support, *i.e.* TiO_2, which involved covalent binding and resulted in high and stable HER rates comparable to those of the benchmark Pt/TiO_2.[25]

This work sets to provide a more comprehensive understanding of the benefits and limitations of heterogenization strategy. Specifically, we aim to directly compare the activity, stability, and

View Article Online
DOI: 10.1039/D3SE01658G

other important performance indicators of surface-anchored $[Mo_3S_{13}]^{2-}$ clusters with their performance towards HER under strictly homogeneous conditions. Our data reveal that despite $[Mo_3S_{13}]^{2-}$ is able to deliver excellent HER performance under homogeneous conditions, strong and rapid deactivation is imminent for this photosystem. In contrast to this, heterogenized $[Mo_3S_{13}]^{2-}$ shows much more stable HER performance with no apparent cluster degradation. Our photoluminescence spectroscopy quenching studies further compare redox pathways in both the photosystem and quantitatively compare their charge transfer kinetics. The data reveal that the performance of the heterogenized $[Mo_3S_{13}]^{2-}$ can be strongly limited by the degree and effectiveness of the electron-hole separation and that an increase of the $[Mo_3S_{13}]^{2-}$ loading or support surface area available for cluster immobilization may play crucial role in unravelling full potential of this and other relevant thiomolybdate catalysts.[20]

2. Results and Discussion

We start by describing two photosystems – a homogeneous and a heterogeneous – involving thiomolybdate $[Mo_3S_{13}]^{2-}$ cluster as an HER catalyst. On one hand, we evaluate HER performance of the cluster under strictly homogeneous conditions – denoted here as Mo_3/Ru – which involves the use of a state-of-the-art molecular dye, tris(bipyridine)ruthenium (II) ($[Ru(bpy)_3]^{2+}$), as a visible-light photosensitizer (Figure 1a left).[18,26] On the other hand, we explore the performance of the heterogenized $[Mo_3S_{13}]^{2-}$ cluster following its deposition on thermally-exfoliated graphitic carbon nitride (GCN, details on synthesis are in Experimental section). This photosystem is denoted here as Mo_3/GCN. As shown in Figure 1a (right), GCN sheets take the role of the light absorber (i.e. photosensitizer), while the $[Mo_3S_{13}]^{2-}$ clusters anchored on the surface act as a formal co-catalyst,[21,22] i.e. they extract the photoexcited charge carriers from GCN bulk and promote the reaction of interest by reducing H^+ to H_2. Compared to our previous work in which $[Mo_3S_{13}]^{2-}$ was anchored onto titania surface,[25] the use of narrow-band gap GCN enables absorption of visible-light photons and thus allows a direct comparison of Mo_3/GCN with the homogeneous visible-light-driven Mo_3/Ru photosystem (Figure 1b and Section 2 ESI).

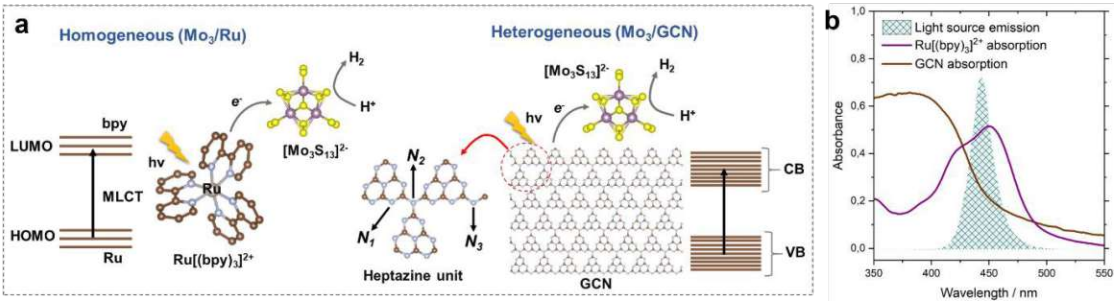

Fig. 1 | Photocatalytic HER mechanisms on (a) Mo_3/Ru (homogeneous) and Mo_3/GCN (heterogeneous) photosystems (brown: C; blue: N; purple: Mo; yellow: S) showing their main components as well as the photoexitation and charge transfer pathways; LUMO and HOMO stand for the lowest unoccupied and the highest occupied molecular orbitals of $[Ru(bpy)_3]^{2+}$; CB and VB stand for the conduction and valence bands of GCN; N_1, N_2 and N_3 correspond to three types of N atoms building the heptazine unit of the GCN framework, **(b)** Absorption spectra of $[Ru(bpy)_3]^{2+}$ (in methanol, 10^{-5} M) and GCN (via diffuse-reflectance spectroscopy, DRS, details in Experimental section) used to construct the photosystems overlaid with the emission spectrum of the narrow-band LED lamp (center wavelength of 445 nm, details in Experimental section) used in the photocatalytic studies.

The heterogeneous Mo_3/GCN will be first described from the point of view of its composition and structure. Following this, photocatalytic HER results – in terms of activity, mechanism and stability – of Mo_3/Ru and Mo_3/GCN will be presented and compared aiming to reveal factors that control or limit their catalytic performance.

View Article Online
DOI: 10.1039/D3SE01658G

2.1 **Heterogenized Mo_3/GCN photosystem**

$Na_2[Mo_3S_{13}]$ and graphitic carbon nitride (GCN) were synthesized according to previously established methods (see Experimental section) and their purity and structure were confirmed using powder X-ray diffraction (XRD) and IR spectroscopy (Figure S1). Diffuse reflectance spectroscopy (DRS) of as-obtained GCN nanosheets reveal pronounced absorption in the visible range (absorption tail beyond 500 nm) corresponding to the expected optical band gap of 2.75 eV (Figure S2a and b), which confirms the capability of the supporting GCN to absorb in the range of the molecular $[Ru(bpy)_3]^{2+}$ sensitizer.[27] The $[Mo_3S_{13}]^{2-}$/GCN composite (Mo_3/GCN) was synthesized following a wet-impregnation route (for more details see Experimental section). Compared to the DRS spectrum of bare GCN, the DRS spectra of the Mo_3/GCN show an additional broad band centered at 456 nm (Figure S3), which can be ascribed to characteristic ligand-to-metal charge transfer transition of $[Mo_3S_{13}]^{2-}$ suggesting successful deposition of $[Mo_3S_{13}]^{2-}$ onto GCN surface.[28] Total reflection X-ray fluorescence spectroscopy (TXRF) further confirms the presence of Mo in the composite and allows to estimate the real $[Mo_3S_{13}]^{2-}$ loading to be around 3.9 wt.% (Table 1, details in Experimental section). Interestingly, this value is significantly lower compared to the intended loading of 10 wt.% and – in contrast to oxide-based supports[25] – indicates a weaker nature of the interaction between organic GCN and $[Mo_3S_{13}]^{2-}$. A similar actual-to-expected loading is also attained for 1 wt.% nominal loading value (Table 1), which further corroborates that the adsorption of $[Mo_3S_{13}]^{2-}$ on GCN is not governed by the presence of suitable adsorption sites on the GCN surface, but is rather defined by the adsorption/desorption equilibrium.

Table 1: Quantification of real loadings of $[Mo_3S_{13}]^{2-}$ cluster in Mo_3/GCN composites derived from TXRF data.

Composites	Nominal loadings $[Mo_3S_{13}]^{2-}$ (wt.%)	Real loadings $[Mo_3S_{13}]^{2-}$ (wt.%)
Mo_3/GCN	10	3.9
	1	0.36
Mo_3/H-GCN	10	5.1

Attenuated total reflectance Fourier transform infrared spectroscopy (ATR-FTIR) spectra of the pristine GCN (Figure S4) match well with literature, confirming the formation of heptazine-based scaffold (Figure 1a, right).[27] Notably, the results for Mo_3/GCN composites show no vibrations corresponding to $[Mo_3S_{13}]^{2-}$, as expected from the low cluster loadings. Therefore, scanning transmission electron microscopy (STEM) was used to provide evidence for the presence of $[Mo_3S_{13}]^{2-}$ on GCN surface. Energy dispersive X-ray (EDX) maps acquired on the nanoscale (Figure 2a and b) confirm chemical identity of the elements and reveal an even distribution of Mo and S over the entire surface of the GCN aggregates. High-resolution Fast-Fourier transformed (FFT) image in Figure 2c focuses on the edge of a typical GCN flake and shows the presence of multiple bright spots. Considering the high Z-contrast between Mo and C/N atoms, these spots likely correspond to heavy Mo atoms dispersed on GCN and their high density further indicates close proximity of the clusters. Interestingly, a closer look on Figure 2c also reveals the formation of chain-like structures suggesting the possibility of partial cluster oligomerization, in line with MoS_x-based nanostructuring observed on similar carbon-based surfaces.[29]

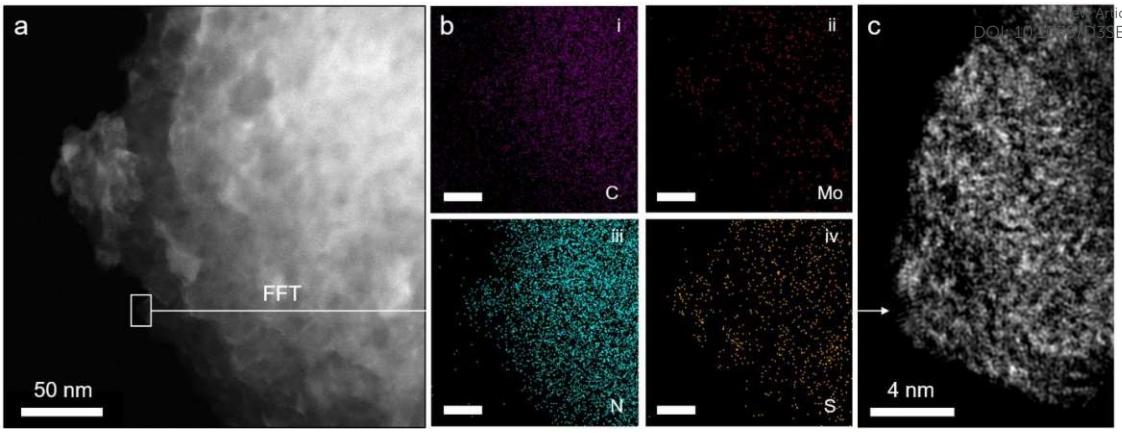

Fig. 2 | STEM micrographs of the Mo_3/GCN composite (a) High-resolution high-angle annular dark field (HAADF) STEM image of Mo_3/GCN composite showing an aggregate of GCN nanoflakes along with its **(b)** EDS-derived elemental mappings featuring the distribution of (i) C, (ii) Mo, (iii) N, and (iv) S elements, **(c)** FFT-transformed magnified region of one of the GCN flake's edges (see selected area in (a)), showing collections of bright spots that correspond to the heavy Mo atoms.

Surface-sensitive X-ray photoelectron spectroscopy (XPS) was further used to verify the structure of $[Mo_3S_{13}]^{2-}$ after attachment. The survey spectra confirm the presence of all elements expected from the Mo_3/GCN composition (Figure S5). The detailed Mo 3d profile of Mo_3/GCN in Figure 3a only shows peaks corresponding to Mo^{4+} with an overall profile that resemble that of the free $[Mo_3S_{13}]^{2-}$ cluster. This indicates the preference for a trinuclear structure of the cluster cores and further suggests that neither oxidation nor decomposition of the central $\{Mo_3\}$ units of the cluster occurred upon anchoring. Importantly, we also observe a shift of the Mo 3d peaks maxima by 1.2 eV to higher binding energies, which is indicative of electronic interactions involving charge transfer from the cluster to the support, in line with the anionic nature of $[Mo_3S_{13}]^{2-}$. The S 2p signal profile of the Mo_3/GCN undergoes a more significant change upon attachment, which suggests a restructuring of the S-containing ligands. A closer look at the deconvoluted profiles (Figure 3b) indicates partial loss of bridging disulfides, which can be linked to the partial transformation of the clusters into more complex MoS_x fragments, in line with cluster oligomerization observed in STEM.[30] Detailed analysis of the N 1s edge (Figure 3c) further allows to evaluate the nature of the cluster binding and the degree of $[Mo_3S_{13}]^{2-}$/GCN interactions from the support point of view. In the case of Mo_3/GCN composite, we observe a strong drop in the major C=N-C component (N_1) and a concurrent rise of the quaternary N-$(C)_3$ signal (N_2), which suggests that the cluster attachment causes the disruption of the GCN framework – specifically its heptazine/triazine units – in line with electrostatic binding model (Figure 1a, right). Overall, the data suggest successful heterogenization of high-density thiomolybdates on the surface of exfoliated GCN nanosheets and confirm their homogeneous deposition along with intact nature of their $\{Mo_3\}$ cores.

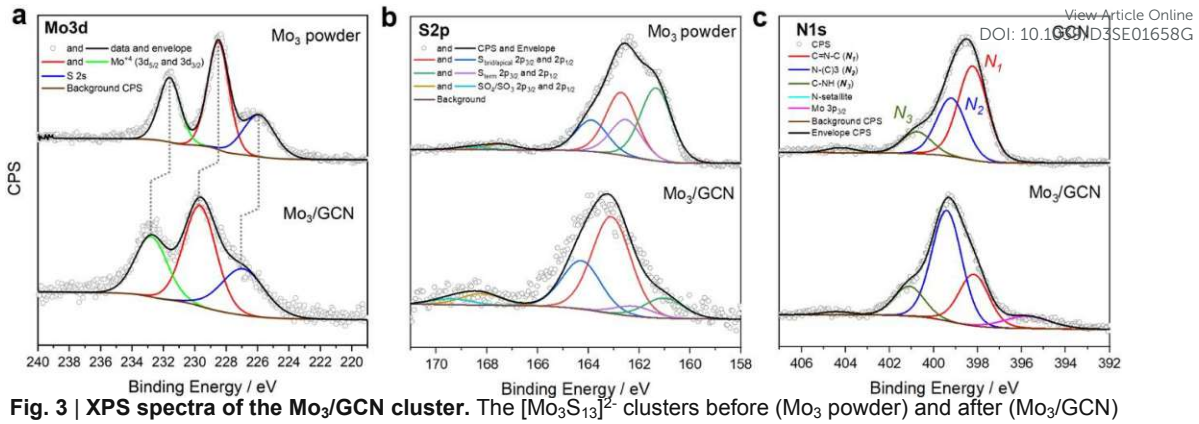

Fig. 3 | XPS spectra of the Mo_3/GCN cluster. The $[Mo_3S_{13}]^{2-}$ clusters before (Mo_3 powder) and after (Mo_3/GCN) attachment to the GCN surface **(a)** Mo3d, **(b)** S2p, **(c)** N1s (N_1: Pyridinic nitrogen; N_2: Quaternary nitrogen; N_3: Secondary amine), with corresponding fits.

2.2 **Optimization of HER conditions**

Homogeneous photosystem. We first established experimental HER protocols for the Mo_3/Ru molecular catalyst/absorber dyad. Two works have recently reported photocatalytic HER performance of $NH_4[Mo_3S_{13}]$ clusters under homogeneous conditions, which laid the foundation for our study. Dave *et al.*[18] performed visible-light-driven HER experiments using a custom-built reactor filled with 2 mL of reaction mixture consisted of 0.3 μM $[Mo_3S_{13}]^{2-}$ as a catalyst, 20 μM $[Ru(bpy)_3]^{2+}$ as a sensitizer and 0.1 M ascorbic acid (H_2A) as an electron donor using methanol:water (MeOH:H_2O, 9:1) as a mixed solvent system. In parallel, Lei *et al.*[26] evaluated HER performance of $[Mo_3S_{13}]^{2-}$ with $[Ru(bpy)_3]PF_6$ as a sensitizer, using 0.1 M of H_2A as sacrificial agent in a acetonitrile:water (ACN:H_2O, 9:1) solvent mixture. Considering the relatively similar set of conditions reported in these works, we first validated our Mo_3/Ru photosystem by using both MeOH:H_2O and CH_3CN:H_2O solvent mixtures with various sensitizer-to-catalyst concentration ratios: 65-to-1 (similar to conditions by Dave *et al.*) and 13-to-1 (similar to conditions by Lei *et al.*) – details in Experimental section. Table S1 shows that the Mo_3/Ru couple could generate H_2 in both solvent systems with apparent quantum yield (AQY) values of up to 0.5%, whereas a 5-fold decrease of $[Mo_3S_{13}]^{2-}$ concentration only resulted in 2-fold drop in H_2 amount generated. This non-correlated behavior indicates that the HER performance of this homogeneous photosystems is rather limited by light capture efficiency i.e. photosensitization.

Next, aiming for the ultimate comparison of homogeneous Mo_3/Ru and heterogenized Mo_3/GCN samples, apart from the ascorbic acid previously employed as an electron donor, we also considered methanol (MeOH, being a representative alcohol) and triethanolamine (TEOA, being a representative tertiary amine) commonly used as sacrificial agents in literature (details in Section 3 in ESI). Two important results can be highlighted. Firstly, since the use of MeOH/H_2O solvent mixture originally proposed by Dave *et al.* yielded much higher HER performance of the Mo_3/Ru couple (4-fold increase), we aimed to verify if MeOH additionally acts as an electron and proton donor.[31] HER experiments in MeOH solutions with and without the addition of sacrificial donor (H_2A) in Figure S6 show that no H_2 could be generated in absence of H_2A, confirming that MeOH acts only as a solvent. Secondly, we observed that the replacement of H_2A with TEOA yielded no H_2 (see Table 2), which we relate to the inability of $[Ru(bpy)_3]^{2+}$ to oxidize the amine due to its low-lying redox potential. Based on these results, we continue the benchmarking of the Mo_3/Ru performance obtained from methanolic H_2A solutions.

View Article Online
DOI: 10.1039/D3SE01658G

Table 2: Amount of H_2 produced by $[Mo_3S_{13}]^{2-}$ in homogeneous (Mo_3/Ru) and heterogenous (Mo_3/GCN) photosystems after 60 min of visible light illumination with 445 nm. Turnover frequencies (TOFs) are calculated based on the real $[Mo_3S_{13}]^{2-}$ loadings derived from TXRF (Table 1). Blank experiments in the absence of $[Mo_3S_{13}]^{2-}$ resulted in negligible (<0.1 nmol) amount of H_2 generated.

Phase	Catalyst	Sacrificial donor	Solvent	Photosensitizer	H_2 (nmol)	TOF (min^{-1})
Homogeneous	$[Mo_3S_{13}]^{2-}$ 50 µM	H_2A 0.1M	MeOH: H_2O (9:1)	$[Ru(bpy)_3]PF_6$ 0.645 mM	390	0.065
		TEOA 0.1M			< 0.1	-
Heterogeneous	Mo_3/GCN 10 wt.%	H_2A 0.1M	H_2O	none	52	0.062
		TEOA 0.1M			197	0.237
	Mo_3/GCN 1 wt.%	TEOA 0.1M			9	0.117
	Mo_3/H-GCN 10 wt.%	TEOA 0.1M			241	0.221

Heterogenized photosystem. The HER performance of Mo_3/GCN was evaluated with an identical photocatalytic setup (description in Experimental section) using 0.5 mg/mL of Mo_3/GCN photocatalyst suspensions in water. The choice of the sacrificial agent, however, becomes a crucial aspect for the comparison: while our data show that H_2A yields highest HER rates for Mo_3/Ru under homogeneous conditions (Figure S6), the overwhelming majority of literature employs tertiary amines (such as triethanolamine, TEOA) for GCN-based photocatalysts to allow for efficient hole scavenging at the GCN/solution interfaces. On one hand, TEOA acts as an amphiphilic surfactant allowing to bridge the relatively non-polar surface of GCN with water molecules;[32] on the other hand, it helps the dispersion of GCN nanostructures (often two-dimensional sheets) in the solution,[33] which in turn facilitates the extent of charge separation and transfer. In view of these factors, for further benchmarking, the HER performance of Mo_3/GCN is discussed using both sacrificial agents: H_2A and TEOA.

2.3 **Comparison of both photosystems**

HER performance. Table 2 provides an overview of the photocatalytic performance of the homogeneous Mo_3/Ru and the heterogeneous Mo_3/GCN. While substantially more H_2 could be generated by $[Mo_3S_{13}]^{2-}$ under homogeneous conditions by using H_2A (390 umol/h vs 52 umol/h, for Mo_3/Ru and Mo_3/GCN, respectively), both conditions reveal similar activity per thiomolybdate cluster when considering the number of $[Mo_3S_{13}]^{2-}$ species present ($TOF_{Mo3/Ru}$ is 0.065 min^{-1} and $TOF_{Mo3/GCN}$ is 0.062 min^{-1}). This result shows that heterogenized $[Mo_3S_{13}]^{2-}$ clusters are able to deliver HER performance on par with that of their homogeneous counterpart. The use of TEOA for the Mo_3/GCN composite – as a more reactive electron donor – further results in a substantial boost of its TOF values reaching as much as 0.237 min^{-1}, which suggest that the HER performance of the Mo_3/GCN composite could be limited by the inefficient (slow) scavenging of the holes photoexcited in GCN rather than by H^+ reduction.

Limiting factors. We next probed other factors that could be in control of the HER performance of the Mo_3/GCN composite by examining the impact of $[Mo_3S_{13}]^{2-}$ loading and its attachment strength on the photocatalytic activity. First, we compared the HER performance of Mo_3/GCN samples loaded with 3.9 and 0.36 wt.% of $[Mo_3S_{13}]^{2-}$ (refer to Table 1 for nominal values) and revealed that the higher loading yielded a 22-fold increase in H_2 amounts generated (i.e. 197 vs 9 nmol). This strong activity-loading correlation suggests that the overall performance of the heterogeneous Mo_3/GCN is restricted by the number of catalytic sites – $[Mo_3S_{13}]^{2-}$ – available on the GCN surface. Second, we prepared a composite using protonated GCN (H-

View Article Online
DOI: 10.1039/D3SE01658G

GCN) with positively charged surface which offers more favorable interactions with the anionic $[Mo_3S_{13}]^{2-}$ (for more details, see Methods).[21,34,35] As expected, impregnation of H-GCN with $[Mo_3S_{13}]^{2-}$ resulted in 5.1 wt.% thiomolybdate loading, a 30% increase compared to the case of bare GCN (3.9 wt.%, see Table 1). Nevertheless, when normalizing HER performances of both composites to the number of $[Mo_3S_{13}]^{2-}$ present (Table 2), similar TOF values are obtained for Mo_3/GCN (0.237 min^{-1}) and Mo_3/H-GCN (0.221 min^{-1}). This strongly suggests, that the kinetics of the interfacial charge transfer from GCN to $[Mo_3S_{13}]^{2-}$ is not a factor that restricts charge separation and utilization.

These performance-related findings indicate that: (a) the number of electrons taking part in H^+ reduction (i.e. HER) is directly proportional to the amount of $[Mo_3S_{13}]^{2-}$ on the surface, suggesting that the overall HER performance can be improved by having more $[Mo_3S_{13}]^{2-}$ sites present. (b) The transfer of photoexcited electrons from GCN to $[Mo_3S_{13}]^{2-}$ is rapid with respect to H^+ reduction (i.e. HER) and is not improved when a stronger $[Mo_3S_{13}]^{2-}$ to GCN interaction/interface is created. (c) The effective scavenging of photoexcited holes can be seen as a performance-limiting factor, which needs to be addressed possibly by introducing other sacrificial agents or appropriate oxidation co-catalysts to aid in efficient charge extraction, separation and utilization.

HER mechanism. Photoluminescence (PL) emission spectroscopy quenching studies were conducted to get further insights into the mechanism of photocatalytic HER by Mo_3/Ru and Mo_3/GCN systems. For Mo_3/Ru photosystem, the addition of different amounts of H_2A quenched the PL emission of $[Ru(bpy)_3]^{2+}$ (Figure 4a) with a rate constant ($K_{q,red}$) of $1.2*10^7$ M^{-1} s^{-1} when calculated from a linear Stern-Volmer fitting assuming the dynamic quenching mechanism (Figure S8a). This is in line with H_2A acting as an electron donor as its ascorbate anion (HA^-) can reductively quench the excited $*[Ru(bpy)_3]^{2+}$ to $[Ru(bpy)_3]^{+}$. When using different concentrations of $[Mo_3S_{13}]^{2-}$ (Figure 4b), we can also observe oxidative quenching of the excited state of $*[Ru(bpy)_3]^{2+}$ with a rate constant ($K_{q,ox}$) of $1.8x10^{10}$ M^{-1} s^{-1} (Figure S8b), which is three orders of magnitude higher than that measured for H_2A. Since our photocatalytic system includes both the H_2A (1 mM) and $[Mo_3S_{13}]^{2-}$ (50 μM), both oxidative and reductive quenching mechanisms (*I* and *II* in Figure 4d) take part in the electron transfer processes. However, given the much higher $K_{q,ox}$ compared to $K_{q,red}$, the oxidative quenching (extraction of the electron by thiomolybdate cluster) is likely to dominate the process under turnover conditions, which can be in part explained by the strong electrostatic interaction (ion pairing) between cationic $[Ru(bpy)_3]^{2+}$ and anionic $[Mo_3S_{13}]^{2-}$. These data allow to suggest the following mechanism for the Mo_3/Ru photosystem (Figure 4d): excited $*[Ru(bpy)_3]^{2+}$ state formed after light absorption undergoes rapid oxidatively quenching by the transfer of electrons to $[Mo_3S_{13}]^{2-}$ catalyst where H^+ are reduced to H_2. Meanwhile, the oxidized $[Ru(bpy)_3]^{3+}$ is reductively quenched to its ground state by the H_2A present in solution, thereby completing the catalytic cycle.

For Mo_3/GCN, PL spectra of the composites feature two absorption maxima at around 440 and 480 nm that correspond to the π–π* and n–π* transitions within GCN (Figure 4c).[27] Compared to the emission of the bare GCN, the deposition of $[Mo_3S_{13}]^{2-}$ leads to a strong PL quenching which can be associated with the facilitated charge separation that highlights the role of $[Mo_3S_{13}]^{2-}$ as a reductive co-catalyst capable of effective extraction of photoexcited electrons. Following the idea of concentration-dependent quenching studies of our Mo_3/Ru, we also observed that heterogenized Mo_3/GCN composites with different loadings of $[Mo_3S_{13}]^{2-}$ exhibit different emission intensities. As can be seen in Figure 4c, increasing the cluster content from 5 wt.% to 10 wt.% (nominal values) results in more pronounced PL quenching indicating that charge transfer at the $[Mo_3S_{13}]^{2-}$/GCN interface is further facilitated when higher number of $[Mo_3S_{13}]^{2-}$ is present at the surface. Analyzing the Mo_3/GCN quenching datasets

View Article Online
DOI: 10.1039/D3SE01658G

based on three $[Mo_3S_{13}]^{2-}$ loading values – and assuming that Stern-Volmer relationship can be applied to describe the kinetics of the GCN quenching – yields a quenching constant $K_{q,ox}$ of around 4.1×10^7 M^{-1} s^{-1} (Figure S8c). This value is several orders of magnitude lower than the one obtained for the homogeneous Mo_3/Ru case (1.8×10^{10} M^{-1} s^{-1}), which is expected for the solid/liquid Mo_3/GCN interface. In conjunction with HER discussion above, these insights suggest that the use of photoactive supports with higher surface area available for $[Mo_3S_{13}]^{2-}$ immobilization could lead to further optimization of the Mo_3/GCN photosystem's performance.

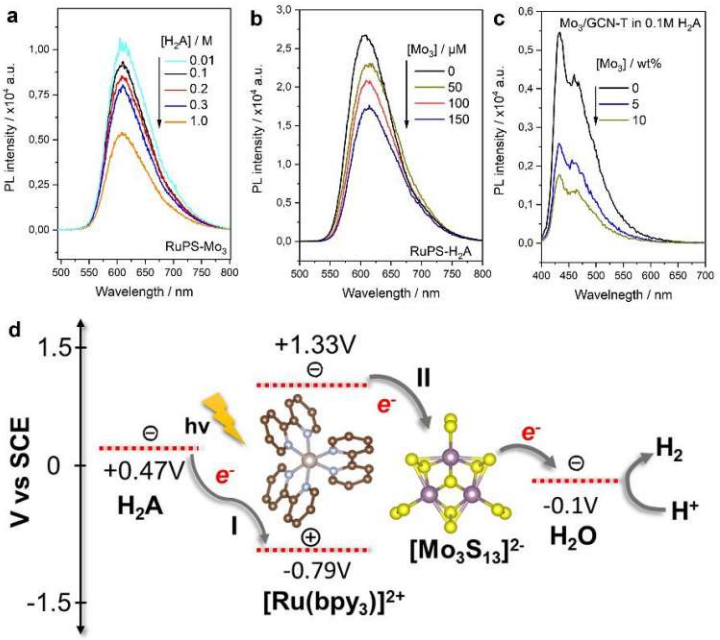

Fig. 4 | PL emission spectra of Mo_3/Ru system with varying (a) H_2A and **(b)** $[Mo_3S_{13}]^{2-}$ concentrations, **(c)** Mo_3/GCN system with varying $[Mo_3S_{13}]^{2-}$ loading, **(d)** Schematic of reductive (I) and oxidative (II) quenching mechanisms of $[Ru(bpy)_3]^{2+}$ photosensitizer in the presence of $[Mo_3S_{13}]^{2-}$ catalyst and H_2A sacrificial donor. Energy levels are based on the relevant literature source.[26]

Stability under turnover conditions. Long-term visible-light-driven HER experiments were performed using Mo_3/Ru and Mo_3/GCN photosystems (details in Experimental section). Figure 5a reveals that the homogeneous Mo_3/Ru couple, despite exhibiting outstanding HER performance (i.e. high TOF values) at the initial stage of the illumination, experiences strong and rapid deactivation, which leads to 8-fold drop in activity after 5 hours. Detailed re-loading experiments confirm that this deactivation is not related solely to the photosensitizer or sacrificial agent depletion, but rather indicate gradual degradation of the $[Mo_3S_{13}]^{2-}$ species (for more details, see ESI section 5 and Figure S9).

In contrast to this, the heterogenized Mo_3/GCN (Figure 5b) shows no pronounced deactivation, but rather stable performance – despite with lower average TOFs – over the time course of 5 hours illumination. XPS of the Mo_3/GCN composites recovered after the HER run indicates that partial loss (dissolution/leaching) of the clusters takes place during the reaction, which is also suggested by the recovered C=N-C contribution of the GCN observed in the N1s edge (see Figure S10 for more details). This result is further in agreement with elemental analyses using TXRF (Table S2), which indicates that only 50% of the original $[Mo_3S_{13}]^{2-}$ species are present in the Mo_3/GCN after HER. In view of the relatively stable HER performance observed for the Mo_3/GCN composites (Figure 5b), however, we can propose that this partial leaching of the $[Mo_3S_{13}]^{2-}$ takes place at the initial stages of the reaction and does not affect long-term HER performance. In fact, detailed Mo 3d and S 2p XPS profiles look qualitatively similar to

View Article Online
DOI: 10.1039/D3SE01658G

those of the as-prepared Mo_3/GCN composite (Figure S10), suggesting that no transformation of the surface-bound Mo_3-species takes place. These remaining $[Mo_3S_{13}]^{2-}$ clusters (1.7 wt.% compared to the original 3.9 wt.% loading) likely constitute stable and active catalytic sites for HER that are able to effectively extract the electrons photogenerated in the GCN support and drive stable H_2 generation.

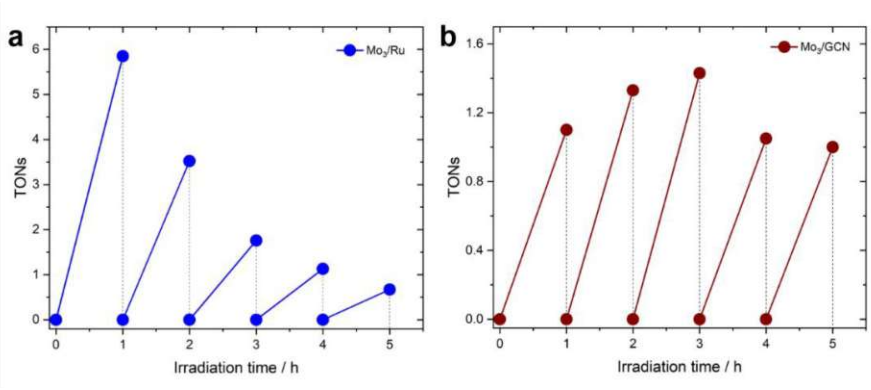

Fig. 5 | **Long-term HER profiles (in H_2A) of (a)** Mo_3/Ru system, and **(b)** Mo_3/GCN system. TONs for Mo_3/GCN system were calculated based on real loadings of $[Mo_3S_{13}]^{2-}$ clusters on GCN mentioned in Table 1. The experiments were conducted using LED 445 nm lamp (see Methods section 4.4.1 for more details).

3. Conclusions

Here, we compared HER performances of homogeneous and heterogeneous photosystems involving all-inorganic molecular $[Mo_3S_{13}]^{2-}$ cluster as an HER site. On one hand, we explored a prototypical homogeneous Mo_3/Ru couple in which visible light excitation leads to a rapid oxidative quenching of $*[Ru(bpy)_3]^{2+}$ (PS*) by the anionic $[Mo_3S_{13}]^{2-}$. When combined with H_2A hole scavenger, this photosystem delivered high TOFs and AQY_{445} values up to 0.5%; it however suffered from rapid photo-degradation. On the other hand, we demonstrated that $[Mo_3S_{13}]^{2-}$ can be immobilized onto the surface of GCN by relying on electrostatic interactions with its triazine/heptazine framework. We show that this heterogenized Mo_3/GCN photosystem could generate H_2 under visible-light with TOF values close to those measured for its homogeneous counterpart. Despite significant leaching of the $[Mo_3S_{13}]^{2-}$ species from the surface of Mo_3/GCN, the rest of the $\{Mo_3\}$-based centers remain structurally intact. They are able to deliver stable long-term HER performance, which is in strong contrast to that of the Mo_3/Ru, which showed photodegradation after 1 hour of photocatalytic reaction. Mechanistic and photoluminescence quenching studies further demonstrated that the performance of Mo_3/GCN may still be largely limited by the extent of the Mo_3/GCN interface and the efficiency of electron-hole separation. These results provide valuable insights into the challenges in activity evaluation and comparison for photosystems that involve well-defined catalytic centers (be it clusters or single-metal-atoms or sites), which will help develop similar surface-supported (photo)catalysts for various energy applications.

4. Experimental section

4.1 Chemicals

The chemicals used for the synthesis were obtained from commercial suppliers and include ammonium molybdate tetrahydrate ($(NH_4)_6[Mo_7O_{24}]\cdot 4H_2O$, Sigma-Aldrich, 99.98% trace metals basis), hydroxylamine hydrochloride ($NH_2OH.HCl$, Sigma-Aldrich, 98.0%, ACS Reagent), ammonium sulfide solution ($(NH_4)_2S_x$, Sigma-Aldrich, 20 wt.% in H_2O), carbon disulfide (CS_2, Sigma-Aldrich, 99.9 %), sodium chloride (NaCl, Carl Roth), sodium hydroxide (NaOH, Carl Roth) and dicyandiamide ($C_2H_4N_4$, 99%, Sigma-Aldrich). The solvents used for

View Article Online
DOI: 10.1039/D3SE01658G

the synthesis were deionized water, ethanol (EtOH, from Chem-Lab NV), HPLC-gradient grade methanol (MeOH, from VWR), diethyl ether (from Sigma-Aldrich), N,N-dimethylformamide (DMF, from Acros Organics, 99.8%, extra dry over the molecular sieve, acroseal).

4.2 Synthetic procedures

Synthesis of $(NH_4)_2[Mo_3S_{13}]$. Following the original works[36], we developed microwave-assisted synthesis where 250 mg of ammonium molybdate tetrahydrate ($(NH_4)_6[Mo_7O_{24}]\cdot 4H_2O$ and 187.5 mg hydroxylamine hydrochloride ($NH_2OH.HCl$) were added to 5 mL of ammonium sulfide solution in 30 mL microwave vial. This mixture was stirred for 30 minutes followed by heating at 150°C for 20 min at a stirring rate of 600 rpm in a microwave furnace set at a pressure of 20 bars. The bright red product was filtered, washed with 50 mL of water, ethanol, CS_2 and ether and dried in air at 60 °C.

Synthesis of $Na_2[Mo_3S_{13}]$. The as-prepared $(NH_4)_2[Mo_3S_{13}]$ was used to synthesize $Na_2[Mo_3S_{13}]$ following a reported method[37], wherein 250 mg of $(NH_4)_2[Mo_3S_{13}]$ was dissolved in 40 mL of 1% NaOH solution and stirred for 2 hours under vacuum. This solution was then filtered into 10% NaCl solution and kept for 12 hours to allow for the formation of $Na_2[Mo_3S_{13}]$ precipitate. The bright red product was dried in air at 60 °C and stored in desiccator.

Synthesis and protonation of GCN. This work employed thermally expanded graphitic carbon nitride (GCN) reported and characterized previously.[27,38] Briefly, a certain quantity of dicyandiamide was loaded into a sealed quartz crucible and placed in a Microwave Muffle Furnace Phoenix™ (CEM Corporative). The temperature was then gradually raised at 2 °C min^{-1} until it reached 450 °C and kept for 30 min. Subsequently, the temperature was further increased from 450 °C to 550 °C at the same rate (2 °C min^{-1}) and held for 60 min under air atmosphere. The collected sample (labeled as bulk) was washed and dried at 100 °C. To enhance the specific surface area of the photocatalyst, a second thermal treatment at 500 °C was applied for 2 h to the bulk material, resulting in GCN photocatalyst with nearly 15-fold increase in the specific surface area (from 7 to 105 m^2/g).

The protonation of GCN was carried out following a procedure already reported[34] wherein GCN was dispersed in 10 mL of 37% HCl solution and stirred for 4 hours at room temperature. The solution was then filtered and washed with water until neutral pH was achieved. The so-modified sample denoted as H-GCN was dried in air at 105°C overnight.

Synthesis of Mo_3/GCN composites. The composites of $Na_2[Mo_3S_{13}]$ cluster with GCN was synthesized by a method reported previously.[22] Briefly, the GCN was dispersed in methanol and sonicated for 2 h. The $Na_2[Mo_3S_{13}]$ solution in methanol (10 wt.% with respect to GCN mass) was then added to the GCN suspension and kept for stirring overnight. After 24 h the composites were filtered and washed with excess of methanol followed by drying in air at 60 °C.

4.3 Methods

UV-Vis spectroscopy was performed on a Jasco V670 UV-Vis spectrometer. The samples were prepared in methanol and aqueous methanol (1:1 vol.) solution with a concentration of 0.05 mM; UV-Vis spectra were recorded in absorbance mode. Absorption spectra of powdered samples were measured in solid-state via diffuse-reflectance spectroscopy (DRS) using $MgSO_4$ and GCN as a reference.

View Article Online
DOI: 10.1039/D3SE01658G

ATR-FTIR spectra of the samples were recorded via PerkinElmer FTIR Spectral UATR-TWO with a spectrum two Universal ATR (Single Reflection Diamond) instrument. Powdered samples were directly loaded onto the sample holder and the spectra were recorded in the region of 4000-400 wavenumbers (cm^{-1}). Raman measurements were performed with a WITec alpha 300 RSA+ Raman microscope equipped with a 488 nm excitation laser (532 nm) maintaining the laser intensity at 5 mW.

The quantitative elemental analysis of the samples was performed with X-ray photoelectron spectroscopy (XPS) using a custom-built SPECS XPS-spectrometer equipped with a monochromatized Al-K_α X-ray source (μ 350) and a hemispherical WAL-150 analyzer (acceptance angle: 60°). To improve the sensitivity of the measurements, Mo_3/TiO_2 samples were prepared and investigated in the form of thin-films (see Additional Methods in SI). This was followed by wet impregnation of the $Na_2[Mo_3S_{13}]$ clusters from methanolic solutions. For a single XPS measurement, pass energies of 100 eV and 30 eV and energy resolutions of 1 eV and 100 meV were used for survey and detail spectra, respectively (excitation energy: 1486.6 eV, beam energy and spot size: 70 W onto 400 μm, angle: 51° to sample surface normal, base pressure: 5×10^{-10} mbar, pressure during measurements: 2×10^{-9} mbar). Data analysis was performed using CASA XPS software, employing transmission corrections (as per the instrument vendor's specifications), Shirley backgrounds and Scofield sensitivity factors. Charge correction was applied so the adventitious carbon peak (C–C peak) was shifted to 284.8 eV binding energy (BE). All content values shown are in units of relative atomic percent (at.%), where the detection limit in survey measurements usually lies around 0.1–1 at.%, depending on the element.

Quantitative determination of the $[Mo_3S_{13}]^{2-}$ cluster loadings was performed by X-ray fluorescence spectroscopy in total reflection geometry (TXRF) using an ATOMIKA 8030C X-ray fluorescence analyzer (Atomika Instruments GmbH, Oberschleissheim, Munich, Germany). The X-ray tube was employed at 50 kV and 47 mA and the selected excitation source was the continuous spectrum of tungsten monochromatized at 35 keV. The samples were excited for 100 s and a Si(Li)-detector was used for X-rays acquisition. The samples were prepared by suspending 1 mg in 1 mL H_2O for 10 minutes (c = 1 mg/mL). 10 μL of a 1000 ppm Yttrium internal standard (for quantification) were added to the suspension, which was subsequently vortexed for 1 min. 5 μL of the suspension with internal standard were drop casted onto a clean quartz reflector, which was then dried for 5 minutes on a hot plate. After this time, the residue was sealed with 5 μL of a 1% PVA solution and dried for further 5 minutes on a hot plate. The absolute amounts of Mo with respect to Y were then quantified based on the calibration curve and the proportion of Mo (K-line) and Y peak (K-line) areas. This calculation yielded real $[Mo_3S_{13}]^{2-}$ loading values presented in Table 1, considering the undisturbed stoichiometry of Mo to S.

Scanning electron microscopy (SEM) images were acquired using an FEI Quanta 250 FEG scanning electron microscope to obtain visual information on the morphology of the samples. Typically, acceleration voltage of 10 kV and secondary electron detection mode were used.

High-angle annular dark field (HAADF) STEM imaging and energy dispersive X-ray spectroscopy (EDS) were performed by using Titan Cubed G2 60-300 (TEM/STEM, FEI Co., now Thermo Fisher Scientific) operated at 300 kV. This microscope has an aberration corrector for STEM (DCOR, CEOS), four-quadrant windowless super-X SDD (silicon drift detector) system. The probe current was ~60 pA for STEM observation as well as EDS. The convergence semi-angle of the electron probe was 18 mrad. The typical probe diameter was less than 0.1 nm. Forward scattered electrons of an angular range from 38 to 184 mrad were detected by a HAADF detector for STEM imaging.

View Article Online
DOI: 10.1039/D3SE01658G

Powder X-ray diffraction (XRD) of $(NH_4)_2[Mo_3S_{13}]$ and $Na_2[Mo_3S_{13}]$ was performed using an XPERT II: PANalytical XPert Pro MPD (Θ–Θ Diffractometer) for the *ex situ* experiments. The sample was placed on a Si sample holder and irradiated with a Cu X-ray source (8.04 keV, 1.5406 Å). The signals were then acquired with Bragg–Brentano Θ/Θ-diffractometer geometry ranging from 5° to 80° degrees using a semiconductor X'Celerator (2.1°) detector. XRD analysis of GCN powder was carried out in a PANalytical X'Pert MPD equipped with an X'Celerator detector and secondary monochromator (Cu Kα λ = 0.154 nm, 50 kV, 40 mA; data recorded at a 0.017° step size, 100 s/step).

Steady state photoluminescence (PL) measurements were performed using PicoQuant FluoTime 300 spectrophotometer. Xe arc lamp (300 W power) was the excitation source, coupled with a double-grating monochromator. The detection system comprised of a PMA Hybrid 07 detector along with a high-resolution double monochromator. The PL properties of homogeneous solutions were observed using 445 nm excitation wavelength whereas 370 nm light excitation was used to probe the PL spectra of heterogeneous catalysts suspended in water; the concentration of each reaction component was set to mimic those from the corresponding HER experiments. The Mo_3/GCN samples were prepared by dispersion of composite in water (0.5 mg/mL), sonication for 30 min, and centrifugation for 30 min. The supernatant solution was diluted with water and 0.1M ascorbic acid. The data was collected and later fitted using EasyTau2 software. The Stern-Volmer treatment was applied to extract the bimolecular rate constant based on the $[Ru(bpy)_3]^{2+}$ lifetime of 198.58 ns measured at 615 nm.

4.4 Photocatalytic experiments

The visible-light-driven hydrogen evolution experiments were carried using a 5 mL batch reactor equipped with a monochromatic LED light source (445±13 nm, Thorlabs SOLIS). For the experiments in homogeneous phase, the reactor was filled with a 2 mL of reaction mixture which comprises of 1:1 MeOH/H_2O containing $[Ru(bpy)_3]^{2+}$ (bpy stands for 2,2′-Bipyridine) as a photosensitizer (0.645 mM), L-ascorbic acid (H_2A) as a proton donor (0.1 M), and the corresponding catalyst $Na_2[Mo_3S_{13}]\cdot H_2O$ (50 μM). For the heterogeneous hydrogen evolution experiments the reactor was filled with 2 mL of water containing 0.5 mg/mL of Mo_3/GCN photocatalyst and 0.1M sacrificial donor (0.1M L-ascorbic acid (H_2A) and triethanolamine (TEOA), details in Figure S7 and S8d). Exposure to ambient light was minimized during the solution mixture preparation and transfer to the reactor. The reaction volume was purged with Ar (15 mL/min) for 10 min to ensure the removal of headspace and dissolved oxygen prior to reaction start. The temperature of the reactor was maintained at 15 °C with a water-cooling system. The reaction mixture was stirred at 600 rpm. The H_2 produced was monitored by sampling the reactor headspace (200 μL) and analyzing its composition via gas chromatography (Shimadzu GC 2030) equipped with a barrier ionization discharge detector and a Micropacked-ST column using helium as a carrier gas. Injections were done with an interval of 30 minutes. The calibration was done using a range of H_2 in argon gas mixtures. A set of blank experiments in the absence of $[Mo_3S_{13}]^{2-}$ was conducted otherwise mimicking the conditions of both the homogeneous and heterogeneous HER tests resulting in negligible (<0.1 nmol) amounts of H_2 generated.

4.4.1 HER stability experiments

Long-term HER experiments for both homogeneous (Mo_3/Ru) and heterogeneous (Mo_3/GCN) systems were performed using purging-degassing method to investigate and compare stability of both. For both the systems, the photocatalytic reaction solutions (for Mo_3/Ru, 50 μM of Mo_3, 0.45 mM of $[Ru(bpy)_3]^{2+}$ in 0.1 M of H_2A and for Mo_3/GCN, 10Mo_3/GCN in 0.1 M H_2A) were

View Article Online
DOI: 10.1039/D3SE01658G

purged with Ar for 10 min. The reaction mixture was then illuminated for 1 h with LED 445 nm and the sampling was done from the headspace for H_2 quantification. The headspace was then degassed and purged again for 10 min before illuminating for 1 more hour. This process was repeated five times to monitor the stability of both the systems.

4.5 TON, TOF, and AQY Calculation

The H_2 concentrations in ppm (derived from the chromatograms) were converted to µmol and turnover numbers (TONs – expressed per $[Mo_3S_{13}]^{2-}$ species) based on reactor parameters and the ideal gas equation. Initial turnover frequencies (TOFs) were calculated after 10 minutes of illumination (in most of the cases a close to linear H_2 evolution trend within the first 60 minutes of HER was observed). The calculation of the apparent quantum yield (AQY) values considered the ratio between the number of reacted electrons and the number of photons absorbed by the reaction solution.[39,40] The latter was extracted using a power meter PM100D (Thorlabs) by measuring photon flux at the reactor position (12 mW/cm^2). To estimate the number of photons absorbed by the reaction solution we first measured intensity of light that reach the detector after passing through the reactor filled with pure solvent, and then measured intensity of light that reached the detector after passing through the reactor filled with Mo_3/Ru photocatalyst dissolved within the solution. The difference between the values indicated amount of light that has been trapped by Mo_3/Ru.

Author contributions

Conceptualization, SB and AC; methodology, SB and AC; formal analysis, SB, JS, PA; investigation, SB, JS, PA, HS, MJS and ES; resources, DE; data curation, SB; writing: original draft preparation, SB; writing: review and editing, SB, JLF and AC; visualization, SB; supervision, CGS, JLF, DE and AC; project administration, AC; funding acquisition, CGS, JLF and AC.

All authors have read and agreed to the published version of the manuscript.

Funding

This research was funded in whole, or in part, by the Austrian Science Fund (FWF) (grant number P32801-N and Cluster of Excellence MECS). The authors would like to thank the financially supported from LA/P/0045/2020 (ALiCE), UIDB/50020/2020 and UIDP/50020/2020 (LSRE-LCM), funded by national funds through FCT/MCTES (PIDDAC). MJS acknowledges FCT funding under the Scientific Employment Stimulus – Institutional Call (CEECINST/00010/2021). Open Access is funded by the Austrian Science Fund (FWF).

Acknowledgments

The authors would like to acknowledge the facilities of the Technische Universität Wien (TU Wien) for technical support and fruitful discussions: X-Ray Center; Analytical Instrumentation Center and Electron Microscopy Center (USTEM). The authors would like to further acknowledge Dr. Sreejith P. Nandan of his support of XRD and PL measurements, Stephen Nagaraju Myakala for his support in samples preparation and Dr. Dogukan H. Apaydin for his support with FTIR measurements.

Conflicts of interest

There are no conflicts of interest to declare.

References

View Article Online
DOI: 10.1039/D3SE01658G

[1] A. Fujishima, K. Honda, *Nature* **1972**, *238*, 37–38.
[2] H. Lyu, T. Hisatomi, Y. Goto, M. Yoshida, T. Higashi, M. Katayama, T. Takata, T. Minegishi, H. Nishiyama, T. Yamada, Y. Sakata, K. Asakura, K. Domen, *Chem. Sci.* **2019**, *10*, 3196–3201.
[3] H. Nishiyama, T. Yamada, M. Nakabayashi, Y. Maehara, M. Yamaguchi, Y. Kuromiya, Y. Nagatsuma, H. Tokudome, S. Akiyama, T. Watanabe, R. Narushima, S. Okunaka, N. Shibata, T. Takata, T. Hisatomi, K. Domen, *Nature* **2021**, *598*, 304–307.
[4] D. Bahnemann, P. Robertson, C. Wang, W. Choi, H. Daly, M. Danish, H. de Lasa, S. Escobedo, C. Hardacre, T. H. Jeon, B. Kim, H. Kisch, W. Li, M. Long, M. Muneer, N. Skillen, J. Zhang, *J. Phys. Energy* **2023**, *5*, 012004.
[5] K. Maeda, K. Domen, *J. Phys. Chem. Lett.* **2010**, *1*, 2655–2661.
[6] Ž. Kovačič, B. Likozar, M. Huš, *ACS Catal.* **2020**, *10*, 14984–15007.
[7] R. Huang, X. Li, W. Gao, X. Zhang, S. Liang, M. Luo, *RSC Adv.* **2021**, *11*, 14844–14861.
[8] S. Subudhi, D. Rath, K. M. Parida, *Catal. Sci. Technol.* **2018**, *8*, 679–696.
[9] R. Lang, T. Li, D. Matsumura, S. Miao, Y. Ren, Y.-T. Cui, Y. Tan, B. Qiao, L. Li, A. Wang, X. Wang, T. Zhang, *Angew. Chem. Int. Ed.* **2016**, *55*, 16054–16058.
[10] G. Gao, Y. Jiao, E. R. Waclawik, A. Du, *J. Am. Chem. Soc.* **2016**, *138*, 6292–6297.
[11] P. Ayala, A. Giesriegl, S. P. Nandan, S. N. Myakala, P. Wobrauschek, A. Cherevan, *Catalysts* **2021**, *11*, 417.
[12] A. I. Nguyen, K. M. Van Allsburg, M. W. Terban, M. Bajdich, J. Oktawiec, J. Amtawong, M. S. Ziegler, J. P. Dombrowski, K. V. Lakshmi, W. S. Drisdell, J. Yano, S. J. L. Billinge, T. D. Tilley, *Proc. Natl. Acad. Sci. U. S. A.* **2019**, *116*, 11630–11639.
[13] C. Copéret, A. Comas-Vives, M. P. Conley, D. P. Estes, A. Fedorov, V. Mougel, H. Nagae, F. Núñez-Zarur, P. A. Zhizhko, *Chem. Rev.* **2016**, *116*, 323–421.
[14] G. Jeantelot, M. Qureshi, M. Harb, S. Ould-Chikh, D. H. Anjum, E. Abou-Hamad, A. Aguilar-Tapia, J.-L. Hazemann, K. Takanabe, J.-M. Basset, *Phys. Chem. Chem. Phys.* **2019**, *21*, 24429–24440.
[15] P. García-García, M. Müller, A. Corma, *Chem. Sci.* **2014**, *5*, 2979–3007.
[16] S. P. Nandan, N. I. Gumerova, J. S. Schubert, H. Saito, A. Rompel, A. Cherevan, D. Eder, *ACS Mater. Au* **2022**, *2*, 505–515.
[17] J. Kibsgaard, T. F. Jaramillo, F. Besenbacher, *Nat. Chem.* **2014**, *6*, 248–253.
[18] M. Dave, A. Rajagopal, M. Damm-Ruttensperger, B. Schwarz, F. Nägele, L. Daccache, D. Fantauzzi, T. Jacob, C. Streb, *Sustain. Energy Fuels* **2018**, *2*, 1020–1026.
[19] J. McAllister, N. A. G. Bandeira, J. C. McGlynn, A. Y. Ganin, Y.-F. Song, C. Bo, H. N. Miras, *Nat. Commun.* **2019**, *10*, 370.
[20] S. Batool, M. Langer, S. N. Myakala, M. Heiland, D. Eder, C. Streb, A. Cherevan, *Adv. Mater.* **n.d.**, *n/a*, 2305730.
[21] F. Guo, Y. Hou, A. M. Asiri, X. Wang, *Chem. Commun.* **2017**, *53*, 13221–13224.
[22] A. Rajagopal, E. Akbarzadeh, C. Li, D. Mitoraj, I. Krivtsov, C. Adler, T. Diemant, J. Biskupek, U. Kaiser, C. Im, M. Heiland, T. Jacob, C. Streb, B. Dietzek, R. Beranek, *Sustain. Energy Fuels* **2020**, *4*, 6085–6095.
[23] Y.-J. Cheng, R. Wang, S. Wang, X.-J. Xi, L.-F. Ma, S.-Q. Zang, *Chem. Commun.* **2018**, *54*, 13563–13566.
[24] T. N. Nguyen, S. Kampouri, B. Valizadeh, W. Luo, D. Ongari, O. M. Planes, A. Züttel, B. Smit, K. C. Stylianou, *ACS Appl. Mater. Interfaces* **2018**, *10*, 30035–30039.
[25] S. Batool, S. P. Nandan, S. N. Myakala, A. Rajagopal, J. S. Schubert, P. Ayala, S. Naghdi, H. Saito, J. Bernardi, C. Streb, A. Cherevan, D. Eder, *ACS Catal.* **2022**, *12*, 6641–6650.
[26] Y. Lei, M. Yang, J. Hou, F. Wang, E. Cui, C. Kong, S. Min, *Chem. Commun.* **2018**, *54*, 603–606.
[27] E. S. Da Silva, N. M. M. Moura, A. Coutinho, G. Dražić, B. M. S. Teixeira, N. A. Sobolev, C. G. Silva, M. G. P. M. S. Neves, M. Prieto, J. L. Faria, *ChemSusChem* **2018**, *11*, 2681–2694.
[28] A. Müller, R. Jostes, W. Jaegermann, R. Bhattacharyya, *Inorganica Chim. Acta* **1980**, *41*, 259–263.

[29] P. D. Tran, T. V. Tran, M. Orio, S. Torelli, Q. D. Truong, K. Nayuki, Y. Sasaki, S. Y. Chiam, R. Yi, I. Honma, J. Barber, V. Artero, *Nat. Mater.* **2016**, *15*, 640–646.
[30] E. Ronge, S. Hildebrandt, M.-L. Grutza, H. Klein, P. Kurz, C. Jooss, *Catalysts* **2020**, *10*, 856.
[31] A. S. Hainer, J. S. Hodgins, V. Sandre, M. Vallieres, A. E. Lanterna, J. C. Scaiano, *ACS Energy Lett.* **2018**, *3*, 542–545.
[32] V. Kumaravel, M. D. Imam, A. Badreldin, R. K. Chava, J. Y. Do, M. Kang, A. Abdel-Wahab, *Catalysts* **2019**, *9*, 276.
[33] J. Kröger, A. Jiménez-Solano, G. Savasci, P. Rovó, I. Moudrakovski, K. Küster, H. Schlomberg, H. A. Vignolo-González, V. Duppel, L. Grunenberg, C. B. Dayan, M. Sitti, F. Podjaski, C. Ochsenfeld, B. V. Lotsch, *Adv. Energy Mater.* **2021**, *11*, 2003016.
[34] Y. Zhang, A. Thomas, M. Antonietti, X. Wang, *J. Am. Chem. Soc.* **2009**, *131*, 50–51.
[35] J. Zhang, F. Guo, X. Wang, *Adv. Funct. Mater.* **2013**, *23*, 3008–3014.
[36] A. Müller, S. Pohl, M. Dartmann, J. P. Cohen, J. M. Bennett, R. M. Kirchner, *Z. Für Naturforschung B* **1979**, *34*, 434–436.
[37] V. P. Fedin, J. Czyzniewska, R. Prins, T. Weber, *Appl. Catal. Gen.* **2001**, *213*, 123–132.
[38] M. J. Sampaio, A. R. L. Ribeiro, C. M. R. Ribeiro, R. A. Borges, M. F. Pedrosa, A. M. T. Silva, C. G. Silva, J. L. Faria, *Chem. Eng. J.* **2023**, *459*, 141617.
[39] A. Cherevan, P. Gebhardt, A. Kunzmann, R. D. Costa, D. Eder, *ACS Appl. Energy Mater.* **2018**, *1*, 1259–1267.
[40] M. Qureshi, K. Takanabe, *Chem. Mater.* **2017**, *29*, 158–167.

Electronic Supporting Information (ESI)

Thiomolybdate Cluster for Visible-Light Driven Hydrogen Evolution: Comparison of Homogeneous and Heterogeneous Approaches

Samar Batool[1], Jasmin S. Schubert[1], Pablo Ayala[1], Hikaru Saito[2], Maria J. Sampaio[3,4], Eliana S. Da Silva[3,4,#], Cláudia G. Silva[3,4], Joaquim L. Faria[3], Dominik Eder[1], Alexey Cherevan[1]*

[1] TU Wien, Institute of Materials Chemistry, Getreidemarkt 9/BC/02, 1060, Vienna, Austria

[2] Institute for Materials Chemistry and Engineering, Kyushu University, 6-1 Kasugakoen, Kasuga, Fukuoka 816-8580, Japan

[3] LSRE-LCM – Laboratory of Separation and Reaction Engineering – Laboratory of Catalysis and Materials, Faculty of Engineering, University of Porto, Rua Dr. Roberto Frias, 4200-465 Porto, Portugal

[4] ALiCE – Associate Laboratory in Chemical Engineering, Faculty of Engineering, University of Porto, Rua Dr. Roberto Frias, 4200-465 Porto, Portugal

 # current address: Departament de Química, Universitat Autònoma de Barcelona, Cerdanyola del Vallès, 08193 Barcelona (Spain)

Contents:

1. Materials characterization

XRD and FTIR of the Mo-Clusters

Successful formation of $[Mo_3S_{13}]^{2-}$ clusters was confirmed using FTIR spectroscopy. Figure S1a shows the FTIR spectra of $Na_2[Mo_3S_{13}]$ revealing three peaks at 542 cm^{-1}, 505 (510/501 doublet) cm^{-1}, and 458 cm^{-1} in the fingerprint region that correspond to bridging, terminal, and apical sulfur ligands in the cluster framework.[1,2] Additionally, only OH bending and stretching vibrations are observed at ~1600 cm^{-1} and ~3300 cm^{-1}, which correspond to residual and crystalline water. The purity of the product (e.g. complete cation exchange) is manifested by no extra peaks observed in the IR spectrum. The purity and crystallinity of the $(NH_4)_2[Mo_3S_{13}]$, $Na_2[Mo_3S_{13}]$, and GCN were further confirmed by powder XRD spectra (Figure S1b) that match well with the literature and the database.[1–3]

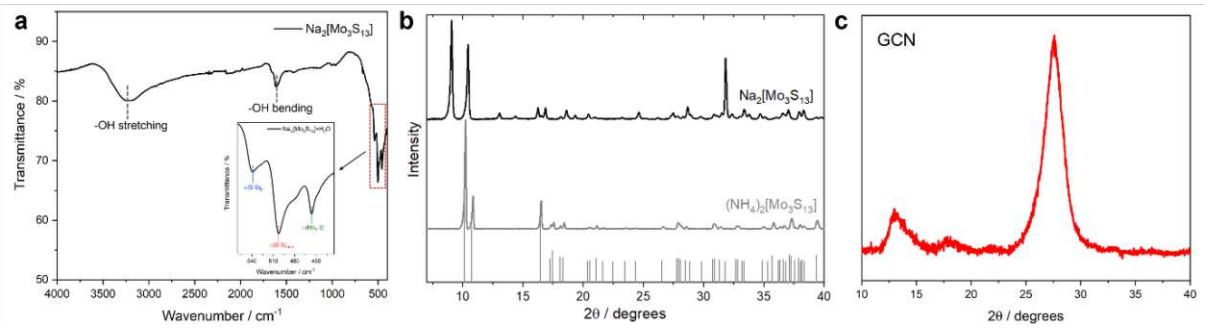

Figure S1 | (a) IR Spectra of $Na_2[Mo_3S_{13}]$, and XRD spectra of **(b)** $Na_2[Mo_3S_{13}]$ and $(NH_4)_2[Mo_3S_{13}]$, **(c)** GCN powder.

DRS

Optoelectronic properties of as-prepared (GCN) and protonated (H-GCN) carbon nitride (details in Experimental section) have been investigated using diffuse-reflectance spectroscopy (DRS). Figure S2a shows as-obtained profiles that highlight strong absorption of both GCN materials in visible-light range (400-700 nm). Tauc analyses (Figure S2b) reveal the band gap of ca. 2.75 eV, which corresponds well to the literature.[4]

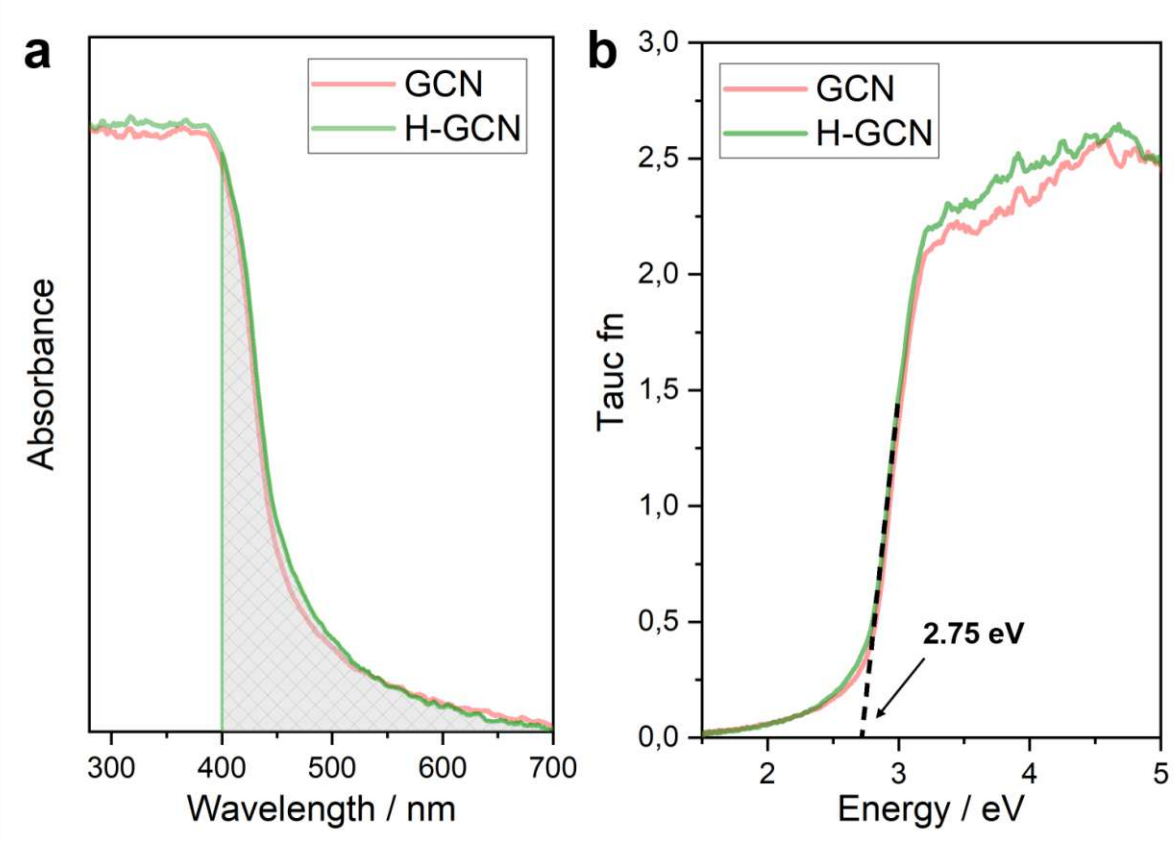

Fig. S2 | DRS plots of **(a)** GCN and H-GCN powders, **(b)** Tauc plots of bare GCN and H-GCN. Shaded area corresponds to the range of visible-light absorption (i.e. >400 nm).

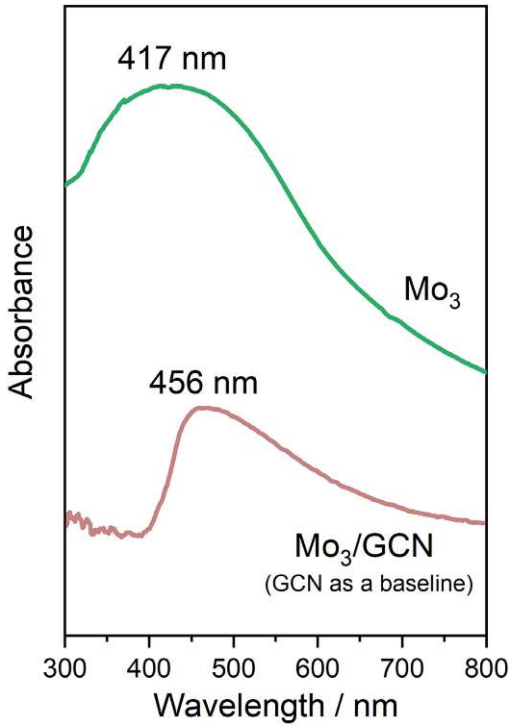

Fig. S3 | DRS plots of $[Mo_3S_{13}]^{2-}$ (Mo_3) and 10Mo_3/GCN composite, the latter is measured taking GCN as a baseline. The broad peak centered at ~456 nm is the qualitative indication for the presence of Mo_3 on the surface of GCN. The quantitative assessment of the loading values is performed via TXRF (Table 1).

FTIR of Mo_3/GCN

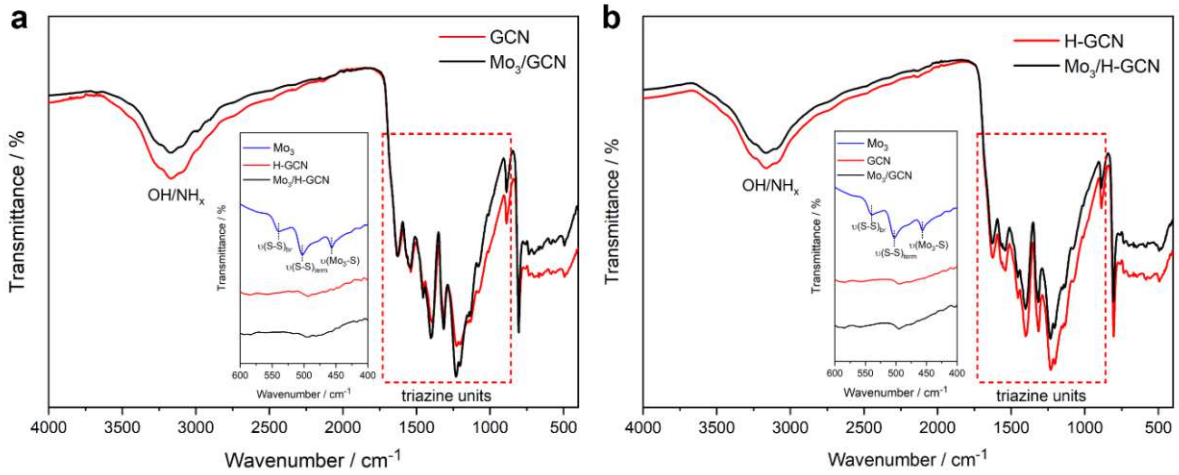

Fig. S4 | FTIR spectra of **(a)** GCN and 10Mo_3/GCN, **(b)** H-GCN and 10Mo_3/H-GCN. Insets from 600-400 cm-1 shows the comparison of signature bands of $[Mo_3S_{13}]^{2-}$ (Mo_3) with GCNs and Mo_3/GCNs.

XPS of Mo_3 and Mo_3/GCN

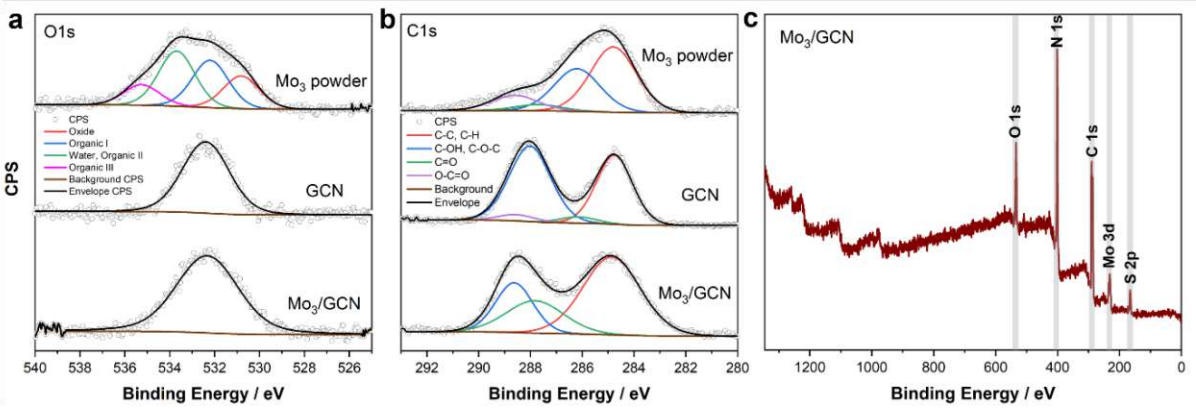

Fig. S5 | XPS spectra **(a)** O1s, **(b)** C1s, of pure $[Mo_3S_{13}]^{2-}$ (Mo_3) clusters, bare GCN, and Mo_3/GCN system. and **(c)** Survey spectra of Mo_3/GCN (see details in experimental section).

2. Choice of photosensitizers and illumination conditions

Comparison of Mo_3/GCN and Mo_3/Ru in terms of excitation source

First, we verified if the heterogenized $[Mo_3S_{13}]^{2-}$ clusters of the Mo_3/GCN composite are able to promote the desired HER under visible-light illumination. Figure 1b compares absorption spectra of the GCN (measured in reflectance mode) and $[Ru(bpy)_3]^{2+}$ (measured in transmission mode) compared to the output spectrum of the visible-light emitter used in this work to evaluate light-driven HER performance of both Mo_3/GCN and Mo_3/Ru. The band gap value of GCN can be estimated to around 2.75 eV (see Figure S2), which allows 445 nm photons to trigger band-to-band excitation (C 2p to N 2p) and generate an electron-hole pair. We note, however, that – compared to the extent of the $[Ru(bpy)_3]^{2+}$ absorption – only edge-to-edge transition in GCN is likely to be triggered by the light source leaving the generated electron-hole pairs with little-to-no overpotential for further reaction.

3. Optimization of HER conditions

Table S1. Optimization of parameters for hydrogen evolution reaction under homogeneous conditions. The concentration of $[Ru(bpy)_3]PF_6$ photosensitizer was kept 0.645 mM for all the experiments mentioned in the table and the reaction mixture was illuminated for 30 min with LED lamp 445 nm.

$[Mo_3S_{13}]^{2-}$ concentration	Solvent	Sacrificial donor	H_2 produced (ppm)	Apparent quantum yield (AQY, %)
10 μM	ACN/H_2O (9:1)	Ascorbic acid (0.1M)	247	0.086
50 μM			515	0.178
10 μM	MeOH/H_2O (9:1)		1100	0.380
50 μM			1508	0.520

*ACN : Acetonitrile, MeOH : Methanol

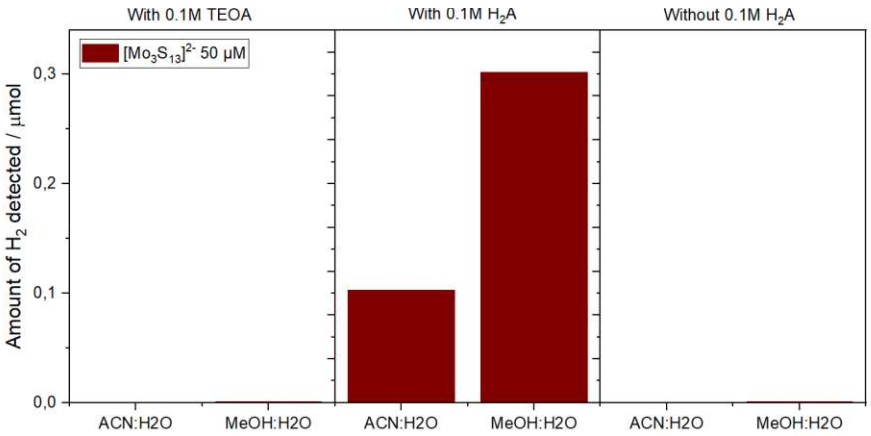

Fig. S6 | Homogeneous HER experiments with and without the addition of electron donor in the photocatalytic system. Conditions: 50 µM $[Mo_3S_{13}]^{2-}$, 0.645 mM $[Ru(bpy)_3]^{2+}$, 0.1M H_2A in MeOH:H_2O (9:1) and ACN:H_2O (9:1) solvent system which is illuminated for 30 min by LED lamp 445 nm.

Overall, several factors are in control of hole scavenging capability of these electron donors (MeOH, TEOA, H_2A): their polarity, which defines the degree of interaction with the photosensitizer (be it a molecule, ion or heterogeneous surface) and their redox properties, which define the thermodynamics of their oxidation.[5–7] However, ascorbic acid (H_2A) produces an intermediate during the hole scavenging process which is reported to oxidize Ru-based PS and therefore reduces the overall hydrogen evolution performance.[5,8] This makes the stability of the Mo_3/Ru photosystem questionable as Ru-PS degrades with increase in illumination time as well as it recombines with oxidized intermediate of ascorbic acid promoting charge recombination. However, when assessing overall HER performance of the photosystem, one should also consider other less direct contributions. First of all, the choice of the solvent system and the associated dielectric constant of the reaction medium affect the final availability of sacrificial donor as well as the efficiency of the charge transfer process.[6] Besides this, the mechanism of electron donor oxidation (via hole trapping) often involves intermediate species that may affect the reaction in a number of ways e.g. act as recombination centers.[5]

4. Photoluminescence emission spectroscopy

Role of sacrificial agent

To verify the role of H_2A as an electron donor in our HER experiments performed with the Mo_3/GCN photosystem, we conducted PL quenching experiments using $[Mo_3S_{13}]^{2-}$-free and $[Mo_3S_{13}]^{2-}$-loaded GCN suspensions in water in and without the presence of H_2A. The reason for this is that the two-electron oxidized species of ascorbate (i.e., dehydroascorbate) as well as radicals generated from H_2A are known to react with the reduced from of the ruthenium dye. Despite the first reaction is slowed by its bimolecular nature, we still consider both being relevant under our reaction conditions.[8,5] As summarized in Figure S7, the addition of 0.1M H_2A to the GCN suspensions ($[Mo_3S_{13}]^{2-}$-free in *a*, with 1 wt.% $[Mo_3S_{13}]^{2-}$ in *b* and with 10 wt.% $[Mo_3S_{13}]^{2-}$ in *c*) reduce the PL intensities in all cases compared to those obtained in pure water. This result confirms the role of H_2A as an efficient hole acceptor, which leads to a better separation of charge carriers photoexcited in GCN under our reaction conditions.

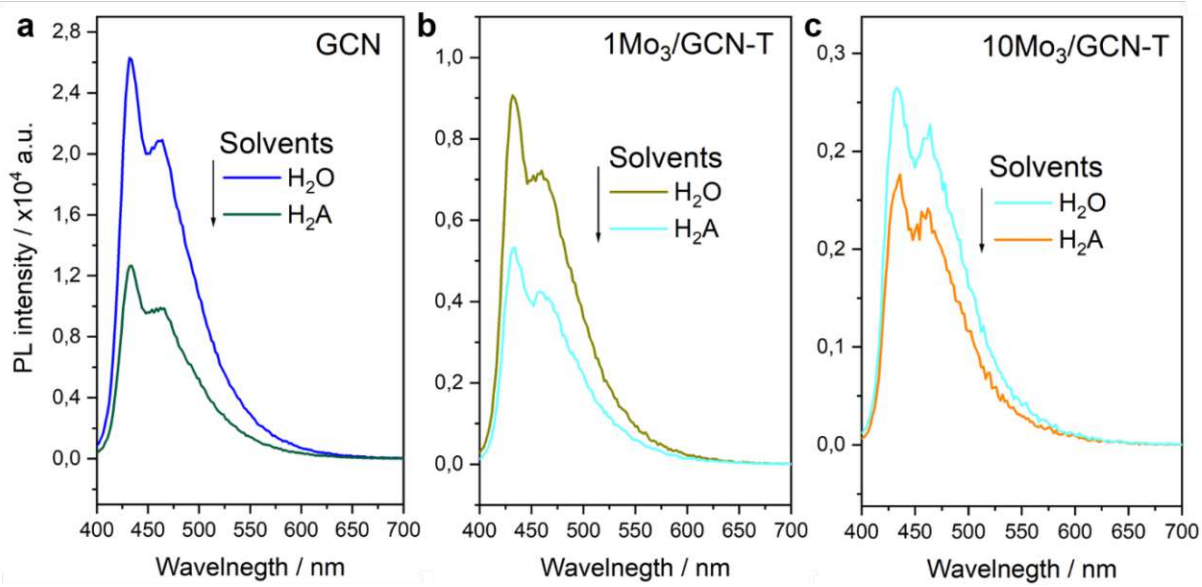

Fig. S7 | PL spectra of **(a)** GCN, **(b)** 1Mo_3/GCN, **(b)** 10Mo_3/GCN, mimicking the photocatalytic HER experiment (see details in experimental section).

Choice of H_2A concentration

To further justify the choice of H_2A concentration (0.1 M) used in our HER experiments performed with the Mo_3/GCN photosystem, we conducted additional PL quenching experiments. Figure 8d shows that the addition of low concentrations (0-0.05 M) of H_2A to Mo_3/GCN gradually reduces the PL emission intensity of GCN, which suggests that reductive quenching mechanism is in place and it leads to improved electron/hole separation (i.e. thus affording higher HER performances). It is noteworthy, however, that higher concentrations of H_2A (> 0.05 M) do not lead to further quenching (i.e. saturation is reached). This result indicates that hole extraction by H_2A is not a performance-limiting factor at H_2A concentrations above ~0.1 M and that the use of this H_2A concentration can be justified when conducting HER studies.

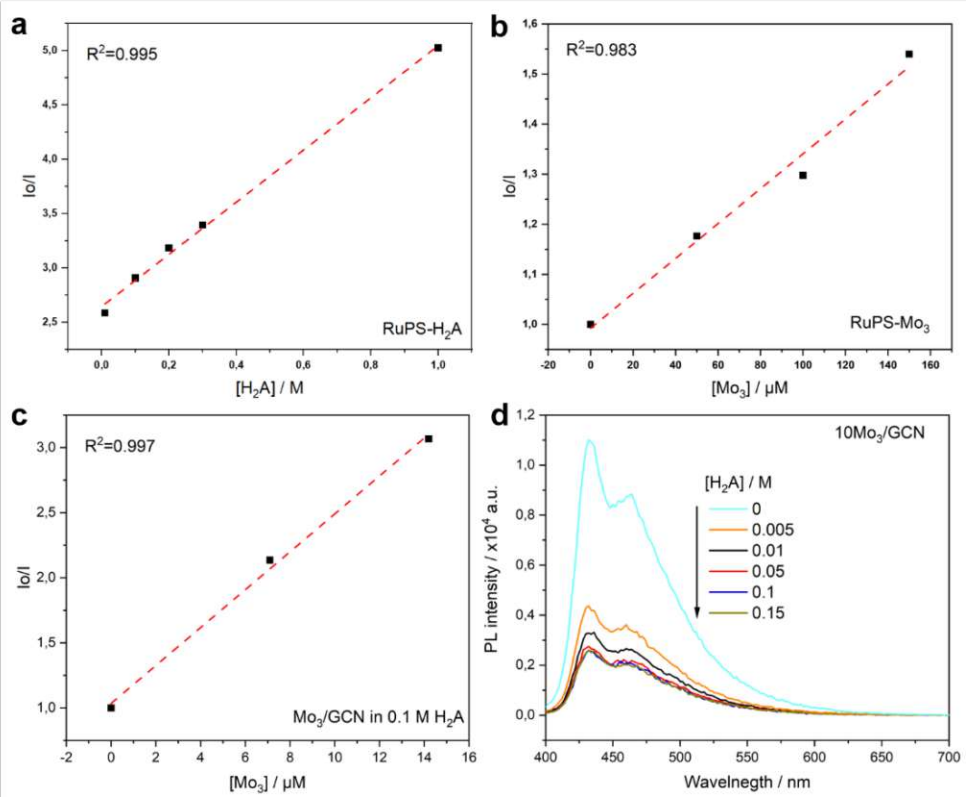

Fig. S8 | Stern-Volmer fitting plots of Mo_3/Ru system with varying concentration of **(a)** H_2A and **(b)** $[Mo_3S_{13}]^{2-}$ **(c)** Mo_3/GCN system with varying concentration of $[Mo_3S_{13}]^{2-}$ (see details in experimental section), **(d)** Mo_3/GCN system with varying H_2A concentration.

5. Reloading experiments

To investigate the stability of $Na_2[Mo_3S_{13}]$ in Mo_3/Ru photosystem, a solution containing 2 mL (4.5:4.5:1) of $[Ru(bpy)_3]^{2+}$ photosensitizer (PS, 0.645 mM in MeOH), the $[Mo_3S_{13}]^{2-}$ catalyst (50 µM in MeOH), and H_2A proton donor (0.1 M in H_2O) solvent mixture was irradiated and the H_2 was detected by gas chromatography until saturated, indicated by a plateau (red curve in Figure S9, the point of 120 min). After this point was reached, the reaction mixture was recharged with 100 µL of a freshly prepared solution of $[Ru(bpy)_3]^{2+}$ photosensitizer (0.645 mM) and 100 µL H_2A to yield 2.2 mL of a reloaded reaction mixture with 545 mM $[Ru(bpy)_3]^{2+}$ PS, 0.9 mM H_2A and 45 µM $[Mo_3S_{13}]^{2-}$, thereby mimicking the initial Mo_3/Ru (1:13) molar ratios of the first HER cycle. Afterwards, sealing, de-gassing and irradiation of the reloaded reaction mixture initiated the second HER cycle (blue curve in Figure S9). In another experiment, after the first HER cycle, the solution was recharged with just the PS (grey curve in Figure S9). Both secondary datasets (grey and blue curves) show that the original activity of the freshly-made Mo_3/Ru photosystem can not be reached when PS (or PS and H_2A) are reloaded. This, in turn, indicates that at least partial degradation of $[Mo_3S_{13}]^{2-}$ takes place along with PS and SA depletion.

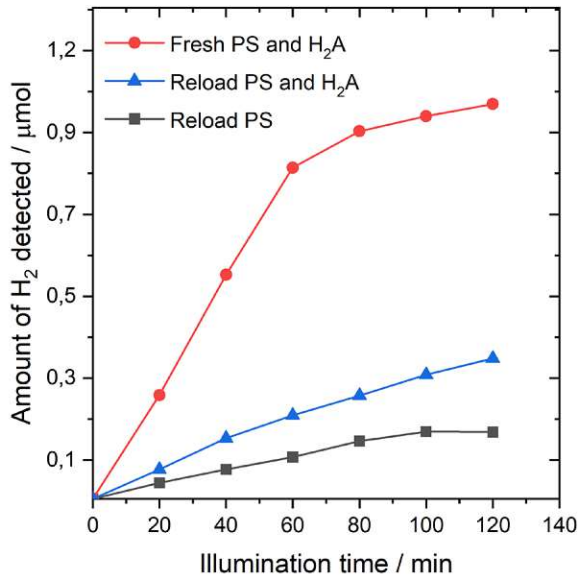

Fig. S9 | Reloading experiments showing the effect of catalytic components on the HER performance. The reaction solution (50 µM $[Mo_3S_{13}]^{2-}$, 0.645 mM $[Ru(bpy)_3]^{2+}$ (PS), and 0.1 M H_2A) after the first HER cycle (red) was recharged with $[Ru(bpy)_3]^{2+}$ (PS) and H_2A (blue) as described above. After purging, the second HER cycle didn't recover the original HER activity. Reloading only the PS after the first HER cycle (grey) accounted for the quarter of original HER activity.

6. Postcatalytic characterization

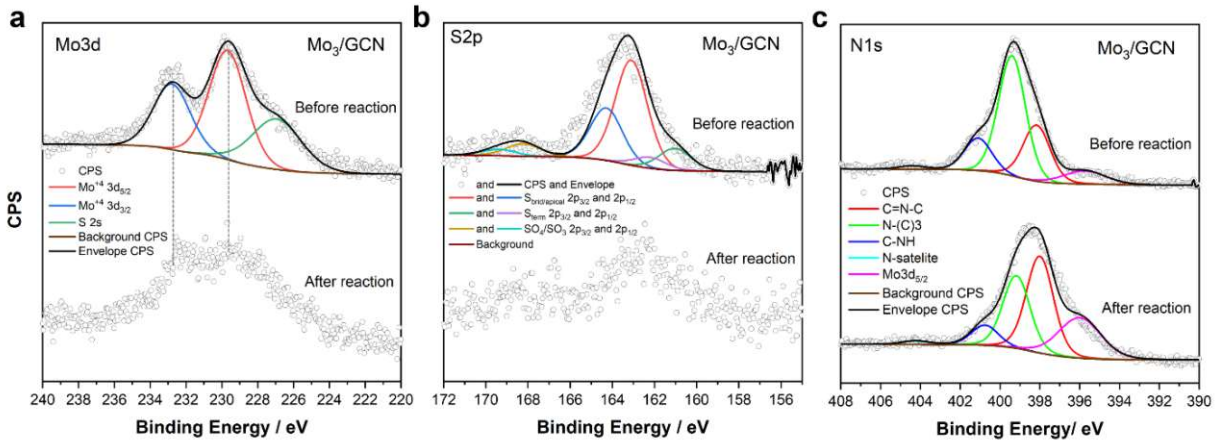

Fig. S10 | XPS spectra **(a)** Mo3d, **(b)** S2p, **(c)** N1s, of the Mo_3/GCN system before and after HER in 0.1M H_2A (see details in experimental section).

Table S2. TXRF of Mo_3/GCN composites before and after hydrogen evolution reaction in ascorbic acid and TEOA sacrificial donors to quantify remaining cluster loadings in wt.%.

Composite	**Loading before HER (wt.%)**	**Loading after HER (wt.%)**	
		0.1M H_2A	0.1M TEOA
Mo_3/GCN	3.9	1.7	0.6

7. References

[1] A. Rajagopal, E. Akbarzadeh, C. Li, D. Mitoraj, I. Krivtsov, C. Adler, T. Diemant, J. Biskupek, U. Kaiser, C. Im, M. Heiland, T. Jacob, C. Streb, B. Dietzek, R. Beranek, *Sustain. Energy Fuels* **2020**, *4*, 6085–6095.

[2] S. Batool, S. P. Nandan, S. N. Myakala, A. Rajagopal, J. S. Schubert, P. Ayala, S. Naghdi, H. Saito, J. Bernardi, C. Streb, A. Cherevan, D. Eder, *ACS Catal.* **2022**, *12*, 6641–6650.

[3] A. Müller, E. Diemann, E. Krickemeyer, H. J. Walberg, H. Bögge, A. Armatage, *Eur. J. SOLID STATE Inorg. Chem.* **1993**, *30*.

[4] E. S. Da Silva, N. M. M. Moura, A. Coutinho, G. Dražić, B. M. S. Teixeira, N. A. Sobolev, C. G. Silva, M. G. P. M. S. Neves, M. Prieto, J. L. Faria, *ChemSusChem* **2018**, *11*, 2681–2694.

[5] Y. Pellegrin, F. Odobel, *Comptes Rendus Chim.* **2017**, *20*, 283–295.

[6] M. Wang, S. Shen, L. Li, Z. Tang, J. Yang, *J. Mater. Sci.* **2017**, *52*, 5155–5164.

[7] X. Zhou, Y. Li, Y. Xing, J. Li, X. Jiang, *Dalton Trans.* **2019**, *48*, 15068–15073.

[8] G. Neshvad, M. Z. Hoffman, *J. Phys. Chem.* **1989**, *93*, 2445–2452.

4.3 Contributions in other publications

During my Ph.D., I developed collaborations on other projects, in which my main contribution was to do the PL measurements of liquid and solid samples, data acquisition, evaluation, discussion, and preparation of the corresponding manuscript parts. The publications of the collaborated work are listed below:

1. Lisa Eisele, Wilaiwan Chaikhan, Samar Batool, Alexey Cherevan, Dominik Eder, Katharina Bica-Schröder*; *Photocatalytic CO_2 reduction co-catalyzed by ionic liquids*, ChemCatChem, accepted.

2. Stephen Nagaraju Myakala, Hannah Rabl, Jasmin S. Schubert, Samar Batool, Pablo Ayala, Dogukan Hazar Apaydin*, Alexey Cherevan*, Dominik Eder; *MOCHAs: An Emerging Class of Materials for Photocatalytic H_2 Production*, advanced energy materials, under revision.

Conclusions and outlook

This thesis was focused on the synthesis of structurally well-defined molecular clusters (Ni-based polyoxometalates and thiomolybdates) and their utilization as catalysts/co-catalysts for photocatalytic hydrogen evolution reaction. The efficiency of these catalysts was investigated under homogeneous and heterogeneous conditions to highlight the advantages and disadvantages of both approaches. This consequently led us to develop a highly stable and entirely inorganic photosystem to curb the limitations and combine the advantages of homogeneous and heterogeneous photocatalysis.

In this thesis, I first presented a review on the recent developments in experimental and theoretical aspects of thiomolybdates catalysis such as the evaluation of reaction mechanisms, investigation of active sites, heterogenization on different substrates, and their prominent applications. I also discussed the studies that inspect the HER performance of thiomolybdates transitioning from the solution-phase to surface-supported, with particular attention towards their application in electrocatalysis and photocatalysis. After thorough analysis and exploration of the pertinent literature, I performed a case study employing Ni-based POMs as catalysts for hydrogen evolution reaction under rigorous homogeneous conditions. The HER performance was shown to be dependent on the number of Ni_4O_4 cubane cores present in the POM structure. Therefore, the high quantum yield exhibited by these Ni-POMs was the highest value for Ni-POMs reported to date. While these POMs demonstrated high stability and recyclability, the overall stability of the system is affected by the use of degradable Ru-dye. Therefore, I designed a model photocatalyst consisting of a solid-state titanium oxide support for stabilizing the molecular thiomolybdate cluster (Mo_3) anchored on its surface. These clusters are attached to the titania surface via hydroxyl groups forming a strong Mo-O-Ti bond. The loading of Mo_3 clusters was limited by the surface area of the oxide support. These clusters acted as highly efficient and stable co-catalyst for hydrogen evolution reaction with performance close to that of the benchmark platinum co-catalyst. It additionally showed a high stability when illuminated for a longer time. The HER activity significantly declined for Mo_3 clusters thermally treated under nitrogen and oxygen atmosphere. This suggested that the structural coherence of Mo_3 clusters plays a crucial role in high HER performance. The loss of most of the terminal disulfide ligands during attachment suggested that the bridging disulfide ligands and the under-coordinated Mo-sites could be the potential active sites for hydrogen evolution reaction. To allow for visible-light-driven hydrogen evolution reaction, I replaced UV-absorbing titania support with graphitic carbon nitride (GCN) for the adsorption of Mo_3 clusters. I used such a configuration for the direct comparison of HER performance with that of the homogeneous counterpart comprising ruthenium photosensitizer. I optimized the hydrogen evolution reaction conditions for both homogeneous (Mo_3/Ru) and heterogeneous systems (Mo_3/GCN). I showed that for Mo_3/Ru system, there is a strong correlation between the activity and the concentration of catalyst as well as the type of sacrificial donor used. However, for Mo_3/GCN system, the activity is influenced by the loading of Mo_3 co-catalyst, the surface area of GCN

support, and the kind of sacrificial donor used. The highest amount of cluster loaded was 3.9 wt.%, however, I successfully achieved a higher loading of clusters by protonating the GCN surface (H-GCN). Despite the different Mo_3 loading values, both Mo_3/GCN and Mo_3/H-GCN photocatalysts displayed similar turnover frequencies (TOFs) of 0.237 min^{-1} and 0.237 min^{-1}. These results suggested that the kinetics of interfacial charge transfer does not limit the charge extraction from GCN. In addition to these studies, the Mo_3/GCN system showed a stable performance over time. On the contrary, the HER activity for Mo_3/Ru system decreased over time. Hereby, this thesis highlights that the heterogenization of molecular clusters on different supports results in the development of stable, robust, and highly efficient photocatalysts for hydrogen evolution reaction. Several factors impact the efficiency of such systems such as the cluster content on the support surface, the strength of binding between the cluster and the support, the surface area of support, and the nature of the sacrificial donor used. Despite careful and extensive investigation of diverse factors and parameters, numerous unresolved issues remain and need to be understood and inquired.

Finally, I present a brief overview of potential future investigations aimed at a more insightful comprehension of photosystems. The replacement of some of the disulfide ligands in Mo_3 with oxo-ligands is capable of affecting the attachment, performance, and active sites. Therefore, I propose the investigation of other complex molecular systems such as thiotungstates, oxothiometalaes, and selenide-containing derivatives other than Mo_3 prototype used in this thesis. Since carbon nitride (GCN) used in article # 4 can only absorb a fragment of the visible light spectrum, the use of substrates capable of absorbing most of the visible spectrum is desirable. Furthermore, being aware of the challenges in the evaluation of HER performance, a photosystem with optimized components can be designed to improve the overall efficiency of reaction. Additionally, thiomolybdates can be merged with functional substrates such as metal-organic frameworks (MOFs), narrow bandgap semiconductors, and polymers, leading to the development of sophisticated composites. In the domain of MOFs chemistry, one study successfully reported the formation of porous frameworks based on thiomolybdates, demonstrating the hydrogen evolution reaction (HER) performance of these innovative materials.[92] Furthermore, another research group developed 2D WS_2 based photoelectrodes immobilizing thiomlybdate and oxothiomolybdate clusters for photoelectrocatalytic water splitting.[93] I am convinced that there is a huge potential for the exploration of a greater variety of functional molecular, hybrid, and solid-state materials through the utilization of thiometalates and their derivatives.

Curriculum vitae

Personal Data

Date of Birth:	30.10.1994
LinkedIn:	https://www.linkedin.com/in/samar-batool-38566a209//
Google scholar:	https://scholar.google.com/citations?user=Iy1rj9sAAAAJhl=enoi=sra
ORCID:	0000-0003-0314-9903
E-mail:	samar.batool@tuwien.ac.at

Education

06.2020 – 02.2024	PhD in Technical Chemistry *Vienna University of Technology, Vienna, Austria* PhD thesis *"Molecular chalcogen-based metalate clusters for light-driven hydrogen evolution reaction"*
10.2016 – 07.2018	Master of Science in Chemistry *Bilkent University, Ankara Turkey* Master thesis *"Cyanoiron polypyridyl sensitized photoanodes for water oxidation"*
10.2013 – 07.2017	Bachelor in Inorganic/Analytical Chemistry *Quaid-I-Azam University, Islamabad Pakistan*

Awards and scholarships

June 2023	Researcher development and travel grant from the Royal Society of Chemistry
June 2020	Fully funded FWF-Austrian Science Fund fellowship for my PhD thesis
Sept. 2017	Graduate research scholarship from Bilkent University for my Master's studies
Sept. 2016	Scholarship of academic excellence from Quaid-I-Azam University

Teachings

09.2017 - 01.2020	Lab assistant for Bachelor laboratory courses *Bilkent University*

Conferences and workshops

07.2023	16^{th} International Conference on Materials Chemistry
Dublin, Ireland	Oral Presentation: $[Mo_3S_{13}]^{2-}$ thiomolybdate cluster as a stable and efficient co-catalyst for photocatalytic hydrogen evolution reaction
06.2022	16^{th} International Conference on Nanostructured Materials
Sevilla, Spain	Oral Presentation: Surface-anchoring and modification of molecular $[Mo_3S_{13}]^{2-}$ cluster co-catalysts for photocatalytic water splitting
09.2021	FemChem Scientific Workshop
Vienna, Austria	Poster Presentation: Molecular thiometalate clusters as co-catalysts for photocatalytic water splitting

References

[1] Payam Nejat, Fatemeh Jomehzadeh, Mohammad Mahdi Taheri, Mohammad Gohari, and Muhd Zaimi Abd. Majid. A global review of energy consumption, co2 emissions and policy in the residential sector (with an overview of the top ten co2 emitting countries). *Renewable and Sustainable Energy Reviews*, 43:843–862, 2015.

[2] Ronald Lee. The outlook for population growth. *Science*, 333(6042):569–573, 2011.

[3] Swapan Kumar Ghosh. Fossil fuel consumption trend and global warming scenario: Energy overview. *Global Journal of Engineering Sciences*, 2020.

[4] Albert Polman, Mark Knight, Erik C. Garnett, Bruno Ehrler, and Wim C. Sinke. Photovoltaic materials: Present efficiencies and future challenges. *Science*, 352(6283):aad4424, 2016.

[5] Victor Gold, editor. *The IUPAC Compendium of Chemical Terminology: The Gold Book*. International Union of Pure and Applied Chemistry (IUPAC), Research Triangle Park, NC, 4 edition, 2019.

[6] Akira Fujishima and Kenichi Honda. Electrochemical Photolysis of Water at a Semiconductor Electrode. *Nature*, 238(5358):37–38, July 1972.

[7] Mimicking natural photosynthesis. *Chemical & Engineering News Archive*, 76(43):37–46, 1998.

[8] Wah Soon Chow. Photosynthesis: From natural towards artificial. *Journal of Biological Physics*, 29:447–459, 2003.

[9] Matthew P. Johnson. Photosynthesis. *Essays in Biochemistry*, 60:255 – 273, 2016.

[10] Naeem Abas, Esmat Kalair, Anam Kalair, Qadeer ul Hasan, and Nasrullah Khan. Nature inspired artificial photosynthesis technologies for hydrogen production: Barriers and challenges. *International Journal of Hydrogen Energy*, 45(41):20787–20799, 2020.

[11] Han Zhou, Runyu Yan, Di Zhang, and Tongxiang Fan. Challenges and perspectives in designing artificial photosynthetic systems. *Chemistry – A European Journal*, 22(29):9870–9885, 2016.

[12] Devens Gust and Thomas A. Moore. A synthetic system mimicking the energy transfer and charge separation of natural photosynthesis. *Journal of Photochemistry*, 29(1):173–184, 1985.

[13] Yiou Wang, Hajime Suzuki, Jijia Xie, Osamu Tomita, David James Martin, Masanobu Higashi, Dan Kong, Ryu Abe, and Junwang Tang. Mimicking natural photosynthesis: Solar to renewable h2 fuel synthesis by z-scheme water splitting systems. *Chemical Reviews*, 118(10):5201–5241, 2018. PMID: 29676566.

[14] Akihiko Kudo and Yugo Miseki. Heterogeneous photocatalyst materials for water splittingw. *Chemical Society Reviews*, 2008.

[15] Shasha Zhu and Dunwei Wang. Photocatalysis: Basic Principles, Diverse Forms of Implementations and Emerging Scientific Opportunities. *Advanced Energy Materials*, 7(23):1700841, 2017.

[16] Dan Kong, Yun Zheng, Marcin Kobielusz, Yiou Wang, Zhiming Bai, Wojciech Macyk, Xinchen Wang, and Junwang Tang. Recent advances in visible light-driven water oxidation and reduction in suspension systems. *Materials Today*, 21(8):897–924, 2018.

[17] Jenny Schneider and Detlef W. Bahnemann. Undesired Role of Sacrificial Reagents in Photocatalysis. *The Journal of Physical Chemistry Letters*, 4(20):3479–3483, October 2013.

[18] Felipe Guzman, Steven S. C. Chuang, and Cheng Yang. Role of methanol sacrificing reagent in the photocatalytic evolution of hydrogen. *Industrial & Engineering Chemistry Research*, 52(1):61–65, 2013.

[19] Krishnamoorthy Sathiyan, Ronen Bar-Ziv, Vered Marks, Dan Meyerstein, and Tomer Zidki. The role of common alcoholic sacrificial agents in photocatalysis: Is it always trivial? *Chemistry – A European Journal*, 27(64):15936–15943, 2021.

[20] Greta M. Haselmann, Bettina Baumgartner, Jia Wang, Karin Wieland, Tushar Gupta, Christopher Herzig, Andreas Limbeck, Bernhard Lendl, and Dominik Eder. In Situ Pt Photodeposition and Methanol Photooxidation on Pt/TiO2: Pt-Loading-Dependent Photocatalytic Reaction Pathways Studied by Liquid-Phase Infrared Spectroscopy. *ACS Catalysis*, 10(5):2964–2977, March 2020.

[21] Hideshi Ooka, Jun Huang, and Kai S. Exner. The sabatier principle in electrocatalysis: Basics, limitations, and extensions. *Frontiers in Energy Research*, 9, 2021.

[22] Jens Kehlet Nørskov, Thomas Bligaard, Ashildur Logadottir, JR Kitchin, Jingguang G Chen, S Pandelov, and U Stimming. Trends in the exchange current for hydrogen evolution. *Journal of The Electrochemical Society*, 152(3):J23, 2005.

[23] R. S. Khnayzer, V. S. Thoi, M. Nippe, A. E. King, J. W. Jurss, K. A. El Roz, J. R. Long, C. J. Chang, and F. N. Castellano. Towards a comprehensive understanding of visible-light photogeneration of hydrogen from water using cobalt(ii) polypyridyl catalysts. *Energy Environ. Sci.*, 7:1477–1488, 2014.

[24] Warrick K. C. Lo, Carmen E. Castillo, Robin Gueret, Jérôme Fortage, Mateusz Rebarz, Michel Sliwa, Fabrice Thomas, C. John McAdam, Geoffrey B. Jameson, David A. McMorran, James D. Crowley, Marie-Noëlle Collomb, and Allan G. Blackman. Synthesis, characterization, and photocatalytic h2-evolving activity of a family of [co(n4py)(x)]n+ complexes in aqueous solution. *Inorganic Chemistry*, 55(9):4564–4581, 2016. PMID: 27064169.

[25] Sebastiano Campagna, Fausto Puntoriero, Francesco Nastasi, Giacomo Bergamini, and Vincenzo Balzani. *Photochemistry and Photophysics of Coordination Compounds: Ruthenium*, pages 117–214. Springer Berlin Heidelberg, Berlin, Heidelberg, 2007.

[26] Michael S. Lowry and Stefan Bernhard. Synthetically tailored excited states: Phosphorescent, cyclometalated iridium(iii) complexes and their applications. *Chemistry – A European Journal*, 12(31):7970–7977, 2006.

[27] Daniel Nnaemaka Tritton, Fung-Kit Tang, Govardhana Babu Bodedla, Fu-Wa Lee, Chak-Shing Kwan, Ken Cham-Fai Leung, Xunjin Zhu, and Wai-Yeung Wong. Development and advancement of iridium(iii)-based complexes for photocatalytic hydrogen evolution. *Coordination Chemistry Reviews*, 459:214390, 2022.

[28] Yue Wang, Xinyu Zhao, Yingnan Zhao, Tianzhi Yang, Xingman Liu, Jiaxin Xie, Guangfu Li, Dongxia Zhu, Huaqiao Tan, and Zhongmin Su. Photosensitizers based on ir(iii) complexes for highly efficient photocatalytic hydrogen generation. *Dyes and Pigments*, 170:107547, 2019.

[29] $[Ru(bpy)_3]^{2+}$ absorption & emission.

[30] Timothy M. Monos and Corey R. J. Stephenson. *Photoredox Catalysis of Iridium(III)-Based Photosensitizers*, chapter 11, pages 541–581. John Wiley Sons, Ltd, 2017.

[31] YuriiV. Geletii, Bogdan Botar, Paul Kögerler, DanielA. Hillesheim, DjamaladdinG. Musaev, and CraigL. Hill. An all-inorganic, stable, and highly active tetraruthenium homogeneous catalyst for water oxidation. *Angewandte Chemie International Edition*, 47(21):3896–3899, 2008.

[32] Andrea Sartorel, Mauro Carraro, Gianfranco Scorrano, Rita De Zorzi, Silvano Geremia, Neal D. McDaniel, Stefan Bernhard, and Marcella Bonchio. Polyoxometalate embedding of a tetraruthenium(iv)-oxo-core by template-directed metalation of [-siw10o36]8: A totally inorganic oxygen-evolving catalyst. *Journal of the American Chemical Society*, 130(15):5006–5007, 2008. PMID: 18345628.

[33] Claude Rocchiccioli-Deltcheff and Michel Fournier. Catalysis by polyoxometalates. part 3.—influence of vanadium(v) on the thermal stability of 12-metallophosphoric acids from in situ infrared studies. *J. Chem. Soc., Faraday Trans.*, 87:3913–3920, 1991.

[34] Jinli Zhao, Yong Ding, Jie Wei, Xiaoqiang Du, Yongze Yu, and Ruixin Han. A molecular keggin polyoxometalate catalyst with high efficiency for visible-light driven hydrogen evolution. *International Journal of Hydrogen Energy*, 39(33):18908–18918, 2014.

[35] Craig L. Hill. Progress and challenges in polyoxometalate-based catalysis and catalytic materials chemistry. *Journal of Molecular Catalysis A: Chemical*, 262(1):2–6, 2007. Polyoxometalates in Catalysis.

[36] James J. Walsh, Alan M. Bond, Robert J. Forster, and Tia E. Keyes. Hybrid polyoxometalate materials for photo(electro-) chemical applications. *Coordination Chemistry Reviews*, 306:217–234, 2016.

[37] Hongjin Lv, Yingnan Chi, Jan vanLeusen, Paul Kögerler, Zheyuan Chen, John Bacsa, Yurii V. Geletii, Weiwei Guo, Tianquan Lian, and Craig L. Hill. [Ni4(OH)3AsO44(b--pw9o34)4]28: A new polyoxometalate structural family with catalytic hydrogen evolution activity. *Chemistry – A European Journal*, 21(48):17363–17370, 2015.

[38] Hongjin Lv, Jie Song, Haiming Zhu, Yurii V. Geletii, John Bacsa, Chongchao Zhao, Tianquan Lian, Djamaladdin G. Musaev, and Craig L. Hill. Visible-light-driven hydrogen evolution from water using a noble-metal-free polyoxometalate catalyst. *Journal of Catalysis*, 307:48–54, 2013.

[39] Hongjin Lv, Weiwei Guo, Kaifeng Wu, Zheyuan Chen, John Bacsa, Djamaladdin G. Musaev, Yurii V. Geletii, Sarah M. Lauinger, Tianquan Lian, and Craig L. Hill. A noble-metal-free, tetra-nickel polyoxotungstate catalyst for efficient photocatalytic hydrogen evolution. *Journal of the American Chemical Society*, 136(40):14015–14018, 2014. PMID: 25243410.

[40] Minrui Gao, Wenchao Sheng, Zhongbin Zhuang, Qianrong Fang, Shuang Gu, Jun Jiang, and Yushan Yan. Efficient water oxidation using nanostructured -nickel-hydroxide as an electrocatalyst. *Journal of the American Chemical Society*, 136(19):7077–7084, 2014. PMID: 24761994.

[41] Lihua Yao, Ding Wei, Yuanman Ni, Dongpeng Yan, and Changwen Hu. Surface localization of cdzns quantum dots onto 2d g-c3n4 ultrathin microribbons: Highly efficient visible light-induced h2-generation. *Nano Energy*, 26:248–256, 2016.

[42] Vincent Artero and Marc Fontecave. Some general principles for designing electrocatalysts with hydrogenase activity. *Coordination Chemistry Reviews*, 249(15):1518–1535, 2005. Hydrogenases.

[43] Monte L. Helm, Michael P. Stewart, R. Morris Bullock, M. Rakowski DuBois, and Daniel L. DuBois. A synthetic nickel electrocatalyst with a turnover frequency above 100,000 s^{−1} for h₂ production. *Science*, 333(6044):863–866, 2011.

[44] Ping Liu and José A. Rodriguez. Catalysts for hydrogen evolution from the [nife] hydrogenase to the ni2p(001) surface: the importance of ensemble effect. *Journal of the American Chemical Society*, 127(42):14871–14878, 2005. PMID: 16231942.

[45] Xin-Bao Han, Chao Qin, Xin-Long Wang, Yuan-Zhi Tan, Xin-Jing Zhao, and En-Bo Wang. Bio-inspired assembly of cubane-adjustable polyoxometalate-based high-nuclear nickel clusters for visible light-driven hydrogen evolution. *Applied Catalysis B: Environmental*, 211:349–356, 2017.

[46] Y. Pan and M. Wen. Noble metals enhanced catalytic activity of anatase tio2 for hydrogen evolution reaction. *International Journal of Hydrogen Energy*, 43(49):22055–22063, 2018.

[47] Shuang Liang, Guanting He, Guozhe Sui, Jinlong Li, Dongxuan Guo, Ze Luo, Rongping Xu, Hong Yao, Chao Wang, and Zhiyong Xing. Zif-l-derived c-doped zno via a two-step calcination for enhanced photocatalytic hydrogen evolution. *Journal of Molecular Structure*, 1276:134787, 2023.

[48] Zhaoyong Lin, Chun Du, Bo Yan, and Guowei Yang. Amorphous fe2o3 for photocatalytic hydrogen evolution. *Catal. Sci. Technol.*, 9:5582–5592, 2019.

[49] Shaofeng Li, Kexin Long, Xianke Sun, Honglei Yuan, and Wei Li. Activities in photocatalytic hydrogen evolution of in2o3/in2s3 heterostructure and in2o3/in2s3@pan nanofibers. *Ceramics International*, 49(14, Part A):24093–24099, 2023.

[50] H. Pan, S. Zhu, X. Lou, L. Mao, J. Lin, F. Tian, and D. Zhang. Graphene-based photocatalysts for oxygen evolution from water. *RSC Adv.*, 5:6543–6552, 2015.

[51] Wan Zhao, Zhi Chen, Xiuru Yang, Xiaoxiao Qian, Chunxi Liu, Dantong Zhou, Tao Sun, Ming Zhang, Guoying Wei, Pavani Dulanja Dissanayake, and Yong Sik Ok. Recent advances in photocatalytic hydrogen evolution with high-performance catalysts without precious metals. *Renewable and Sustainable Energy Reviews*, 132:110040, 2020.

[52] Akira Fujishima, Xintong Zhang, and Donald A. Tryk. Tio2 photocatalysis and related surface phenomena. *Surface Science Reports*, 63(12):515–582, 2008.

[53] Christopher G. Thomson, Ai-Lan Lee, and Filipe Vilela. Heterogeneous photocatalysis in flow chemical reactors. *Beilstein Journal of Organic Chemistry*, 16:1495–1549, 2020.

[54] Hui Yan, Xudong Wang, Man Yao, and Xiaojie Yao. Band structure design of semiconductors for enhanced photocatalytic activity: The case of tio2. *Progress in Natural Science: Materials International*, 23(4):402–407, 2013.

[55] Haowei Peng, Jingbo Li, Shu-Shen Li, and Jian-Bai Xia. First-principles study of the electronic structures and magnetic properties of 3d transition metal-doped anatase tio2. *Journal of Physics: Condensed Matter*, 20(12):125207, feb 2008.

[56] M Landmann, E Rauls, and W G Schmidt. The electronic structure and optical response of rutile, anatase and brookite tio2. *Journal of Physics: Condensed Matter*, 24(19):195503, apr 2012.

[57] W. H. Baur and A. A. Khan. Rutile-type compounds. IV. SiO_2, GeO_2 and a comparison with other rutile-type structures. *Acta Crystallographica Section B*, 27(11):2133–2139, Nov 1971.

[58] Refinement of the structure of anatase at several temperatures*. *Zeitschrift für Kristallographie*, 136(3-4):273–281, 1972.

[59] L. Kavan, M. Grätzel, S. E. Gilbert, C. Klemenz, and H. J. Scheel. Electrochemical and photoelectrochemical investigation of single-crystal anatase. *Journal of the American Chemical Society*, 118(28):6716–6723, 1996.

[60] Yasuhiro Yamada and Yoshihiko Kanemitsu. Determination of electron and hole lifetimes of rutile and anatase TiO2 single crystals. *Applied Physics Letters*, 101(13):133907, 09 2012.

[61] Yusuke Kakuma, Atsuko Y. Nosaka, and Yoshio Nosaka. Difference in tio2 photocatalytic mechanism between rutile and anatase studied by the detection of active oxygen and surface species in water. *Phys. Chem. Chem. Phys.*, 17:18691–18698, 2015.

[62] Xiaodan Chen, Seyed Naveed Hosseini, and Marijn A. van Huis. Heating-induced transformation of anatase tio2 nanorods into rock-salt tio nanoparticles: Implications for photocatalytic and gas-sensing applications. *ACS Applied Nano Materials*, 5(1):1600–1606, 2022.

[63] N. Ramesh Reddy, U. Bhargav, M. Mamatha Kumari, K.K. Cheralathan, and M. Sakar. Review on the interface engineering in the carbonaceous titania for the improved photocatalytic hydrogen production. *International Journal of Hydrogen Energy*, 45(13):7584–7615, 2020. 2nd International Conference on Sustainable Environment and Energy (ICSEE-2019).

[64] M.B. Tahir, Abdullah M. Asiri, and Tasmia Nawaz. A perspective on the fabrication of heterogeneous photocatalysts for enhanced hydrogen production. *International Journal of Hydrogen Energy*, 45(46):24544–24557, 2020.

[65] Xinchen Wang, Kazuhiko Maeda, Arne Thomas, Kazuhiro Takanabe, Gang Xin, Johan M Carlsson, Kazunari Domen, and Markus Antonietti. A metal-free polymeric photocatalyst for hydrogen production from water under visible light. *Nature materials*, 8(1):76–80, 2009.

[66] Yuanjian Zhang, Arne Thomas, Markus Antonietti, and Xinchen Wang. Activation of carbon nitride solids by protonation: Morphology changes, enhanced ionic conductivity, and photoconduction experiments. *Journal of the American Chemical Society*, 131(1):50–51, 2009. PMID: 19072044.

[67] Jiuqing Wen, Jun Xie, Xiaobo Chen, and Xin Li. A review on g-c3n4-based photocatalysts. *Applied Surface Science*, 391:72–123, 2017. 2nd International Symposium on Energy and Environmental Photocatalytic Materials.

[68] Shengming Yin, Jianyu Han, Tianhua Zhou, and Rong Xu. Recent progress in g-c3n4 based low cost photocatalytic system: activity enhancement and emerging applications. *Catal. Sci. Technol.*, 5:5048–5061, 2015.

[69] Jinshui Zhang, Jianhua Sun, Kazuhiko Maeda, Kazunari Domen, Ping Liu, Markus Antonietti, Xianzhi Fu, and Xinchen Wang. Sulfur-mediated synthesis of carbon nitride: Band-gap engineering and improved functions for photocatalysis. *Energy Environ. Sci.*, 4:675–678, 2011.

[70] Pramila Murugesan, JA Moses, and C Anandharamakrishnan. Photocatalytic disinfection efficiency of 2d structure graphitic carbon nitride-based nanocomposites: a review. *Journal of Materials Science*, 54(19):12206–12235, 2019.

[71] Berit Hinnemann, Poul Georg Moses, Jacob Bonde, Kristina P. Jørgensen, Jane H. Nielsen, Sebastian Horch, Ib Chorkendorff, and Jens K. Nørskov. Biomimetic hydrogen evolution: mos2 nanoparticles as catalyst for hydrogen evolution. *Journal of the American Chemical Society*, 127(15):5308–5309, 2005. PMID: 15826154.

[72] Thomas F. Jaramillo, Kristina P. Jørgensen, Jacob Bonde, Jane H. Nielsen, Sebastian Horch, and Ib Chorkendorff. Identification of active edge sites for electrochemical h₂ evolution from mos₂ nanocatalysts. *Science*, 317(5834):100–102, 2007.

[73] Hemamala I. Karunadasa, Elizabeth Montalvo, Yujie Sun, Marcin Majda, Jeffrey R. Long, and Christopher J. Chang. A molecular mos₂ edge site mimic for catalytic hydrogen generation. *Science*, 335(6069):698–702, 2012.

[74] Se Won Seo, Sangbaek Park, Hui-Yun Jeong, Sang Hyeon Kim, Uk Sim, Chan Woo Lee, Ki Tae Nam, and Kug Sun Hong. Enhanced performance of natao3 using molecular cocatalyst [mo3s4]4+ for water splitting into h2 and o2. *Chem. Commun.*, 48:10452–10454, 2012.

[75] M. Dave, A. Rajagopal, M. Damm-Ruttensperger, B. Schwarz, F. Nägele, L. Daccache, D. Fantauzzi, T. Jacob, and C. Streb. Understanding homogeneous hydrogen evolution reactivity and deactivation pathways of molecular molybdenum sulfide catalysts. *Sustainable Energy Fuels*, 2:1020–1026, 2018.

[76] Rongguo Zhang, Kewei Gong, Fuying Du, and Shunan Cao. Highly efficient thiomolybdate [mo2s12]2- nanocluster cocatalyst decorated on tio2 to boost photocatalytic hydrogen evolution. *International Journal of Hydrogen Energy*, 47(45):19570–19579, 2022. The Fifth International Hydrogen Technologies Congress.

[77] Achim Müller, Sabyasachi Sarkar, Ram Gopal Bhattacharyya, Siegfried Pohl, and Mechtild Dartmann. Directed synthesis of [mo3s13]2, an isolated cluster containing sulfur atoms in three different states of bonding. *Angewandte Chemie International Edition in English*, 17(7):535–535, 1978.

[78] Wikipedia contributors. Geology applications of fourier transform infrared spectroscopy — Wikipedia, the free encyclopedia, 2023. [Online; accessed 28-January-2024].

[79] JASCO. Instrumentation of a uv-visible spectrophotometer.

[80] JASCO. Diffuse reflectance and integrating spheres.

[81] Sulochanadevi Baskaran. Structure and regulation of yeast glycogen synthase. 01 2010.

[82] Alex von Bohlen. Total reflection x-ray fluorescence and grazing incidence x-ray spectrometry — tools for micro- and surface analysis. a review. *Spectrochimica Acta Part B: Atomic Spectroscopy*, 64(9):821–832, 2009.

[83] TGA instruments.

[84] Phuong Vuong. *Optical spectroscopy of boron nitride heterostructures*. Theses, Université Montpellier, October 2018.

[85] What is fluorescence spectroscopy?

[86] Gas chromatography fundamentals.

[87] Overview of gas chromatography.

[88] Samar Batool, Marcel Langer, Stephen Nagaraju Myakala, Magdalena Heiland, Dominik Eder, Carsten Streb, and Alexey Cherevan. Thiomolybdate clusters: from homogeneous catalysis to heterogenization and active sites. *Advanced Materials*, n/a(n/a):2305730.

[89] Elias Tanuhadi, Joan Cano, Samar Batool, Alexey Cherevan, Dominik Eder, and Annette Rompel. Ni12 tetracubane cores with slow relaxation of magnetization and efficient charge utilization for photocatalytic hydrogen evolution. *J. Mater. Chem. C*, 10:17048–17052, 2022.

[90] Samar Batool, Sreejith P. Nandan, Stephen Nagaraju Myakala, Ashwene Rajagopal, Jasmin S. Schubert, Pablo Ayala, Shaghayegh Naghdi, Hikaru Saito, Johannes Bernardi, Carsten Streb, Alexey Cherevan, and Dominik Eder. Surface anchoring and active sites of [mo3s13]2– clusters as co-catalysts for photocatalytic hydrogen evolution. *ACS Catalysis*, 12(11):6641–6650, 2022.

[91] Samar Batool, Jasmin S. Schubert, Pablo Ayala, Hikaru Saito, Maria J Sampaio, Eliana Sousa Da Silva, Cláudia Gomes Silva, Joaquim Faria, Dominik Eder, and Alexey S. Cherevan. Thiomolybdate cluster for visible-light driven hydrogen evolution: comparison of homogeneous and heterogeneous approaches. *Sustainable Energy Fuels*, pages –, 2024.

[92] Zhe Ji, Christopher Trickett, Xiaokun Pei, and Omar M. Yaghi. Linking molybdenum–sulfur clusters for electrocatalytic hydrogen evolution. *Journal of the American Chemical Society*, 140(42):13618–13622, 2018. PMID: 30299951.

[93] Juliana Barros Barbosa, Pierre Louis Taberna, Valerie Bourdon, Iann C. Gerber, Romuald Poteau, Andrea Balocchi, Xavier Marie, Jerome Esvan, Pascal Puech, Antoine Barnabé, Lucianna Da Gama Fernandes Vieira, Ionut-Tudor Moraru, and Jean Yves Chane-Ching. Mo thio and oxo-thio molecular complexes film as self-healing catalyst for photocatalytic hydrogen evolution on 2d materials. *Applied Catalysis B: Environmental*, 278:119288, 2020.